Aberystwyth University

Doctoral Thesis

Axisymmetric Problems Involving Fractures with Moving Boundaries

Author:
Daniel Peck

Supervisor:
Prof. Gennady Mishuris

A thesis submitted in fulfillment of the requirements for the degree of Doctor of Mathematics

in the

Department of Mathematics

May 1, 2018

Declaration of Authorship

Word count of thesis: _____

Declaration:
This work has not previously been accepted in substance for any degree and is not being concurrently submitted in candidature for any degree.

Candidate Name: _____

Signed: _____

Date: _____

Statement 1:
This thesis is the result of my own investigations, except where otherwise stated. Where correction services[1] have been used, the extent and nature of the correction is clearly marked in a footnote(s).

Other sources are acknowledged by footnotes giving explicit references. A bibliography is appended.

Signed: _____

Date: _____

Statement 2:
I hereby give consent for my thesis, if accepted, to be available for photocopying and for inter-library loan, and for the title and summary to be made available to outside organisations.

Signed: _____

Date: _____

[1] this refers to the extent to which the text has been corrected by others

ABERYSTWYTH UNIVERSITY

Abstract

Department of Mathematics
Institute of Mathematics, Physics and Computer Science

Doctor of Mathematics

Axisymmetric Problems Involving Fractures with Moving Boundaries

by Daniel Peck

In this thesis, the class of axisymmetrical problems with moving boundaries, which are related to fracture, is considered. This is achieved through investigations into three separate examples; solid particle erosion, hydraulic fracturing, and particles in the Hele-Shaw cell. In this way, the methods used to study such problems will be demonstrated.

The first examination considers the case of an axisymmetric indenter, defined by a power law, impacting an elastic medium. The primary motivation of this work is to determine the cause of the threshold fracture paradox, which concerns the relationship between the indenter shape and the initial energy required to cause a fracture in the impacted medium. In this study, the formation of cracks is determined through an incubation time based approach, which accounts for the dynamic nature of the impact. The effect of incorporating inertial terms in the medium is also examined, and the implications for the study of high velocity impacts by small indenters are discussed.

Next, the problem of a radial (penny-shaped) hydraulic fracture is considered, with a 3D axisymmetric crack forming around a point source in the center. The aim of this effort is to provide a high accuracy numerical solver, based on an explicit level set algorithm. This is achieved through application of the proper Stefan-type condition, which describes the moving boundary, alongside extensive use of the known relationships between the parameters crack-tip asymptotics. Two cases are considered; the first is the classical formulation, while the second incorporates the effect of tangential stress induced by the fluid on the fracture walls. The level of computational error is determined against newly constructed analytical benchmarks. The obtained solutions are used to determine the accuracy of other results available in the literature.

Finally, the case of multiple moving particles and stationary obstacles inside the Hele-Shaw cell is examined. The boundary is assumed to be free-moving, with additional fluid entering or leaving the system through a point source at the origin. The evolution of the fluid boundary is modeled based on a Green's function approach, which is approximated asymptotically. A numerical solver is developed to provide high accuracy approximations for the systems development over time, which also accounts for collisions between the particles. A method of utilizing this model to study the apparent viscosity of fluids used in hydraulic fracturing is outlined.

Acknowledgements

First and foremost, I would like thank my supervisor Prof. Gennady Mishuris. None of this would have been possible without his constant encouragement, support and guidance. I can not imagine having a better supervisor.

I would also like to express my gratitude to my coauthors: Dr Gregory Volkov, Prof. Sergei Rogosin, Prof. Yuri Petrov and Dr. Monika Perkowska, for their help and advice. In particular I would like to thank Dr Michal Wrobel, from whom I learnt a huge amount during these few years. I am also grateful to Dr Mike Nieves for taking the time to explain his work to me, and to Dr Adam Vellender for the advice he gave me throughout the course of my PhD.

I acknowledge the support of the EU FP7 Marie Curie grant scheme, which enabled me to undertake this research project, and to attend numerous conferences and workshops. In particular, the grants HYDROFRAC (PIAP-GA-2009-251475-HYDROFRAC), PARM2 (PIAP-GA-2012-284544-PARM2) and TAMER (IRSES-GA-2013-610547). I would also like to thank all of the staff in the Department of Mathematics, whose direct assistance and work behind the scenes over my 8 years at Aberystwyth University have made this possible. I'm indebted to everyone at Eurotech, ISOTOP and the V.N. Bakul Institute for Superhard Materials for everything they did to make my visits more enjoyable, and to make me feel at home.

Finally, I'd like to extend my thanks to Maud Becker for being such a good friend over the last 4 years, and always being there for me. To the fellow members of Gennady's research group, for the kindness you've shown. Last, but certainly not least, I greatly appreciate the support my family has shown during my time in Aberystwyth, in particular my parents, without which I would never have made it this far.

Contents

List of Figures

List of Tables

Nomenclature

$a(t)$	contact radius	m
B	shape constant	m
c	wave-speed in the medium	m/s
c_k	drag coefficient of particle k	
E	Young's modulus	$\mathrm{N/m^2}$
G	Incubation time based fracture criterion	
$K_{\{I,f\}}$	stress or shear-stress intensity factor	$\mathrm{Nm^{-3/2}}$
K_{Ic}	material toughness	$\mathrm{Nm^{-3/2}}$
$l(t)$	fracture length	m
l_*	initial (non-zero) fracture length	m
m	mass	kg
M	fluid consistency index	$\mathrm{Ns^n/m^2}$
n	fluid behaviour index	
N	number of nodes used in simulations	
p_0	mean contact pressure	$\mathrm{N/m^2}$
$p(r,t)$	pressure distribution	$\mathrm{N/m^2}$
P	total contact pressure	N
$q(r,t)$	fluid flow rate	$\mathrm{m^2/s}$
$q_l(r,t)$	fluid leak-off rate	m/s
Q_0	fluid pumping rate	$\mathrm{m^3/s}$
r^*	position of initial fracture	m
$S(w)$	contact area	$\mathrm{m^3}$
t_0	half-time of erosion impact	s
t_*	duration of supersonic impact stage	s
t_{**}	total impact duration	s
t^*	time of initial fracture	s
$v(r,t)$	(particle) velocity	m/s
$v_k(t)$	$\mathrm{k^{th}}$ asymptotic coefficient of the particle aperture	
V	volume	$\mathrm{m^3}$
$w(r,t)$	moving boundary wall (aperture or fluid front)	m

$w_*(r)$	initial (non-zero) fracture aperture	m
$w_k(t)$	k^{th} asymptotic coefficient of the aperture	
$z_0(t)$	position of particle center	
$\mathcal{G}$	Green's function	
$\mathcal{K}$	Kernel function	
$\mathcal{M}$	Kernel function	
δf	relative error/deviation of function f	
ϵ	radius of a particle/obstacle	m
ϵ_0	initial energy	J
$\gamma(r,t)$	criterion function	
$\Gamma(t)$	free fluid boundary	
κ_k	friction coefficient	
λ	shape parameter	
λ^*	critical shape parameter	
ν	Poisson ratio	
μ	viscosity	$\mathrm{Ns/m^2}$
$\Omega(t)$	open simply connected domain	
$\Omega(r,t)$	modified pressure derivative	$\mathrm{Nm^{-3}}$
$\Phi(r,t)$	reduced particle velocity	$\mathrm{m^2/s}$
ρ	normalized radial coordinate	
$\rho_{\{0,m,f\}}$	density of the indenter, medium or fluid	$\mathrm{kg/m^3}$
$\sigma_{\{r,\theta,z\}}(r,t)$	stress function in the r, θ or z direction	$\mathrm{Nm^{-2}}$
σ_c	tensile stress	$\mathrm{Nm^{-2}}$
σ^*_{max}	critical stress amplitude	$\mathrm{Nm^{-2}}$
τ	incubation time of fracture process (constant)	s
$\omega(t)$	shape function of an impact loading pulse	
$\Upsilon(t)$	gluing function	

Chapter 1

Introduction

1.1 Motivation

In the course of this work, the problems which will be examined meet four fundamental requirements. The first is that the problems are axisymmetric in nature, with a 1D examination of the problem being able to provide a three-dimensional picture of the physical process. In addition, these problems will involve free boundaries whose position is, in principle, unknown. These boundaries will also be moving and evolving over time, according to some specific condition or criterion. In most cases, it will be assumed that this movement is slow, and as such inertial terms can be ignored. Finally, the problems will be related to fracture, either through a direct examination of crack formation or growth, or through having potential applications in studies related to fracture.

While there are a wide range of problems matching this description, in various fields and research areas, it is clear that not all can be considered here. Instead, a representative sample of such systems has been chosen, that will help to illustrate some of the unique issues encountered when investigating this topic.

The first such example is that of solid particle erosion. Here, a small indenter, defined by a power-law, impacts into a medium, possibly at high speed. The investigation will examine the initial energy of an impacting object required to cause a fracture. This work will study the classical problem of solid-solid interaction, with a rigid indenter hitting an elastic medium. It should be noted however that erosion problems are not limited to just solid-solid impacts, and it can be a solid-fluid interaction in some cases (e.g. water-based erosion, or a plane flying through clouds). A primary aspect of this investigation will be the incorporation of time-based effects, which is a departure from the largely quasi-static methods found in the literature.

For the next examination, the case of hydraulic fracture (HF) will be considered. This is the process by which large quantities of fluid, containing particles, is pumped into a small fracture within a layer of rock. The pressure exerted by the fluid subsequently causes the fracture to expand and extend. This complicated solid-fluid interaction has been the subject of extensive study over the years, in part due to its wide range of applications; not just in fracking, but also geothermal energy, carbon-storage and even biomedical studies. In spite of this, there is still no model which can incorporate all of the important characteristics of such a fracture. Even the classical, highly simplified 1D models, which were initially developed in the 1960's, only began to obtain accurate solutions in recent years. This work will focus on the radial (penny-shaped) formulation of HF, developing more accurate and efficient numerical solvers for the classical model, as well as incorporating the previously neglected effect of tangential stress.

The final system to be considered will be that of multiple moving particles and obstacles in the Hele-Shaw cell. The cell comprises of two plates, pressed together such that the gap is sufficiently small, with a fluid placed between them. This fluid will then have a continuous boundary, which can expand or shrink as more fluid is added to, or removed from, the system. While the problem is not inherently axisymmetric in nature, nor containing fractures, it is analogous to problems encountered in hydraulic fracturing. In this vein, an examination of the effect of solid particle inclusion on the fluid boundary development, where the initial fluid domain is defined by a unit circle, can yield important results concerning the apparent viscosity of fluids used in HF (more details are provided in Appendix. G). Carrying out such efforts however requires that the simulations of particles in the Hele-Shaw cell be able to incorporate deviations in the growth of the fluid boundary, and so an initial, generalized, investigation is required. This is what will be provided here, developing a numerical model capable of simulating the evolution of the fluid boundary, as well as the movement of particles within the fluid, over time.

While work on these largely 1D problems may seem simple, the unique features associated often prevents the use of standard approaches. One such interesting dynamic of these problems is that, while the equations involved may often be linear, the problems themselves are inherintly non-linear. This is simply the result of the moving free boundary, and the need to model its evolution over time, typically through the use of a Stefan-type condition. As such, when attempting to obtain solutions to these systems, often methods from linear problems can be adapted (for example: use of Green's functions, conformal mappings, integral equations, etc). However, even in this case, the final form of the solution will remain non-linear when considered over time.

In spite of this, it will sometimes be possible to obtain analytical solutions, such as for the PKN model of HF [129], the Polubarinova-Galin solutions for the Hele-Shaw cell [64, 179], or for the threshold fracture energy in solid particle erosion [10]. This will however only be true in very specific cases. In practice, particularly when studying the general case rather than specific examples, the problems become more complicated, and require dedicated numerical techniques in order to obtain resolutions.

1.2 Structure of the thesis

The thesis is structured such that each problem variant has its own dedicated chapter, with the problem of solid particle erosion being considered in Chapter 3, the development of a radial hydraulic fracture in Chapter 4, and finally the movement of particles in the Hele-Shaw cell in Chapter 5. In order to ensure conciseness in each chapter, material which is of importance, but is not fundamental to understanding the problem and its resolution, is relegated to the appendices. A more detailed outline is provided below.

In Chapter 2, background theories concerning the criterion which describe the moving boundaries are outlined. In Sect. 2.2, the *Stefan* condition, and Stefan-type conditions, are examined. This begins with an examination of the initial *Stefan* problem, describing the freezing of water to ice, and the evolution of the boundary between the two layers. Analogous conditions are provided for each of the problem variants, with a brief discussion of their usefulness and applicability in each case. The second part of the chapter, Sect. 2.3, concerns the fracture criterion which are used in the case of particle erosion and hydraulic fracture. The classical *Griffith-Irwin* criterion is outlined, and its applicability to each specific problem is discussed. Where required, alternative fracture criterion are provided, alongside an examination of their benefits.

The problem of solid particle erosion, and the radial fractures which result from it, is investigated in Chapter 3. The primary aim of the work is to explain the paradoxical result obtained by *Argatov, Mishuris & Petrov* [10], who found that the qualitative behaviour of the threshold fracture energy solely depends upon the impact duration.

Due to the huge body of work which has been developed into the phenomena of erosion impact, a full summary of the state of the art is not feasible, however a description of the most relevant theories is provided in Sect. 3.1, alongside a review of the literature. In Sect. 3.2, the first investigation into the threshold fracture energy is conducted. This attempts to resolve the paradox by improving the accuracy of the previous approach, which is achieved through an examination of the stress function at fixed spacial points.

Additionally, a method for predicting the time and location of the initial radial fracture is outlined, and the effect of various problem parameters examined.

In Sect. 3.3, a second investigation into the effect case of a single erosion impact into an elastic half-space is conducted. This aims to update the model by *Argatov, Mishuris & Petrov* [10] by incorporating the effect of inertial terms during the initial phase of the impact. This is achieved by incorporating a supersonic stage into the model, based on the formulation provided by *Borodich* [27]. The subsonic stage is then reformulated to incorporate the new initial conditions, with a transitory phase added to ensure a smooth transition between the two formulations. Once the full system of equations has been derived, the numerical algorithm for obtaining the threshold fracture energy is introduced, and results are presented. Finally, a summary of all results presented in the chapter, as well as their meaning with regards to the threshold fracture paradox and the study of erosion, is given in Sect. 3.4.

In Chapter 4, the case of a radial hydraulic fracture (sometimes referred to as penny-shaped HF) is examined. This begins in Sect. 4.1, with a review of the theoretical background for 1D formulations of HF, and an examination of the literature. After this, derivations for the governing equations of specific importance to the presented work are given, as well as providing a mathematical description of the fluid and solid behaviour. The investigation into radial HF begins in Sect. 4.2, with an examination of the classical formulation of a penny-shaped crack. A new approach, based on that of *Wrobel & Mishuris* for the PKN/KGD models of HF [229], is outlined. This involves rigorous use of the system asymptotics, combined with a modular construction of the numerical algorithm, to provide a method of finding solutions to the problem with a higher level of accuracy and efficiency than previous efforts. Self-similar solutions are provided for the case of an impermeable solid, alongside an analysis of the results, and a comparison with previous benchmark/asymptotic solutions is conducted.

The second part of this chapter, Sect. 4.3, is dedicated to formulating, resolving and examining an updated formulation of radial HF. This new formulation accounts for the effect of tangential stress, induced by the fluid on the fracture walls. This previously neglected characteristic has recently been shown to play a crucial role on the qualitative behaviour of the system in the case of small fracture toughness [230]. The new formulation is outlined, and a high accuracy solver is developed to obtain solutions. Comparisons with the classical penny-shaped model are provided, alongside an examination of the effect of incorporating tangential stress on the efficiency of the computational algorithm.

In Chapter 5, a model is developed to examine the effect of placing multiple obstacles and moving particles in the Hele-Shaw cell. An outline of the problem is provided

in Sect. 5.1, where important concepts and equations are also given, and a literature review is conducted. A discussion of practical applications is provided at the end of the section, with an outline for a method of investigating the apparent viscosity of fluids used in hydraulic fracturing being relegated to Appendix. G. In Sect. 5.2, a mathematical formulation of the problem is provided, alongside an asymptotic solution based on the method by *Maz'ya, Movchan & Nieves* [138, 139]. A computational algorithm is outlined and implemented. The effect of particle inclusion on the fluid boundary is examined. Methods for handling particle interaction, which is not incorporated directly into the analytical model, are provided. An examination of the effect of including large numbers of particles in the Hele-Shaw cell is conducted.

Finally, in Chapter 6, a summary of the results is provided. Here, the unique aspects of axisymmetric problems with moving boundaries are again discussed. Additional context for the investigations is given, and potential future avenues of research for each problem variant is provided.

Chapter 2

Theoretical background

2.1 Introduction

In this thesis three problems which are largely separate, but have common themes, are considered. For the sake of clarity, the full theoretical background for each of them will be provided at the beginning of each individual chapter, rather than having them collected here. Instead, in this chapter we will outline the commonalities between the different systems being studied, in order to better understand the underlying philosophy of the techniques used to study axisymmetric problems with moving boundaries.

2.2 Stefan type condition for moving boundary problems

A Stefan condition describes the law of motion on the boundary between two different phases of matter. This condition is typically derived from investigations into the conservation laws of the system, in terms of either energy or volume depending on the problem. As such this condition will often provide a detailed physical explanation of the system. Unfortunately, it is not always well posed, and may even degenerate, preventing the obtaining of useful information about the problem. A more detailed examination of the Stefan condition, as well as its relevance to the problems investigated, is provided below.

2.2.1 The classical Stefan problem

The condition is named for *Josef Stefan*, who derived the heat balance condition for a liquid-solid interface in 1D [208, 209]. The original aim of the model was to provide an

improved theory for the growth and shrinking of polar ice, which had previously been examined assuming an unrealistic linear temperature profile in the solid phase [225].

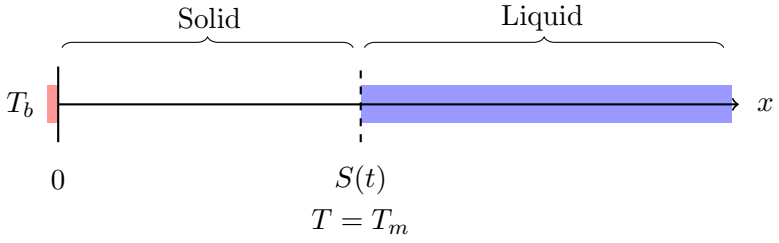

FIGURE 2.1: The problem formulation for the 1D Stefan problem, at some time $t > 0$. Here the fixed left boundary $x = 0$ is at fixed temperature $T = T_b$, while the moving boundary $S(t)$ has temperature $T = T_m$, where T_m is the melting point of the liquid.

The schematic for the classical Stefan problem is provided in Fig. 2.1. It is defined over a semi-infinite region $x \geq 0$, which is initially filled with a liquid. The fixed boundary $x = 0$ is assumed to always have temperature $T = T_b < T_m$, with T_m being the known melting point of the liquid. As a result the fluid will solidify over time, with the process beginning at $x = 0$ and slowly progressing through the liquid. The solid-liquid interface between the two layers, labeled $S(t)$, will be defined by the temperature condition $T = T_m$. The primary aim of the model is to study the movement of this boundary, and the factors which affect it.

The equations defining the temperature in each region are simply provided by the Fourier heat laws [85] as follows:

Solid layer:

$$C_S \rho_S \frac{\partial T_S}{\partial t} = K_S \frac{\partial^2 T_S}{\partial x^2}, \quad 0 < x < S(t), \quad t > 0, \tag{2.1}$$

$$T_S(0, t) = T_b < T_m, \quad t > 0, \tag{2.2}$$

where K is the thermal conductivity, C is the specific heat, and ρ is the density. The subscripts S and L denote the solid and liquid layers respectively, while subscript M is used for the interface.

Liquid layer:

$$C_L \rho_L \frac{\partial T_L}{\partial t} + C_L \rho_L u_x \frac{\partial T_L}{\partial x} = K_L \frac{\partial^2 T_L}{\partial x^2}, \quad S(t) < x < \infty, \quad t > 0, \tag{2.3}$$

$$T_L(x, 0) = T_0, \quad T_L(x, t)|_{x \to \infty} = T_0. \tag{2.4}$$

Additionally, if the density of the solid and liquid layers are different, the term u_x is obtained from the mass balance condition:

$$\rho_L u_x = (\rho_L - \rho_S)\frac{dS}{dt}. \tag{2.5}$$

Interface:
The definition of the interface layer $x = S(t)$, is given by the conditions:

$$T_S = T_m = T_L, \quad S(0) = 0. \tag{2.6}$$

As we are focusing on the *Stefan condition*, the key aim here is to obtain an expression for the growth of the boundary $S(t)$. This can be achieved through an examination of the heat within the system, which must maintain the balance:

$$\left[K\frac{\partial T}{\partial x}\right]_{\text{liquid}}^{\text{solid}} = -\left[H\right]_{\text{liquid}}^{\text{solid}}\frac{dS}{dt}, \tag{2.7}$$

where H is the enthalpy per unit volume. Noting the interrelationships between the various measures of heat in the system, it is a simple matter to expand this equation into the form:

$$K_S\frac{\partial T_S}{\partial x} - K_L\frac{\partial T_L}{\partial x} = \left[l\rho_S + (\rho_L C_L - \rho_S C_S)\,T_m\right]\frac{dS}{dt}, \tag{2.8}$$

where l is the latent heat of fusion. This, combined with equations/conditions (2.1)-(2.6), form the traditional 1D *Stefan* problem. While *Stefan* was only able to provide trivial and approximate solutions, a feat which should not be underestimated, extensive work has since gone towards providing a wider range of techniques for solving such problems, both in 1D as well as higher dimensions, and for a range of geometries [44, 85, 101, 192].

While this problem was originally only envisioned to examine the growth of polar ice caps, the method of examining the moving boundary has had a significant impact on a wide range of problems in applied mathematics. In particular, for its use of equation (2.8), which is known as the *Stefan condition*, to describe the moving interface.

In the case of more general problems involving such interfaces, conditions such as this are known as Stefan-type conditions, and are an invaluable tool for examining the evolution of a system, which contains a moving boundary, over time. As such, they will be a common feature of the problems examined in this work, and the remainder of this section is devoted to providing descriptions of the Stefan-type conditions for each of the considered problems.

2.2.2 Boundary growth in the Hele-Shaw cell

Of all the problems posed here, the Hele-Shaw cell is the one which is most similar to the classical Stefan problem. In this case however, the temperature is assumed constant, and it is the pressure throughout the fluid which determines the movement of the free boundary. The final form of the Stefan condition is given by:

$$\frac{\partial \mathbf{w}}{\partial t} = -\frac{h^2}{12\mu}\nabla p, \tag{2.9}$$

where $\mathbf{w}$ defines the moving boundary, h is the height of the cell, μ is the fluid viscosity and p is the net fluid pressure. The full derivation of this equation is provided in Sect. 5.1.2.1.

It should be noted that, while this is similar to the original Stefan problem, this does not mean that condition (2.9) always provides a successful approach in this case. The general formulation is well-posed in the case of fluid injection, however stability analysis can easily show that the problem becomes ill-posed when considering fluid suction from the domain [157]. This becomes a significant issue in the case of small fluid domains, when the analytical solutions defined using conformal mappings exhibit cusp formation. As such, alternative or updated approaches may be required to examine such problem variants.

In general however, the Stefan condition provides the most efficient and powerful method of examining boundary development in the Hele-Shaw cell, and as such will be the approach utilized in the body of this work.

2.2.3 Hydraulic fracturing and the speed equation

The need for an accurate method of fracture front tracing has long been noted in the study of hydraulic fracture. Unfortunately, singularities in the main equations near the fracture tip often prevent accurate analysis of the crack tip, with previous methods relying on the undetermined product of the aperture and pressure derivative.

In 1990, a Stefan-type condition for tracing the fracture front was outlined by *Kemp* [114], however it was abandoned shortly thereafter. It was only recently, when it was rediscovered by *Linkov* [127], that its significance came to be fully appreciated. Naming this condition the *speed equation*, it has since been shown to allow for the obtaining of high accuracy numerical solutions to the problem of 1D hydraulic fracture [128, 132, 165, 229].

The Stefan-type condition itself is obtained from evaluating the fluid mass balance equation for hydraulic fracturing near the fracture tip. We begin by considering the case of a fracture which is driven by a Newtonian fluid emanating from a point source at the origin (we consider here the toughness dominated regime, i.e. when the material toughness of the rock is greater than zero). As such it will grow axisymmetrically, independent of the angle θ (in cylindrical coordinates). Because of this, the fracture dimensions will be fully described by its length and aperture, which are denoted $\{l(t), w(r,t)\}$ respectively (note that here w again stands for the boundary growth, but is fundamentally separate from the Hele-Shaw cell described previously).

The fluid mass balance equation for this system will be given by (this is derived explicitly later in Sect. 4.1.3.4):

$$\frac{\partial w}{\partial t} + \frac{1}{r}\frac{\partial}{\partial r}(rq) + q_l = 0, \tag{2.10}$$

where $q_l(r,t)$ is the fluid leak-off into the surrounding rock, while the fluid flow rate $q(r,t)$ can be expressed as (derived later in Sect. 4.1.3.1):

$$q = wv = -\frac{w^3}{12\mu}\frac{\partial p}{\partial r}, \tag{2.11}$$

where μ is the fluid viscosity, p is the pressure exerted by the fluid on the fracture walls, and v is the particle velocity (i.e. the velocity of fluid moving within the fracture).

As we are wishing to examine the near-tip region, it is clear that the functions asymptotic approximations will be highly accurate. These can be expressed in the form[1]:

$$p(r,t) = p_0(t)\log\left(l(t)-r\right) + p_1(t) + p_2(t)\sqrt{l(t)-r} + \ldots, \quad r \to l(t), \tag{2.12}$$

$$w(r,t) = w_0(t)\sqrt{l(t)-r} + w_1(t)\left(l(t)-r\right) + \ldots, \quad r \to l(t), \tag{2.13}$$

$$q(r,t) = -\frac{w^3(r,t)}{12\mu}\frac{\partial p}{\partial r} \sim \frac{w_0^3(t)p_0(t)}{12\mu}\sqrt{l(t)-r}, \quad r \to l(t). \tag{2.14}$$

As such, inserting into (2.10), we obtain:

$$\frac{w_0(t)}{2}\left(l'(t) - \frac{w_0^2(t)p_0(t)}{12\mu}\right)\frac{1}{\sqrt{l(t)-r}} + q_l + O\left(1\right) = 0, \quad r \to l(t). \tag{2.15}$$

Assuming that the fluid leakoff is not singular at the fracture front[2]:

$$q_l(r,t) = O\left(1\right), \quad r \to l(t), \tag{2.16}$$

[1] An example of how these are obtained, in the case when incorporated tangential traction in the fluid, is provided in [230]

[2] In fact it need only be a higher order than the leading term in (2.15) for the result here to remain valid. A similar Stefan-type condition can still be obtained if the fluid leak-off at the crack tip is of the same order as in (2.15) (e.g. when Carter leak-off is assumed), using the same method outlined here, however the form of (2.18) will be different and as such this case will not be considered in this work.

then, in order for (2.15) to be satisfied, we must have:

$$l'(t) = \frac{w_0^2(t)p_0(t)}{12\mu}. \tag{2.17}$$

Finally, noting the asymptotics for the particle velocity near the fracture front (compare (2.11) and (2.14)), we obtain the *speed equation*:

$$\frac{dl}{dt} = v_0(t), \tag{2.18}$$

where $v_0(t)$ is the first term of the asymptotics for the particle velocity at the fracture tip. It is worth noting that this equation remains valid irrespective of the fluid rheology [127], as well as in the viscosity dominated regime (where the fracture asymptotics differ).

The form of the *speed equation* is an intuitive result in the absence of fluid lag, where the fluid boundary moves in line with the fracture front. Importantly however, the particle velocity in this region is non-singular, and the asymptotic terms can be readily obtained, providing a computationally efficient method of examining the hydraulic fractures growth.

2.2.4 Erosion

In the case of solid particle erosion, defining the moving boundary is more complicated than in other cases. This is due to the fact that the impacted medium is approximated by an elastic body, and as such deformation of this medium can result in the outer areas of the indenter being below the level of the medium ($z = 0$), but not being in contact with the impacted material (see Fig. 2.2). Due to this, care must be taken to ensure that the contact area is properly defined, and assumptions made concerning the behaviour of the medium will play a crucial role in describing the moving boundary. One consequence of this is that the supersonic and subsonic formulations must be considered separately. Here, only the primary results related to the rate of the growth of the contact radius in each case will be given, with a more complete analysis of the problem being provided at the beginning of Chapter. 3.

2.2.4.1 Subsonic (Hertzian) formulation

In the studies conducted here, it will be assumed that the indenter geometry is defined by the shape function:

$$z = B^{1-\lambda} r^{\lambda}, \quad \lambda > 1, \tag{2.19}$$

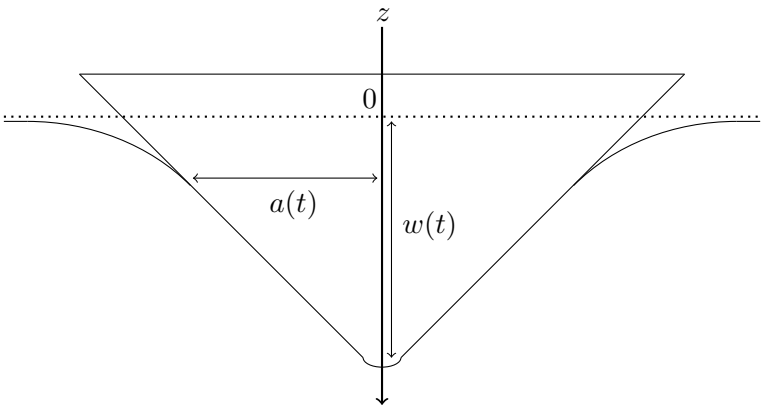

FIGURE 2.2: Elastic deformation of the impacted half-plane in the subsonic regime, shown in the case of a rounded cone indenter. Here $a(t)$ is the contact radius, and $w(t)$ the indenter depth.

which is taken to allow the formulation to model a wide range of indenter geometries (e.g. $\lambda \to 1$ defines a rounded cone, $\lambda = 2$ a half-sphere, and $\lambda \to \infty$ a cylinder), with an aim to determining the effect of particle shape on the characteristics of the resulting impact. In addition, it is assumed that it is perfectly blunt, so deformation, fracturing and chipping of the impacter do not need to be incorporated into the model. Finally, only the case of an orthogonal impact with an elastic medium is considered, as this is the one which imparts the most energy to the elastic medium, and as such will be the type of impact most likely to cause fracture initiation (a more thorough outline of the models assumptions and formulation is provided in Chapter. 3).

In the subsonic case, provided that inertial terms within the impacted medium are neglected, the equation of motion takes the form [65, 66]:

$$m\frac{d^2w}{dt^2} = -k_1 w^{\beta}, \tag{2.20}$$

where m is the mass of the indenter, while k_1 is a known constant. To obtain an equation for the penetration depth over time, we first note the conditions:

$$\left.\frac{dw}{dt}\right|_{t=0} = v_0, \quad w(t_0) = w_0, \tag{2.21}$$

with w_0 being the maximum penetration depth, and v_0 the initial velocity of the indenter. With this, integrating (2.20) twice yields that the penetration depth w can be defined

in the following way (see [10] for the full derivation):

$$w(t) = w_0 U\left(\frac{\lambda+1}{\lambda}; \frac{v_0}{w_0}t\right), \tag{2.22}$$

where the function U is defined by the relationship:

$$\int_0^{U\left(\frac{\lambda+1}{\lambda}; \frac{v_0}{w_0}t\right)} \frac{1}{\sqrt{1-\xi^{\frac{2\lambda+1}{\lambda}}}}\, d\xi = \frac{v_0}{w_0}t. \tag{2.23}$$

Meanwhile, utilizing the fundamental theorem of calculus, we can express the velocity of the indenter over time as:

$$v(t) = \frac{dw}{dt} = v_0\sqrt{1-\left(\frac{w(t)}{w_0}\right)^{\frac{2\lambda+1}{\lambda}}}. \tag{2.24}$$

As such, given that the contact radius $a(t)$ spreads as:

$$\dot{a}(t) = \frac{1}{\lambda}B^{\frac{\lambda-1}{\lambda}}w^{\frac{1-\lambda}{\lambda}}(t)\frac{dw}{dt}, \tag{2.25}$$

we obtain the Stefan-type condition in this case:

$$\dot{a}(t) = \frac{1}{\lambda}B^{\frac{\lambda-1}{\lambda}}v_0 w^{\frac{1-\lambda}{\lambda}}(t)\sqrt{1-\left(\frac{w(t)}{w_0}\right)^{\frac{2\lambda+1}{\lambda}}}. \tag{2.26}$$

It should be noted that in the formulation presented here the Stefan-type condition does not play a crucial role. This is merely due to the fact that simpler relationships between the contact radius and other problem parameters exist (i.e. (3.25)), allowing the erosion front to be traced over time without the use of this equation.

2.2.4.2 Supersonic formulation

We consider the supersonic regime, when the contact radius of the indenter is expanding faster than the wave speed in the medium. This prevents the medium from dissipating the energy induced by the impact as effectively as in the subsonic case, leading to different impact characteristics. One example of this is that, in the supersonic case, the cusp formation exhibited is negligible compared to that in the subsonic stage (compare the level of elastic deformation of the medium around the indenter in Figs. 2.2 & 2.3). It should also be stated that, as the indenter velocity will decrease throughout the course of the impact, it will eventually be moving below the wave speed of the medium, and as such will exit the supersonic regime. Because of this, at some point there will transition

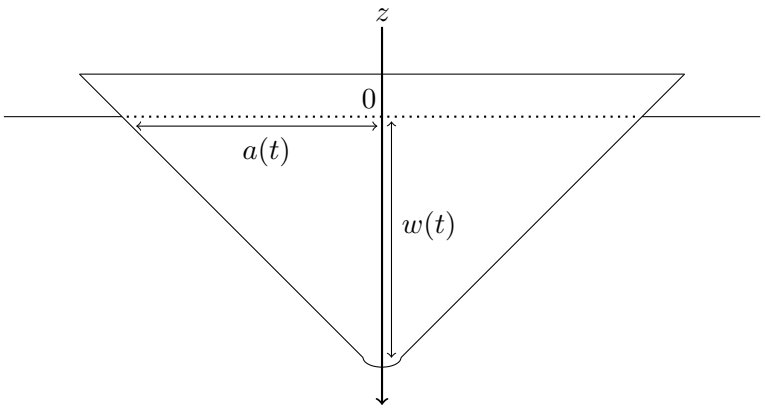

FIGURE 2.3: Elastic deformation of the impacted half-plane in the supersonic stage, for the case of a rounded cone indenter. Here $a(t)$ is the contact radius, and $w(t)$ the indenter depth.

from the supersonic regime to the subsonic case considered previously, with the moment of transition being calculated directly from the Stefan-type condition for this case (this will be explained in more detail below).

We again consider a rigid indenter, defined by a power-law shape function (2.19), impacting an elastic medium, although this time inertial terms within the elastic media will also be incorporated into the model. The equations defining the penetration depth of the indenter over time, equivalent to relations (2.22)-(2.23) obtained in the subsonic case, are instead derived from the generalized solutions provided by *Borodich* [27], which were obtained from a study of the integral equations related to the problem. For a power-law shaped indenter of the form (2.19), we have:

$$w(t) = w_s F^{-1}\left(\frac{v_0}{w_s}t\right), \tag{2.27}$$

where:

$$F(y,\mu) = \int_0^y \frac{1}{1-\xi^\mu}\,d\xi, \quad \mu = \frac{\lambda+2}{\lambda}, \quad 0 < y < 1. \tag{2.28}$$

while w_s is a known constant, and v_0 is the initial velocity of the indenter.

Next, as there is no elastic deformation around the indenter, the relation between the penetration depth and contact radius follows from simply evaluating the particle shape function (2.19) along the boundary:

$$w(t) = B^{1-\lambda}a^\lambda(t), \quad \lambda > 1, \tag{2.29}$$

from which, with only slight manipulation, the rate of expansion of the contact radius can be obtained:

$$\dot{a}(t) = \frac{1}{\lambda} B^{\frac{\lambda-1}{\lambda}} w^{\frac{1-\lambda}{\lambda}}(t) \frac{dw}{dt}. \tag{2.30}$$

Combining the above, and utilizing the fundamental theorem of calculus, we obtain a Stefan-type condition describing the movement of the contact radius:

$$\dot{a}(t) = \frac{1}{\lambda} B^{\frac{\lambda-1}{\lambda}} v_0 w^{\frac{1-\lambda}{\lambda}}(t) \left[1 - \left(\frac{w(t)}{w_s}\right)^{\mu}\right]. \tag{2.31}$$

While the Stefan-type condition does not play a considerable role when examining the subsonic case, here it is crucial. This is because, as mentioned previously, there will be a transition between the supersonic and subsonic case during the course of the impact event, which must be calculated from the Stefan-type condition. Put explicitly, the moment in time t_* when the supersonic stage ceases to apply is defined as the point at which the rate of expansion of the contact radius is identical to the wave speed of the medium, which can be expressed by the condition:

$$\dot{a}(t_*) = c, \quad c = \sqrt{\frac{E}{\rho}}, \tag{2.32}$$

where c is the wave speed in the impacted medium, defined in terms of its Young's modulus E and material density ρ. Given this, any model which attempts to incorporate both regimes will need to take account of the Stefan-type equation (2.31).

2.3 Fracture criterion

2.3.1 The Griffith-Irwin criterion

The *Griffith* approach was originally designed to examine ideal brittle fractures [84]. It considered the energy of new surfaces formed during fracture Γ, often named the specific energy of a fracture. This could then be used to examine when fracture formation would initiate using the energetic balance equation:

$$\Delta U + \Delta\Gamma = \Delta A, \tag{2.33}$$

where U is the deformation energy and A is the work of external forces. This relation was then applied to model a fracture, with half-length a, in an infinite domain which is subject to a remote stress σ at infinity. Assuming that the area of the unloaded zone was circular, and had a radius equal to the half-length of the fracture, integral techniques

can be used to transform this into the relation (see [152] for more details):

$$G = \sigma^2 \pi a, \tag{2.34}$$

where G is the strain energy release rate.

The approach was revolutionary, but its applicability was limited due to the fact that perfectly brittle fractures are fairly rare in nature. This changed when the theory was extended by *Irwin* [104] to cover quasi-brittle fracture[3] as well. This was achieved by defining the stress intensity factor of the material for a mode I crack (this is an 'opening' crack, for more details on different fracture modes see Sect. 4.1.3.2, in particular Fig. 4.4), K_I, as follows:

$$K_I = \sigma \sqrt{\pi a}, \tag{2.35}$$

and performing an analysis of the stress field ahead of the fracture. It was demonstrated that this stress intensity factor remains the dominant force in determining the fracture evolution in the case of quasi-brittle materials, with the new form of (2.34) being:

$$G \propto K_I^2. \tag{2.36}$$

Through a more thorough analysis, and relating this to the static fracture toughness K_{Ic}, the criterion for crack propagation in a quasi-brittle material can be obtained:

$$K_I \leq K_{Ic}, \tag{2.37}$$

Additionally, in the case where cracks grow along a trajectory where K_I is maximal, this criterion can be assumed to take the stronger form:

$$K_I = K_{Ic}, \tag{2.38}$$

which is typically referred to as either the *Irwin* or *Griffith-Irwin* fracture criterion.

The above 'classical' approach has been shown to conform to the results obtained by experiments in numerous cases (a number of examples are provided in [182]), however it is not universal. In some specific cases the assumptions used when deriving or applying (2.38) are not satisfied, and as a result the classical criterion requires updating. Two relevant examples of this are outlined below.

[3] These are fractures where the crack surface effectively acts as the boundary between elastic and plastic regions, in particular at the fracture tip. Because of this, the interaction between the two can be effectively modeled as cohesion forces. See [16] for more details.

2.3.2 High velocity erosion impact

In the case of when short-term pulses are applied, the quantitative accuracy of predictions made using the *Griffith-Irwin* criterion decreases considerably.

In the experimental paper by *Kalthoff & Shockey* [110], an essentially rectangular tensile load pulse was utilized in impacts whose duration lasted only a few microseconds. Their setup allowed for the creation of a large number of cracks in the target, as well as examining the stability of the impacted plates to further impacts. Their experiment conclusively demonstrated that the traditional criterion of unstable crack germination was poorly suited to the dynamic case.

Since then numerous experiments (for example: [33, 98]), investigating dynamic fractures in brittle materials, have observed a similar failure of classical approaches to accurately predict results. This is in part due to the fact that, for dynamic impacts, the discrete ('quantum') characteristic of the process as load pulses are applied becomes increasingly important. Additionally the inability of the material to dissipate energy (or 'relax'), means that the incubation time prior to fracture plays a decisive role, and static attempts to examine the system fail as a result. Both of these aspects can be demonstrated by studying dynamic fracture in a lattice structure [76, 201, 202].

In response to this, several alternative methods and criteria for modeling dynamic brittle fracture have been suggested, many of which are outlined in [149]. The culmination of these is the incubation time based fracture criterion (sometimes referred to as the structural-temporal criterion), which takes the following form [166]:

$$\frac{1}{\tau}\int_{t-\tau}^{t}\frac{1}{d}\int_{0}^{d}\sigma(r,t')\,dr\,dt' \leq \sigma_c, \tag{2.39}$$

where σ_c is the static strength of the material and σ is the tension stress. The parameter τ is the experimentally obtained incubation constant, which characterizes the strain (stress) rate sensitivity of the material, and whose physical meaning is related to the relaxation time of the material. Meanwhile d is a length scale parameter, which is determined in static tests on specimens with microcracks. It is worth noting that, if *Irwin's* small yielding approximation is assumed:

$$d = \frac{2K_{Ic}^2}{\pi\sigma_c^2}, \tag{2.40}$$

then this criterion reduces to the *Irwin* criterion (2.38) under quasi-static conditions. This criterion can therefore replicate the accuracy of the classical criterion in standard static tests, but has also been shown to produce accurate predictions in dynamics tests [171, 173].

In simple 1D cases (2.39) can be simplified to:

$$\gamma(r,t) = \frac{1}{\sigma_c \tau} \int_{t-\tau}^{t} \sigma(r,t')\, dt', \tag{2.41}$$

with the incubation time based fracture criterion being formulated as:

$$G(r) = \{\min t \in [0,T] : \gamma(r,t) = 1\}, \tag{2.42}$$

here T is the impact duration, while G represents the minimum time to fracture for any fixed radial position r. It is worth noting that, provided function G is injective, we can define the time of initial fracture t^*, alongside associated position r^*, as follows:

$$t^* = \min G(r), \quad r^* = G^{-1}(t^*), \tag{2.43}$$

where G^{-1} is the inverse of the fracture criterion function (2.42).

2.3.3 Hydraulic fracture and tangential stress

In the case of 1D hydraulic fracture models, typically the classical *Irwin* criterion (2.38) has been utilized. This was considered appropriate because it was traditionally assumed that the effect of hydraulically induced shear stress, denoted τ, was negligible in comparison with the fluid pressure:

$$|\tau| \ll |p|, \tag{2.44}$$

This has been assumed for all 1D models since their creation (for example; in the KGD case [207]).

However, in the recent work of *Wrobel, Mishuris & Piccolroaz* [230], it was demonstrated that (2.44) was not satisfied at the crack opening, while the tangential term may also influence the asymptotic behaviour at the fracture tip. This is particularly troubling due to the fact that the near-tip behaviour is crucial to the solution [34, 35].

An updated fracture criterion has been proposed by *Wrobel, Mishuris & Piccolroaz*, which was developed from an examination of the energy release rate, utilizing a J-integral approach first introduced by *Rice* [185], near the fracture tip [230]:

$$K_{Ic}^2 = K_I^2 + 4(1-\nu) K_I K_f \tag{2.45}$$

where ν denotes the Poisson ratio, while K_f is the shear stress intensity factor. Meanwhile K_{Ic} represents the material toughness, which is separate from the static fracture

toughness considered previously, and is a constant characterizing the resistance of a given material to crack extension (for more details see [16]).

It is immediately apparent that (2.45) reduces to the classical *Irwin* criterion when taking $K_f = 0$. It should be noted as well that the stress intensity factors K_I and K_f are not independent. They are in fact related by the following formula:

$$K_f = \frac{p_0}{G - p_0} K_I, \tag{2.46}$$

where $p_0(K_{Ic})$ is the leading term of the pressure asymptotics at the fracture tip, while G denotes the shear modulus. One important caveat to this relationship is the fact that:

$$p_0(K_{Ic}) \to G, \quad K_{Ic} \to 0. \tag{2.47}$$

As such, in the case of zero material toughness, only the non-local component K_I vanishes, while the shear stress intensity factor takes a non zero value $K_f > 0$. This has a significant effect on the fracture asymptotics in the zero or small toughness case, eliminating the singular perturbation problem which previously arose when transitioning between the viscosity and toughness dominated regimes.

Chapter 3

Threshold fracture energy in solid particle erosion

This work was published in the papers:
Threshold fracture energy in solid particle erosion: improved estimate for a rigid indenter impacting an elastic medium, Meccanica 50(12):2995-3011, 2015
Resolution of the threshold fracture energy paradox for solid particle erosion, Philosophical Magazine, 96(36):3775-3789, 2016

3.1 Theoretical background and literature review

3.1.1 Problem description and motivation

Erosion impact describes a range of problems, unified by the fact that they typically involve small indenters colliding with a larger medium. While the study of erosion in other fields almost universally describes volume loss, within the field of applied mathematics it is not always required for the term to qualify. Instead, any damage to the impacted medium (e.g. fracture) caused by an indentation event warrants use of the term.

Erosion may come in numerous forms. One simple example is the number of indentations involved, typically split into the case of a single event, or multiple impacts. Another is whether the indentation is slow (quasi-static), which is more easily resolved, or if it occurs quickly (dynamic), in which case numerous additional factors need to be taken into account. Other differences may be more subtle. In the case of erosion by a fluid particle, the solid-fluid interaction which occurs may be difficult to predict. This is especially true if the fluid indenter is a corrosive substance, when the resulting interplay

between the mechanical damage of the impact and the corrosion of the impacted medium needs to be approached as an entirely unique 'erosion-corrosion' problem.

On top of the variation between the number of indenters and their form, there is also a wide variety of factors which need to be accounted for in a specific impact. The initial angle of the indenter will determine how much of the energy is transfered to the medium, and how much material is lost. There will also be large differences in system behaviour depending on the velocity of the impacter, particularly if it is initially traveling at supersonic velocities. The characteristics will also clearly depend on the impacted material, will its response be elastic or plastic, brittle or ductile.

This wide range of variability between problems has made it difficult to construct generalized approaches, and means that the field relies heavily on experimental results. A good overview of erosion, both experimental and theoretical, can be found in [182].

Despite its difficulties, this is obviously a phenomena of great importance, with applications not just in natural processes such as meteorite impacts [142], but also in various technological processes, for example shot peening [200] and the development of armor/anti-armor materials [109]. In the case of impact by a fluid, the relevance to sea-based erosion, the movement of planes through clouds, and inside industrial steam turbines [231] are also immediately obvious. Due to this wide range of uses, erosion has been a much studied phenomena, with numerous avenues of investigation in the literature.

As a result of the large scope of this topic a full summary of the field can not be provided here, however, in the remainder of this section, we will explore in more detail those which are most relevant to the current investigation. In particular we will describe the initial *Hertzian* models developed to describe particle indentation, alongside their limitations. Important effects to consider when examining a single impact will also be briefly outlined for the sake of completeness, however only so far as is needed to justify either incorporating or neglecting them within the following investigation. Finally, a thorough description of the threshold fracture energy of an impact, whose study is the primary motivation of this work, will be provided alongside a detailed review of existing research into the subject.

3.1.2 Hertzian formulations

In the 1880's, the first analytical solutions for the impact of a blunt indenter with an elastic half-plane where provided by *Hertz* [93, 94] (translations into English are provided in [95]). The model assumed that friction forces could be safely ignored, and that

the indenter was impacting normal to the surface. These initial works, alongside later additions (most notably be *Harding & Sneddon* [89]), provided the impact geometries and stress fields for a small number of fixed indenter shapes. This framework was so influential that such events came to be known as *Hertzian* impacts, and much of the current work into erosion impacts can trace its roots back to these original papers (including the formulation presented in the body of this chapter). As such, a brief introduction to these models in the case of a cone, sphere and flat-bottomed cylinder will be provided below. A more in-depth analysis of the key results of these early models can be found in books [61, 108].

3.1.2.1 Rigid cone

The case of a rigid cone indenter was first derived by *Sneddon* [205]. It should be noted that the formulation provided there merely requires that the indenter is 'conical-headed' (pencil shaped), and as such is more general than the other Hertzian solutions. The version given below is provided explicitly in [61, p. 96-99].

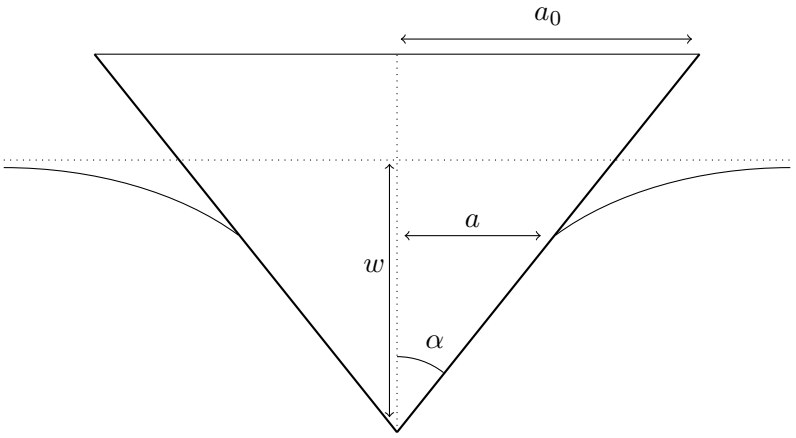

FIGURE 3.1: Geometry of the conical-headed indenter, here α is the half-angle used to define the shape of the cone in the Hertz formulation. The full height of the indenter is not defined.

The indenter depth, w, is given by the following formula:

$$w(r) = \begin{cases} \left(\frac{\pi}{2} - \frac{r}{a}\right) \alpha \cot(\alpha), & r \leq a \\ \alpha \left[\arcsin\left(\frac{a}{r}\right) + \sqrt{\frac{r^2}{a^2} - 1} - \frac{r}{a}\right] \cot \alpha, & r > a \end{cases} \tag{3.1}$$

where a is the contact radius. The total pressure on the contact area, P, is meanwhile given by:

$$P = \begin{cases} \frac{2E \tan(\alpha)}{\pi(1-\nu^2)} w_0^2, & w_0 \leq \frac{1}{2}\pi a_0 \cot(\alpha) \\ \frac{2Ea_0}{1-\nu^2}\left(w_0 - \frac{1}{4}\pi a_0 \cot(\alpha)\right), & w_0 > \frac{1}{2}\pi a_0 \cot(\alpha) \end{cases} \tag{3.2}$$

where E is the Young's modulus, ν the Poisson ratio, a_0 the radius of the conical-headed punch, and w_0 is the penetration depth (i.e. $w_0 = \max_r w(r)$). The mean contact pressure takes the form:

$$p_0 = \frac{E}{2\left(1-\nu^2\right)} \cot\left(\alpha\right), \tag{3.3}$$

through which the stresses along the surface, σ_r, can be expressed as:

$$\sigma_r(r) = \begin{cases} \left[-\operatorname{arccosh}\left(\frac{1}{\rho}\right) + \frac{(1-2\nu)}{2\rho^2}\left\{1 - \sqrt{1-\rho^2} + \rho^2 \log\left(\frac{1+\sqrt{1-\rho^2}}{\rho}\right)\right\}\right] p_0, & \rho \leq 1 \\ \frac{(1-2\nu)}{2\rho^2} p_0, & \rho > 1 \end{cases} \tag{3.4}$$

where $\rho = r/a$ is the dimensionless radial coordinate.

3.1.2.2 Spherical indenter

The case of a perfectly spherical indenter was initially provided by *Hertz* [95], while a more explicit description of the formulation is provided in [61, p. 87-90].

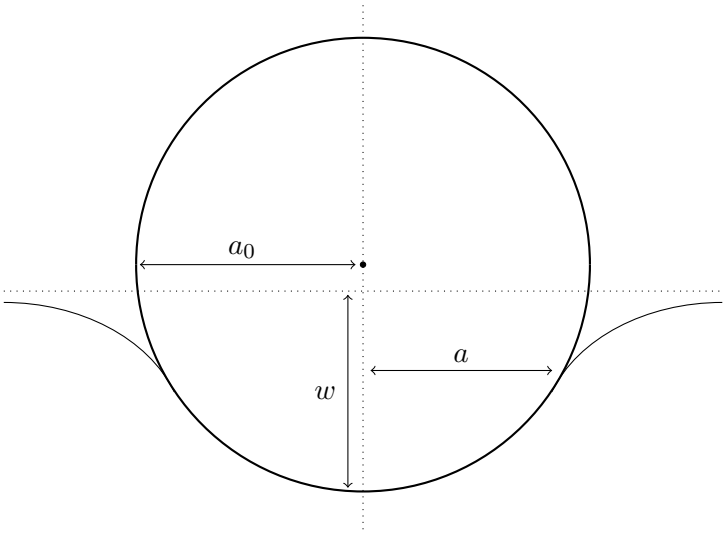

FIGURE 3.2: Geometry of the spherical indenter, with radius a_0, used in the Hertz formulation.

The penetration depth of the indenter is given by:

$$w(r) = \begin{cases} \frac{3\pi(1-\nu^2)}{8Ea}\left(2a^2 - r^2\right) p_0, & r \leq a \\ \frac{3(1-\nu^2)}{4Ea}\left[\left(2a^2 - r^2\right)\arcsin\left(\frac{a}{r}\right) + ar\sqrt{1-\frac{a^2}{r^2}}\right] p_0, & r > a \end{cases} \tag{3.5}$$

where p_0 is the mean pressure beneath the indenter, while p is the contact pressure distribution, given by:

$$p(r) = \frac{3P}{2\pi a^2}\sqrt{1-\frac{r^2}{a^2}}, \quad r \leq a. \tag{3.6}$$

As a result, the loading force takes the form:

$$P = \frac{4E\sqrt{a_0}}{3(1-\nu^2)} w_0^{\frac{3}{2}}, \tag{3.7}$$

where a_0 is the radius of the indenter and w_0 is the penetration depth (i.e. $w_0 = \max_r w(r)$).

The radial stress distribution on the surface is:

$$\sigma_r(r) = \begin{cases} \left[\frac{(1-2\nu)a^2}{2r^2}\left(1-\sqrt{1-\frac{r^2}{a^2}}\right) - \frac{3}{2}\sqrt{1-\frac{r^2}{a^2}}\right] p_0, & r \leq a, \\ \frac{(1-2\nu)a^2}{2r^2} p_0, & r > a. \end{cases} \tag{3.8}$$

3.1.2.3 Flat-bottomed cylinder

The solution to the problem of indentation of an elastic half-plane by a flat-bottomed cylinder was first obtained by *Sneddon* [203]. The resulting formulation, taken from the original paper alongside the representation given in [61, p. 92-96], is presented below.

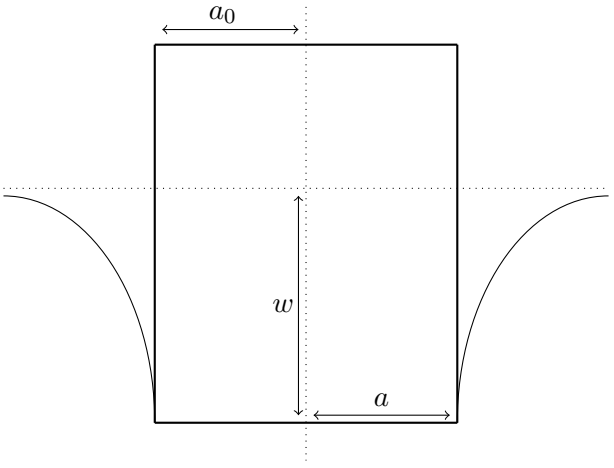

FIGURE 3.3: Geometry of the indentation by a flat-bottomed cylinder, with radius a_0, used in the Hertz formulation.

The penetration depth of the indenter takes the form:

$$w(r) = \begin{cases} \frac{\pi(1-\nu^2)}{2E} a p_0, & r \leq a, \\ \frac{1-\nu^2}{E} a p_0 \arcsin\left(\frac{a}{r}\right), & r > a, \end{cases} \tag{3.9}$$

where p_0 is the mean pressure applied by the indenter, while the contact pressure distribution is given by:

$$p(r) = \frac{P}{2\pi a^2 \sqrt{1 - \frac{r^2}{a^2}}}. \tag{3.10}$$

As a result of this, the total load on the pillar can be shown to be:

$$P = \frac{2E}{1 - \nu^2} a w_0, \tag{3.11}$$

where w_0 is the penetration depth (i.e. $w_0 = \max_r w(r)$).

Finally, the surface stresses beneath the indenter are given by:

$$\sigma_r(r) = \frac{P}{2\pi a^2} \left[-\frac{1}{\sqrt{1-\rho^2}} + \frac{1-2\nu}{\rho^2} \left(1 - \sqrt{1-\rho^2} \right) \right], \quad \rho \leq 1, \tag{3.12}$$

where $\rho = r/a$ is the dimensionless coordinate.

3.1.2.4 The limitations of Hertz theory

While the *Hertz* theory provided a solid basis for future investigations into erosion impact, it was not without its limitations.

One clear but significant downside of the given approach was that it modeled indenters of fixed shape. As such, while it was able to provide a relatively accurate description of specific impacts it could, at best, provide weak bounds for predicting the effects of real-world erosion problems. This inherent weakness is however common in indentation studies.

A more serious detriment of the theory is that it provides only a quasi-static description. As such it fails to take account of dynamic effects, which can play a crucial role in the fracture of brittle materials (see Sect. 2.3.2).

An addition problem with the *Hertz* theory was found when attempting to utilize it to predict fracture. An experimental investigation was conducted by *Auerbach* into 'ring' (circumferential) fractures forming in glass, following an impact by a spherical indenter with radius a_0. When examining the maximum impact load P required to initiate such a crack, he found that $P \sim a_0$ for small indenters [15]. This relationship contradicts that predicted by the Hertzian approach where, utilizing (3.7) and taking a maximum tensile stress fracture criterion, the relationship $P \sim a_0^2$ is obtained. This discrepancy came to be known as *Auerbach's* law, and it prompted numerous investigations attempting to provide a physical explanation for its existence (see e.g. [60, 62]).

One final criticism of the approach was best expressed by *Storey*, stating that it: "assumed that, in the neighbourhood of contact, the surfaces of the bodies and, hence, the distance between their corresponding points can be represented by second degree equations." [210]. This assumption further limited the predictive capabilities of the theory, and became a key point on which others would attempt to improve.

3.1.2.5 Shtaerman-Kilchevsky theory of quasi-static blunt impact

One (previously mentioned) problem with *Hertz* theory was that it assumed that the surface of interacting bodies could be described by second degree equations. This approach, while greatly simplifying the mathematics involved, did not necessarily provide an accurate description of the problem. The first successful efforts to correct this flaw were undertaken by *Shtaerman* [199, 210]. However, they were not widely followed up.

In another paper *Shtaerman*, utilizing advances in the study of integral equations and potential theory, managed to generalize the approach of *Hertz* to cover punches defined by a monomial function of r to the degree λ, where $\lambda \geq 2$ is an even number [198]. This was later extended by *Kilchevsky* to provide an accurate description for any $\lambda > 1$ [117]. These generalizations greatly increased the applicability of the theory, and allowed for more accurate studies into the effect of indenter shape on the impact characteristics.

During this time, additions to the model were made by *Galin* [66], who managed to provide addition quasi-static relations between various impact parameters (provided here in (3.15)-(3.16)). This, combined with the results by *Shtaerman & Kilchevsky*, yields a fully quasi-static theory of erosion by a power-law shaped indenter.

Unfortunately, these results were not widely adopted outside of the Soviet Union. This was likely, in part, due to the fact that few of the papers were translated into other languages. Similarly, incorporating the effects of a general particle shape was, and still remains, an at best secondary concern to most researchers working in the field.

3.1.3 Important effects and alternate approaches

While there were clear limitations to the initial *Hertzian* theories, their potential for describing erosion impacts lead others to improve and update the approach. This was achieved through updating the initial model, the incorporation of additional, previously neglected, effects, and through comparison with experimental results.

A brief, and by no means complete, examination of these efforts is given below. The aim is to provide a description of the theories underlying the current work, as well as

examinations of other developments which are of importance to understanding both the achievements, as well as the limitations, of the presented model.

3.1.3.1 Incorporating friction and adhesion

Efforts to study the effect of adhesion (normal contact) and friction (sliding contact) in erosion impacts largely owe their beginnings to the work of *Galin* [66], who conducted some of the first examinations of the phenomena. These preliminary investigations were analogous to the aforementioned *Hertz* solutions, utilizing the same framework to investigate the effect of each phenomena.

When working with axisymmetric punch impacts involving friction, *Galin* assumed that the indenter was rotating with a fixed angular momentum. The aim of which was to obtain the relationship between the indenter shape and the momentum required to rotate the object during the impact, the results of which have clear application to industry. In this work *Galin* was able to provide solutions to specific cases, using a similar quasi-static formulation to that of the *Hertz* solutions.

More recent investigations however have tended to focus on the effect of purely sliding motion, or have been concerned with tribology (where both contacting objects are in motion). Summaries of developments in these areas can be found in [80, 81].

Meanwhile, the first full solutions for punch indentation with adhesion where provided for specific cases, with a spherical indenter being given by *Soldatenkov* [206], followed by a rigid cone geometry by *Borodich et al* [29]. These efforts where later generalised by *Borodich, Galanov & Suarez-Alvarez* [30], who provided a solution for erosion by a power-law shaped axisymmetric punch, incorporating an adhesive (no-slip) condition at the contact region. This was achieved through the framework of the *Boussinesq-Kendall* approach to erosion impacts [31], with the inclusion of the JKR (*Johnson, Kendall & Roberts*) model of adhesive contact [115]. Using such a model to make quantitative predictions is not a simple matter however, due to difficulties in estimating the adhesive properties of the contacting materials [28].

Additionally, more complicated models have been developed, particularly in recent years. These models deal with indentation into a material containing multiple 'layers', instead of a single elastic half-space. A good example of such an approach is given in [12].

It should be also noted that the work presented here will neglect the effects of both friction and adhesion at the contact interface, which do play a role, especially for oblique impacts [13]. However, this simplifying assumption is often made in the literature in the case of normal impact incidence [106], as considered here. Additionally, as this

work is a preliminary investigation into the viability of the presented approach, it is more appropriate to first take the simplest form, with the potential to incorporate other complicated phenomena at a later time.

3.1.3.2 Supersonic stage

While the standard approach to impact erosion, through the assumption of a slow moving indenter impacting a half-plane, provides a reasonable approximation to most problems, there are special cases where it fails to take account of crucial effects. One particularly notable example is when the initial velocity of the indenter is higher than the wavespeed of the impacted medium. In this case, the ability of the medium to dissipate energy is greatly reduced, while the energy imparted by the impact is obviously higher than in subsonic impacts. This is particularly relevant to the investigation conducted here, given the important role that the ability of the material to 'relax' plays in the formation of fracture (see Sect. 2.3.2). The differing qualitative characteristics between the two regimes also leads to different problem geometries, such as the differing cusp formation between subsonic and supersonic impacts, as noted in Sect. 2.2.4 (compare Fig. 2.2 & 2.3).

The extent to which this difference will play a role however is not entirely clear. This is because the indenter velocity will rapidly decrease during the impact, and as such the supersonic, and intermediate transonic, regimes will only take up a small fraction of the total impact duration. Whether this small portion of the total time will be sufficient to significantly alter the impact characteristics is open to debate. Additionally, this is not something which can be easily examined through experimental techniques, as having the indenter begin in the supersonic regime will require you to increase its initial velocity, or change the impacted material to one with a lower density, making it difficult to determine which effects are solely a response to the differing regime.

This uncertainty about the effect of neglecting any potential supersonic stage, combined with the prevalence of quasi-static approaches, and the increased difficulty associated with incorporating inertial terms, means that there are few extensive examinations of this topic in the literature.

One particularly interesting recent investigation was conducted by *Wang, Fleck & Evans* [226], who performed an FEM-based investigation into a potentially supersonic erosion impact into thermal barrier coatings. The use of purely numerical techniques allowed them to avoid the difficulties associated with incorporating wave effects directly into an analytical approach. In addition, it allowed for a large range of effects to be examined, such as impact angle, initial velocity and indenter shape. Unfortunately, given the

non-linear nature of the problem, the accuracy of such techniques has not been proven conclusively.

An alternative method for examining the problem is through asymptotic approaches. One notable example is the work of *Argatov* [11], which investigated the asymptotics of a spherical indenters equation of motion in the supersonic and subsonic regimes. It was shown that there could be significant deviations from the results obtaining using Hertzian approaches, although this depended on the values of the problem parameters (i.e. medium density, Young's modulus, etc..). Unfortunately, while this approach shows great promise, it requires the formulation to be highly specialized, preventing a more generalized examination of the phenomena.

More relevant to the current work however are the purely analytical approaches to the problem of a rigid punch impacting an elastodynamic half-plane. The first of which was provided in the paper by *Thompson & Robinson* [214], who developed a 'simple' solution for such a system, subject to certain constraints, utilizing a self-similar potential based approach. This was later improved upon by *Borodich* [27], whose more general investigation considered an arbitrarily shaped indenter impacting an elastodynamic half-space, a problem geometry similar to previous Hertzian approaches. Through the use of integral equations, *Borodich* was able to provide exact solutions for the important problem parameters, most notably the indenter depth over time (see (2.27)-(2.28)). To the best of the authors knowledge, this remains the only complete and generalized analytical formulation for such an impact, and as such will be the one employed here when attempting to incorporate the effect of inertial terms into the model.

3.1.3.3 Computational methods

While numerous computational models have already been discussed in the above sections, it is important to elaborate further on the use and limitations of such approaches, as well as the effect that modern computing has had on the study of erosion problems.

The application of finite element models (FEMs) to erosion problems began almost as soon as the FEM approaches began to appear in the literature. This is in large part due to their application to studying the effectiveness and efficiency of armour, resulting in significant military interest. As a result of this application however, many of the works in this direction are not released to the general public, making it difficult to assess the true state of the art.

In spite of this, specialized FEM based approaches do still appear in the literature. A good example of early computational models for indentation problems was provided in

[83]. The technical report successfully attempted to provide a qualitatively accurate description of dynamic impact by a soft projectile where, for previously mentioned reasons, the classical Hertzian approach fails to do so. This work has the benefit of being accompanied by experimental data, providing an assessment of the accuracy of the final FEM-based results. Unfortunately, such experimental verification of computational models is rarely conducted in the literature and, noting the non-linearity of the problem (which can cause computational errors to rapidly accumulate), the level of error of obtained solutions is typically not known.

Examples of more recent models include those examining shot-peening [107], erosion based wear [227], as well as the aforementioned supersonic impact into thermal barrier coatings [226], amongst others. This however demonstrates one of the limitations of purely computational approaches, as the numerical simulations have to be extensively tailored to specific cases. Similarly, attempting to account for the non-linearity of these problems means that such simulations are also likely to have lengthy computation times, making them unsuitable for investigations like that provided in Sect. 3.3, where there is a need to conduct thousands of simulations in order to iterate to a final result (see Sect. 3.3.4.1).

In the pursuit of alternative computational approaches, which attempt to avoid some of the more obvious problems of purely numerical techniques, multiple semi-analytical methods have been developed [105, 195], and have shown reasonable success. Unfortunately these are often also tailored to specific cases, and suffer from many of the limitations of the classical approach as well. Most notably, they frequently utilize a fixed indenter shape, greatly limiting their applicability.

While only a very brief look at FEM and semi-analytical methods has been provided here, it is sufficient to see why they are not suitable for the given work. Put simply, the investigation conducted here focuses on the indenter shape, where using the numerical approaches described above would require a unique simulation for each particle geometry. As such, analytical investigation for a generalized indenter are clearly preferable if they provide a viable method of approach. Meanwhile, as previously mentioned, the second investigation requires thousands of simulations to be run in order to iterate towards a final result, which would be overly computationally intensive if based on high accuracy numerical techniques.

As a final note concerning the impact of improved numerical techniques on the study of particle erosion, it is important to make clear the effect that modern computing, and more precisely the development of specialized mathematical software, has had on purely analytical approaches. This new tool has made special and inverse functions, for example the hypergeometric functions, or the inverse of (3.23), easier to compute. As such, it

is now possible to generalize theories which previously would have been impossible to obtain solutions for, such as the work presented here. Additionally, this allows for a more accurate testing of previously obtained analytical solutions, and an easier way to detect misprints, as demonstrated in [63].

3.1.4 Impact induced fracture

3.1.4.1 The geometry of surface fractures

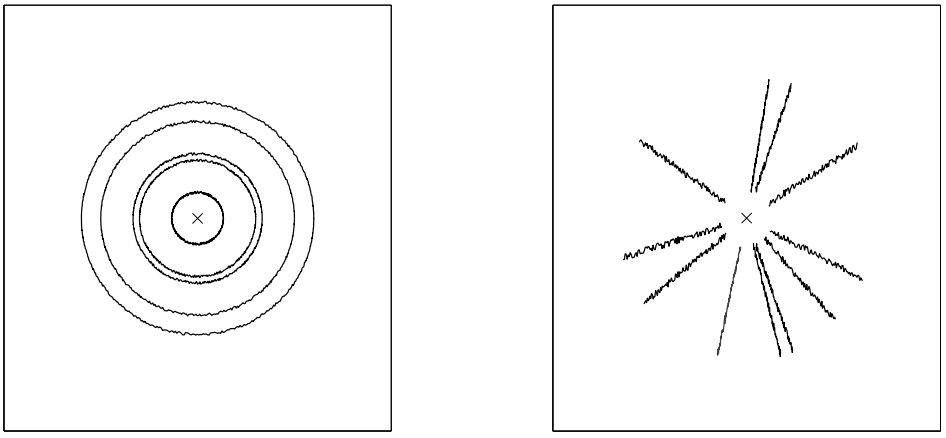

FIGURE 3.4: Geometry of surface fractures, denoted by black lines, which occur following an erosion impact, whose center is marked with an 'x'. Here we show: (a) circumferential fracture (also known as 'Hertzian' rings), (b) radial (tangential) fracture.

In any erosion event, the form of surface fractures which occur, and whether they do occur, is determined by the properties of the impact. This includes not only the initial energy of the indenter, but also the properties of the impacted medium, alongside considerations such as whether it is a static or dynamic indentation. A brief outline of the most common types of surface fracture is given below.

The first common form of surface fracture is circumferential fracture. These are axisymmetric fractures occurring around the impact center (see Fig. 3.4a). This form of fracture is occasionally referred to as a 'Hertzian ring', due to it being predicted by the classical approach of *Hertz*. It should be noted that this is the only common form of surface fracture which does not require any preexisting weaknesses in the impacted medium, but is instead the result of a build-up of tension during the indentation process. As such, circumferential fractures are common in many erosion impacts, however they often require a longer incubation time to form than cracks caused by structural weaknesses in the impacted material. This fracture type is of particular importance, as it is

the primary cause of damage in brittle materials which experience an elastic response to the impact [59].

Radial fracture meanwhile takes the form of rapidly occurring cracks, which spread orthogonal to the impact center (see Fig. 3.4b). This is because they follow lines of preexisting weakness in the indented material, and as such require a lower initial energy to instigate. Due to this condition however, radial fractures will not occur in all erosion impacts, and their behaviour is highly dependent on the properties of the impacted medium.

The final form of surface fracture, which are common in elastic erosion impacts, are micro-cracks. These are by far the hardest form of fracture to predict, and their generation can often be ignored in the case of a single impact. In the case of multiple impacts however, they play a crucial role, due to their effect on the materials stress field and ability to resist tension build-up. Their presence may lead to the type of preexisting weakness required for radial fracture, although typically such weaknesses are instead structural. In the case of circumferential fracture however, small preexisting cracks in the medium can be responsible for the initial activation of the fracture, resulting in a lower threshold energy being required, as well as changing the initial position of the fracture and its incubation time. For this reason, while the generation of micro-cracks is often considered almost trivial in the case of a single impact, their existence in a material greatly increases the difficulty associated with making accurate predictions regarding fracture.

In the body of this work, we will only consider the case of a single erosion impact, into a perfectly elastic medium (i.e. without micro-defects or preexisting weakness). As such, the only form of surface crack which place a significant role will be circumferential fractures, which will be perfectly axisymmetric in nature.

3.1.4.2 Fracture criterion

In fracture mechanics, the classical approach has always relied on the *Griffith* and *Irwin* criterion, which were obtained using a quasi-static approach, to predict fracture, (these have already been outlined in Sect. 2.3). However, it has been demonstrated experimentally that they fail to obtain accurate predictions for dynamic systems (see Sect. 2.3.2). As such, the major transition in the development and use of fracture criterion in recent years has aimed to create a more complete theory, which can provide a better description of both regimes.

One such approach is to simply update the classical *Irwin* criterion, using dynamic stress intensity factors (DSIFs) [154]. This method is only practical however in computational

models, as it simply uses relations between the state of the system and the stress intensity factor(s) to 'update' the value of the DSIFs at each step. Given the unknown accuracy of these numerical approaches, this is best used for very specific problems, rather than the general approach aimed for here.

Updated analytical approaches have also been developed. One of the first was initially formulated by *Barenblatt*, with improvements added by others, and relied on incorporating the effect of 'cohesion' of the material. This integral formulation was closely related to the initial *Irwin* formulation, but relied on different fundamental assumptions. A good summary of the approach can be found in [16]. Unfortunately while this formulation was able to obtain improved predictions for quasi-static problems over classical methods, its usefulness to the dynamic case was never conclusively proven.

In this work however we shall utilize the incubation time based fracture criterion (sometimes referred to as the structural-temporal criterion) previously outlined in Sect. 2.3.2. This is because, while the above criterion can achieve a high degree of accuracy in specific cases, they are unable to account for the important temporal effects which affect small scale impacts. More specifically, the incubation time based approach takes the local rupture stress history into account, which represents the nature of the kinetic processes underlying the formation of macroscopic breaks, yield flow or phase transformation [149]. These dynamic effects become essential for impacts over time periods comparable with the preparatory relaxation processes accompanying the development of micro-defects in the material structure, and make it possible to predict unstable behaviour of the dynamic-strength characteristics.

This incubation time based approach has also been demonstrated to achieve a high correspondence with experimental results in such cases [159]. Further, it offers a more unified interpretation of dynamic effects, with applicability in seemingly different physical processes such as the pulsed fracture of solids [170], electrical breakdown, and phase transitions under the action of fast energy fluxes [167]. As such, it is perfectly suited to the current work.

3.1.4.3 Oblique incidence

Investigations into the effect of impact angle on erosion damage began primarily through numerical and experimental techniques. Unfortunately, due to the nature of the field, most of these investigations have been largely focused on the effect of angle on material volume loss, with fracture being at best a secondary concern.

Theoretical understanding concerning the effects of indentation at an angle is often achieved through examinations of shot-peening [2, 96], which can either be directly applied by industry, or used as an analogy for armour technologies.

The conclusion which can easily be drawn from the results of these endeavors is that, in all cases, the energy of the erosion punch is most efficiently delivered to the medium by an impact normal to the surface. As such, this special case can be considered to produce an upper bound for all possible impact angles when determining the risks of fracture in the medium resulting from an erosion impact[1]. For this reason, considerations of the impact angle can be neglected in these preliminary investigations.

3.1.5 Threshold fracture energy

In the above, a general overview of the study of erosion, from an applied mathematical perspective, was given. This next section will instead look into one specific aspect of erosion impacts, called the threshold fracture energy. This concept, and new methods of studying it, will form the basis of the investigations undertaken in this chapter, and will therefore be covered in more detail.

3.1.5.1 Definition of the threshold fracture energy

The threshold fracture energy of an impact, ϵ_0^*, is defined as the initial energy required for an indenter to cause a fracture in a given medium (i.e. no fracture occurs if $\epsilon_0 < \epsilon_0^*$, while a fracture occurs for $\epsilon_0 \geq \epsilon_0^*$).

The initial motivation for examining this phenomena was provided by experimental results [112, 215]. These experiments, measuring the initial velocity required to cause a fracture in the medium, found that the threshold velocity for particles with a relatively large radius are approximately the same, whereas reducing the radius leads to a significant increase in the threshold velocities. Given that the impact duration depends largely on the particle size, these results demonstrated that the behaviour of the threshold velocity can be divided into two branches: one static, for large-size particles, and the other dynamic, for small-sized indenters. The conventional approach when studying the strength problem only permits one to calculate values of the threshold velocities by applying the critical stress criterion, and as such can only explain the static branch [182].

[1] It should be noted that, as a result of this, volume loss from the impacted material may be higher when the impact is at a low angle instead of normal to the surface. As the presented work is only concerned with fracture however, this effect will be neglected.

As such, investigations of the threshold fracture energy allow researchers to develop methods which overcome the limitations of previous frameworks, resulting in a number of studies into the phenomena in recent years. These new formulations should however be considered preliminary investigations, as it is still not clear whether all of the important impact parameters have been incorporated. In fact, the results of the most recent models appear to give rise to a paradoxical result, indicating that a deeper understanding of the underlying processes is required.

Here the basis of these theories will be provided, as well as a brief overview of their failings. In doing so, the primary motivation for the presented work will be made clear.

3.1.5.2 Theories of threshold fracture energy

Early analytical approaches to the threshold fracture energy typically relied on classical linear elastic fracture mechanics, which as previously mentioned could not explain key experimental results. As such these approaches will not be examined in detail here. A good example of one however is provided in [19], with details of other such models provided in the appendix of the cited paper.

Modern approaches to examining the threshold fracture energy can trace their roots to the preliminary examination carried out by *Morozov et al* [150], examining the creation of impact craters on other planets. This short paper, only three pages long, developed the philosophy of the approaches which would follow. Most notably the use of the incubation time based fracture criterion, which allowed the model to fully account for the dynamic loading pulse. Further, the prediction made by the model was shown to be in line with known results, establishing the credibility of such an approach.

With the underlying philosophy in place, the first models providing a full description of impact events could be provided. These were derived for fixed particle geometries, in order to simplify the mathematics during these initial investigations.

In the paper by *Volkov, Gorbushin & Petrov* [224], the case of a sphere, cylinder, and a particle defined by the shape function $z = Ar^4$, were considered. The structural-temporal approach was again employed. It was shown that the behavior of the threshold energy strongly depends on particle shape. It was also noted that the energy dependence on the radius has a local minimum in the cases of a spherical particle and a particle whose contacting surface is described by the equation $z = Ar^4$, while it does not have such a minimum in the case of a cylinder. This difference has been confirmed analytically [77], although the critical shape parameter for which the change in behaviour occurs wasn't identified in this study.

In order to better examine this phenomenon, the framework was generalized in the recent work by *Argatov, Mishuris & Petrov* [10], which instead modeled a particle defined by the shape function $z = Ar^{\lambda}$, with $\lambda > 1$. Their approach, which utilized the previously mentioned *Shtaerman-Kilchevsky* theory of quasi-static blunt impact, alongside a dynamic evaluation of the impact loading pulse, provided a method of analyzing the impact which was able to account for both spacial and temporal effects. The use of the incubation time based fracture criterion, meant that the final theory was able to provide an analytical relationship between the initial energy of the indenter and the formation of surface fractures, something which could previously only be examined through experimental methods.

3.1.5.3 The threshold fracture paradox

In the more general examination of the relationship between indenter shape and the threshold fracture energy by *Argatov, Mishuris & Petrov* [10], they provided a detailed asymptotic analysis of the transition from smooth indentor shapes (whose contact region varies in the impact process), to a cylindrical shape, providing a bound on the initial energy required for fracture initiation. Using this approach, they demonstrated that the threshold fracture energy, ϵ_0^*, was proportional to the half-time of the impact, t_0, in the following way:

$$\epsilon_0^* \propto t_0^{\frac{\lambda-5.5}{\lambda-1}}. \tag{3.13}$$

While this successfully provided an answer to the question posed in [224], showing that the change in behaviour of the threshold fracture energy occurred for when the shape parameter crossed a critical value, $\lambda^* = 5.5$, it was not clear why this was the case. The papers authors could find no physical justification for this critical value, and why the change in system behaviour was independent of the other problem parameters.

This came to be called the threshold fracture paradox. Put simply: what is the physical meaning of the critical shape parameter $\lambda^* = 5.5$.

There are two obvious resolutions to the problem. The first is that there is some underlying physical process, which has yet to be identified. Alternatively, it could be that there is some important physical aspect of the impact has been neglected, and the fact that it provides this value of the critical shape parameter is just a symptom of the model being unable to make physically realistic predictions. This possibility is especially troubling, given that the initial aim of these studies was to provide approaches capable of overcoming the limitations of previous methods, and accounting for all of the significant impact characteristics.

Given the importance of solving this problem to future investigations of the threshold fracture energy, the primary aim of this chapter will be to provide a clear resolution to the threshold fracture paradox. This will be achieved by making improvements and modifications to the original model by *Argatov, Mishuris & Petrov*, with an aim to provide an understanding of the physical processes which determine the critical shape parameter λ^*.

3.2 An improved estimate for the threshold fracture energy

3.2.1 Introduction

The first investigation into the threshold fracture paradox will attempt to resolve the problem through improvements to the original model by *Argatov, Mishuris & Petrov*, while keeping the design, philosophy and fundamental assumptions of the approach intact. If this manages to provide some physical explanation for the value of the critical shape parameter, or alter the behaviour of the obtained bound (3.13), then the paradox will be resolved. If not, then more drastic alterations will be required in order to determine its cause.

3.2.1.1 Aims of the initial investigation

In this section, we will attempt to improve on the bound for the threshold fracture energy provided in the initial paper by *Argatov, Mishuris & Petrov* [10]. This will be achieved by eliminating a physically unrealistic aspect of the previous evaluation. There, the fracture criterion was evaluated along the contact radius, which varied over time. However, to provide an accurate physical description, only fixed spacial points should be analyzed. As such, the key difference in approach taken here will be to locate the fixed point in the spacial domain for which the integral of the stress function is maximized, with this position then being used to obtain an improved bound on the initial energy required for fracture.

By doing so, it will be possible to demonstrate whether the critical shape parameter, $\lambda^* = 5.5$, is an inherent feature of the previous model, or if some new value is yielded. In either case, a greater understanding of the threshold fracture paradox will be obtained.

In addition to this, switching to evaluating fixed spacial points opens up new possibilities for the model. Most notably, the incubation time based fracture criterion can be applied

for arbitrary initial conditions, in order to determine the time and position of the initial fracture. This is something which is difficult to determine experimentally, and as such providing a new approach could have valuable applications.

3.2.1.2 Philosophy of the given approach

As previously discussed in Sect. 2.3.2 & 3.1.4.2, it is absolutely crucial that time dependent effects are incorporated into the model if an accurate description of fracture initiation resulting from dynamic impact is to be achieved. Unfortunately, the creation of a fully dynamic model which is able to account for various particle geometries, whilst also providing an accurate description of the surface stresses induced in the impacted medium, is beyond the capabilities of current mathematical tools. Because of this, an alternative approach will have to be developed which can provide a reasonable approximation of the impact over time.

This is achieved by combining the relations between problem parameters obtained using quasi-static models with a time dependent description of the indenter penetration depth obtained through a dynamic investigation of the impacts equation of motion. In doing so, it is possible to approximate a time dependent description of each problem parameter, including the surface stresses necessary to predict crack formation using the incubation time based fracture criterion (see Sect. 2.3.2 for a full description of this criterion). It should be noted that such an approach is not uncommon in the literature (e.g. in [10, 150, 224]), including being the central philosophy of the model developed by *Argatov, Mishuris & Petrov* which we wish to examine.

In practice, *Argatov, Mishuris & Petrov* achieved this by utilizing the quasi-static *Shtaerman-Kilchevsky* formulation (see Sect. 3.1.2.5), alongside an associated description of the stress function by *Johnson* [108] (stated here in (3.26)-(3.27)). This yielded detailed relationships between the various problem parameters. A dynamic description of the indenter penetration depth was then obtained (given here by (3.17)-(3.23)). Combining these results, a fully time dependent approximation of the indentation process was then obtained. This was then used to derive a bound on the initial energy of an impact required to cause crack initiation, through analysis of the fracture criterion along the contact radius over the impact duration.

As previously stated, the aim of this work is to eliminate an unrealistic aspect of this approach to obtaining the threshold fracture energy, namely choosing to evaluate the stress function along a moving path rather than for a fixed spacial point. Achieving this first requires an understanding of the behaviour of the surface stress and fracture criterion functions. This can then be used to determine the fixed spacial point at which the

fracture criterion is maximised for any given impact, from which the model of *Argatov, Mishuris & Petrov* can be updated and an improved bound on the threshold fracture energy can be obtained. The behaviour of this new bound can then be compared with the results of the initial paper, which provides the only comparable results available, to determine if there is any change in the critical shape parameter λ^* (the importance and meaning of this parameter is outlined in Sect. 3.1.5.3).

Interestingly, conducting a thorough analysis of the surface stresses will inevitably lead to a numerical model capable of predicting the time and location of any initial circumferential surface fracture resulting from a given impact, for arbitrary initial conditions. This will be achieved using standard numerical techniques, with the details of its construction being given in Sect. 3.2.3.

With this in mind, the initial investigation is organized as follows. In Sect. 3.2.2 we consider the quasi-static case, presenting a comprehensive form of the Shtaerman-Kilchevsky theory of blunt impact [117, 198]. We utilize solutions obtained by Galin [65, 66] for the frictionless case of a general non-polynomial axisymetric indenter. The expression for impulse of the indenter punch is derived. In Sect. 3.2.3 the stress function is formulated and simplified, applying the approach of *Johnson* [108]. Then numerical analysis of the resulting model is conducted using parameters for material properties taken from literature [168]. The incubation time based fracture criterion [149, 166] is introduced in Sect. 3.2.4, and we examine the predicted time and position of initial radial fractures, and the relation between particle parameters and the resulting fracture. In Sect. 3.2.5 the radial distance at which the stress function is maximised for any given impact is identified. This result is applied in Sect. 3.2.6 to obtain the maximum value of the stress function prior to fracture for a given impact. In Sect. 3.2.7 we derive an equation for the threshold fracture energy, and a comparison with previous results [10] is conducted. Finally, a summary of the work and results is provided in Sect. 3.2.8.

3.2.2 Initial problem formulation

We start by considering the case of a blunt indenter acting quasi-statically on an elastic half-space. We will follow the approach by *Argatov, Mishuris & Petrov* [10]. Previous results will be replicated only where necessary.

Let the shape of an axisymmetric punch be described by:

$$z = B^{1-\lambda} r^{\lambda}, \tag{3.14}$$

where $\lambda > 1$ is a real number and B is a constant having dimension $[length]$. From [65] (See also [66]), it follows that the relationship between the contact force, P, and the indenter displacement, w, can be represented in the following way:

$$P = k_1 w^{\frac{\lambda+1}{\lambda}}, \tag{3.15}$$

where:

$$k_1 = \Pi_1(\lambda)\frac{E}{(1-\nu^2)}B^{\frac{\lambda-1}{\lambda}}, \quad \Pi_1(\lambda) = \frac{2^{\frac{2}{\lambda}}\lambda^{\frac{\lambda-1}{\lambda}}}{\lambda+1}\Gamma(\lambda)^{\frac{1}{\lambda}}\Gamma\left(\frac{\lambda}{2}\right)^{-\frac{2}{\lambda}}. \tag{3.16}$$

Here E and ν represent Young's modulus and Poisson's ratio of the semi-infinite elastic body, while $\Gamma(x)$ is the Gamma function.

Equation (3.15) provides a key relationship between important variables involved in the problem, however it is obtained using a quasi-static formulation. As such, in order to account for the crucial time dependent effects discussed previously in Sect. 2.3.2 & 3.1.4.2, this will have to be extended to a time dependent form. This is achieved through the introduction of the indenters equation of motion, which can be used to obtain a time dependent description of the indenter penetration depth over time. Combining these two sets of relations (quasi-static and dynamic) allows for a complete description of the indentation process, which can be used to approximate the time-dependent form of the problem.

Denoting the mass of the indenter as m, its inital velocity as v_0 and noting (3.15), we can write the indenter's equation of motion as follows:

$$m\frac{d^2w}{dt^2} = -k_1 w^{\beta}. \tag{3.17}$$

The initial conditions are:

$$w(0) = 0, \quad \frac{dw}{dt}(0) = v_0, \tag{3.18}$$

with:

$$\beta = \frac{\lambda+1}{\lambda}, \tag{3.19}$$

As the indenter is penetrating an elastic half-space, for an impact duration $T_0 = 2t_0$, we have that t_0 is the time when the indenter depth $w(t)$ reaches its maximum w_0, and further that $v(t_0) = 0$. As a result of this, from [10] and [26], we have that:

$$w_0 = \left(\frac{(\beta+1)\,mv_0^2}{2k_1}\right)^{\frac{1}{\beta+1}}, \tag{3.20}$$

$$t_0 = \frac{w_0}{v_0} I_\beta, \quad I_\beta = \int_0^1 \frac{1}{\sqrt{1-x^{\beta+1}}}\, dx = \frac{\sqrt{\pi}\,\Gamma\left(\frac{1}{\beta+1}\right)}{(\beta+1)\,\Gamma\left(\frac{\beta+3}{2(\beta+1)}\right)}. \tag{3.21}$$

Having obtained equations for w_0 and t_0 we can introduce new dimensionless variables. Following exactly the steps from [10] for equations (3.17) and (3.18), we define the indenter depth in terms of a new parameter $U(\beta; (v_0/w_0)t)$:

$$w(t) = w_0 U\left(\beta; \frac{v_0}{w_0} t\right), \tag{3.22}$$

where:

$$\int_0^{U\left(\beta; \frac{v_0}{w_0}t\right)} \frac{d\xi}{\sqrt{1-\xi^{\beta+1}}} = \frac{v_0}{w_0} t. \tag{3.23}$$

This provides us with an explicit equation for $U(\beta; (v_0/w_0)t)$. If we denote the left-hand side of (3.23) by $F(U)$, then $U(\beta; (v_0/w_0)t) = (w_0/v_0)F^{-1}(t)$, where F^{-1} is the inverse of F. We also note that $I_\beta = F(1)$.

3.2.3 Surface stress distribution of the indented half-plane

3.2.3.1 Analytical formulation

A thorough investigation of the impact process requires both a derivation and understanding of the spacial-temporal stress function. At the start of this subsection we will again follow the approach by *Argatov, Mishuris & Petrov* [10]. The resulting stress function has a more accessible form than that proposed in [10]. A comparison with the Hertz solution is conducted.

The contact pressure beneath a blunt indenter with shape function (3.14) is given by:

$$p(r) = \frac{\lambda+1}{2} p_0 \int_0^{\sqrt{1-\rho^2}} (\rho^2 + \xi^2)^{\frac{\lambda-2}{2}}\, d\xi, \tag{3.24}$$

Here $\rho = r/a$ is the dimensionless radial coordinate, $p_0 = P/(\pi a^2)$ is the mean contact pressure, a is the radius of the contact area given by:

$$a = \left[\frac{\left(1-\nu^2\right) B^{\lambda-1}}{\Pi_1(\lambda) E} P\right]^{\frac{1}{\lambda+1}}, \tag{3.25}$$

where $\Pi_1(\lambda)$ is as defined in (3.16).

From [108, p.76-80] we have that the radial and circular stresses throughout the surface of the elastic half-space can be expressed in terms of the function:

$$\mathcal{L}(\xi) = \int_{\xi}^{1} \frac{\eta p(\eta)\, d\eta}{(\eta^2 - \xi^2)^{1/2}}, \tag{3.26}$$

as follows:

$$\sigma_r(\rho) = \begin{cases} -p(\rho) - \dfrac{2(1-2\nu)}{\pi\rho^2}\left(\displaystyle\int_{\rho}^{1} \frac{\xi\mathcal{L}(\xi)\, d\xi}{(\xi^2-\rho^2)^{1/2}} - \int_{0}^{1} \mathcal{L}(\xi)\, d\xi\right), & \rho \leq 1 \\ \dfrac{2(1-2\nu)}{\pi\rho^2}\displaystyle\int_{0}^{1} \mathcal{L}(\xi)\, d\xi, & \rho > 1, \end{cases} \tag{3.27}$$

$$\sigma_\theta(\rho) = \begin{cases} -2\nu p(\rho) + \dfrac{2(1-2\nu)}{\pi\rho^2}\left(\displaystyle\int_{\rho}^{1} \frac{\xi\mathcal{L}(\xi)\, d\xi}{(\xi^2-\rho^2)^{1/2}} - \int_{0}^{1} \mathcal{L}(\xi)\, d\xi\right) \\ \qquad + \dfrac{4}{\pi\rho}\left(\nu\dfrac{d}{d\rho} + \dfrac{1-\nu}{\rho}\right)\displaystyle\int_{0}^{\rho} \frac{\xi\mathcal{L}(\xi)\, d\xi}{(\rho^2-\xi^2)^{1/2}}, & \rho \leq 1 \\ -\dfrac{2(1-2\nu)}{\pi\rho^2}\displaystyle\int_{0}^{1} \mathcal{L}(\xi)\, d\xi, & \rho > 1. \end{cases} \tag{3.28}$$

These expressions can be simplified by inserting (3.26) and changing the order of integration. We obtain:

$$\sigma_r(\rho) = \begin{cases} -p(\rho) + \dfrac{1-2\nu}{\rho^2}\displaystyle\int_{0}^{\rho} \eta p(\eta)\, d\eta, & \rho \leq 1 \\ \dfrac{1-2\nu}{\rho^2}\displaystyle\int_{0}^{1} \eta p(\eta)\, d\eta, & \rho > 1, \end{cases} \tag{3.29}$$

$$\sigma_\theta(\rho) = \begin{cases} -2\nu p(\rho) - \dfrac{1-2\nu}{\rho^2}\displaystyle\int_{0}^{\rho} \eta p(\eta)\, d\eta \\ \qquad + \dfrac{2}{\pi\rho}\left(\nu\dfrac{d}{d\rho} + \dfrac{1-\nu}{\rho}\right)\displaystyle\int_{0}^{1} \eta p(\eta) \log\left(\frac{\eta+\rho}{|\eta-\rho|}\right) d\eta, & \rho \leq 1 \\ -\dfrac{1-2\nu}{\rho^2}\displaystyle\int_{0}^{1} \eta p(\eta)\, d\eta, & \rho > 1. \end{cases} \tag{3.30}$$

Finally, as noted in [10], from (3.24) we have that:

$$\int_{0}^{1} \eta p(\eta)\, d\eta = \frac{P}{2\pi a^2}, \tag{3.31}$$

which simplifies the stress function for $\rho > 1$.

Remark: In the cases $\lambda = 1$, $\lambda = 2$ and $\lambda \to \infty$ the stress function (3.30) tends to that of the Hertz solution for the impact with an elastic half-space of a rigid cone, sphere and cylinder respectively (see Appendix. A). We note however that the mean contact pressure p_0 doesn't converge to the Hertz solution in the case of a rigid cone ($\lambda = 1$) (for summary of Hertz solutions, see Sect. 3.1.2).

The above equations and relations (3.15)-(3.16), (3.20)-(3.23), (3.24)-(3.25), (3.29)-(3.31) combine to provide a fully time dependent description of the impact, yielding a simple model which describes the indentation penetration depth, contact pressure, stress function and contact radius. In practice, the model is now able to approximate such an impact for arbitrary initial conditions. The fracture criterion will be introduced later to complete this model of erosion induced fracture.

The initial numerical model is, for the most part, developed using standard numerical techniques. Unknown impact constants (e.g. the maximum penetration depth of the indenter w_0) are obtained directly from given their relationships with the arbitrary initial conditions using (3.20)-(3.21) (in the computations provided here these are complimented by (3.62) and (3.67) to ensure consistency of results throughout the paper). The inverse relation of (3.23) is obtained using a cubic-spline based approximation. This is then placed into (3.22) to develop a time dependent description of the penetration depth. Relations (3.15), (3.25) are used to provide time dependent forms of the contact force and contact radius respectively. The non-time dependent components of the stress function, for fixed spacial points, are obtained from (3.24), (3.29). Numerical techniques, such as evaluation of the leading asymptotic terms analytically, are used to increase the accuracy and efficiency of computations. The stress function can then be extended to the temporal case by introducing the known time dependent forms of the contact force and radius. With this, a complete picture of the impact domain over time is realized.

3.2.3.2 Numerical examination of stress behaviour

In order to utilize the incubation time approach for this impact problem we have to integrate the stress function over multiple time periods. The final derivation of an equation for the threshold fracture energy will require knowledge of the period over which this integral is maximized for fixed spacial positions. As a result it is important to examine the shape of the radial stress function (3.29), as a function of both time and position, and analyse how it changes as we vary the shape parameter λ.

In Fig. 3.5 & 3.6 we present graphs of the stress function for $\epsilon_0 = 375$ J, $V = 2 \times 10^{-6}$ m^3, and the material properties corresponding to gabbro-diabase[2] [168]: $E = 6.2{\times}10^9$ N/m^2, $\nu = 0.26$, $\rho_0 = 2400$ kg/m^3. Remaining values were obtained using (3.14)-(3.16), (3.21)-(3.23), (3.62) and (3.67).

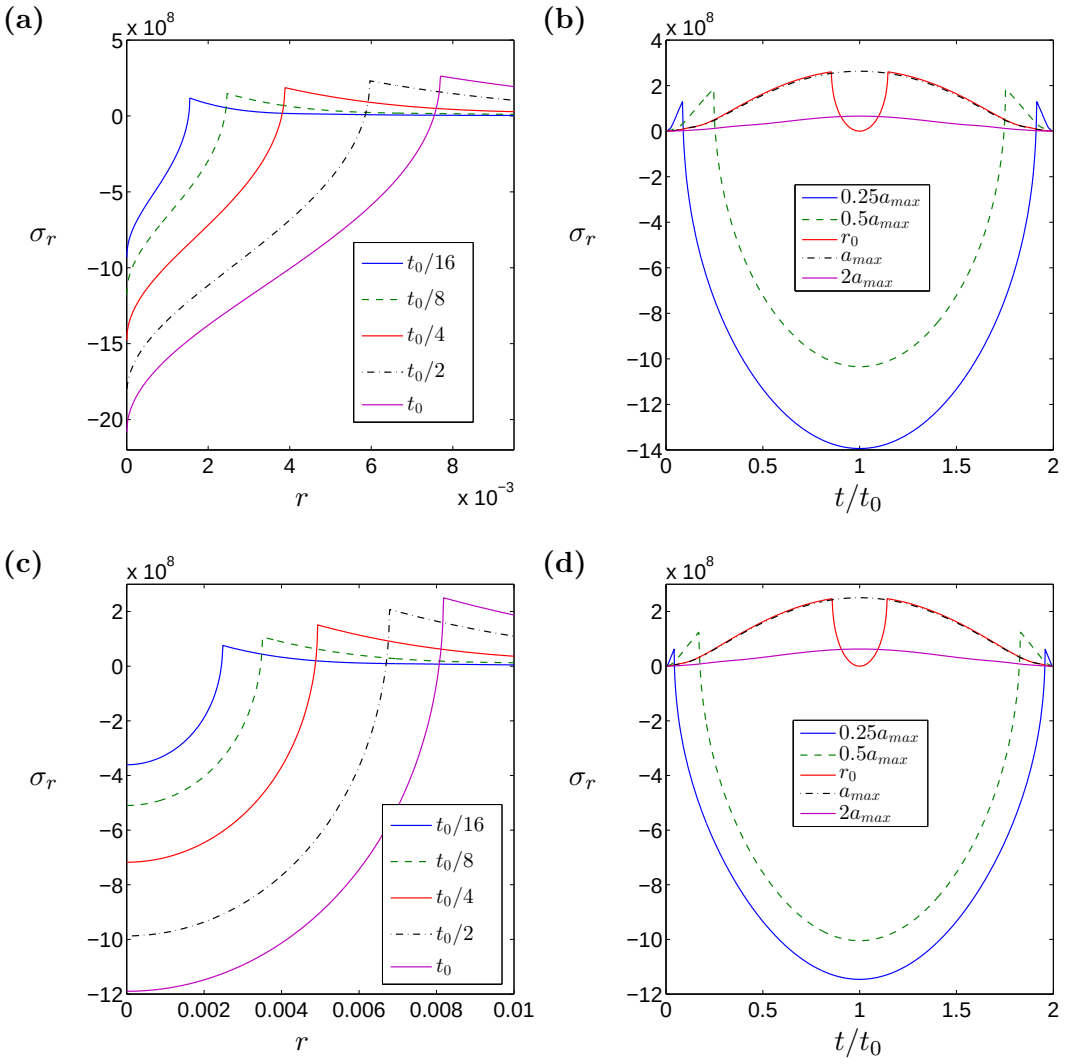

FIGURE 3.5: The stress function (3.29) for (a,b) $\lambda = 1.5$ and (c,d) $\lambda = 2$. Here figures on the left show the stress over r for fixed time, while those on the right show how the stress for a set r behaves over time $2t_0$. Note a clear change in behaviour when $\lambda \geq 2$ in comparison with $\lambda < 2$ at the point $r = 0$..

In cases where r is fixed, we always ensure to evaluate the stress function at two λ-dependent points; $a_{max} = a(t_0)$ and r_0 defined as:

$$r_0 = \{\min r : \sigma_r(r,t) \geq 0 \quad \forall \quad t \in [0, 2t_0]\}\,. \tag{3.32}$$

There are many observations that can be made about the behaviour of the stress function as λ increases. The first is that, for $\lambda{\leq}2$ the minimum of the stress function occurs

[2] A type of concrete for which all necessary material parameters are known.

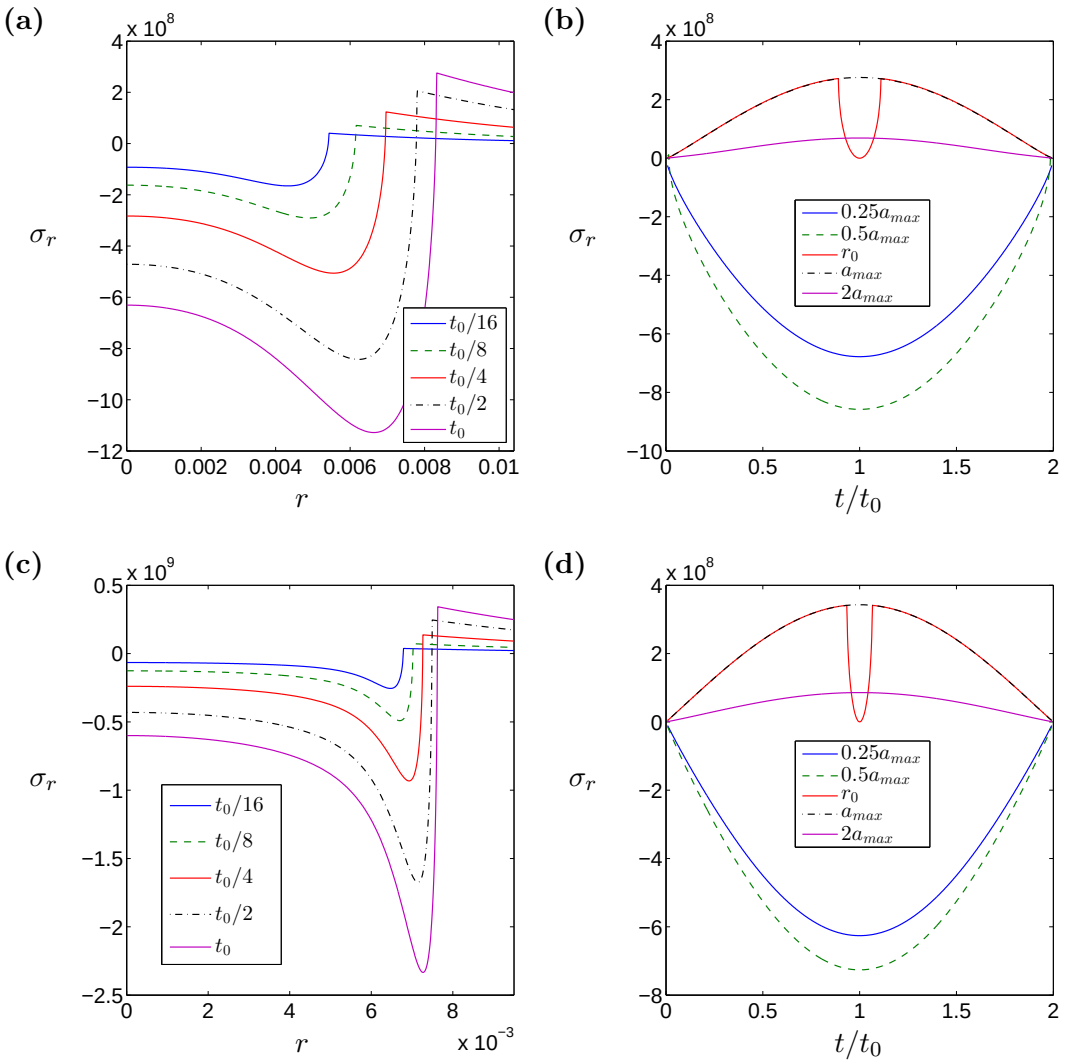

FIGURE 3.6: The stress function (3.29) for (a,b) $\lambda = 5.5$, (c,d) $\lambda = 20$. Graphs (a,c) are over r for fixed time, while (b,d) show how the stress for a set r behaves over time $2t_0$.

at the point of impact ($r = 0$), however this minimum tends quickly towards the edge of the contact region as the shape parameter increases. This is highlighted in the example $\lambda = 20$ in Fig. 3.6.

Another observation is that, except for $\lambda < 2$, the maximum magnitude of the stress function rises as λ increases. Additionally, for all λ, the stress function is maximised for $r = a_{max}$, $t = t_0$ and, along the line $r = a_{max}$, it increases monotonically for $t < t_0$ and decreases monotonically for $t > t_0$.

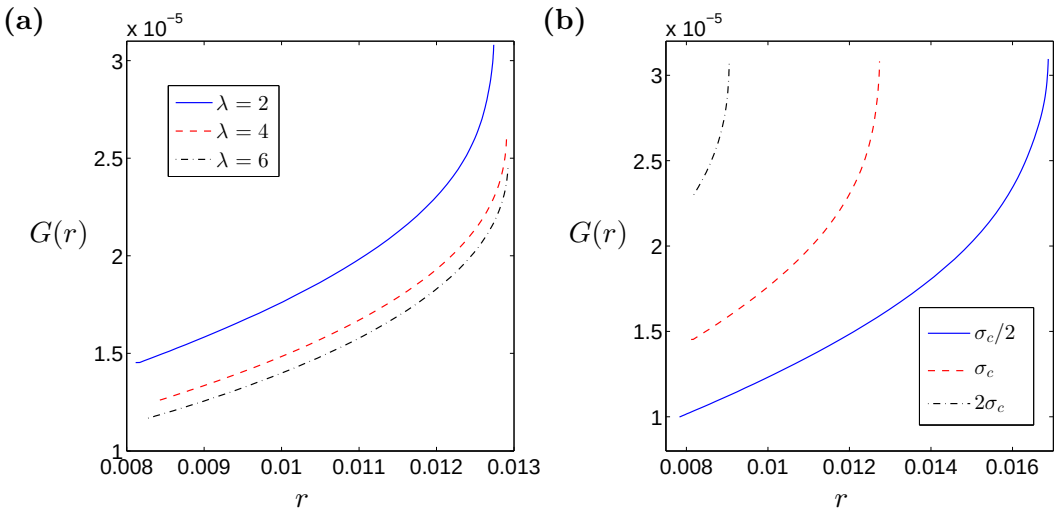

FIGURE 3.7: The function $G(r)$ (seconds) (3.34), denoting the minimum time to fracture for various fixed spacial positions r. Here we take $V = 2 \times 10^{-6} m^3$, while showing: (a) the results for various fixed $\lambda = \{2, 4, 6\}$, (b) the minimum time to fracture for fixed $\lambda = 2$, with various values of the tensile stress σ_c. Here the benchmark static material strength is $\sigma_c = 44.04 \times 10^6$ Nm^{-2}. We note that in each case there is a pronounced minimum for the function G.

3.2.4 Incubation time based fracture criterion

For the reasons outlined in Sect. 2.3.2, we utilize an incubation time based fracture criterion [169, 172] to predict fracture. Stated briefly, this criterion incorporates the relaxation time of the material, and can thus account for the stress buildup occurring during dynamic impact. As a result, it is able to accurately predict previously neglected temporal effects, and has been shown to coincide with experimental results [149, 172]. It should also be noted that it reduces to the classical *Irwin* criterion (2.38) under quasi-static conditions, meaning that its inclusion will ensure the model is accurate for both dynamic and quasi-static impacts.

In the simplest case, for the impact interaction of a superellipsoid particle with an elastic half-space, it is defined in terms of the criterion function:

$$\gamma(r,t) = \frac{1}{\tau\,\sigma_c} \int_{t-\tau}^{t} \sigma_r(r,s)\,ds. \tag{3.33}$$

The incubation time based fracture criterion G can then be formulated as follows [166]:

$$G(r) = \{\min t \in [0,\, 2t_0] : \gamma(r,t) = 1\}\,, \tag{3.34}$$

where σ_c is the tensile strength of the elastic material (a parameter evaluated under quasi-static loading conditions), τ is the incubation time of the fracture process (a measure of stress-rate sensitivity of the material, which is calculated quasi-experimentally).

It is clear that G may not be surjective however, assuming that criterion (3.34) is injective, we can obtain the inverse of G. Denoting the time of the initial fracture t^* for any impact, with associated position r^*, we can state these in terms of the time criterion G (3.34):

$$t^* = \min G(r), \quad r^* = G^{-1}(t^*). \tag{3.35}$$

This simple formulation is only intended to define the initial breakage and can't be used to predict subsequent behaviour.

3.2.4.1 Predicted fracture time

The time-based fracture criterion is designed to allow the calculation of the minimum time to fracture of a material over a range of scale levels [166].

To apply this criterion we need to find $G(r)$ (3.34), from which t^* and r^* can be obtained by (3.35). Graphs of $G(r)$ are shown in Fig. 3.7, while the relationship between different indenter properties and the incubation time prior to fracture are displayed in Fig. 3.8 & 3.9. In simulations the same constants are used as in Sect. 3.2.3.2, in addition to $\tau = 44$ μs, $\sigma_c = 44.04{\times}10^6$ Nm^{-2} (as for gabbro-diabase, [168]).

In Fig. 3.7a we can see the general characteristics of the incubation time based fracture criterion. From Fig. 3.7b however it is clear that, when σ_c grows, there is a large increase in the expected incubation time, accompanied by a small increase in the position of the initial fracture.

From the plots of t^* and r^* in Fig. 3.8 it follows that there is a clear change of behaviour as λ increases, although beyond this it is obvious that the volume of the indenter plays a more important role.

The effect on t^* and r^* when varying the initial velocity in Fig. 3.9 is more readily apparent. It is clear that a higher initial velocity reduces the incubation time prior to fracture.

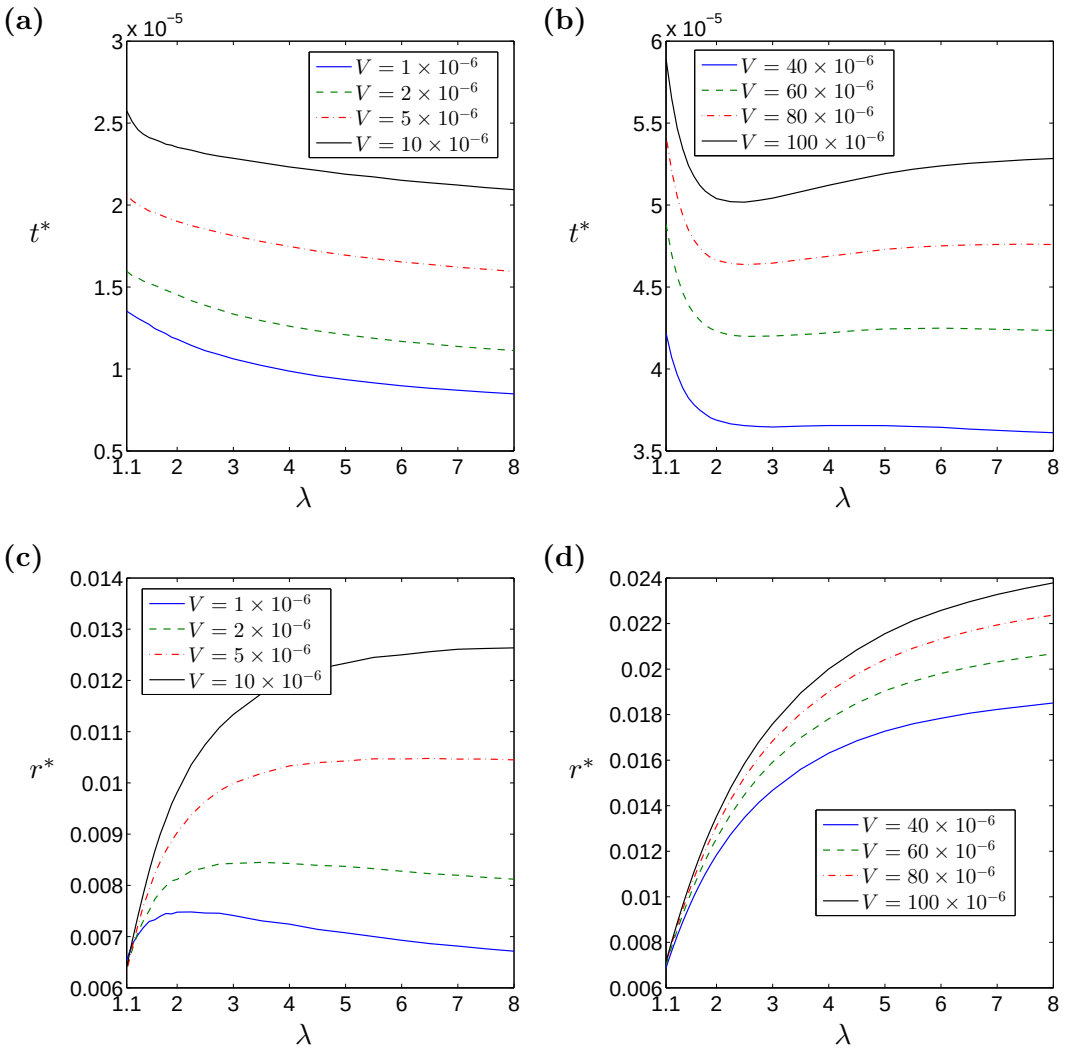

FIGURE 3.8: The (a,b) minimum time to fracture t^* (3.35) and the (c,d) minimum radial distance r^* at which it will occur over λ for various fixed indenter volumes V (note that smaller volumes correspond to higher initial velocities and, for fixed λ, longer impact durations).

3.2.5 Analysis of the properties of function γ involved in the fracture criterion

With the underlying model developed, and a method of determining the value of the criterion function γ devised, we are now in a position to fix the physically unrealistic assumption of the initial model by *Argatov, Mishuris & Petrov* [10]. This will be achieved by finding the spacial position, and associated time period, over which the fracture criterion function γ is maximized for any given impact. Once this is determined we will be able to state with certainty that, if the fracture criterion is not satisfied when evaluated at this point, then no fracture will occur in the medium for the given impact.

As a result, the threshold fracture energy for a set of given initial conditions will simply be the initial energy required to satisfy the fracture criterion at this point, allowing a

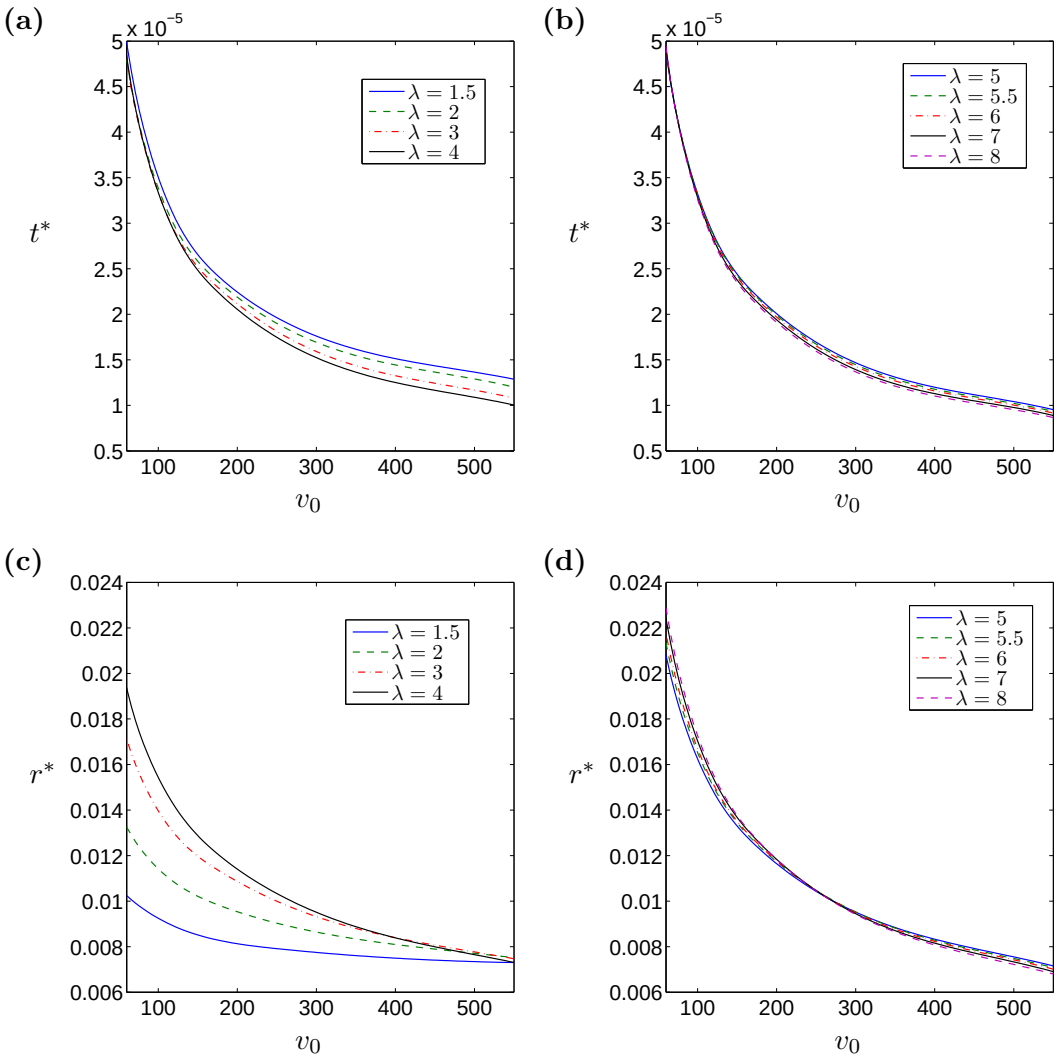

FIGURE 3.9: The (a,b) minimum time to fracture t^* (3.35) and the (c,d) minimum radial distance r^* at which it will occur over v_0 for various fixed λ.

comparison with the original results by *Argatov, Mishuris & Petrov* to be conducted. With this in mind, we begin the analysis of the properties of the criterion function γ.

3.2.5.1 Maximum of γ for fixed point r_{max}

We wish to determine the value of the (spatial) radial coordinate, and associated time period $[t-\tau, \quad t]$, for which the criterion function (3.33) is maximised. In doing this it will be possible to find the conditions necessary for (3.34) to be uniquely valued, providing an explicit condition for fracture initiation and an improved estimate of the threshold fracture energy.

Let us define the time dependent position r_{max} as follows:

$$r_{max}(t) = \{r : \gamma(r,t) = \max \gamma(r,t), \quad t \in [0, 2t_0]\}\,. \tag{3.36}$$

The criterion (3.33) can then be maximised for time t_{max}:

$$t_{max} = \{t \in [0,\, 2t_0] : \gamma(r_{max},t) = \max \gamma(r_{max},t)\}\,. \tag{3.37}$$

It is clear from the integral interval in (3.33) that there will be two seperate cases when evaluating this criterion, defined by whether or not the condition $\tau > 2t_0$ is satisfied, as shown in Fig. 3.10. We will examine these possibilities separately before collating the results.

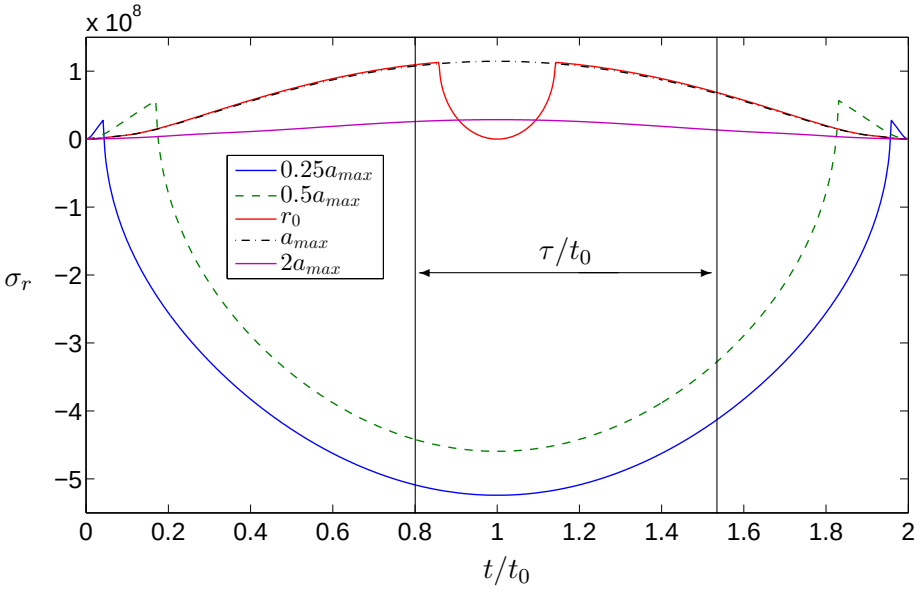

FIGURE 3.10: In the case $\tau \geq 2t_0$, the criterion function (3.33) can only be evaluated for regions beginning at the y-axis ($t = 0$). However for the case $\tau < 2t_0$, as shown above, it can integrate over intervals throughout the range, allowing different starting points of integration, and therefore changing the resulting behaviour of the time criterion.

The case $\tau \geq 2t_0$

Graphs of the function γ (3.33) are shown in Fig. 3.11, while the value of r_{max} for values of t (when evaluating the region $[0\,, t\,]$) are shown in Fig. 3.12. In all simulations the properties of gabbro-diabase are used, with a projectile of fixed initial energy and volume, the constants for which are stated explicitly in Sect. 3.2.3.2 & 3.2.4.1.

It is clear from Fig. 3.11 & 3.12 that the equation for $r_{max}(t)$, evaluated for any time t, yields:

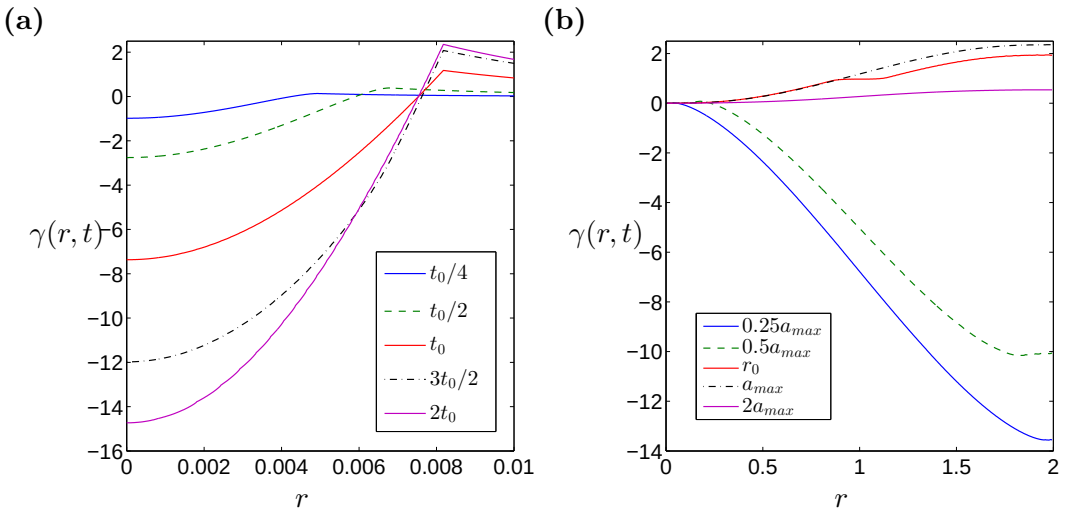

FIGURE 3.11: Plot of the criterion function γ (3.33) for $\lambda = 2$, $t_0 \leq \tau/2$ for: (a) a fixed range of time over which the integral is evaluated and varying r, (b) the effect of varying the integral range on fixed values of r. It is clear that γ is maximised when evaluated over the whole time interval.

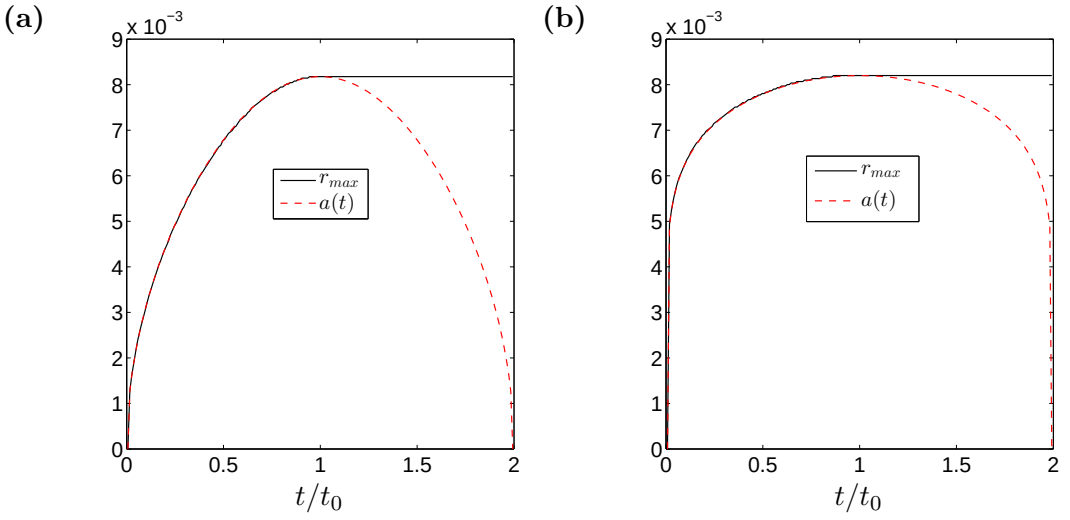

FIGURE 3.12: The value of r_{max} for which the criterion function γ is maximised when evaluated over time $[0, t]$ for $2t_0 \leq \tau$ with (a) $\lambda = 2$ and (b) $\lambda = 7$.

$$r_{max}(t) = \begin{cases} a(t), & t < t_0, \\ a(t_0) = a_{max}, & t_0 \leq t \leq 2t_0. \end{cases} \tag{3.38}$$

From the behaviour of the stress function it follows that $\sigma_r\left(r_{max}(t), t\right) \geq 0$ for $t \in [0,\ 2t_0]$. As a result, for the case $\tau \geq 2t_0$, the time criterion will be maximised when evaluated over the entire impact duration.

Combining the above we can state with confidence that, in the case $\tau > 2t_0$, no fracture

will occur as a result of the impact if the time criterion (3.34) is not achieved when evaluating the point $r = a_{max}$ over the time range $[0, 2t_0]$.

The case $\tau < 2t_0$

In order to achieve an impact duration larger than those previously modeled, we change the volume of the indenter to $V = 100{\times}10^{-6}$ m^3 (the remaining constants are kept the same as previously stated).

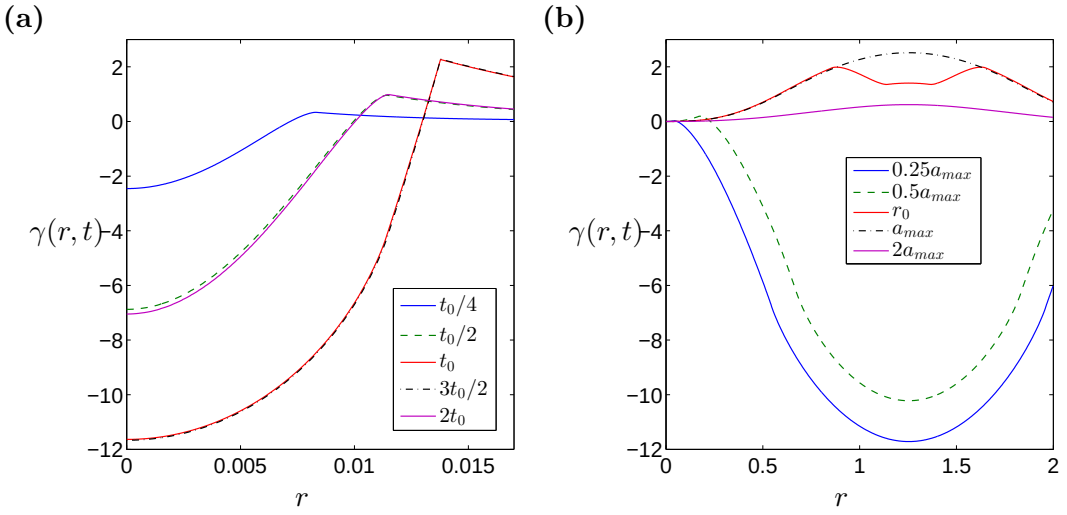

FIGURE 3.13: Plot of the criterion function γ (3.33) for $\lambda = 2$, $2t_0 > \tau$, for: (a) a fixed range of time over which the integral is evaluated for varying r, (b) the effect of varying the integral range for fixed values of r.

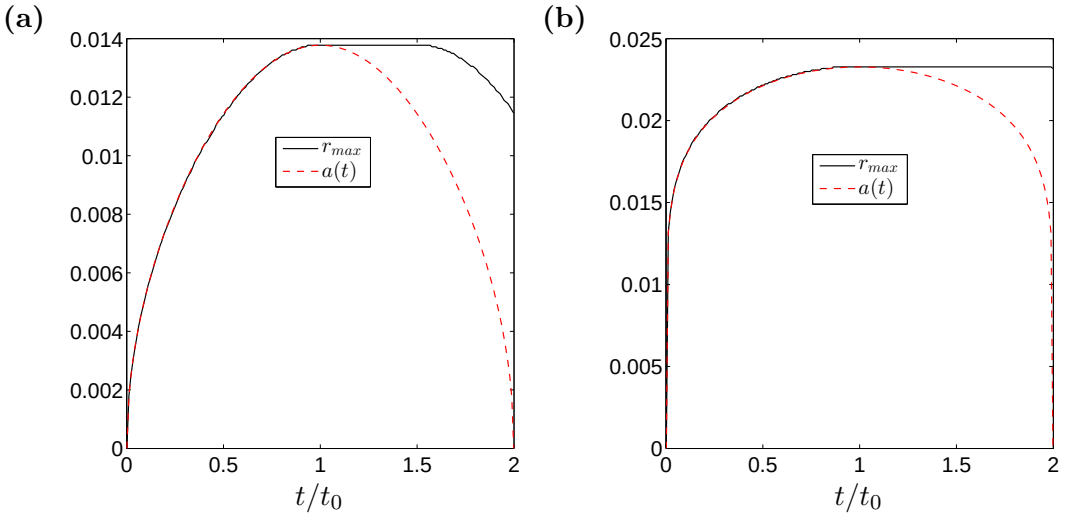

FIGURE 3.14: The value of r_{max} (3.36) for which the time criterion is maximised when evaluated over time $[0, t]$ for $2t_0 > \tau$ with (a) $\lambda = 2$ and (b) $\lambda = 7$.

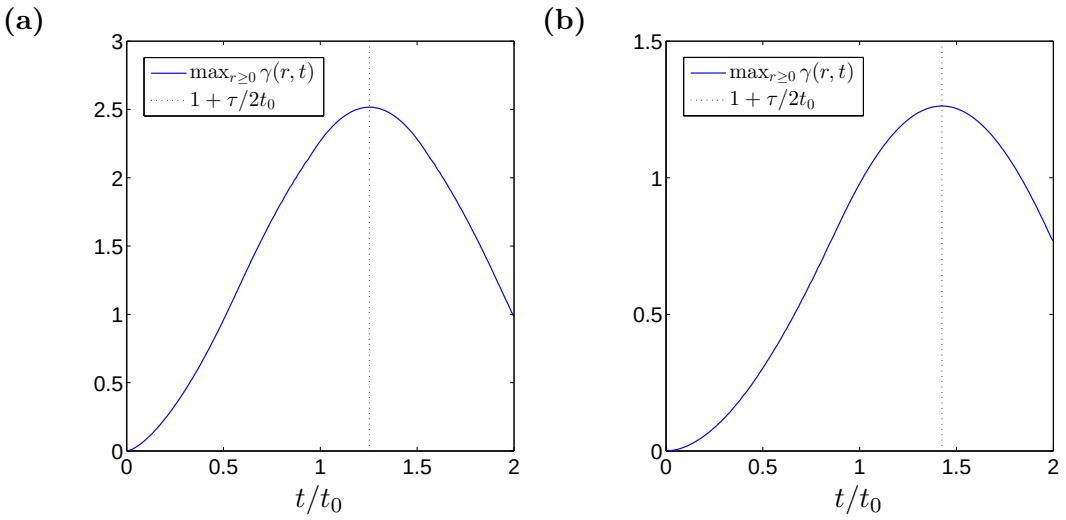

FIGURE 3.15: The criterion function $\gamma(r_{max}(t),t)$ for (a) $\lambda = 2$ and (b) $\lambda = 7$, $2t_0 > \tau$. The monotonic nature of the function has disappeared, however there is a clear maximum value at $t = t_0 + \tau/2$.

From Fig. 3.13 it follows that, unlike in the previous case, the function $\gamma(a_{max},t)$ is no longer monotonically increasing, and its distribution is instead far more similar to the behaviour of the stress function. Therefore the time interval over which we wish to evaluate $\gamma(r_{max}(t),t)$ in order to maximise G (3.34) will be different from that found in the previous case. The behaviour of the maximum of the criterion function is shown in Fig. 3.15.

Similarly, for large t_0, Fig. 3.14 shows that the formula for r_{max}, while identical to the previous case for $t \leq t_0$, differs in the region where $t > t_0$. The explicit equation for $r_{max}(t)$ in this case is:

$$r_{max}(t) = \begin{cases} a(t), & t < t_0, \\ a(t_0) = a_{max}, & t_0 \leq t \leq t_0 + \tau, \\ a(t-\tau), & t_0 + \tau < t \leq 2t_0. \end{cases} \tag{3.39}$$

It is clear from analysis of the stress function in Sect. 3.2.4 that $\sigma_r(a_{max},t)$ achieves its maximum at the midpoint t_0. Combining this fact with the results from Fig. 3.15 it stands to reason that, for the case $\tau < 2t_0$, the region of integration for which (3.34) will be maximised is $[t_0 - \tau/2,\, t_0 + \tau/2\,]$, for $r = a_{max}$.

3.2.5.2 Time dependent stress function for $r = a_{max}$

From the previous subsection it is clear that the criterion function γ (3.33) achieves it's maximum when evaluated along the point $r = a_{max}$. In order to make use of this in deriving the minimum energy required for fracture initiation we need to obtain the time dependent stress function $\sigma_r(a_{max}, t)$.

Let us start by noting that we have $\rho = a_{max}/a(t) > 1$ except in the case $t = t_0$ when $\rho = 1$. What's more, as $p(1) = 0$, the stress function from (3.29) takes the form:

$$\sigma_r(a_{max}, t) = \frac{(1-2\nu)a(t)^2}{a_{max}^2} \int_0^1 \eta p(\eta)\, d\eta. \tag{3.40}$$

Now, by (3.31), and applying equations (3.14)-(3.16) we have:

$$\sigma_r(a_{max}, t) = \frac{\Pi_1(\lambda) E\,(1-2\nu)}{2\pi\,(1-\nu^2)\,a_{max}^2} B^{1-\lambda} a(t)^{\lambda+1}. \tag{3.41}$$

Using the same steps as above for the point $\rho = 1$, it can be easily shown that the time dependent stress function along the line $r(t) = a(t)$ yields:

$$\sigma_r(a(t), t) = \frac{\Pi_1(\lambda) E\,(1-2\nu)}{2\pi\,(1-\nu^2)} B^{1-\lambda} a(t)^{\lambda-1}. \tag{3.42}$$

Taking $t = t_0$ in (3.41), and using the notation $\sigma_r(a_{max}, t_0) = \sigma_{max}$, we obtain the boundary condition:

$$\sigma_{max} = \frac{\Pi_1(\lambda) E\,(1-2\nu)}{2\pi\,(1-\nu^2)} B^{1-\lambda} a_{max}^{\lambda-1}. \tag{3.43}$$

Note that this condition also holds for (3.42). Placing (3.43) into (3.41) and (3.42) we obtain the relations:

$$\sigma_r(a_{max}, t) = \sigma_{max} \left(\frac{a(t)}{a_{max}} \right)^{\lambda+1}, \tag{3.44}$$

$$\sigma_r(a(t), t) = \sigma_{max} \left(\frac{a(t)}{a_{max}} \right)^{\lambda-1}. \tag{3.45}$$

By combining (3.44) and (3.45), one can find the following formula for the stress functions:

$$\sigma_r(a(t), t) = \sigma_{max}^{\frac{2}{\lambda+1}}\, \sigma_r(a_{max}, t)^{\frac{\lambda-1}{\lambda+1}}. \tag{3.46}$$

Finally, we use (3.41) and (3.43) to eliminate the term a_{max}, and then by applying (3.14) the final formulae for the stress function is derived:

$$\sigma_r(a_{max}, t) = \left[\frac{\Pi_1(\lambda) E\,(1-2\nu)}{2\pi\,(1-\nu^2)} B^{\frac{1-\lambda}{\lambda}} \right]^{\frac{\lambda+1}{\lambda-1}} \sigma_{max}^{-\frac{2}{\lambda-1}}\, w(t)^{\frac{\lambda+1}{\lambda}}. \tag{3.47}$$

3.2.6 The maximum of the stress function prior to fracture

Now that the spacial position for which the fracture criterion is maximised is known, and the function describing the surfaces stresses at this point has been derived, determining the threshold fracture energy simply requires obtaining the critical value of this stress function needed to initiate a fracture for a given impact. As the fracture criterion is time dependent, this will require a dynamic description of the surface stress, which can be obtained by assuming a sinusoidal impact loading pulse, and determining its behaviour by comparison with the time dependent indenter penetration depth. Once this is completed, it will simply be a matter of manipulating the known equations in order to determine the threshold fracture energy.

We let $\omega(t)$, $t \in [0, T_0]$, be the shape function of an impact loading pulse. Then, the stress variation along the contact region is given by:

$$\sigma_r(a(t), t) = \sigma_{max}\, \omega(t). \tag{3.48}$$

By (3.46), we can obtain this in terms of the stress function for a_{max}:

$$\sigma_r(a_{max}, t) = \sigma_{max}\, \omega(t)^{\frac{\lambda+1}{\lambda-1}}. \tag{3.49}$$

Substituting expression (3.49) into (3.48), before using (3.34) evaluated at the point $r = a_{max}$, we arrive at the critical (threshold) stress amplitude leading to fracture, σ^*_{max}:

$$\sigma^*_{max} = \frac{\tau\, \sigma_c}{\max_{t\in[0,T_0]} \int_{t-\tau}^{t} \omega(s)^{\frac{\lambda+1}{\lambda-1}}\, ds}. \tag{3.50}$$

Meanwhile, using equations (3.16), (3.19) and (3.20) we have, for the maximum indentation:

$$w_0 = \Pi_2(\lambda) \left[\frac{1-\nu^2}{E}\right]^{\frac{\lambda}{2\lambda+1}} B^{\frac{1-\lambda}{2\lambda+1}} \left[m v_0^2\right]^{\frac{\lambda}{2\lambda+1}}, \tag{3.51}$$

where, for $\Pi_1(\lambda)$ as in (3.16):

$$\Pi_2(\lambda) = \left(\frac{2\lambda+1}{2\lambda\, \Pi_1(\lambda)}\right)^{\frac{\lambda}{2\lambda+1}}. \tag{3.52}$$

Now, substituting (3.19), (3.21), (3.22), (3.51) into (3.47), and noting (3.49), one obtains:

$$\sigma_{max} = \Pi_3(\lambda)\, (1-2\nu) \left[\frac{E}{1-\nu^2}\right]^{\frac{\lambda+2}{2\lambda+1}} B^{\frac{3(1-\lambda)}{2\lambda+1}} \left[m v_0^2\right]^{\frac{\lambda-1}{2\lambda+1}}, \tag{3.53}$$

$$\omega(t) = U^{\frac{\lambda-1}{\lambda}}\left(\frac{\lambda+1}{\lambda}; \frac{I_\beta}{t_0} t\right), \tag{3.54}$$

where:

$$\Pi_3(\lambda) = \frac{\Pi_1(\lambda)\Pi_2(\lambda)^{\frac{\lambda-1}{\lambda}}}{2\pi}. \tag{3.55}$$

Since the shape function of the impact loading pulse is symmetric around $t = t_0$, we can transform (3.50) into the following form:

$$\sigma^*_{max} = \frac{\tau\,\sigma_c}{\int_{t_0-\tau/2}^{t_0+\tau/2} \omega(s)^{\frac{\lambda+1}{\lambda-1}}\,ds}. \tag{3.56}$$

Noting (3.54), we introduce the auxiliary function:

$$\Upsilon(\beta, t_0) = \frac{1}{2t_0}\int_{t_0-\tau/2}^{t_0+\tau/2} U^\beta\left(\beta; \frac{I_\beta}{t_0}s\right) ds. \tag{3.57}$$

The evaluation of Υ depends on the relation between the incubation time τ and the impact duration $T_0 = 2t_0$. For $2t_0 \leq \tau$ we have:

$$\Upsilon(\beta, t_0) = \frac{1}{t_0}\int_0^{t_0} U^\beta\left(\beta; \frac{I_\beta}{t_0}s\right) ds. \tag{3.58}$$

Changing the order of integration by using the variable $\chi = I_\beta s/t_0$, we obtain the following simplification:

$$\Upsilon(\beta, t_0) = \frac{1}{I_\beta}\int_0^{I_\beta} U^\beta(\beta; \chi)\,d\chi. \tag{3.59}$$

Using the same method for $\tau < 2t_0$, one has:

$$\Upsilon(\beta, t_0) = \frac{1}{I_\beta}\int_{I_\beta(1-\tau/2t_0)}^{I_\beta} U^\beta(\beta; \chi)\,d\chi. \tag{3.60}$$

Then, combining the above with (3.56), it is clear that:

$$\sigma^*_{max} = \frac{\tau\,\sigma_c}{2t_0\Upsilon(\beta, t_0)}. \tag{3.61}$$

3.2.7 Prediction of the threshold fracture energy

In order to ensure results comparible with [10], we take the mass of a general axisymmetric superellipsoid centered on the coordinate origin to be described by the following equation:

$$m = \Pi_4(\lambda)\rho_0 B^3, \tag{3.62}$$

where ρ_0 is the material density of the indenter and:

$$\Pi_4(\lambda) = \frac{4\pi}{3}\lambda^{-\frac{(\lambda+2)}{\lambda-1}}\Gamma\left(\frac{2}{\lambda}\right)\Gamma\left(\frac{1}{\lambda}\right)\Gamma\left(\frac{3}{\lambda}\right)^{-1}. \tag{3.63}$$

Substitution of (3.62) into (3.53) yields:

$$\sigma_{max} = \Pi_5(\lambda)(1-2\nu)\left[\frac{E}{1-\nu^2}\right]^{\frac{\lambda+2}{2\lambda+1}} \rho_0^{\frac{\lambda-1}{2\lambda+1}} v_0^{\frac{2(\lambda-1)}{2\lambda+1}}, \tag{3.64}$$

where:

$$\Pi_5(\lambda) = \Pi_3(\lambda)\Pi_4(\lambda)^{\frac{\lambda-1}{2\lambda+1}}. \tag{3.65}$$

Rearranging (3.64) one obtains an expression for v_0:

$$v_0 = \left(\frac{\sigma_{max}}{\Pi_5(\lambda)(1-2\nu)}\right)^{\frac{2\lambda+1}{2(\lambda-1)}} \left[\frac{1-\nu^2}{E}\right]^{\frac{\lambda+2}{2(\lambda-1)}} \rho_0^{-\frac{1}{2}}. \tag{3.66}$$

Now, combining (3.16), (3.19), (3.20), (3.21), (3.52) and (3.62), we can show that:

$$t_0 = \Pi_6(\lambda)\left[\frac{1-\nu^2}{E}\right]^{\frac{\lambda}{2\lambda+1}} B\rho_0^{\frac{\lambda}{2\lambda+1}} v_0^{-\frac{1}{2\lambda+1}}, \tag{3.67}$$

where:

$$\Pi_6(\lambda) = I_\beta \Pi_2(\lambda)\Pi_4(\lambda)^{\frac{\lambda}{2\lambda+1}}. \tag{3.68}$$

After substituting (3.66) into (3.67) and some simple transformations, constant B takes the value:

$$B = \frac{t_0}{\Pi_6(\lambda)}\left[\frac{\sigma_{max}}{\Pi_5(\lambda)\,(1-2\nu)}\right]^{\frac{1}{2(\lambda-1)}} \left[\frac{E}{1-\nu^2}\right]^{\frac{\lambda-2}{2(\lambda-1)}} \rho_0^{-\frac{1}{2}}. \tag{3.69}$$

Finally, by utilizing (3.62), (3.66), (3.69) and using the definition of kinetic energy we obtain the initial energy required for fracture ϵ_0:

$$\epsilon_0 = \alpha_\lambda \sigma_{max}^{\frac{4\lambda+5}{2(\lambda-1)}} t_0^3, \tag{3.70}$$

$$\alpha_\lambda = \frac{\Pi_4(\lambda)}{2\Pi_6(\lambda)^3}\left[\frac{1}{\Pi_5(\lambda)(1-2\nu)}\right]^{\frac{4\lambda+5}{2(\lambda-1)}} \left[\frac{E}{1-\nu^2}\right]^{\frac{\lambda-10}{2(\lambda-1)}} \rho_0^{-\frac{3}{2}}. \tag{3.71}$$

Note that the form of ϵ_0 is the same as the one calculated along the contact region in [10]. By expanding the term for σ_{max} from (3.61) in (3.70) the critical shape parameter value $\lambda^* = 5.5$ is easily identified:

$$\epsilon_0 \propto t_0^{\frac{\lambda-5.5}{\lambda-1}} \Upsilon(\beta, t_0)^{-\frac{(4\lambda+5)}{2(\lambda-1)}}. \tag{3.72}$$

A comparison of this prediction of the threshold fracture energy and that derived in [10] is provided in Fig. 3.16. It is clear that in all cases the newly derived bound is higher for all λ, and that there is a far less sharp change in behaviour at the point $t_0 = \tau/2$

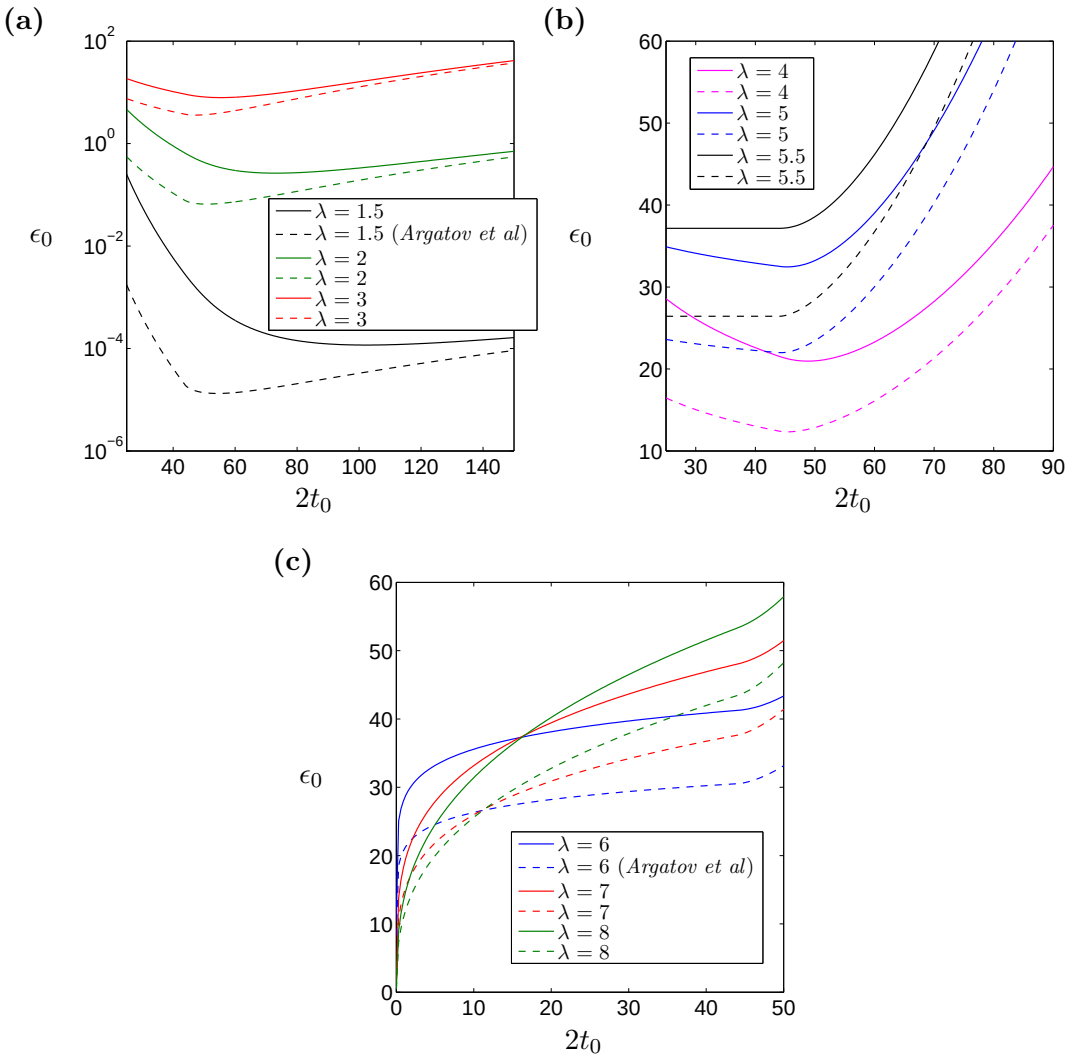

FIGURE 3.16: Comparison of the newly derived bound (3.70) on the initial energy required for fracture initiation (Solid lines on the graph) with the previously derived equivalent [10] (dashed lines) for various fixed values of λ, as a function of the impulse length $2t_0$ (μs). The apparent intersection in (c) is explored further in Fig. 3.17.

$(2t_0 = 44\mu s)$.

3.2.8 Summary

It has been shown in Sect. 3.2.4.1 that we can now predict the time to fracture, with associated radial position, for a wide range of particle shapes, sizes and initial conditions, which gives a deeper understanding of the important parameters in erosion fractures. The relation between particle shape and time to fracture is shown to be strongly dependent on the particle volume. However in general having a blunter indenter results in the initial fracture located further away from the impact center. It was shown that

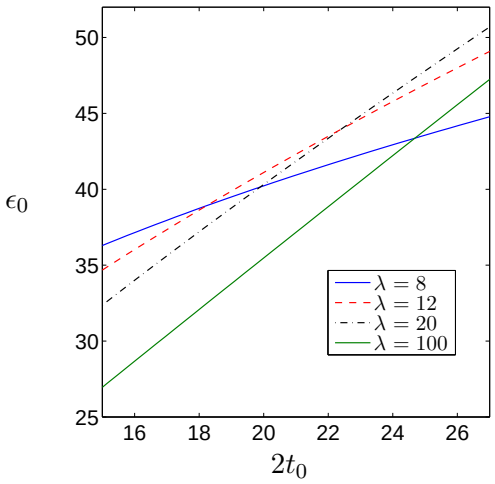

FIGURE 3.17: Evaluation of the threshold fracture energy ϵ_0 (3.72) for large fixed values of the shape function λ. It is clearly seen that the apparent intersection in Fig. 3.16c is not representative of a greater trend or phenomena.

increasing the initial velocity of the particle reduces the time to fracture initiation, with the initial fracture occurring closer to the impact center.

Additionally the threshold particle energy estimation corresponding to the initiation of surface fracture in the elastic half-space shows considerable improvement on the previous effort of *Argatov, Mishuris & Petrov* [10]; both in terms of being a tighter quantitative bound, and in having better qualitative behaviour during the change between cases at the point $t_0 = \tau/2$ as a result of more physically realistic assumptions (see comparison in Fig. 3.16). It confirms that the value of the fracture energy does significantly depend on the load duration and has a marked global minimum in the so-called subcritical case when $\lambda < \lambda^*$. It is also shown that for $\lambda > \lambda^*$ the fracture energy achieves its zero global minimum with decreasing impact duration. The existence of energetically optimal modes of dynamic impact has been demonstrated. In particular, it has been shown that the energy input for fracture can be optimized to minimize the energy cost of the process. It is important that the effect itself turns out to be dependent on the bluntness of the particle's contacting surface.

Unfortunately however, in this section we set out to explain the value of the critical shape parameter λ^*; to either demonstrate that it's appearance was the result of a lack of accuracy in the previous approach, or to find some physical explanation of the phenomena. Ultimately, while an explicit relation for the threshold energy required for surface fracture has been obtained, this hasn't yielded any new information concerning this unexplained parameter.

This 'non-result' is telling, as it makes it clear that the critical shape parameter is intrinsic to the model itself. As a result, if no physical explanation can be found for it

within the model, then this paradox indicates that important characteristics of erosion impact over small timescales are being neglected by the current approach.

3.3 An updated model for solid particle erosion

3.3.1 Introduction

From the results of the preceding investigation, it is clear that the value of the critical shape parameter is in some way embedded into the original model of *Argatov, Mishuris & Petrov* [10]. As such, in order to determine whether this is due to a yet unknown physical effect, or a failure of the previous model to produce accurate predictions, we will have to modify the model.

Noting that the original approach was designed to examine high velocity impacts, and that the effect is related to the indenter shape, there is only one assumption which is likely to significantly effect the final result, namely the failure to incorporate inertial terms (i.e. energy dissipation through wave effects in the elastic medium). However, this assumption was made in order to simplify the underlying mathematics, and incorporating this effect throughout the duration of the model is beyond the ability of current analytical approaches. Given this, an intelligently chosen compromise will have to be made.

This can be achieved by noting that, in general, the effect of energy dissipation is particularly important during the initial, supersonic, stage of the impact. Therefore, as the aim of this investigation is to determine the meaning of the critical shape parameter, and not to develop a predictive model, it will be sufficient to only include inertial terms during the early moments of the indentation.

There are however complications which arise from using such an approach. Most importantly, the different assumptions used when determining the elastic deformation of the impacted material (see Sect. 2.2.4), result in differing formulations for the contact pressure and radius between the two stages. As no model for axisymmetric indentation exists which precisely describes the transition between these two cases, this will instead have to be approximated. This can be achieved by 'gluing' the solutions together, using an appropriately chosen smooth 'sewing' function, but comes at a cost. While real-life transitions between supersonic and subsonic stages are accompanied by a shock wave, which dissipates energy through the medium, the glued solution will not exhibit such behaviour. Because of this, the total energy in the system might not be conserved during

the transition. In principle, this could be overcome using a specifically calibrated sewing function, but that will not be investigated here.

To state this explicitly, the system derived and obtained here will provide the basic qualitative behaviour necessary to determine the effect of the supersonic stage on the critical shape parameter λ^*, but will not have any quantitative predictive capabilities in its presented form.

Another factor worthy of note is that here we attempt to update the model of *Argatov, Mishuris & Petrov* [10], and not the approach displayed in Sect. 3.2. This means that the threshold fracture energy will be evaluated along the contact radius, rather than for a fixed spacial point. This will successfully provide a lower bound on the initial energy required for fracture initiation, however is less accurate and physically realistic than that shown previously. The reason for this approach is two fold: i.) evaluating along the contact radius greatly simplifies the mathematics of the model, which is a advantageous for this preliminary investigation, ii.) it was demonstrated previously that this assumption will not effect the final qualitative behaviour of the system, and as this model is not designed to provide quantitative predictions, modeling each fixed spacial point only adds unnecessary complications.

The remainder of this chapter is constructed as follows. Sect. 3.3.2 sees the construction of an updated model for single erosion impact during the various regimes. In Sect. 3.3.2.1 *Borodich's* solution for the supersonic stage is stated, and the resulting set of equations determining the initial moments of the impact are formulated. Following this in Sect. 3.3.2.2 the relevant equations from the previous model by *Argatov, Mishuris & Petrov* are given, with some being rederived to account for the new initial conditions when entering the subsonic stage. Finally in Sect. 3.3.2.3 any discontinuities between the two approaches are eliminated. The numerical results are detailed in Sect. 3.3.3. We briefly reintroduce the incubation time based fracture criterion in Sect. 3.3.3.1, before formulating the initial algorithm in Sect. 3.3.3.2, and calculating the threshold fracture energy for various λ in Sect. 3.3.3.3, with some details being relegated to Appendix. B. This is followed by an examination and discussion of the critical shape parameter in Sect. 3.3.4. Finally the important results are collated and discussed in Sect. 3.3.5.

3.3.2 Constructing a new model of erosion impact

3.3.2.1 The supersonic stage

The general solution of the contact problem during the supersonic stage was presented by *Borodich* [27], and allows one to obtain the temporal dependencies of both the contact

force and the penetration depth. The general formulation for an arbitrary convex shaped indenter was presented, with specific shapes in the form of a cone, elliptic paraboloid and a pyramid being evaluated. Here, the results from [27] are used to describe the indentation process during the supersonic stage, for an axisymmetric blunt indenter, again defined by the shape function (3.14). As a result, the contact area, $S(w)$, is related to the penetration depth w as:

$$S(w) = \pi B^{2-\frac{2}{\lambda}} w^{\frac{2}{\lambda}}. \tag{3.73}$$

In an accordance with *Borodich's* solution, the time dependence of the penetration depth w can be implicitly calculated as follows:

$$\begin{aligned} t(W) &= \int_0^W \frac{dw}{v_0 - \frac{\rho_m c \pi}{m\mu} B^{3-\mu} w^{\mu}}, \\ \mu &= \frac{\lambda + 2}{\lambda}, \quad 1 < \mu < 3, \end{aligned} \tag{3.74}$$

where v_0 and m are the initial velocity and mass of the projectile respectively, ρ_m is elastic media density and c is the velocity of the longitudinal waves. Some simple algebraic transformations of (3.74) yield:

$$\begin{aligned} t(W) &= \frac{w_s}{v_0} \int_0^{\frac{W}{w_s}} \frac{d\xi}{1 - \xi^{\mu}}, \\ w_s &= B \left(\frac{\mu m v_0}{\pi \rho_m c} B^{-3} \right)^{\frac{1}{\mu}}. \end{aligned} \tag{3.75}$$

Thus we know the function $F(y, \mu)$, which implicitly describes the relationship between the penetration depth w and the time t

$$F(y, \mu) = \int_0^y \frac{d\xi}{1 - \xi^{\mu}}, \quad 0 < y < 1. \tag{3.76}$$

It should be noted that $F(y, \mu)$ is a monotonic increasing function over $0 < y < 1$ for every $1 < \mu < 3$, and its value increases from zero to infinity. It is however possible to determine the inverse function, F^{-1}, which allows us to obtain the particular solution for a considered projectile shape.

As a result, the supersonic indentation of a blunt indenter into the elastic half-plane is defined by the following relationship (3.76):

$$w_d(t) = w_s F^{-1} \left(\frac{v_0}{w_s} t \right), \tag{3.77}$$

while the other problem parameters: the indenter velocity, $v_d(t)$, and total force, $P_d(t)$, are given by the following relations:

$$\begin{aligned} v_d(t) &= \dot{w}_d(t), \\ P_d(t) &= \pi \rho_m c v_d(t) B^2 \left(\frac{w_d(t)}{B} \right)^{\mu-1}. \end{aligned} \tag{3.78}$$

The end of the supersonic stage, denoted t_*, is that moment in time when the outward velocity of the contact area becomes equal to velocity of the longitudinal waves c. The value of t_* can be calculated as the solution to the equation

$$\dot{a}(t_*) = c, \tag{3.79}$$

where the longitudinal wave speed is that of a one-dimensional solid, namely:

$$c = \sqrt{\frac{E}{\rho_m}}, \tag{3.80}$$

equation (3.79) can be written in the form:

$$\dot{a}(t_*) = \frac{1}{\lambda} \left(w_d(t_*) \right)^{\frac{1}{\lambda}-1} B^{\frac{\lambda-1}{\lambda}} v_0 \left(1 - \left(\frac{w_d(t_*)}{w_s} \right)^{\mu} \right). \tag{3.81}$$

Thus, one can now evaluate the time t_* and calculate boundary values of the penetration depth $w_* = w_d(t_*)$, contact radius, $a_* = a_d(t_*)$, and the projectile velocity $v_* = v_d(t_*)$.

Moreover, one can observe that $t_* \to 0$ as $\rho_m \to 0$.

Unfortunately there are no exact solutions for the stress distribution during the supersonic stage, only the normal stresses for the central point $r = 0$ of projectile.

3.3.2.2 The subsonic stage

During the subsonic stage ($t > t_*$) we utilize the Shtaerman-Kilchevsky theory, which has previously been applied to the case of quasi-static blunt impact by *Argatov, Mishuris & Petrov* [10], and outlined in Sect. 3.2.2. In this case we will add the subscript qs to variables to denote the subsonic stage (quasi-static approach).

The primary initial equations remain the same as those given in (3.14)-(3.19), however they now utilize the following initial conditions from the supersonic stage [10]:

$$w_{qs}(t_*) = w_*, \quad \frac{dw_{qs}}{dt}|_{t=t_*} = v_*. \tag{3.82}$$

Multiplying both sides of equation (3.17) by $\frac{dw}{dt}$ before integrating, we obtain:

$$\frac{m}{2}(v_{qs}^2 - {v_*}^2) = -\frac{k_1}{\beta+1}(w_{qs}^{\beta+1} - {w_*}^{\beta+1}). \tag{3.83}$$

The maximum penetration depth w_0 can be calculated by substituting $v_{qs} = 0$ into equation (3.83)

$$w_0 = \left(\frac{(\beta+1)m{v_*}^2}{2k_1} + {w_*}^{\beta+1}\right)^{\frac{1}{\beta+1}}. \tag{3.84}$$

A second integration of (3.83) gives us the the temporal dependence of the penetration depth $w_{qs}(t)$ during the subsonic stage

$$\int_{t_*}^{t} dt = t - t_* = \Delta t = w_0\sqrt{\frac{m(\beta+1)}{2k_1{w_0}^{\beta+1}}}\; U\left(\frac{w_{qs}}{w_0}, \beta\right), \tag{3.85}$$

where:

$$U\left(\frac{w_{qs}}{w_0}, \beta\right) = \int_{\frac{w_*}{w_0}}^{\frac{w_{qs}}{w_0}} \frac{dh}{\sqrt{1-h^{\beta+1}}}. \tag{3.86}$$

Thus, the estimated time, t_{qs}, when the penetration reaches its maximum value w_0 is as follows

$$\int_{t_*}^{t_0} dt = t_0 - t_* = t_{qs} = w_0\left(\frac{m(\beta+1)}{2k_1{w_0}^{\beta+1}}\right)^{\frac{1}{2}} U(1,\beta), \tag{3.87}$$

where t_0 is time duration of the load stage. Using (3.84) this can transformed into:

$$t_0 = t_* + \frac{w_0}{v_*}\sqrt{1 - \frac{2k_1 w_*^{\beta+1}}{(\beta+1)\,mv_*^2 + 2k_1 w_*^{\beta+1}}}\; U\left(1,\beta\right). \tag{3.88}$$

Since damping occurs, due to the quasi static nature of the formulation, the duration of the unload stage $t_{**} - t_0$ exaggerates the value t_0. For this reason we have to solve the equation (3.17) one more time with the new initial conditions:

$$w_{qs}(t_0) = w_0, \quad \frac{dw_{qs}}{dt}\Big|_{t=t_0} = 0. \tag{3.89}$$

The first integration give us the projectile velocity in the reverse direction:

$$\frac{dw_{qs}}{dt} = -\sqrt{\frac{2k_1{w_0}^{\beta+1}}{(\beta+1)m}} \cdot \sqrt{1 - \left(\frac{w_{qs}}{w_0}\right)^{\beta+1}}. \tag{3.90}$$

Thus, the value of t_{**} can be determined from the following expression:

$$t_{**} - t_0 = w_0\sqrt{\frac{(\beta+1)m}{2k_1{w_0}^{\beta+1}}}\int_0^1 \frac{dh}{\sqrt{1-h^{\beta+1}}}. \tag{3.91}$$

Note that $t_{**} - t_0 > t_0$. Indeed, the latter is equivalent to

$$w_0\sqrt{\frac{(\beta+1)m}{2k_1 {w_0}^{\beta+1}}}\int_0^{\frac{w_*}{w_0}}\frac{dh}{\sqrt{1-h^{\beta+1}}} > t_*.$$

3.3.2.3 Coupling of the solutions for supersonic and subsonic stages

Because of the peculiarities of the dynamic solution by Borodrich and quasi-static solution by Shtaerman, the function which describes the temporal dependence of the contact area radius will be discontinuous at the time t_*. This is due to the fact that the supersonic and subsonic stages have different physical principles determining the relationship between penetration depth and contact area, and the penetration depth $w(t)$ is continuous in this model (by design). In order to avoid this irregularity, let us introduce the smooth function $\chi(x)$, which continuously matches the two solutions within the interval $[0.95t_*, 1.05t_*]$

$$\chi(t) \quad = \quad \begin{cases} 1, & 0 < t < 0.95t_*, \\ 0, & 1.05t_* < t. \end{cases} \tag{3.92}$$

Also, we employ this function $\chi(x)$ to sew the contact force $P(t)$, the equation of which also has a discontinuity at the point t_*.

$$\begin{aligned} a(t) &= a_d(t)\chi(t) + a_{qs}(t)\big(\chi(t)-1\big), \quad 0 < t < t_{**}, \\ P(t) &= P_d(t)\chi(t) + P_{qs}(t)\big(\chi(t)-1\big), \quad 0 < t < t_{**}. \end{aligned} \tag{3.93}$$

Additionally the mean contact area, which allows us to calculate the stress field under the projectile, is defined as $p_0 = P/(\pi a^2)$ and can be approximated in a similar way:

$$p_0(t) = \frac{P_d(t)}{\pi a_d^2(t)}\chi(t) + \frac{P_{qs}(t)}{\pi a_{qs}^2(t)}\big(\chi(t)-1\big), \quad 0 < t < t_{**}. \tag{3.94}$$

Since Borodich's solution does not contain any information about the surface stresses, we enrich the quasi-static solution by extrapolating the corresponding results into the supersonic stage. As such we assume the contact pressure beneath the indenter takes the form (3.24), while the surface stresses are calculated according to (3.29). This approximation will be sufficient as we are only attempting to examine the behaviour along the edge of the contact area ($\rho = r/a(t) = 1$), and are only seeking a qualitatively accurate result. We have, from (3.29) and (3.31), that the maximum radial stresses along the contact radius are given by:

$$\sigma_r(1,t) = (1-2\nu)\int_0^1 \eta p(\eta)d\eta = \frac{(1-2\nu)\,P}{2\pi a^2} = \frac{(1-2\nu)}{2}p_0(t). \tag{3.95}$$

As a result, at any time during the penetration process, the approximated solution to the problem will be given by the formulas (3.24), (3.94), (3.95). Note that all of these representations are exact near the ends of the time interval. Indeed, for very small times, Borodich's formulas give the exact solution for the supersonic regime, while the Shtaerman solution precisely describes the projectile behavior during the quasi-static stage.

3.3.3 Estimation of the energy costs for the fracture initiation

3.3.3.1 Incubation time fracture criterion

The previous analysis [10] allows us to produce a lower bound on the fracture pulse of the tensile stresses. Additionally, in Sect. 3.2, it was shown that instead considering the stress pulses for fixed points on the material surface doesn't qualitatively alter the final behavior of the threshold energy in relation to the impact duration. Hence, here, we employ the lower estimate of the fracture pulses with a view to avoiding additional computational difficulties.

The threshold amplitudes of pulses caused by particle impacts are again evaluated using an incubation time approach, which can be effectively applied to explain a number of general dynamic fracture effects caused both by high strain rate and short pulse loading [20, 169, 174]. Further details of the corresponding fracture criterion, referred to as the incubation time based fracture criterion, are provided in Sect. 2.3.2. Here, we take it in its simplest form, for a brittle fracture, which can be written as follows:

$$\frac{1}{\tau}\int_{t-\tau}^{t}\sigma(s)\,ds \le \sigma_c, \tag{3.96}$$

where σ_c is the static strength of the material and τ is the incubation time of the fracture. This criterion has been successfully used to model a multitude of fracture problems, and has proved itself to be a quite simple and effective method of fracture prediction. It permits us to determine the necessary conditions required for fracture over a wide range of impacts.

3.3.3.2 Description of the algorithm

The algorithm used to calculate the threshold fracture energy for a fixed value of λ utilizes the fact that the stress function at the fracture front is a positively valued function, which monotonically increases with increasing v_0. As such we define the following

function:

$$\Upsilon\left(v_0\right) = \frac{1}{\tau\sigma_c} \max_{t\in[0,t_{**}]} \left(\int_{t-\tau}^{t} \sigma(\acute{t}) d\acute{t} \right) - 1, \tag{3.97}$$

which has the property that:

$$\Upsilon(v_0) \begin{cases} > 0, & v_0 = v_0^* + \delta, \\ \equiv 0, & v_0 = v_0^*, \\ < 0, & v_0 = v_0^* - \delta, \end{cases} \tag{3.98}$$

for any arbitrary $\delta > 0$. As such a simple iterative procedure can be utilized in order to obtain v_0^* to a desired level of accuracy.

A second concern is to ensue consistency of results between this paper and the previous investigations in [10] and Sect. 3.2. In order to achieve this the constants B and m will have to be chosen in such a way as to coincide as $\rho_m \to 0$. This is completed in the first step of the algorithm, and as such the first step could be discarded when carrying out a more general investigation.

With this in place, the algorithm is defined as follows:

1. Choose an arbitrary t_p, which will approximate t_0. From this calculate the constants B and m using equations (50) and (57) in [10]. Additionally compute an initial expected value of the initial velocity required for fracture initiation, v_p, using equation (56) in the aforementioned paper.

   Note: While the value $t_p \to t_0$ as $\rho_m \to 0$, the two will not be related in this formulation. It is simply an arbitrary starting point chosen to ensure the results are consistent with previous investigations, and is discarded after this step.

2. Using the value v_p create an initial interval in which v_0^*, the initial velocity required for fracture initiation, is expected to occur (e.g. $v_\delta = [v_p - \delta, v_p, v_p + \delta]$).

3. Compute the system of equations given in Sect. 3.3.2 for each value of v_δ, and obtain the time dependent stress function.

4. Compute the function $\Upsilon\left(v_0\right)$ from (3.97) for each value of v_δ. Use its properties (3.98) to obtain a refined interval v_δ containing v_0^*.

5. Iterate steps 2-4 until a desired level of accuracy is reached. The threshold fracture energy ϵ_0 is then calculated from the obtained v_0^*.

3.3.3.3 Results for fixed λ

The material constants used in calculations are those for gabbro-diabase [168], which is the same as used previously in [10] and Sect. 3.2. The values are as follows: $E = 6.2\times10^9$ N/m^2, $\nu = 0.26$, $\sigma_c = 44.04 \times 10^6$ N/m^2, $\tau = 44$ μs, while the density of the indenter is given by: $\rho_0 = 2400$ kg/m^3. Results are displayed in Fig. 3.18, for $\lambda = \{2, 3, 4, 5\}$.

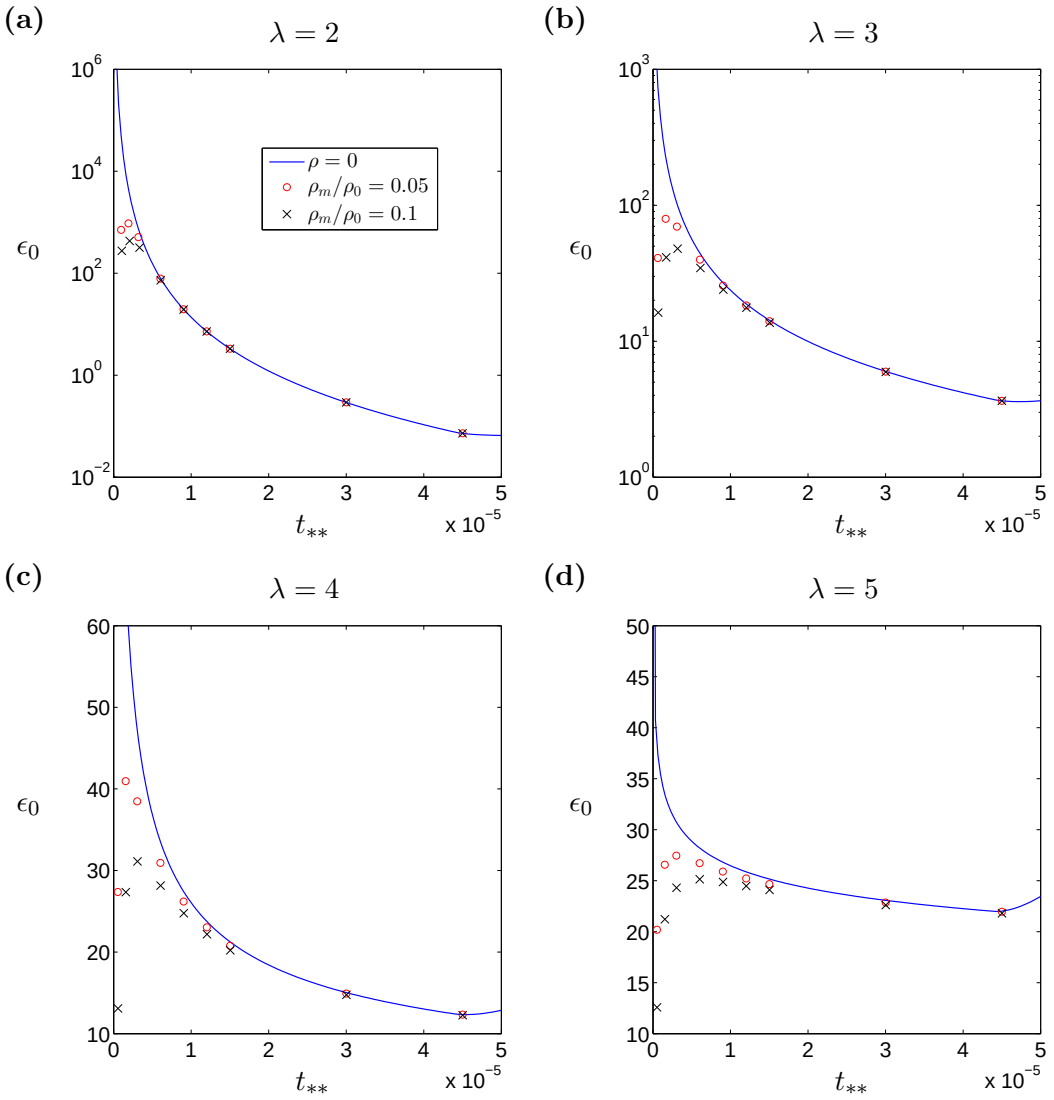

FIGURE 3.18: Values of the threshold fracture energy ϵ_0, for various fixed impacted material densities ρ_m, when (a) $\lambda = 2$ (b) $\lambda = 3$ (c) $\lambda = 4$ (d) $\lambda = 5$. Here $\rho_0 = 2400$ kg/m^3 is the density of the indenter.

It is clear from these results that the threshold fracture energy decreases as the material density ρ_m increases, however the effect is only apparent for impacts with short durations. This makes intuitive sense, given that v_0 decreases monotonically as the impact duration is increased, and as such the supersonic stage will play a far greater role in rapid impacts.

Additionally, it is immediately apparent from the results in Fig. 3.18 that the critical shape parameter λ^* will decrease when eroding a more dense material, as no unique minimum exists for ϵ_0 when taking $\lambda \geq 2$ when $\rho_m \geq 0.05\rho_0$ but does for $\rho_m = 0$ (this is explained in more detail below e.g. Fig. 3.19). Furthermore, given that the threshold fracture energy seems to tend to zero for all λ in these graphs, it is safe to assume that the critical shape parameter will have $\lambda^* \to 1$ rapidly as the material density is increased.

3.3.4 Critical shape parameter λ^* for various material densities

3.3.4.1 Obtaining the critical shape parameter

With the basis of the model now developed, it is possible to begin an investigation into the nature of the critical shape parameter, λ^*, when a non-zero density of the impacted medium is assumed. In this way, we will be able to show whether a physical explanation can be given for the previously obtained paradoxical value of $\lambda^* = 5.5$.

The method of obtaining the critical shape parameter λ^* relies on noting the behaviour of the threshold fracture energy for very small impact durations t_{**}. As demonstrated in Fig. 3.19, when $\lambda < \lambda^*$, the derivative of the threshold fracture energy ϵ_0 will be negative, while this derivative will be positive for $\lambda > \lambda^*$ and zero for the critical shape parameter. As such the algorithm is designed to obtain the sign of this derivative near the origin for a range of λ, before using the results to iteratively work towards the desired critical shape parameter. A full explanation of the algorithm is given below.

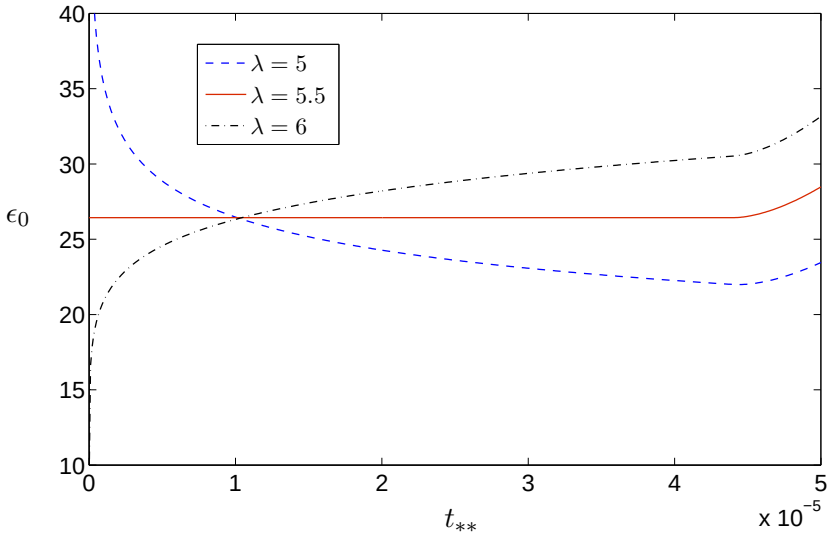

FIGURE 3.19: Behaviour of the threshold fracture energy ϵ_0 for small t_{**}, shown here for $\rho_m = 0$.

1. Choose a value of the impacted material density ρ_m. Alongside this an initial overestimate $\lambda_p = [\lambda_1, \ldots, \lambda_n]$ for the potential range of λ^* is taken.
2. Then, for each $\lambda \in \lambda_p$:
   - Arbitrary initial points $0 < t_p^1 < t_p^2$ are taken[3]. These approximate t_0 as in the previous algorithm, and must be sufficiently small to predict the behaviour of the derivative of ϵ_0 as $t_{**} \to 0$.
   - The threshold fracture energy, ϵ_0, is obtained, for each value of $t_p = \{t_p^1, t_p^2\}$, using the algorithm outlined in Sect. 3.3.3.2, to a required level of accuracy.
   - The derivative of ϵ_0, with respect to t_{**}, is approximated between t_p^1 and t_p^2.
3. With the value of the derivative obtained for each $\lambda \in \lambda_p$, a new interval in which λ^* exists for the given ρ_m is obtained.
4. A new λ_p is defined using the obtained interval for λ_*, and steps 2-3 are repeated until a desired level of accuracy is reached.

This algorithm allows one to obtain the value of λ^* for a given material density ρ_m, and as such by repeating the we can begin to study the relationship between the impacted material density and the threshold fracture energy. In practice we have found that it is often simpler to instead begin with a value λ, and then iterate to discover the density ρ_m^* for which it is the critical shape parameter.

3.3.4.2 Results for various impacted material densities

Numerical simulations were conducted using the same values for the impact parameters as in Sect. 3.3.3.3, with the addition of taking $t_p = \{2, 2.5\} \times 10^{-6}$ seconds. The results obtained are shown in Fig. 3.20.

It is clear from this that the critical shape parameter λ^* decreases when impacting materials with higher densities. There is however a clear divergence from previous results which must be expanded upon, which isn't made obvious in the above figure.

In previous investigations, it has been the case that taking $\lambda = \lambda^*$ will yield a non-unique minimum energy required for fracture. However this will not always be the case under the revised scheme. In order to explain this further, we define the following:

$$\rho_m^*(\lambda) = \{\rho_m : \lambda^*(\rho_m) = \lambda\}$$

[3]Here the values t_p^1, t_p^2 must be small enough to accurately model the asymptotic behaviour, but also not so small as to require infeasible velocities. See Appendix B for a more thorough examination of this choice.

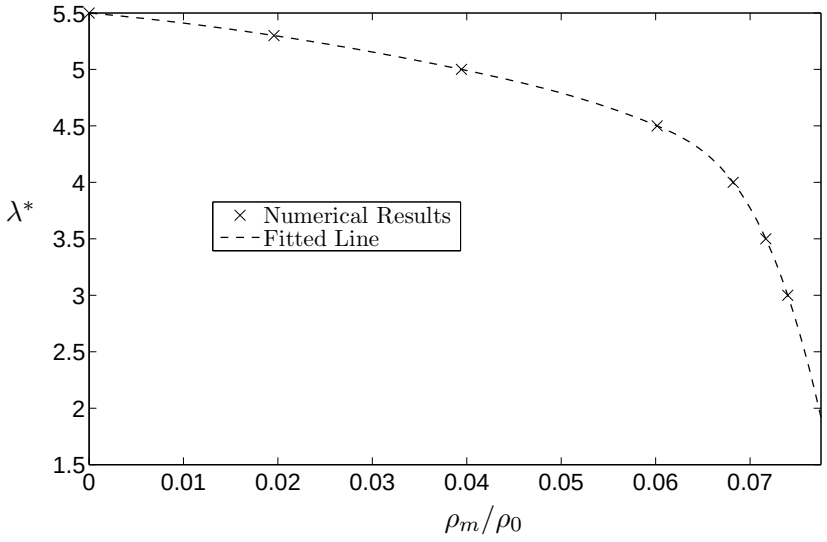

FIGURE 3.20: Numerically obtained lower bound of the critical shape parameter λ^* for various impacted material densities ρ_m. Here $\rho_0 = 2400$ kg/m^3 is the density of the indenter material.

An example of the threshold fracture energy, evaluated taking $\rho_m = \rho_m^*$ when $\lambda = 3$ is given in Fig. 3.21.

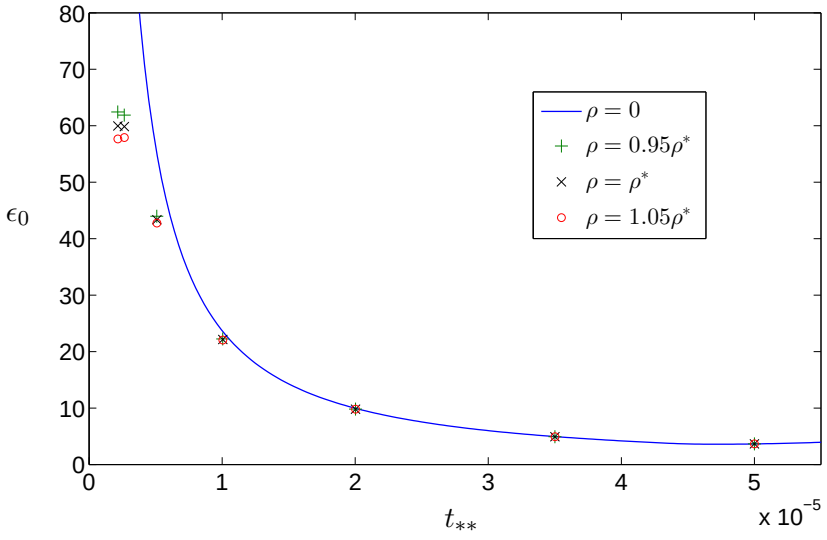

FIGURE 3.21: Value of the threshold fracture energy ϵ_0, evaluated when $\lambda = 3$ for $\rho_m = 0$ (blue line), $\rho_m = \rho_m^*$ (black crosses) and $\rho_m = \rho_m^* \times 1 \pm 0.05$ (green crosses, red circles). It is clear that a unique minimum occurs for both $\rho_m \leq \rho_m^*$, however we will have $\epsilon_0 \to 0$ for $\rho_m > \rho_m^*$.

It is clear from this that the minimum energy required for fracture is not unique, however as any increase in the impacted material density results in having $\epsilon_0 \to 0$ as $t_{**} \to 0$ it is the highest value of λ for which a minimum threshold fracture energy exists. As a result, while this value of λ^* still maintains its most important quality, that of defining

the point when a change in case between having a unique threshold fracture energy and none existing occurs, it is of a weaker form than described in previous papers.

3.3.5 Summary of results for the updated model

In this section, an updated approach to erosion impact was created, which incorporated both the supersonic stage from *Borodich* [27] and the subsonic regime from *Argatov, Mishuris & Petrov* [10]. The final model provides a qualitative description of the event, in a dynamic setting, with the surface fractures which occur being predicted using an incubation time based fracture criterion, which accounts for the temporal-structural characteristics of the impact.

Through an examination of the updated model, it was demonstrated that the critical shape parameter λ^* is dependent on the speed of waves propagating in the impacted medium. This confirms the previous stated hypothesis, that the value $\lambda^* = 5.5$ which was obtained by *Argatov, Mishuris & Petrov* [10], and evaluated using a higher accuracy approach in Sect. 3.2, was due to a failure of the model to incorporate the effect of inertial terms in the elastic half-plane. With this result, the threshold fracture paradox has been resolved.

It should be noted again that the results provided by the final model only demonstrate the qualitative behaviour of the solution. The current formulation utilizes a non-unique gluing function, and as such can not make quantitatively accurate predictions. However, should an accurate scheme for modeling the transonic regime be developed, to link the dynamic supersonic stage with the quasi-static subsonic stage, then this approach could potentially be used to form the basis for such a predictive model. This wasn't attempted here as it was not required to resolve the threshold fracture paradox, and as such would only have introduced numerous unnecessary complications (outlined in Sect. 3.1).

3.4 Concluding remarks about threshold fracture energy in solid particle erosion

In this chapter, an examination of axisymmetric erosion, through a dynamic formulation which accounted for the moving contact boundary, was conducted. The primary motivational effort was to determine the meaning of the critical shape parameter $\lambda^* = 5.5$, which was obtained in the investigation by *Argatov, Mishuris & Petrov* [10]. This has clearly been achieved, with it being successfully demonstrated that this occurred due to a failure of the original model to incorporate the effect of inertial terms during the initial,

supersonic, stage of the impact. It is noteworthy that incorporating the proper Stefan-type condition during the early stages of the impact played a crucial role in determining the true physical characteristics of the erosion process.

This result runs counter to the traditional wisdom that, for short-time impacts into an elastic half-plane, the effects of waves in the medium will be negligible and can be safely ignored. While this may be the case for indenters with a low (subsonic) initial velocity, there will be important qualitative differences in behaviour of the impact when the initial impact velocity is faster than the waves in the medium.

This result may not be entirely unique or surprising, the fact that systems display differing behaviour when supersonic speeds are involved is not new, but it does have some troubling implications.

The most obvious of these is the fact that no analytical model exists which allows for a range of particle geometries, whilst also incorporating both the supersonic and subsonic stages, and the transition between them, in a way which allows for quantitative predictions. While the model outlined in Sect. 3.3 presents a useful starting point in this endeavour, the lack of a uniquely defined transition between the two regimes severely limits its applicability. Devising such a linkage may be possible through an examination of the energy within the system, but is clearly well beyond the limit of this investigation.

Chapter 4

Particle velocity based hydrofracturing algorithm for a penny-shaped crack

This work will form the basis for three papers, which are currently in preparation.

In this chapter, all variables with a "$\sim$" symbol are normalized, while the self-similar formulation is denoted with "$\wedge$".

4.1 Theoretical background and literature review

4.1.1 Motivations and difficulties

Hydraulic fracturing (HF) is the term used to describe a fluid driven crack, a phenomena which occurs in nature (e.g. sub-glacial drainage), but has come to the forefront due to its use in industry, in such technologies as: shell-gas retrieval [43], the extraction of geothermal energy [153] or as a byproduct of underground waste storage [4]. The large variety of applications necessitates a greater understanding of the process, however attempting to model HF is both mathematically and numerically challenging. Some of the notable physical, mathematical and computational difficulties are:

- A need to take account of the moving fracture front, which is complicated by the fact that the fracture front boundary conditions are ill-posed [127].
- The need to incorporate interactions between the solid and fluid phases, which leads to both non-linearity of the governing equations (which may also degenerate

at singular points in the domain), as well as a typically non-local relationship between the fracture aperture and fluid pressure.

- Hydraulic fracturing occurs over a wide variety of length and time scales, with consequences for certain processes that define fracture growth.
- The fluids used in hydraulic fracturing, referred to as the treatment, often exhibit non-Newtonian behaviour [36]. Additionally, particles (proppant) are regularly added during later stages in the HF process, which must also be accounted for.
- Fluid leak-off into the surrounding rock formation. This can have a dramatic impact on the behaviour of a fracture, however due to the pressures, length scales and other factors attempts to reproduce and model it in a laboratory are often unreliable [162]. Additionally, this is typically approximated using *Carter's law* [39], however this formulation has little experimental verification, and relies on theoretical assumptions which can not be used in real-time operations [23].
- The fracture front will typically travel faster than the fluid, creating a region with essentially zero pressure between them [67].

As a result of these difficulties, among others, simplified models are often used when studying hydraulic fracture. Such models both allow for important interrelationships between the various mechanisms and parameter of the problem to be obtained/approximated, as well as providing useful points of comparison for sophisticated computational models.

4.1.2 1D models of hydraulic fracturing

The first simplified theoretical models of hydraulic fractures were created in the 1950s (see for example [90] and [103]). Over time however, subsequent research led to the formulation of the three so-called classic 1D models. All of the models are capable of incorporating fluid leak-off, non-Newtonian fluid rheology and allow the fracture to develop over time. In some cases fluid lag can be incorporated into the models, however this is not typically assumed.

The basic founding principles, as well as the subsequent differences between these models, are outlined below.

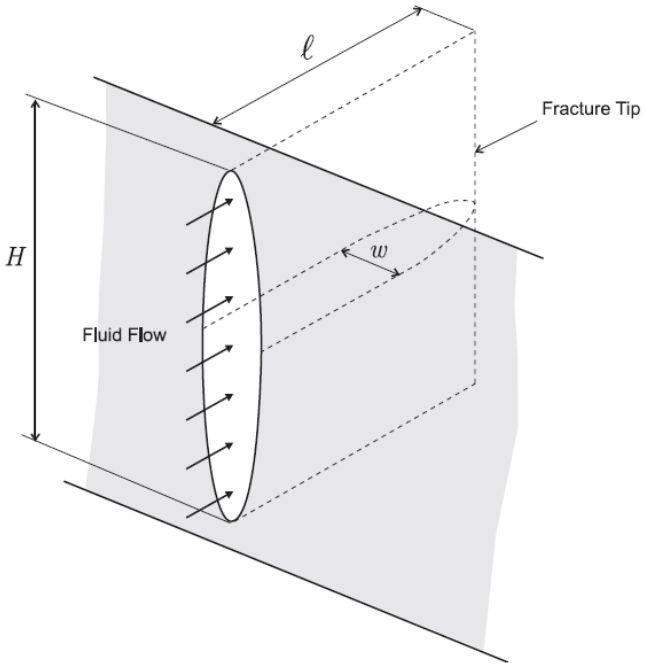

FIGURE 4.1: Schematic illustrating the PKN model [6].

4.1.2.1 The PKN model

The simplest of the three, the PKN model was first proposed by *Perkins & Kern* [163], with later additions by *Nordgren* [156] delivering the form which is recognized today. The fracture geometry is shown in Fig. 4.1, with the crack assumed to be of fixed height. This assumption results in the elasticity equation taking the form of a linear, local relationship between the aperture and pressure, as opposed to the inherently non-linear, non-local elasticity usually encountered when attempting to model HF.

It is worth stating that this simplification does not inhibit the usefulness of the model. The PKN formulation provides a reliable approximation of long fractures whose height is limited, while having cross sections which are elliptical in nature [219]. As a result this approach, alongside the KGD model, continued to be used when designing fracture treatments into the 1990's [6]. In addition, investigations into the PKN model can yield results which have significance for more complicated approaches, such as the notable investigation by *Kemp* into the behaviour of the solution at the fracture front [114], which was later extended to the other 1D models in the form of the *speed equation* based approach to fracture front tracing [127, 128, 132, 165, 229].

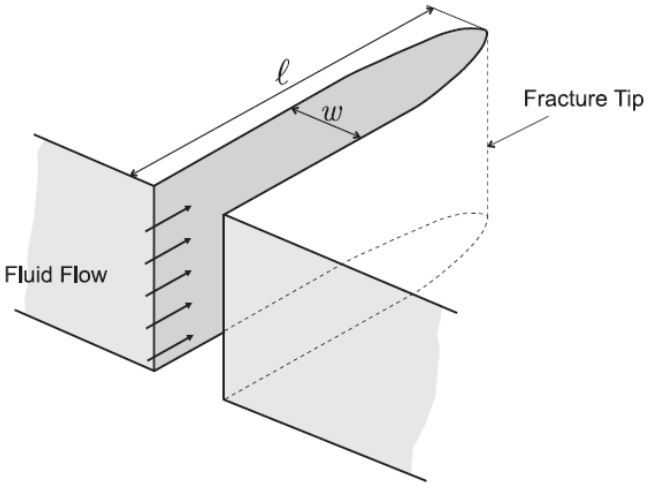

FIGURE 4.2: Schematic illustrating the KGD model [6].

4.1.2.2 The KGD model

Originally formulated independently by *Khristianovic & Zheltov* [116] and *Geertsma & de Klerk* [72], the geometry of the KGD (plane strain) model assumes fracture of infinite height but finite length, as shown in Fig. 4.2. As a result, the elasticity operator providing the relationship between the fracture aperture and net fluid pressure is inherently non-local in nature.

The KGD formulation is primarily applicable for fractures whose height is significantly greater than their length, and for which plane strain assumptions are applicable to horizontal sections [6, 219]. As such this model greatly complements the PKN formulation, where the fracture length is greater than its height, in the design of fracture treatments. An additional benefit of the KGD approach is that the asymptotics at the fracture tip are identical to those in the radial model, allowing a useful point of comparison with both the final 1D model and experimental results [34].

4.1.2.3 The radial model

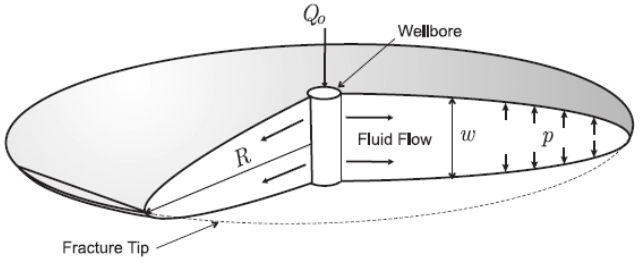

FIGURE 4.3: Schematic illustrating the radial (penny-shaped) model [6].

The radial model of hydraulic fracture, sometimes referred to as the penny-shaped model, was first proposed by *Sneddon* [3, 204]. The basic geometry of the fracture is provided in Fig. 4.3, with the fluid entering the crack through a point-source, resulting in a singular fluid flow rate at the center, which the fracture grows about in a symmetrical fashion.

The radial formulation is primarily applicable to homogeneous reservoir conditions, but requires that the fluid injection can be reasonably considered a point source. It however has the distinction of being the only one of the 1D models to approximate a three dimensional system, making it a useful point of comparison when developing more advanced 3D computer models [125].

4.1.2.4 Significance of the radial model

Although these models are highly simplified they were used for decades to investigate inherent features of the underlying physical process, the mathematical structure of the solution, and to help design hydraulic fracture treatments. Additionally the last thirty years has seen a substantial advance through the cyclical revision of these classic formulations. However, they have been superseded by more advanced models in most practical applications, specifically the various pseudo 3D [134], planar 3D [51, 161, 221] and fully 3D models [6, 46]. These often have the advantage of being able to incorporate additional features, such as piecewise extension of the fracture front due to fluid lag [37], or the case involving multiple cracks [122]. Unfortunately, while in rare case these models can be tested against experiments [123], this typically is not possible.

As such, despite the existence of more advanced approaches, the 1D approximations still have some notable uses:

- To investigate some inherent features of the underlying physical phenomenon and corresponding mathematical solutions (e.g. [68]).
- To construct and validate computational algorithms [147], most notably those which rely on phase field [144], distinct element [46] and peridynamic [151] based approaches, which allow for efficient modeling of complex geometries but do not model the crack explicitly.
- The KGD and radial models of hydraulic fracture mimic the tip behaviour of a planar 3D fracture [34].
- The solutions obtained by this model can be successfully applied as a benchmark when investigating he performance of 2D and 3D computational schemes (see [125]).

In light of these applications, having high accuracy numerical benchmark solutions which can be computed quickly and efficiently, particularly for the radial formulation, is of the upmost importance in the study of hydraulic fracture.

Unfortunately there is not a substantial body of suitable benchmarks available for the radial model. One can mention here the work by *Advani et al* [7], where the approximate time-dependent solution for both Newtonian and non-Newtonian fluids was obtained for special cases using a Lagrangian formulation. However, its accuracy has not been convincingly proven. An early simulator of penny-shaped fracture was presented by *Meyer* [143]; it relies on transforming non-linear equations into "more linear" ones, that are solved using integral equations. Numerical solutions, alongside with comparison with earlier results, were also provided. However, the accuracy of the final results is unknown.

The field saw a major advancement with the work of *Savitski & Detournay* [196], where asymptotic solutions for zero and large toughness regimes were given for a Newtonian fluid. The authors' use of the crack tip asymptotics, combined with appropriate multi-scaling techniques, allowed them to obtain a solution in the form of an infinite series of base functions. An additional asymptotic solution for the toughness dominated regime, for a Newtonian fluid, over small and large time scales was given by *Bunger, Detournay & Garagash* [35]. These asymptotic solutions were later shown to agree reasonably well with experimental results [34].

Recent work by *Kanaun* [111] provides a completely different discretized approach to the time-dependent form of the problem, with a three-parameter approximation of the solution also given. The model provides an approximate solution for Newtonian fluids in the toughness dominated regime without fluid leak-off, correlated with that from [143]. However, the approach cannot be applied to small toughness and the viscosity dominate regimes.

In work of *Dontsov* [50], closed-form approximate solutions are given based on the known solution asymptotics, with the numerical solver remaining valid in each of the limiting regimes. The accuracy of this approach was analyzed against previous numerical results, achieving an error below 1% for the crack opening, but as high as 2% when approximating the pressure function. Finally, we mention the numerical solution of *Linkov* [131, 132] for a class of Newtonian and shear-thinning fluids, with computations provided for the viscosity dominated case. A comparison of the numerical data with that from [196] shows perfect agreement in the respective cases. Neither of the mentioned solutions however were carefully verified, nor yield simple formulas (such as those for the KGD model in [165, 229], that can be easily used by researchers as benchmarks without constructing the numerical algorithm).

It is clear from this that examination that there is still work to be done, as no complete benchmark exists which accounts for all the properties of the fracture: fluid rheology, viscosity/toughness dominated regimes and the effects of fluid leak-off. Meanwhile previous work on the PKN/KGD models demonstrated that the combination of utilizing a particle velocity based approach, along with the inverse elasticity operator, yielded a benchmark which modeled all these features while also achieving the highest level of accuracy and efficiency [129, 165, 229].

4.1.3 The governing equations for radial HF

As the radial model of hydraulic fracture includes numerous interrelations between its variables, as well as a variety of methodologies with which to describe the fluid rheology, proppant inclusion and fluid leak-off, not all will be outlined here. However some of the equations and parameters are important to this investigation, and as such are outlined below.

4.1.3.1 The Poiseuille equation

The Poiseuille equation is the relation between the fluid flow, fracture aperture and the pressure. It is derived analogously to the case of the Hele-Shaw cell (Sect. 5.1.2.1), with an examination of the unidirectional fluid flow between two parallel boundary walls. In order to ensure a comparison between the two cases, we will consider here only the case of a Newtonian fluid.

The initial investigation begins with the *Navier-Stokes* equations. These are a set of non-linear partial differential equations which describe the flow of fluids, taking the following form in Cartesian coordinates:

$$\rho\left(\frac{\partial \mathbf{v}}{\partial t} + \mathbf{v}.\nabla\mathbf{v}\right) = \nabla.\left(-p\mathbf{I} + \tau\right) + \rho\mathbf{g}, \tag{4.1}$$

where $\mathbf{v} = (v_x, v_y, v_z)$ is the velocity vector, p represents the fluid pressure, τ the stress tensor and $\mathbf{g}$ denotes the body forces, which we will neglect from here on.

Given the geometry of the hydraulic fracture, we can assume that the fluid moves according to a parabolic distribution of the velocity vectors $\mathbf{v}$. Therefore, provided the flow is slow and parallel to the boundary wall, then [223]:

$$\frac{\partial \mathbf{v}}{\partial t} = 0, \quad v_z = 0. \tag{4.2}$$

It can also be assumed that the fluid is incompressible:

$$\nabla.\mathbf{v} = 0. \tag{4.3}$$

Composing (4.1) into three scalar components, while noting with the above, the systems governing equations becomes:

$$\frac{\partial v_x}{\partial x} + \frac{\partial v_y}{\partial y} = 0, \tag{4.4}$$

$$\begin{aligned} \frac{\partial p}{\partial x} &= \frac{\partial \tau_{xx}}{\partial x} + \frac{\partial \tau_{xy}}{\partial y} + \frac{\partial \tau_{xz}}{\partial z}, \\ \frac{\partial p}{\partial y} &= \frac{\partial \tau_{xy}}{\partial x} + \frac{\partial \tau_{yy}}{\partial y} + \frac{\partial \tau_{yz}}{\partial z}, \\ \frac{\partial p}{\partial z} &= \frac{\partial \tau_{xz}}{\partial x} + \frac{\partial \tau_{yz}}{\partial y} + \frac{\partial \tau_{zz}}{\partial z}. \end{aligned} \tag{4.5}$$

For the stress tensor, we assume that the only non-zero component is the shear stress:

$$\tau_{xz} = \mu \frac{\partial v_x}{\partial z}, \quad \tau_{yz} = 0, \tag{4.6}$$

Combining with $(4.5)_1$, we have:

$$\frac{\partial}{\partial z}\left[\frac{\partial v_x}{\partial z}\right] = \frac{1}{\mu}\frac{\partial p}{\partial x}. \tag{4.7}$$

With this, we define the aperture of the fracture as $w(x)$, with the crack walls at $z = \pm w/2$, and impose a symmetry condition around the centerline:

$$\left.\frac{\partial v_x}{\partial z}\right|_{z=0} = 0, \tag{4.8}$$

alongside the no-slip boundary condition:

$$v_x\left(z = \pm\frac{w}{2}\right) = 0. \tag{4.9}$$

As such, integrating (4.7) twice and imposing the above conditions, we obtain:

$$v_x = \frac{1}{2\mu}\frac{\partial p}{\partial x}\left[z^2 - \left(\frac{w}{2}\right)^2\right], \tag{4.10}$$

Now, we examine the average velocity of the fluid within the fracture, which is obtained by averaging over the height of the fracture. This will be described by:

$$v(x) = \frac{1}{w}\int_{-w/2}^{w/2} v_x \, dz = -\frac{w^2}{12\mu}\frac{\partial p}{\partial x}, \tag{4.11}$$

as a result, the fluid flow rate in the fracture will take the form:

$$q(x) = vw = -\frac{w^3}{12\mu}\frac{\partial p}{\partial x}. \tag{4.12}$$

It should be noted that, while we have only considered the Newtonian case here, the method of obtaining the Poiseuille equation for shear-thinning fluids remains the same, with the only difference being that the shear stress term (4.6) will instead take the form:

$$\tau_{xz} = M\left|\frac{\partial v_x}{\partial z}\right|^{n-1}\frac{\partial v_x}{\partial z}, \tag{4.13}$$

where the constants M, n define the rheology of the fluid, using a power-law based approach (see Sect. 4.1.3.5).

4.1.3.2 Elasticity equations (solid mechanics)

The relationship between the fracture aperture and the net pressure exerted on the solid walls was first obtained by *Arin & Erdogan* [14]. This was achieved by approximating the crack as a layer sandwiched between two dissimilar infinite half-planes. The relationship between these two crucial system parameters were then obtained through the framework of elasticity theory, assuming that the fracture only propagated as a straight crack in Mode I (see Fig. 4.4).

The obtained relationship between the fracture aperture and pressure in this case, labeled the elasticity equations, is given by:

$$p(r,t) = \frac{E}{(1-\nu^2)l(t)}\mathcal{A}[w](r,t), \quad w(r,t) = \frac{(1-\nu^2)l(t)}{E}\mathcal{A}^{-1}[p](r,t) \tag{4.14}$$

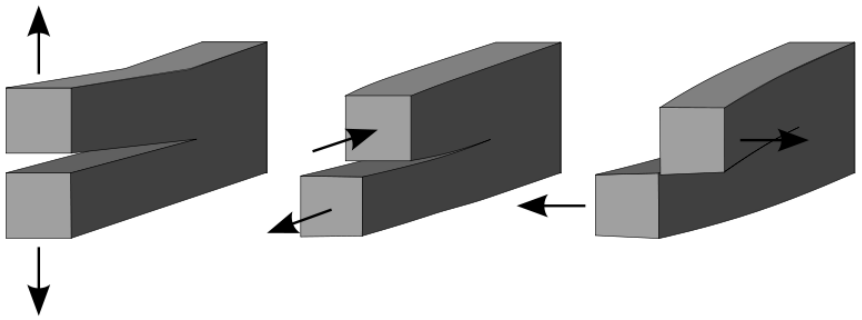

FIGURE 4.4: The three modes of fracture, credit: Wikimedia Commons.

with the operator $\mathcal{A}$ and its inverse taking the form:

$$\mathcal{A}[w] = -\int_0^1 \frac{\partial w(\eta l(t),t)}{\partial \eta} M\left[\frac{r}{l(t)},\eta\right] d\eta \tag{4.15}$$

$$\begin{aligned}\mathcal{A}^{-1}[p] &= \frac{8}{\pi}\int_{r/l(t)}^1 \frac{\xi}{\sqrt{\xi^2-(r/l(t))^2}}\int_0^1 \frac{\eta p(\eta\xi l(t),t)}{\sqrt{1-\eta^2}}\,d\eta\,d\xi \\ &\equiv \frac{8}{\pi}\int_0^1 \eta p(\eta l(t),t) G\left[\frac{r}{l(t)},\eta\right] d\eta\end{aligned} \tag{4.16}$$

where the kernels of the pertinent operators are:

$$M\left[\xi,s\right] = \frac{1}{2\pi}\begin{cases}\frac{1}{\xi}K\left(\frac{s^2}{\xi^2}\right)+\frac{\xi}{s^2-\xi^2}E\left(\frac{s^2}{\xi^2}\right), & \xi > s \\ \frac{s}{s^2-\xi^2}E\left(\frac{\xi^2}{s^2}\right), & s > \xi\end{cases} \tag{4.17}$$

$$G(\xi,s) = \begin{cases}\frac{1}{\xi}F\left(\arcsin\left(\sqrt{\frac{1-\xi^2}{1-s^2}}\right)\middle|\frac{s^2}{\xi^2}\right), & \xi > s \\ \frac{1}{s}F\left(\arcsin\left(\sqrt{\frac{1-s^2}{1-\xi^2}}\right)\middle|\frac{\xi^2}{s^2}\right), & s > \xi\end{cases} \tag{4.18}$$

with K, E being complete elliptic integrals of the first and second kinds respectively, and F the incomplete elliptic integral of the first kind (the full definitions of these are provided in [5]). An example of how the above kernels are obtained is provided in Appendix. E.2, where relations $(4.41)_1$, (4.42), (4.17) are derived. It is immediately apparent that these relationships are inherently non-local in nature (i.e. evaluating the aperture $w(r)$ for fixed r in $(4.41)_2$, (4.43), requires integrating the pressure over the whole domain, and visa versa, so the behaviour of these functions are not determined locally).

While this is the form of the elasticity relations used in the classical formulation of radial hydraulic fracture, the fact that it only applies to fractures propagating in Mode I means that it fails to account for the effect of shear-stress induced by the fluid on the walls of the crack, which was recently shown by *Wrobel, Mishuris & Piccolroaz* to play a not insignificant role in the fracture behaviour [230]. As such the elasticity equation requires updating if it is to incorporate this effect.

This can be achieved using the results of the recent paper by *Piccolroaz & Mishuris* [176]. In this work, they again approximated the crack as a layer sandwiched between two dissimilar infinite half-planes, however they were able to provide formulae for the relationship between the fracture pressure and the displacement in the general 3D case, incorporating all three fracture modes (see Fig. 4.4). The results, for a crack lying on the plane $x_2 = 0$, are detailed below.

Defining the average, $< f >$, and the jump, $[[f]]$, of a function across the plane containing the crack as follows:

$$< f > (x_1, x_3) = \frac{1}{2}\left[f(x_1, 0^+, x_3) + f(x_1, 0^-, x_3)\right], \tag{4.19}$$

$$[[f]](x_1, x_3) = f(x_1, 0^+, x_3) - f(x_1, 0^-, x_3), \tag{4.20}$$

the relationship between the pressure and the displacement is given by:

$$< \mathbf{p} > + \mathcal{A}^{(s)}[[\mathbf{p}]] = \mathcal{B}^{(s)}[[\mathbf{u}]]^{(-)}, \quad \sqrt{x_1^2 + x_3^2} < L(t). \tag{4.21}$$

where $L(t)$ is the fracture length and, provided the medium is homogeneous, we have:

$$\mathcal{A}^{(s)} = \frac{1-2\nu}{8(1-\nu)}\mathcal{Q}^{(s)}\begin{bmatrix} 0 & -\frac{\partial}{\partial x_1} & 0 \\ \frac{\partial}{\partial x_1} & 0 & \frac{\partial}{\partial x_3} \\ 0 & -\frac{\partial}{\partial x_3} & 0 \end{bmatrix}, \tag{4.22}$$

$$\mathcal{B}^{(s)} = \frac{E}{8(1-\nu^2)}\mathcal{Q}^{(s)}\begin{bmatrix} \frac{\partial^2}{\partial x_1^2} + (1-\nu)\frac{\partial^2}{\partial x_3^2} & 0 & \nu\frac{\partial^2}{\partial x_1 \partial x_3} \\ 0 & \frac{\partial^2}{\partial x_1^2} + \frac{\partial^2}{\partial x_3^2} & 0 \\ \nu\frac{\partial^2}{\partial x_1 \partial x_3} & 0 & (1-\nu)\frac{\partial^2}{\partial x_1^2} + \frac{\partial^2}{\partial x_3^2} \end{bmatrix}, \tag{4.23}$$

with:

$$\mathcal{Q}^{(s)} = \mathcal{P}_- \mathcal{Q} \mathcal{P}_-, \quad \mathcal{P}_- = \begin{cases} \phi(x_1), & \sqrt{x_1^2 + x_3^2} \leq L(t) \\ 0, & \text{otherwise} \end{cases}, \tag{4.24}$$

$$\mathcal{Q}(\phi) = \frac{1}{\pi}\int_{-\infty}^{\infty}\int_{-\infty}^{\infty} \frac{\phi(\xi_1, \xi_3)}{\sqrt{(x_1 - \xi_1)^2 + (x_3 - \xi_3)^2}}\, d\xi_1\, d\xi_3. \tag{4.25}$$

It should be noted that this formulation is in Cartesian coordinates, and as such will have to be transformed into radial coordinates if the elasticity relations are to be updated.

4.1.3.3 Boundary condition

The fracture opening ($r = 0$)

The boundary condition on the fracture opening ($r = 0$) defines the rate at which fluid is pumped into the fracture. It is worth noting that, as this is assumed to be a point source, the fluid flux q will be singular at this point. It can in fact be shown asymptotically that:

$$q \sim \frac{q_0(t)}{r}, \quad r \to 0, \tag{4.26}$$

for some unknown $q_0(t)$.

In addition to this, we must note that the fluid will be entering the fracture uniformly from this source, traveling orthogonal from the center towards the fracture tip (no rotation). As such, the boundary condition can be obtained by averaging the fluid flow emanating from the source, giving the following conditions:

$$\int_{\partial\Omega_0} q.\mathbf{n}\, dr = Q_0, \quad \int_{\partial\Omega_0} q.\mathbf{s}\, dr = 0, \tag{4.27}$$

here $\mathbf{n}$ and $\mathbf{s}$ are the normal and parallel vectors respectively, while the boundary domain $\delta\Omega_0$ is defined as:

$$\partial\Omega_0 = \left\{ \lim_{\varepsilon\to 0} \varepsilon e^{i\theta} : \theta \in [0, 2\pi) \right\} \tag{4.28}$$

Noting that in this case we have $\mathbf{n} = r\, dr/d\theta$, alongside that the first asymptotic term (4.26), condition $(4.27)_1$ yields:

$$Q_0 = \int_0^{2\pi} q_0(t)\, d\theta = 2\pi q_0(t) \tag{4.29}$$

As such, combining the above with (4.26) and taking the limit, the boundary condition immediately follows:

$$\lim_{r\to 0} rq = \frac{Q_0}{2\pi}. \tag{4.30}$$

The fracture tip ($r = l(t)$)

The boundary conditions at the fracture tip depend on the assumptions used when creating the model. In hydraulic fracturing, it has been shown experimentally that the fluid inside the crack does not always extend to the fracture tip, a phenomenon referred to as fluid lag [21, 49]. Instead there is a cyclical process, described in [175] as follows: "The growth of macroscopic tension fractures consists of short periods of extension of the crack by fracture, separated by longer periods during which the pore fluid flows into the crack." This step-wise extension of the fracture front has been demonstrated experimentally in hydrogels [37, 177].

This effect is most often ignored when examining the 1D models of hydraulic fracture, as the effect of fluid lag is typically small, and is considered to be highly localized. In spite of this, attempts have been made to incorporate it into the early stages of the model, or for shallow fractures, where the influence of this phenomena will be more pronounced [69, 70, 124, 130].

In the work presented here however, it will be assumed that no fluid lag occurs. This is in line with the classical formulation of 1D hydraulic fracture, and as such the crack tip

boundary conditions are given by:

$$w(1,t) = 0, \quad q(1,t) = 0, \tag{4.31}$$

4.1.3.4 Fluid mass and balance equations

The fluid mass conservation equation, sometimes referred to as the continuity equation, is one of the most fundamental and well known equations in fluid mechanics, and as such its derivation will not be repeated here (a full explanation and derivation can be found in [17]). In the case of penny-shaped hydraulic fracture, this equation will be given in radial coordinates by:

$$\frac{\partial w}{\partial t} + \frac{1}{r}\frac{\partial}{\partial r}(rq) + q_l = 0, \quad 0 < r < l(t), \tag{4.32}$$

where $w(r,t)$ is the fracture aperture, q is the fluid flow rate and q_l is the fluid leak-off to the surrounding rock. This equation simply ensures that the quantity of fluid in the system is accounted for at any given moment in time.

An alternative representation of this is the Reynolds equation, which is obtained by substituting the Poiseuille equation (4.12) into the continuity equation (4.32):

$$\frac{\partial w}{\partial t} = \frac{1}{12\mu r}\frac{\partial}{\partial r}\left(rw^3\frac{\partial p}{\partial r}\right) - q_l, \quad 0 < r < l(t). \tag{4.33}$$

This equation simply describes the relationship between the pressure and aperture over time.

In order to obtain the fluid balance equation, we multiply the continuity equation (4.32) by the radial coordinate r, before integrating twice, for the fluid domain $[0, l(t)]$ over time $[0, t]$:

$$\int_0^t \int_0^{l(s)} r\frac{\partial w}{\partial s}\, dr ds + \int_0^t \int_0^{l(s)} \frac{\partial}{\partial r}(rq(r,s))\, dr ds + \int_0^t \int_0^{l(s)} rq_l(r,s)\, dr ds = 0. \tag{4.34}$$

Assuming that we can safely change the order of integration in the leftmost integral, and noting the boundary conditions at both the fracture front and opening (4.30)-(4.31), we can express this as:

$$\int_0^{l(t)} r \int_0^t \frac{\partial w}{\partial s}\, ds dr + \int_0^t \int_0^{l(s)} rq_l(r,s)\, dr ds = \frac{1}{2\pi}\int_0^t Q_0(s)\, ds. \tag{4.35}$$

Finally, if we take the following non-zero initial conditions:

$$l(0) = l_*, \quad w(r,0) = w_*(r), \tag{4.36}$$

we obtain the final form of the fluid balance equation:

$$\int_0^{l(t)} r\left[w(r,t) - w_*(r)\right]\, dr + \int_0^t \int_0^{l(s)} r q_l(r,s)\, dr ds = \frac{1}{2\pi}\int_0^t Q_0(s)\, ds. \tag{4.37}$$

This equation simply ensures that the volume of fluid within the system is accounted for over time. It is worth noting that this equation has previously been used to trace the fracture front in the absence of a proper Stefan-type condition (as it links the known pumping rate with the total volume of fluid in the fracture, allowing the rate of fracture growth to be determined if relations between the fluid volume, pressure and aperture are assumed predefined).

4.1.3.5 Fluid rheology

When studying fluid driven fracture, it is clearly of vital importance that the rheological properties of the fracturing fluid are properly accounted for. While in special cases the fluid can be modeled as a Newtonian one (for example in low permeability reservoirs), most fracturing fluids used in conventional reservoirs exhibit non-Newtonian behaviour. As such the representation of the relation between the shear stress and strain rates shown in (5.2) no longer applies, and to correctly model this behaviour a power law approach will be employed. Such a modification is common in the literature, and which has been shown to reasonably approximate the necessary properties [36, 219]:

$$\tau = M\dot{\gamma}^n \tag{4.38}$$

where n is the "fluid behaviour index" and M is the "consistency index". Newtonian fluids have behavioural index $n = 1$, in which case the consistency index is simply the dynamic viscosity $M = \mu$. Meanwhile $n = 0$ denotes the case of a perfectly plastic fluid, with $M = \sigma_Y$ is the yield stress. Finally fluids in the range $0 < n < 1$ are referred to as shear-thinning fluids.

It should be noted that this two-parameter model can't accurately approximate the fracturing fluids behaviour at high or low shear rates [197], and that alternative models do exist in the literature more able to approximate the fluids rheological properties. One of the most powerful examples is the Carreau model [38], however this approach proves too complicated to use in conjuncture with 1D hydraulic fracturing problems, as no closed form of the Poiseuile equation can be obtained. Alternative three (the Hershel-Bulkley law [92]) or four (truncated power law [120]) parameter models do exist, however they are scarcely used in the literature for problems of this form. In order to maintain consistency with past results we therefore revert to the two-parameter power model for the fracturing fluid.

4.2 The classical penny-shaped model

4.2.1 Outline and motivation

As outlined in Sect. 4.1.2.4, while the penny-shaped model plays a significant role in investigations into hydraulic fracture, there is a notable lack of efficient, accurate benchmarks. This is most notable in the case of a toughness dominated fracture containing a power-law based fluid, where there are no published benchmarks with a known level of accuracy.

For this reason, we begin this investigation by attempting to remedy this deficiency in the literature. This means providing a numerical solver, which is capable of resolving problems in both the viscosity and toughness dominated regimes, for a power-law based fluid, to a high level of accuracy, and without compromising computation times to do so.

This will be achieved utilizing the approach outlined for the PKN and KGD cases in [165, 229]. There, the *speed equation* (2.18), which is a Stefan-type condition, was employed to trace the evolution of the fracture front. In this way, the singular nature of the pressure function at the crack tip was overcome, allowing a far more accurate evaluation of this crucial part of the fracture. This, combined with intelligent use of the crack tip asymptotics, regularization of the Tikhonov type (the technical details of which can be found in [118, 228]), and a specialised modular construction of the numerical algorithm (referred to as the 'universal algorithm'), enables the scheme to achieve highly accurate results without sacrificing computation time.

Introducing similar methods to the case of a penny-shaped fracture has recently been achieved in the viscosity dominated case, with *Linkov* providing a numerical solution with a claimed relative error below 10^{-4} [132]. This setup however lacked the previously mentioned efficient modular structure used in the PKN and KGD cases, and as such required $N = 1000$ boundary nodes to achieve this level of accuracy. Therefore, with proper construction of the numerical algorithm, this level of accuracy can be achieved with far shorter simulation times, which is a necessary step if the goal of computing numerical solutions in real-time is to be achieved. Extending this effort to the toughness dominated regime is also essential, if the effect of shear-stress induced by the fluid is to be incorporated into the model.

This investigation into the classical penny-shaped model is organised as follows. The basic system of equations describing the problem is given in Sect. 4.2.2. Next, normalization to the dimensionless form is carried out. In Sect. 4.2.3, comprehensive information about the solution asymptotics is presented, which is heavily utilized in the subsequent

numerical implementation. New computational variables, the reduced particle velocity and modified pressure derivative, are introduced. The advantages of both are outlined, and the problem is reformulated in terms of the new variables. In Sect. 4.2.4 the governing system of equations is reduced to the time independent self-similar form. This formulation is used in Sect. 4.2.5 to construct the computational algorithm. The accuracy and efficiency of computations are examined against newly introduced analytical benchmark examples, whose construction is outlined in Appendix. D. Alternative error measures are proposed for the cases where no closed-form analytical solution is available. Then, numerical reference solutions are proposed for the variant of an impermeable solid. Finally, the computational algorithm is used to verify other solutions available in the literature.

4.2.2 Problem formulation

Let us consider a 3D penny-shaped crack, defined in polar coordinates by the system $\{r, \theta, z\}$, with associated crack dimensions $\{l(t), w(t)\}$ as the fracture radius and aperture respectively, noting that both are a function of time. The crack is driven by a point source of power-law fluid located at the origin, and has a known pumping rate: $Q_0(t)$. The fluid's rheological properties are described by a power-law [36]. We have that, as the flow is axisymmetric, all variables will be independent of the angle θ.

The fluid mass balance equation is as follows:

$$\frac{\partial w}{\partial t} + \frac{1}{r}\frac{\partial}{\partial r}(rq) + q_l = 0, \quad 0 < r < l(t), \tag{4.39}$$

where $q_l(r,t)$ is the fluid leak-off function, representing the volumetric fluid loss to the rock formation in the direction perpendicular to the crack surface per unit length of the fracture. Throughout this paper we will assume it to be predefined and bounded at the fracture tip, but it will not be prescribed any specific formulation.

Meanwhile, $q(r,t)$ is the fluid flow rate inside the crack, given by the Poiseuille law:

$$q^n = -\frac{w^{2n+1}}{M'}\frac{\partial p}{\partial r}, \tag{4.40}$$

with $p(r,t)$ being the net fluid pressure on the fracture walls (i.e. $p = p_f - \sigma_0$, where p_f is the total pressure and σ_0 is the confining stress), while the constant M' is a modified fluid consistency index $M' = 2^{n+1}(2n+1)^n/n^n M$, where $0 \leq n \leq 1$ is the fluid behaviour index.

The non-local relationships between the fracture aperture and the pressure (elasticity equations) are as follows:

$$p(r,t) = \frac{E'}{l(t)}\mathcal{A}[w](r,t), \quad w(r,t) = \frac{l(t)}{E'}\mathcal{A}^{-1}[p](r,t), \tag{4.41}$$

where $E' = E/(1-\nu^2)$, with E being the Young's modulus and ν the Poisson ratio. The operator $\mathcal{A}$ and its inverse take the form:

$$\mathcal{A}[w] = -\int_0^1 \frac{\partial w(\eta l(t),t)}{\partial \eta} M\left[\frac{r}{l(t)},\eta\right] d\eta, \tag{4.42}$$

$$\begin{aligned}\mathcal{A}^{-1}[p] &= \frac{8}{\pi}\int_{r/l(t)}^1 \frac{\xi}{\sqrt{\xi^2-(r/l(t))^2}}\int_0^1 \frac{\eta p(\eta\xi l(t),t)}{\sqrt{1-\eta^2}}\,d\eta\,d\xi \\ &\equiv \frac{8}{\pi}\int_0^1 \eta p(\eta l(t),t) G\left[\frac{r}{l(t)},\eta\right] d\eta\,,\end{aligned} \tag{4.43}$$

for the pertinent kernels [113]:

$$M\left[\xi,s\right] = \frac{1}{2\pi}\begin{cases}\frac{1}{\xi}K\left(\frac{s^2}{\xi^2}\right) + \frac{\xi}{s^2-\xi^2}E\left(\frac{s^2}{\xi^2}\right), & \xi > s \\ \frac{s}{s^2-\xi^2}E\left(\frac{\xi^2}{s^2}\right), & s > \xi\end{cases} \tag{4.44}$$

$$G(\xi,s) = \begin{cases}\frac{1}{\xi}F\left(\arcsin\left(\sqrt{\frac{1-\xi^2}{1-s^2}}\right)\middle|\frac{s^2}{\xi^2}\right), & \xi > s \\ \frac{1}{s}F\left(\arcsin\left(\sqrt{\frac{1-s^2}{1-\xi^2}}\right)\middle|\frac{\xi^2}{s^2}\right), & s > \xi\end{cases} \tag{4.45}$$

K, E are the complete elliptic integrals of the first and second kinds respectively, and F the incomplete elliptic integral of the first kind, given in [5].

These equations are supplemented by the boundary condition at $r = 0$, which defines the intensity of the fluid source, Q_0:

$$\lim_{r\to 0} rq(r,t) = \frac{Q_0(t)}{2\pi}, \tag{4.46}$$

the tip boundary conditions:

$$w(l(t),t) = 0, \quad q(l(t),t) = 0, \tag{4.47}$$

and appropriate initial conditions describing the starting crack opening and length:

$$w(r,0) = w_*(r), \quad l(0) = l_0. \tag{4.48}$$

Additionally, it is assumed that the crack is in continuous mobile equilibrium, and as such the classical crack propagation criterion of linear elastic fracture mechanics is imposed:

$$K_I = K_{Ic}, \tag{4.49}$$

where K_{Ic} is the material toughness while K_I is the stress intensity factor. The latter is computed according to the following formula [184]:

$$K_I(t) = \frac{2}{\sqrt{\pi l(t)}} \int_0^{l(t)} \frac{r p(r,t)}{\sqrt{l^2(t) - r^2}}\, dr. \tag{4.50}$$

Throughout this paper we accept the convention that when $K_{Ic} = 0$ the hydraulic fracture propagates in the viscosity dominated regime. Otherwise the crack evolves in the toughness dominated mode. Each of these two regimes is associated with qualitatively different tip asymptotics, which constitutes a singular perturbation problem as $K_{Ic} \to 0$, and leads to serious computational difficulties in the small toughness range.

Finally, noting (4.39) and (4.46), the global fluid balance equation is given by:

$$\int_0^{l(t)} r\left[w(r,t) - w_*(r)\right]\, dr + \int_0^t \int_0^{l(t)} r q_l(r,\tau)\, dr\, d\tau = \frac{1}{2\pi} \int_0^t Q_0(\tau)\, d\tau. \tag{4.51}$$

The above set of equations and conditions represent the typically considered formulation for a penny-shaped hydraulic fracture [196].

In order to facilitate the analysis we shall utilize an additional dependent variable, v, which describes the average speed of fluid flow through the fracture cross-section [147]. It will be referenced to in the text as the particle velocity, and is defined as:

$$v(r,t) = \frac{q(r,t)}{w(r,t)}, \quad v^n(r,t) = -\frac{1}{M'} w^{n+1} \frac{\partial p}{\partial r}. \tag{4.52}$$

Provided the fluid leak-off q_l is finite at the crack tip, v has the following property:

$$\lim_{r \to l(t)} v(r,t) = v_0(t) < \infty. \tag{4.53}$$

Additionally, given that the fracture apex coincides with the fluid front (no lag), and that the fluid leak-off at the fracture tip is weaker than the Carter law variant, the so-called *speed equation* [127] holds:

$$\frac{dl}{dt} = v_0(t). \tag{4.54}$$

This Stefan-type boundary condition constitutes an explicit method, as opposed to an implicit level set method [161], and can be effectively used to construct a mechanism

of fracture front tracing. The advantages of implementing such a condition have been shown in [132, 165, 229].

4.2.2.1 Problem normalization

For the main body of the text, in order to make the presentation clearer, we will assume during derivations that $0 < n < 1$, however all results shown will be calculated according to their respective models. Any modification to the governing equations and numerical scheme in the limiting cases $n = 0$ and $n = 1$ are detailed in Appendix C.

We normalize the problem by introducing the following dimensionless variables:

$$\begin{gathered}\tilde{r} = \frac{r}{l(t)}, \quad \tilde{t} = \frac{t}{t_n^{1/n}}, \quad \tilde{w}(\tilde{r},\tilde{t}) = \frac{w(r,t)}{l_*}, \quad L(\tilde{t}) = \frac{l(t)}{l_*}, \quad \tilde{q}_l(\tilde{r},\tilde{t}) = \frac{t_n^{1/n}}{l_*} q_l(r,t), \\ \tilde{q}(\tilde{r},\tilde{t}) = \frac{t_n^{1/n}}{l_*^2} q(r,t), \quad \tilde{Q}_0(\tilde{t}) = \frac{t_n^{1/n}}{l_*^2 l(t)} Q_0(t), \quad \tilde{v}(\tilde{r},\tilde{t}) = \frac{t_n^{1/n}}{l_*} v(r,t), \\ \tilde{p}(\tilde{r},\tilde{t}) = \frac{t_n}{M'} p(r,t), \quad \tilde{K}_{Ic} = \frac{1}{E'\sqrt{l_*}} K_{Ic}, \quad t_n = \frac{M'}{E'},\end{gathered} \tag{4.55}$$

where $\tilde{r} \in [0,1]$ and l_* is chosen for convenience.

We note that such a normalization scheme has previously been used in [132, 165, 229], and that it is not attributed to any particular influx regime or asymptotic behaviour of the solution.

Under normalization scheme (4.55), the continuity equation (4.39) can be rewritten in terms of the particle velocity (4.52) to obtain:

$$\frac{\partial \tilde{w}}{\partial \tilde{t}} - \frac{L'(\tilde{t})}{L(\tilde{t})} \tilde{r} \frac{\partial \tilde{w}}{\partial \tilde{r}} + \frac{1}{L(\tilde{t})\tilde{r}} \frac{\partial}{\partial \tilde{r}} (\tilde{r}\tilde{w}\tilde{v}) + \tilde{q}_l = 0. \tag{4.56}$$

The particle velocity (4.40) is expressed as:

$$\tilde{v} = \left[-\frac{\tilde{w}^{n+1}}{L(\tilde{t})} \frac{\partial \tilde{p}}{\partial \tilde{r}} \right]^{\frac{1}{n}}, \tag{4.57}$$

while the speed equation is now given by combining (4.52)-(4.54):

$$\tilde{v}_0(\tilde{t}) = L'(\tilde{t}) = \left[-\frac{\tilde{w}^{n+1}}{L(\tilde{t})} \frac{\partial \tilde{p}}{\partial \tilde{r}} \right]^{\frac{1}{n}}_{\tilde{r}=1} < \infty. \tag{4.58}$$

The global fluid balance equation (4.51) is transformed to:

$$\int_0^1 \tilde{r}\left[L^2(\tilde{t})\tilde{w}(\tilde{r},\tilde{t}) - L^2(0)\tilde{w}_*(\tilde{r})\right]\, d\tilde{r} + \int_0^{\tilde{t}}\int_0^1 \tilde{r}L^2(\tau)\tilde{q}_l(\tilde{r},\tau)\, d\tilde{r}\, d\tau = \frac{1}{2\pi}\int_0^{\tilde{t}} L(\tau)\tilde{Q}_0(\tau)\, d\tau. \tag{4.59}$$

The notation for the elasticity equations (4.41)-(4.43) takes the form:

$$\tilde{p}(\tilde{r},\tilde{t}) = \frac{1}{L(\tilde{t})}\mathcal{A}[\tilde{w}](\tilde{r},\tilde{t}), \quad \tilde{w}(\tilde{r},\tilde{t}) = L(\tilde{t})\mathcal{A}^{-1}[\tilde{p}](\tilde{r},\tilde{t}), \tag{4.60}$$

where the operators denote:

$$\mathcal{A}[\tilde{w}](\tilde{r},\tilde{t}) = -\int_0^1 \frac{\partial\tilde{w}(\eta,\tilde{t})}{\partial\eta} M\left[\tilde{r},\eta\right]\, d\eta, \tag{4.61}$$

$$\mathcal{A}^{-1}[\tilde{p}](\tilde{r},\tilde{t}) = \frac{8}{\pi}\int_{\tilde{r}}^1 \frac{\xi}{\sqrt{\xi^2-\tilde{r}^2}}\int_0^1 \frac{\eta\tilde{p}(\eta\xi,\tilde{t})}{\sqrt{1-\eta^2}}\, d\eta\, d\xi. \tag{4.62}$$

From definition (4.50) and the fracture propagation condition (4.49) we have that:

$$\tilde{K}_I = \tilde{K}_{Ic} = \frac{2}{\sqrt{\pi}}\sqrt{L(\tilde{t})}\int_0^1 \frac{\tilde{r}\tilde{p}(\tilde{r},\tilde{t})}{\sqrt{1-\tilde{r}^2}}\, d\tilde{r}. \tag{4.63}$$

Note that through proper manipulation of (4.62) and the use of (4.63), $(4.60)_2$ can be expressed in the following form (see Appendix. E):

$$\tilde{w}(\tilde{r},\tilde{t}) = \frac{8}{\pi}L(\tilde{t})\int_0^1 \frac{\partial\tilde{p}}{\partial y}(y,\tilde{t})\mathcal{K}(y,\tilde{r})\, dy + \frac{4}{\sqrt{\pi}}\sqrt{L(\tilde{t})}\tilde{K}_I\sqrt{1-\tilde{r}^2}, \tag{4.64}$$

for the kernel function $\mathcal{K}$ given by:

$$\mathcal{K}(y,\tilde{r}) = y\left[E\left(\arcsin(y)\,\middle|\,\frac{\tilde{r}^2}{y^2}\right) - E\left(\arcsin(\chi)\,\middle|\,\frac{\tilde{r}^2}{y^2}\right)\right], \tag{4.65}$$

where:

$$\chi = \min\left(1, \frac{y}{\tilde{r}}\right), \tag{4.66}$$

with the function $E(\phi\,|\,m)$ denoting the incomplete elliptic integral of the second kind [5].

While this form of the elasticity operator has not previously been used in the case of a penny-shaped fracture, an analogous form of the elasticity equation for the KGD model has been utilized in [165, 229], where its advantages in numerical computations have been demonstrated. Notably, the kernel function $\mathcal{K}$ exhibits better behaviour than the weakly singular kernel G (4.45), having no singularities for any combination of $\{\tilde{r}, y\}$.

Additionally, equation (4.57) can be easily transformed to obtain p' and then substituted into (4.64), meaning that the latter can be utilized without the additional step of deriving the pressure function needed for the classic form of the operator.

Next the boundary conditions (4.47), in view of (4.53), transform to a single condition:

$$\tilde{w}(1,\tilde{t}) = 0, \tag{4.67}$$

alongside the initial conditions (4.48):

$$\tilde{w}(\tilde{r},0) = \frac{w_*(r)}{l_*}, \quad L_0 = \frac{l_0}{l_*}. \tag{4.68}$$

The source strength (4.46) is now defined as:

$$\frac{\tilde{Q}_0(\tilde{t})}{2\pi} = \lim_{\tilde{r}\to 0} \tilde{r}\tilde{w}(\tilde{r},\tilde{t})\tilde{v}(\tilde{r},\tilde{t}). \tag{4.69}$$

While combining the above with (4.57) we obtain the following relationship:

$$\lim_{\tilde{r}\to 0} \tilde{r}^n \frac{\partial \tilde{p}}{\partial \tilde{r}} = -\left(\frac{\tilde{Q}_0(\tilde{t})}{2\pi}\right)^n \frac{L(\tilde{t})}{\tilde{w}^{2n+1}(0,\tilde{t})}, \tag{4.70}$$

which provides a valuable insight into how the behaviour of the fluid pressure function near to the source varies for differing values of n. The resulting pressure asymptotics at the injection point, with corresponding aperture, are detailed below:

$$\tilde{p}(\tilde{r},\tilde{t}) = \tilde{p}_0^o(\tilde{t}) + \tilde{p}_1^o(\tilde{t})\tilde{r}^{1-n} + O\left(\tilde{r}^{2-n}\right), \quad \tilde{r}\to 0, \tag{4.71}$$

$$\tilde{w}(\tilde{r},\tilde{t}) = \tilde{w}_0^o(\tilde{t}) + \tilde{w}_1^o(\tilde{t})\tilde{r}^{2-n} + O\left(\tilde{r}^2\log(\tilde{r})\right), \quad \tilde{r}\to 0. \tag{4.72}$$

It is worth restating that there are minor differences to both the asymptotics and fundamental equations in the limiting cases $n = 0$ and $n = 1$. These are explained in further detail in Appendix C.

4.2.3 Crack tip asymptotics, the speed equation and proper variables

A universal algorithm for numerically simulating hydraulic fractures has recently been introduced in [165, 229] and tested against the PKN and KGD (plane strain) models for Newtonian and shear-thinning fluids. It proved to be extremely efficient and accurate. Its modular architecture enables one to adapt it to other HF models by simple replacement or adjustment of the basic blocks. In the following we will construct a computational scheme for the radial fracture based on the universal algorithm. To

this end we need to introduce appropriate computational variables, and to define the basic asymptotic interrelations between them. For the sake of completeness detailed information on the solutions tip asymptotic behaviour, for different regimes of crack propagation, are presented below.

4.2.3.1 Crack tip asymptotics

Viscosity dominated regime ($\tilde{K}_{Ic} = 0$)

In the viscosity dominated regime the crack tip asymptotics of the aperture and pressure derivative can be expressed as follows:

$$\begin{aligned}\tilde{w}(\tilde{r},\tilde{t}) = \tilde{w}_0(\tilde{t})\left(1-\tilde{r}^2\right)^{\alpha_0} + \tilde{w}_1(\tilde{t})\left(1-\tilde{r}^2\right)^{\alpha_1} + \tilde{w}_2(\tilde{t})\left(1-\tilde{r}^2\right)^{\alpha_2} \\ + O\left(\left(1-\tilde{r}^2\right)^{\alpha_2+\delta}\right), \quad \tilde{r}\to 1,\end{aligned} \tag{4.73}$$

$$\frac{\partial\tilde{p}}{\partial\tilde{r}}(\tilde{r},\tilde{t}) = \tilde{p}_0(\tilde{t})\left(1-\tilde{r}^2\right)^{\alpha_0-2} + \tilde{p}_1(\tilde{t})\left(1-\tilde{r}^2\right)^{\alpha_0-1} + O\left(1\right), \quad \tilde{r}\to 1. \tag{4.74}$$

The crack tip asymptotics of the pressure function can be derived from the above, however this form is given due to its use in computations (this will be explained in further detail later).

As a consequence the particle velocity behaves as:

$$\tilde{v}(\tilde{r},\tilde{t}) = \tilde{v}_0(\tilde{t}) + \tilde{v}_1\left(\tilde{t}\right)\left(1-\tilde{r}^2\right)^{\beta_1} + O\left(\left(1-\tilde{r}^2\right)^{\beta_2}\right), \quad \tilde{r}\to 1. \tag{4.75}$$

Note that we require $\tilde{v}_0(\tilde{t}) > 0$ to ensure the fracture is moving forward. The values of constants α_i, β_i are given in Table 4.1. The general formulae for the limiting cases $n = 0$ and $n = 1$ remain the same as (4.73)-(4.75), with the respective powers α_i, β_i again being determined according to Table 4.1.

Now, let us adopt the following notation for the crack propagation speed, based on the *speed equation* (4.58) and the tip asymptotics (4.75):

$$\tilde{v}_0(\tilde{t}) = L'(\tilde{t}) = \left[\frac{\mathcal{C}\mathcal{L}(\tilde{w})}{L^2(\tilde{t})}\right]^{\frac{1}{n}}. \tag{4.76}$$

Here $\mathcal{L}(\tilde{w}) > 0$ is a known functional and $\mathcal{C}$ is a positive constant. In the viscosity dominated regime we have that:

$$C = \frac{2n}{(n+2)^2}\cot\left(\frac{n\pi}{n+2}\right), \quad \mathcal{L}(\tilde{w}) = \tilde{w}_0^{n+2}. \tag{4.77}$$

Crack propagation regime	α_0	α_1	α_2	β_1	β_2
Viscosity dominated	$\frac{2}{n+2}$	$\frac{n+4}{n+2}$	$\frac{2n+6}{n+2}$	1	$\frac{2n+2}{n+2}$
Toughness dominated	$\frac{1}{2}$	$\frac{3-n}{2}$	$\frac{5-2n}{2}$	$\frac{2-n}{2}$	1

TABLE 4.1: Values of the basic constants used in the asymptotic expansions for $\tilde{w}$ and $\tilde{v}$ for $0 < n < 1$.

Additionally, we can directly integrate (4.76) in order to obtain an expression for the fracture length:

$$L(\tilde{t}) = \left[L^{1+\frac{2}{n}}(0) + \left(1 + \frac{2}{n}\right) \mathcal{C}^{\frac{1}{n}} \int_0^{\tilde{t}} \mathcal{L}^{\frac{1}{n}}(\tilde{w})\, d\tau \right]^{\frac{n}{n+2}}. \tag{4.78}$$

Toughness dominated regime ($\tilde{K}_{Ic} > 0$)

Near the fracture front the form of the aperture and particle velocity asymptotics remains the same as in the viscosity dominated regime (4.73), (4.75). Meanwhile the pressure derivative asymptotics yields:

$$\frac{\partial \tilde{p}}{\partial \tilde{r}}(\tilde{r}, \tilde{t}) = \tilde{p}_0 \left(1 - \tilde{r}^2\right)^{\alpha_1 - 2} + \tilde{p}_1 \left(1 - \tilde{r}^2\right)^{\alpha_2 - 2} + O(1), \quad \tilde{r} \to 1. \tag{4.79}$$

The values of α_i, β_i for this regime are provided in Table 4.1. The asymptotics in the limiting cases $n = 0$ and $n = 1$ is given in Appendix C (equations (C.10) and (C.1) respectively).

We again use notation (4.76) for the crack propagation speed, however the values of the functional $\mathcal{L}$ and the C will in this case be:

$$C = \frac{(3-n)(1-n)}{4} \tan\left(\frac{n\pi}{2}\right), \quad \mathcal{L}(\tilde{w}) = \tilde{w}_0^{n+1} \tilde{w}_1, \tag{4.80}$$

while the fracture length will be given by (4.78).

4.2.3.2 Reformulation in terms of computational variables

It is readily apparent that the choice of computational variables plays a decisive role in ensuring the accuracy and efficiency of the computational algorithm [118, 147, 229]. Let us introduce a new system of proper variables which are conducive to robust numerical computing.

- The reduced particle velocity $\Phi(\tilde{r},\tilde{t})$:

$$\Phi(\tilde{r},\tilde{t}) = \tilde{r}\tilde{v}(\tilde{r},\tilde{t}) - \tilde{r}^2\tilde{v}_0(\tilde{t}). \tag{4.81}$$

  It is a smooth, well behaved and non-singular variable that facilitates the numerical computations immensely. It is bounded at the crack tip and the fracture origin. The advantages of using an analogous variable in the PKN and KGD models have previously been demonstrated in [165, 229].

- The modified pressure derivative $\Omega(\tilde{r},\tilde{t})$:

$$\tilde{r}^n\Omega(\tilde{r},\tilde{t}) = \tilde{r}^n\frac{\partial\tilde{p}}{\partial\tilde{r}} - \Omega_0(\tilde{t}), \tag{4.82}$$

$$\Omega_0(\tilde{t}) = -\left(\frac{\tilde{Q}_0(\tilde{t})}{2\pi}\right)^n \frac{L(\tilde{t})}{\tilde{w}^{2n+1}(0,\tilde{t})}. \tag{4.83}$$

  It reflects the singular tip behavior of $\tilde{p}'_{\tilde{r}}$, having the same tip asymptotics as the pressure derivative, however it is bounded at the fracture origin. From (4.82) the pressure can be immediately reconstructed as:

$$\tilde{p}(\tilde{r},\tilde{t}) = \frac{\Omega_0(\tilde{t})}{1-n}\tilde{r}^{1-n} + C_p(\tilde{t}) + \int_0^{\tilde{r}} \Omega(\xi,\tilde{t})d\xi, \tag{4.84}$$

  where the term C_p follows from (4.63):

$$C_p(\tilde{t}) = \frac{1}{2}\sqrt{\frac{\pi}{L(\tilde{t})}}\tilde{K}_I - \frac{\sqrt{\pi}\Gamma\left(\frac{3-n}{2}\right)}{2\,(1-n)\,\Gamma\left(2-\frac{n}{2}\right)}\Omega_0(\tilde{t}) - \int_0^1 \Omega(y,\tilde{t})\sqrt{1-y^2}\,dy. \tag{4.85}$$

  This auxiliary variable will primarily be used in numerical computation of the elasticity operator.

The following interrelationship exists between the newly introduced variables:

$$\Omega(\tilde{r},\tilde{t}) = \left(\frac{\tilde{Q}_0(\tilde{t})}{2\pi\tilde{r}}\right)^n \frac{L(\tilde{t})}{\tilde{w}^{2n+1}(0,\tilde{t})} - \frac{L(\tilde{t})}{\tilde{w}^{n+1}(\tilde{r},\tilde{t})}\left[\frac{\Phi(\tilde{r},\tilde{t})}{\tilde{r}} + \tilde{r}\tilde{v}_0(\tilde{t})\right]^n. \tag{4.86}$$

Since under this new scheme Φ is bounded at the fracture tip, the source strength (4.69) and the boundary condition (4.67) can now be expressed as:

$$\tilde{w}(0,\tilde{t})\Phi(0,\tilde{t}) = \frac{\tilde{Q}_0(\tilde{t})}{2\pi}, \quad \tilde{w}(1,\tilde{t}) = 0. \tag{4.87}$$

By utilizing the boundary condition $(4.87)_1$, the relationship between the new variables (4.86) can be represented in the form:

$$\Omega\left(\tilde{r},\tilde{t}\right)=\frac{1}{\tilde{r}^n}\left[\frac{\Phi^n(0,\tilde{t})}{\tilde{w}^{n+1}(0,\tilde{t})}-\frac{\left(\Phi(\tilde{r},\tilde{t})+\tilde{r}^2\tilde{v}_0(\tilde{t})\right)^n}{\tilde{w}^{n+1}(\tilde{r},\tilde{t})}\right]. \tag{4.88}$$

Note that this is not only a more concise representation of (4.86) but also does not depend on $L(\tilde{t})$, which will be beneficial when computing the self-similar formulation. In this way the computational scheme will be based on: the crack opening, $\tilde{w}$, the reduced particle velocity, Φ, and an auxiliary variable, the modified fluid pressure, Ω.

By substituting the new variable Φ from (4.81) into the continuity equation (4.56), we obtain the modified governing equation:

$$\frac{\partial\tilde{w}}{\partial\tilde{t}}+\frac{1}{L(\tilde{t})\tilde{r}}\frac{\partial}{\partial\tilde{r}}\left(\tilde{w}\Phi\right)+\frac{2\tilde{v}_0}{L(\tilde{t})}\tilde{w}+\tilde{q}_l=0,\quad 0<\tilde{r}<1. \tag{4.89}$$

Additionally, the elasticity equation (4.64) can be now expressed as follows:

$$\tilde{w}(\tilde{r},\tilde{t})=\frac{8}{\pi}L(\tilde{t})\int_0^1\Omega(y,\tilde{t})\mathcal{K}(y,\tilde{r})\,dy+\frac{4}{\sqrt{\pi}}\sqrt{L(\tilde{t})}\tilde{K}_I\sqrt{1-\tilde{r}^2}+\frac{8}{\pi}L(\tilde{t})\Omega_0(\tilde{t})\mathcal{X}_n(\tilde{r}), \tag{4.90}$$

where $\mathcal{K}$ is given in (4.65), while $\mathcal{X}_n$ is defined by:

$$\mathcal{X}_n(\tilde{r})=\frac{\sqrt{\pi}\Gamma\left(\frac{3-n}{2}\right)}{2\left(n-1\right)\Gamma\left(2-\frac{n}{2}\right)}\left[\sqrt{1-\tilde{r}^2}+\frac{{}_2F_1\left(\frac{1}{2},\frac{n-2}{2};\frac{n}{2};\tilde{r}^2\right)}{n-2}-\frac{\sqrt{\pi}\tilde{r}^{2-n}\Gamma\left(\frac{n}{2}-1\right)}{2\Gamma\left(\frac{n-1}{2}\right)}\right]. \tag{4.91}$$

It can be easily shown that this function is well behaved in the limits.

4.2.4 Self-similar formulation

In this section we will reduce the problem to its time-independent self-similar version. This formulation will be used to define the computational scheme used later on in the numerical analysis.

We begin by assuming that a solution to the problem can be expressed through the following seperation of variables:

$$\tilde{w}(\tilde{r},\tilde{t})=\Psi(\tilde{t})\hat{w}(\tilde{r}),\quad \tilde{p}(\tilde{r},\tilde{t})=\frac{\Psi(\tilde{t})}{L(\tilde{t})}\hat{p}(\tilde{r}),\quad \tilde{q}(\tilde{r},\tilde{t})=\frac{\Psi^{2+\frac{2}{n}}(\tilde{t})}{L^{\frac{2}{n}}(\tilde{t})}\hat{q}(\tilde{r}),$$

$$\tilde{Q}_0(\tilde{t})=\frac{\Psi^{2+\frac{2}{n}}(\tilde{t})}{L^{\frac{2}{n}}(\tilde{t})}\hat{Q}_0,\quad \tilde{v}(\tilde{r},\tilde{t})=\frac{\Psi^{1+\frac{2}{n}}(\tilde{t})}{L^{\frac{2}{n}}(\tilde{t})}\hat{v}(\tilde{r}),\quad \Phi(\tilde{r},\tilde{t})=\frac{\Psi^{1+\frac{2}{n}}(\tilde{t})}{L^{\frac{2}{n}}}\hat{\Phi}(\tilde{r}),$$

$$\begin{aligned} \tilde{K}_I(\tilde{t}) &= \frac{\Psi(\tilde{t})}{\sqrt{L(\tilde{t})}}\hat{K}_I, \qquad \Omega(\tilde{r},\tilde{t}) = \frac{\Psi(\tilde{t})}{L(\tilde{t})}\hat{\Omega}(\tilde{r}), \\ \Omega_0(\tilde{t}) &= \frac{\Psi(\tilde{t})}{L(\tilde{t})}\hat{\Omega}_0, \qquad\qquad C_p(\tilde{t}) = \frac{\Psi(\tilde{t})}{L(\tilde{t})}\hat{C}_p, \end{aligned} \tag{4.92}$$

where $\Psi(t)$ is a smooth continuous function. By separating the variables in this manner it becomes possible to reduce the problem to a time-independent formulation when Ψ is described by an exponential or a power-law type function. From here on the spatial components will be marked by a 'hat'-symbol, and will describe the self-similar quantities. It is worth noting that the separation of spatial and temporal components given in (4.92) ensures that the qualitative bahaviour of the solution tip asymptotics remains the same as in the time-dependent variant.

4.2.4.1 The self-similar representation of the problem

We wish to examine two variants of the time dependent function:

$$\Psi_1(\tilde{t}) = e^{\gamma\tilde{t}}, \quad \Psi_2(\tilde{t}) = \left(a+\tilde{t}\right)^{\gamma}. \tag{4.93}$$

In both cases the fluid leak-off function will be assumed to take the form:

$$\tilde{q}_l(\tilde{r},\tilde{t}) = \frac{1}{\gamma}\Psi'(\tilde{t})\hat{q}_l(\tilde{r}). \tag{4.94}$$

The self-similar reduced particle velocity (4.81), modified pressure derivative (4.82), (4.83) and pressure (4.84) are defined by:

$$\hat{\Phi}(\tilde{r}) = \tilde{r}\hat{v}(\tilde{r}) - \tilde{r}^2\hat{v}_0, \quad \tilde{r}^n\hat{\Omega}(\tilde{r}) = \tilde{r}^n\frac{d\hat{p}}{d\tilde{r}} - \hat{\Omega}_0, \tag{4.95}$$

$$\hat{p}(\tilde{r}) = \frac{\hat{\Omega}_0}{1-n}\tilde{r}^{1-n} + \hat{C}_p + \int_0^{\tilde{r}}\hat{\Omega}(\xi)d\xi, \tag{4.96}$$

with

$$\hat{\Omega}_0 = -\left(\frac{\hat{Q}_0}{2\pi}\right)^n \frac{1}{\hat{w}^{2n+1}(0)}, \tag{4.97}$$

$$\hat{C}_p = \frac{\sqrt{\pi}}{2}\hat{K}_I - \frac{\sqrt{\pi}\Gamma\left(\frac{3-n}{2}\right)}{2\left(1-n\right)\Gamma\left(2-\frac{n}{2}\right)}\hat{\Omega}_0 - \int_0^1 \hat{\Omega}(y)\sqrt{1-y^2}\,dy. \tag{4.98}$$

It is immediately apparent from (4.76) and (4.92) that the self-similar crack propagation speed is given by:

$$\hat{v}_0 = \lim_{\tilde{r}\to 1}\left[-\hat{w}^{n+1}\frac{d\hat{p}}{d\tilde{r}}\right]^{\frac{1}{n}} = \left(\mathcal{CL}(\hat{w})\right)^{\frac{1}{n}}. \tag{4.99}$$

Note again that the qualitative asymptotic behaviour of the aperture, pressure and particle velocity as $\tilde{r}\to 0$ and $\tilde{r}\to 1$ remains the same as in the time dependent version

of the problem (4.73), (4.74), (4.75), (4.79). The respective asymptotic formulae hold provided that multipliers of the spatial terms are constant rather than being functions of time.

The self-similar counterparts of the elasticity equations (4.60) and (4.61) are now:

$$\hat{p}(\tilde{r}) = \hat{\mathcal{A}}[\hat{w}](\tilde{r}), \tag{4.100}$$

where:

$$\hat{\mathcal{A}}[\hat{w}](\tilde{r}) = -\int_0^1 \frac{d\hat{w}(\eta)}{d\eta} M\left[\tilde{r}, \eta\right] d\eta, \tag{4.101}$$

with its inverse being:

$$\hat{w}(\tilde{r}) = \frac{8}{\pi}\int_0^1 \hat{\Omega}(y)\mathcal{K}(y,\tilde{r})\, dy + \frac{4}{\sqrt{\pi}}\hat{K}_I\sqrt{1-\tilde{r}^2} + \frac{8}{\pi}\hat{\Omega}_0\mathcal{X}_n(\tilde{r}). \tag{4.102}$$

As the integral and function $\mathcal{X}_n(\tilde{r})$ both tend to zero faster than the square root term at the fracture tip, it immediately follows that, in the toughness dominated case ($\hat{K}_{Ic} > 0$), the leading asymptotic term of the aperture (4.73) is given by:

$$\hat{w}_0 = \frac{4}{\sqrt{\pi}}\hat{K}_I. \tag{4.103}$$

The self-similar particle velocity takes the form:

$$\hat{v}(\tilde{r}) = \left[-\hat{w}^{n+1}(\tilde{r})\frac{d\hat{p}(\tilde{r})}{d\tilde{r}}\right]^{\frac{1}{n}}. \tag{4.104}$$

The governing equation (4.89) becomes:

$$\frac{1}{\tilde{r}\hat{v}_0}\frac{d}{d\tilde{r}}\left(\hat{w}\hat{\Phi}\right) = -\left(3-s_n\right)\hat{w} - \left(1-s_n\right)\frac{\hat{q}_l}{\gamma}, \tag{4.105}$$

with the value of s_n in each case, alongside the fracture length, provided in Table 4.2. Meanwhile the fluid balance condition (4.59) becomes:

$$\left(3-s_n\right)\int_0^1 \tilde{r}\hat{w}(\tilde{r})\, d\tilde{r} + \frac{1-s_n}{\gamma}\int_0^1 \tilde{r}\hat{q}_l\, d\tilde{r} = \frac{\hat{Q}_0}{2\pi\hat{v}_0}. \tag{4.106}$$

The self-similar stress intensity factor (4.63) is given by:

$$\hat{K}_I = \hat{K}_{Ic} = \frac{2}{\sqrt{\pi}}\int_0^1 \frac{\tilde{r}\hat{p}(\tilde{r})}{\sqrt{1-\tilde{r}^2}}\, d\tilde{r}. \tag{4.107}$$

Self-similar law	s_n	$L(\tilde{t})$
$\Psi(\tilde{t}) = e^{\gamma\tilde{t}}$	0	$\left[\frac{\hat{v}_0}{\gamma}\right]^{\frac{n}{n+2}} e^{\gamma\tilde{t}}$
$\Psi(\tilde{t}) = \left(a+\tilde{t}\right)^{\gamma}$	$\frac{n}{\gamma(n+2)+n}$	$\left[\frac{(n+2)\hat{v}_0}{\gamma(n+2)+n}\right]^{\frac{n}{n+2}} \left(a+\tilde{t}\right)^{\gamma+\frac{n}{n+2}}$

TABLE 4.2: Table providing the fracture length $L(\tilde{t})$, which is obtained using (4.78) and (4.99), and the constant s_n, used in (4.105) and (4.106), for different variants of the self-similar solution.

Finally, the system's boundary conditions (4.87) transform to:

$$\hat{w}(0)\hat{\Phi}(0) = \frac{\hat{Q}_0}{2\pi}, \quad \hat{w}(1) = 0. \tag{4.108}$$

In the general case with $0 < n < 1$ these equations represent the full self-similar problem. Some modifications are necessary in the special cases when $n = 0$ and $n = 1$. These differences are outlined in Appendix C.

4.2.5 Numerical results

In this section we will construct an iterative computational scheme for numerically simulating hydraulic fracture. The approach is an extension of the universal algorithm introduced in [165, 229]. The computations are divided between two basic blocks, the first of which utilizes the continuity equation and the latter using the elasticity operator. The previously introduced computational variables, alongside the known information about the solution tip asymptotics, are employed extensively. The accuracy and efficiency of the computations are verified against the newly introduced analytical benchmark examples. Then the numerical benchmark solutions are given. Finally, a comparative analysis with other data available in the literature is delivered.

4.2.5.1 Computational scheme

The numerical approach is constructed through the framework of a universal algorithm, previously introduced for the PKN and KGD models in [165, 229]. This is an explicit scheme, as opposed to the implicit level set schemes commonly utilized in the literature (see e.g. [78, 122, 124, 161]). A full description of the algorithm is provided in Appendix. F, however the basic realization is as follows:

1. An initial approximation of the aperture $\hat{w} = \hat{w}^{j-1}$ is taken, such that it has the correct asymptotic behaviour and satisfies the boundary conditions.

2. The fluid balance equation (4.106) is utilized to obtain the asymptotic term(s) $\hat{w}^{j}_{0,1}$ needed to compute the particle velocity $\hat{v}^{j}_{0}$ using (4.99).

3. Having the above values the reduced particle velocity $\hat{\Phi}^{j}$ is reconstructed by direct integration of (4.105). Tikhonov type regularization is employed at this stage.

4. Equation (4.104) is then used to obtain an approximation of the modified pressure derivative $\hat{\Omega}$, and the elasticity equation (4.102) serves to compute the next approximation of the fracture aperture $\hat{w}^{j}$.

5. The system is iterated until all variables $\hat{\Phi}$, $\hat{w}$ and $\hat{v}_0$ converge to within prescribed tolerances.

We will demonstrate in this section that this scheme, combined with an appropriate meshing strategy, yields a highly accurate algorithm. A more detailed description of the algorithm's construction has been outlined in [164, 165, 229].

It is worth noting that, due to the degeneration of the Poiseuille equation when $n = 0$, it can no longer be used to compute the fluid flow rate or the particle velocity. However, thanks to the modular structure of the proposed algorithm, one can easily adapt it to this variant of the problem. In this case a special form of the elasticity equation (C.19) is utilized to obtain the aperture, with the particle velocity being reconstructed using relations (C.20) and (C.21).

4.2.5.2 Accuracy of computations

In this subsection we will investigate the accuracy of computations delivered by the proposed numerical scheme. To this end a newly introduced set of analytical benchmark solutions with a non-zero fluid leak-off function will be used. Alternative measures for testing the numerical accuracy in the absence of exact solutions will then be proposed and analysed. Next, the problem of a penny-shaped hydraulic fracture propagating in an impermeable material will be considered. The accuracy of numerical solutions will be verified by the aforementioned alternative measures. Simple, semi-analytical approximations, which mimic the obtained numerical data to a prescribed level of accuracy, will be provided. Finally, a comparative analysis with other solutions available in the literature will be performed.

4.2.5.3 Analysis of computational errors against analytical benchmarks

The first method of testing the computational accuracy is by comparison with analytical benchmark solutions. Respective closed-form benchmarks with predefined, non-zero, leak-off functions are outlined in Appendix. D. They have been constructed for both the viscosity and toughness dominated regimes, for a class of shear-thinning and Newtonian fluids. All of the analytical benchmarks used for comparison are designed to ensure physically realistic behaviour of the solution while maintaining the proper asymptotic behaviour. In all numerical simulations the power-law variant of the time dependent function Ψ_2 $(4.93)_2$ is used.

The accuracy of computations is depicted in Fig. 4.5, 4.6, for varying number of nodal points N. A non-uniform spatial mesh was used, with meshing density increased near the ends of the interval (the same type of mesh was used for all n). The measures $\delta\hat{w}$, $\delta\hat{v}$, describing the average relative error of the crack opening and particle velocity, are taken to be:

$$\delta\hat{w}(N) = \frac{\int_0^1 \tilde{r}\,|\hat{w}^*(\tilde{r}) - \hat{w}(\tilde{r})|\,d\tilde{r}}{\int_0^1 \tilde{r}\hat{w}^*(\tilde{r})\,d\tilde{r}}, \quad \delta\hat{v}(N) = \frac{\int_0^1 \tilde{r}\,|\hat{v}^*(\tilde{r}) - \hat{v}(\tilde{r})|\,d\tilde{r}}{\int_0^1 \tilde{r}\hat{v}^*(\tilde{r}),d\tilde{r}}, \tag{4.109}$$

where $\hat{w}^*$ and $\hat{v}^*$ denote the exact solutions for $\hat{w}$ and $\hat{v}$.

The results clearly show that the value of both error measures decreases monotonically with growing N. For a fixed number of nodal points N, $\delta\hat{w}$ is lower than $\delta\hat{v}$, but within

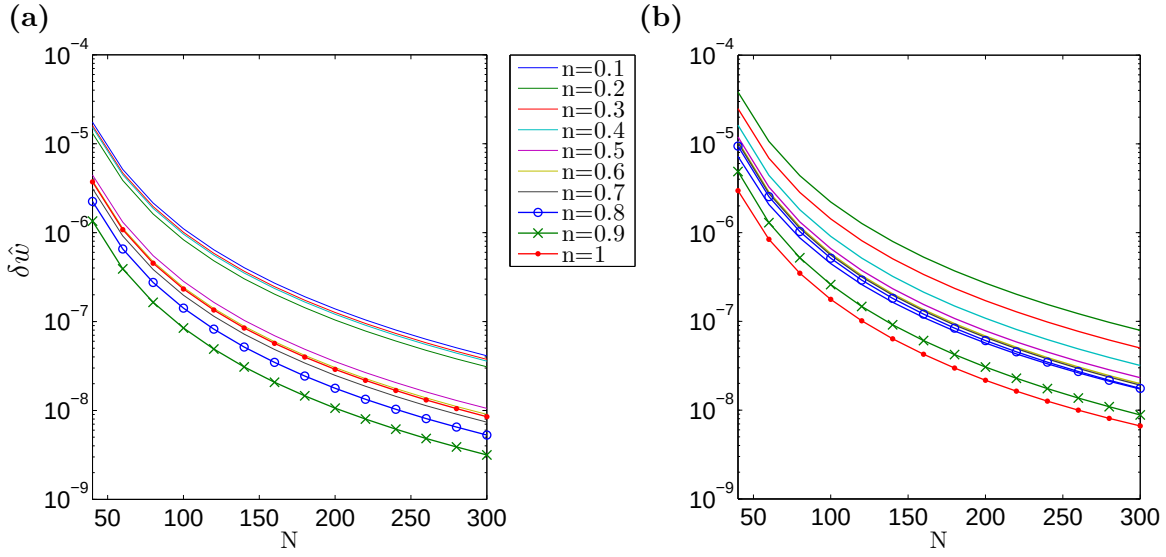

FIGURE 4.5: Relative average error of the crack aperture $(4.109)_1$ obtained against the analytical benchmark over N for the (a) viscosity dominated regime, (b) toughness dominated regime.

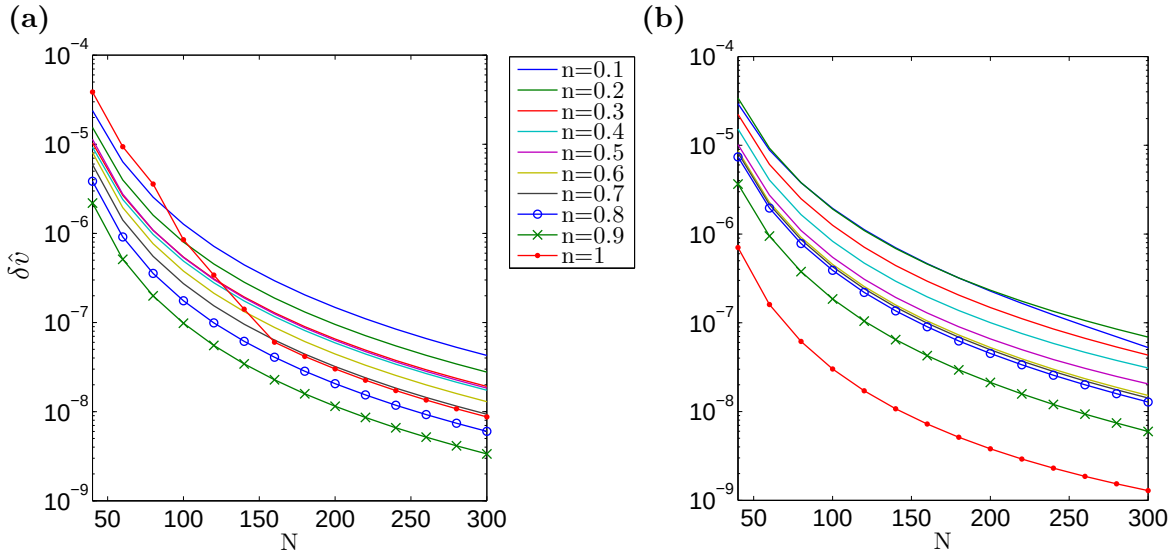

FIGURE 4.6: Relative average error of the particle velocity $(4.109)_2$ obtained against the analytical benchmark over N for the (a) viscosity dominated regime, (b) toughness dominated regime.

the same order of magnitude. One can observe a sensitivity of the results to the value of the fluid behaviour index n. Here, the level of error measures can vary up to one order for a constant N. This trend can be alleviated by adjusting the mesh density distribution to the value of n (i.e. to the varying asymptotics of solution), however, given that the level of accuracy already achieved is far greater than that required in practical application, this will not be conducted here. In general, it takes fewer than $N = 300$ nodal points to achieve the relative errors of the level 10^{-7}.

We note that the algorithm computes in under 30 seconds, even when taking $N = 300$ boundary nodes, regardless of the material toughness or fluid rheology being simulated. A more detailed examination of the relationship between the number of boundary nodes and computation times is provided in Sect. 4.3.5.5.

In cases when the exact solution is not prescribed an alternative method of testing the solution accuracy is required. The method outlined here relies on the fact that the solution converges to the exact value at a known rate, with respect to the number of nodal points, which has been established numerically to behave as $1/N^3$. As a result the following estimation holds:

$$\int_0^1 r g_i(r) dr = A_i + \frac{B_i}{N^3}, \quad i = 1, 2, \tag{4.110}$$

where $g_1(r) = \hat{w}(r)$ and $g_2(r) = \hat{v}(r)$. A_i and B_i are constants which can easily be obtained using a least-squares approximation over various N. Next, one can define the

limiting value of (4.110) as:

$$\lim_{N\to\infty} \int_0^1 r g_i(r) dr = A_i \approx \int_0^1 r g_i^*(r) dr, \quad i = 1, 2, \tag{4.111}$$

where $g_1^*(r) = \hat{w}^*(r)$, $g_2^*(r) = \hat{v}^*(r)$ represent the exact (potentially unknown) solution.

Knowing this, the following alternative error measures can be proposed:

$$e_{g_i}(N) = \frac{\left| A_i - \int_0^1 r \hat{g}_i^*(r)\, dr \right|}{\int_0^1 r \hat{g}_i^*(r)\, dr}, \quad i = 1, 2. \tag{4.112}$$

Using this strategy, it is possible to identify the relative rate at which the solution converges: $e_w(N)$ for the aperture and $e_v(N)$ for the particle velocity. The results are shown in Fig. 4.7, Fig. 4.8. It is notable that both $\delta\hat{w}$ and e_w, as well as $\delta\hat{v}$ and e_v, provide estimates of a similar order for a fixed N. Thus, they can be considered as equivalent error measures and employed in the accuracy analysis in the cases when no exact solution is available. As such, $e_w(N)$ and $e_v(N)$ will be used in the following investigations.

It should be stated that the value of constants A_i and B_i, defining the limiting value of the intregral as the number of boundary nodes tends to infinity, are obtained using a least-squares approximation. Given this, if the integral does not converge to its limiting value as an asymptote (i.e. convergence is uniformly from above, or uniformly from below), then the limiting value obtained will still be obtained accurately enough to provide a measure of the solution error, but the relative rate of convergence to this value may not appear uniform (e.g. the non-monotonic convergene seen in Fig. 4.11a). As such, the measure provides the order of the computation error, but should be interpreted as an estimate rather than an exact value.

4.2.5.4 Impermeable solid - reference solutions

With a suitable measure for testing the solution accuracy in place we move onto examining the solution variant most frequently studied in the literature, the case with a zero valued leak-off function and with $\hat{Q}_0 = 1$. Although there is no analytical solution to this variant of the problem, due to its relative simplicity, it is commonly used when testing numerical algorithms. For this reason it is very important that credible reference data is provided for this case, which can be easily employed to verify various computational schemes. Both the viscosity and toughness dominated regimes (for different values of the material toughness: $\hat{K}_{Ic} = \{1, 10, 100\}$) will be investigated. In the next

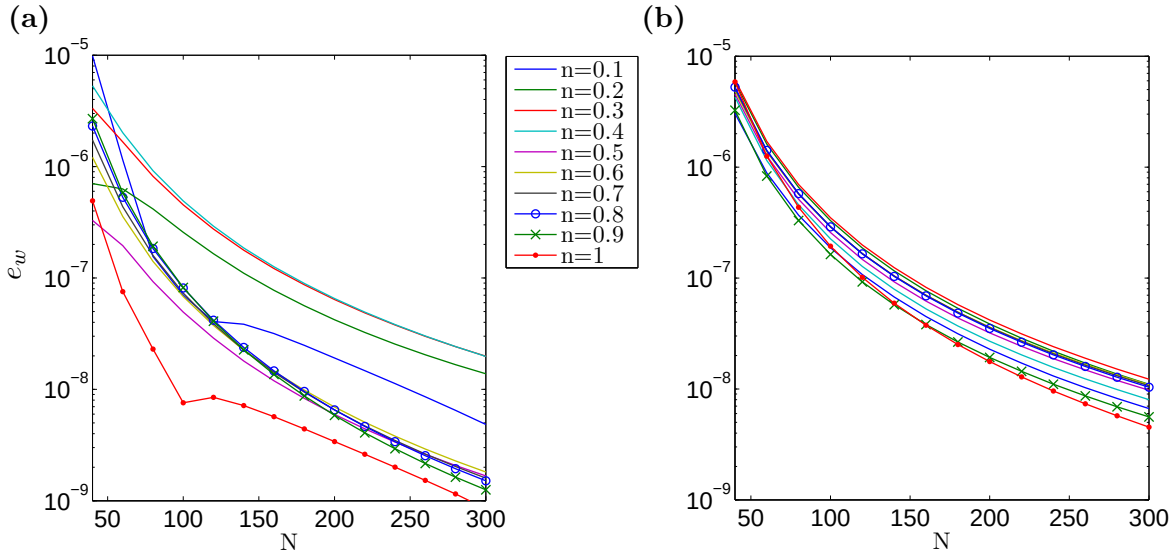

FIGURE 4.7: Rate of convergence e_w (4.112) of the numerical solution for the benchmark example: (a) viscosity dominated regime, (b) toughness dominated regime.

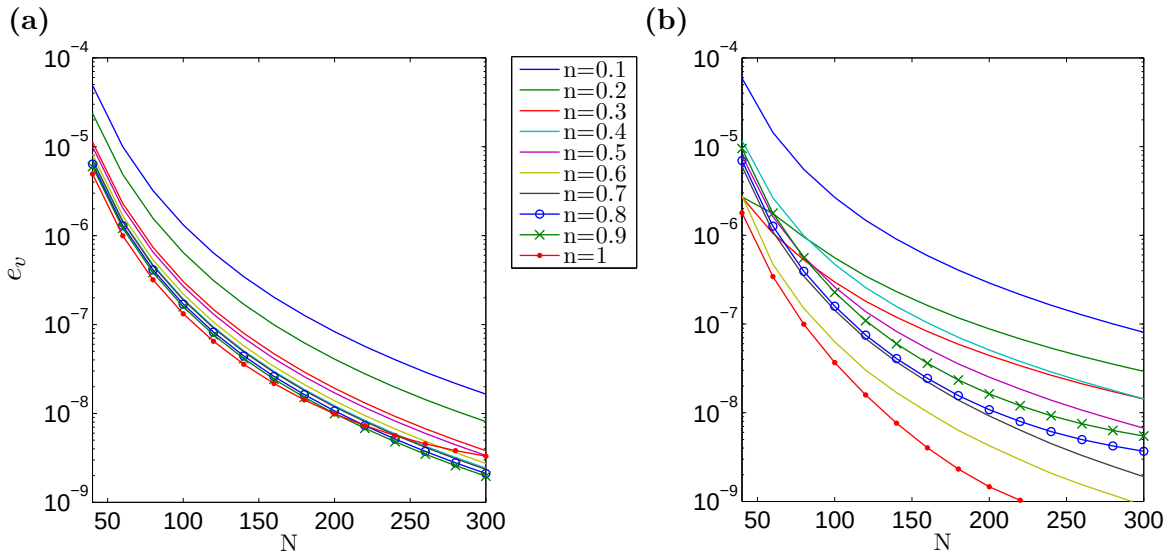

FIGURE 4.8: Rate of convergence e_v (4.112) of the numerical solution for the benchmark example: (a) viscosity dominated regime, (b) toughness dominated regime.

subsection, accurate and simple approximations of the obtained numerical solutions will be provided.

The results for the crack opening and particle velocity convergence rates are shown in Figs. 4.9 - 4.12.

As can be seen, over the analyzed range of N, the computations are very accurate and converge rapidly as the mesh density is increased. It is readily apparent from the above that the computational error of the solver is below 10^{-7} for all values of the material toughness and fluid index when taking $N = 300$ boundary nodes. This is clearly a

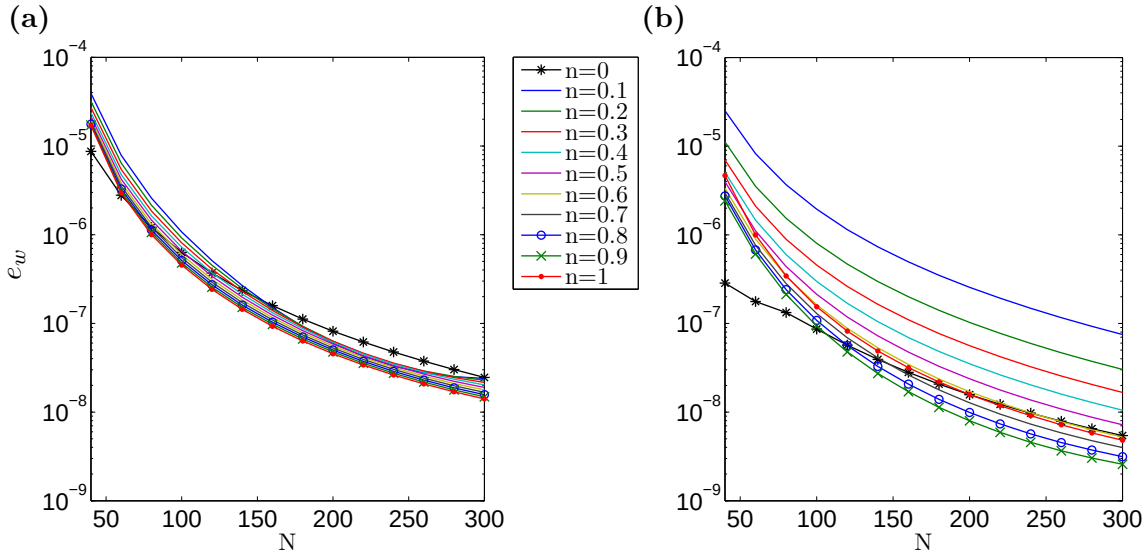

FIGURE 4.9: Rate of convergence e_w (4.112) of the numerical solution when $Q_0 = 1$ with no fluid leak-off for the: (a) viscosity dominated regime, (b) toughness dominated regime with $\hat{K}_{Ic} = 1$.

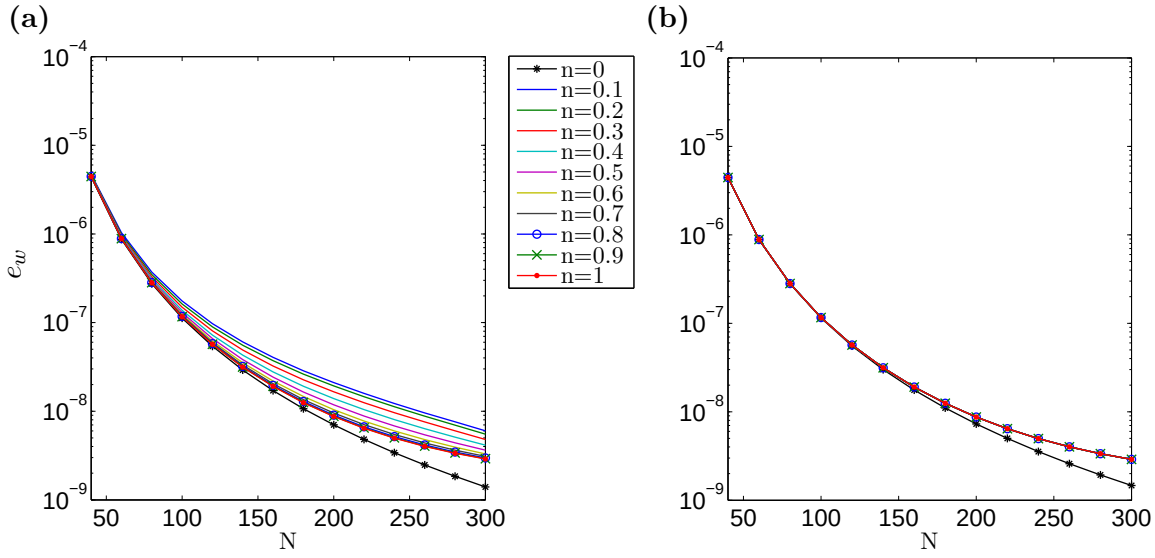

FIGURE 4.10: Rate of convergence e_w (4.112) of the numerical solution when $Q_0 = 1$ with no fluid leak-off for the toughness dominated regime with: (a) $\hat{K}_{Ic} = 10$ and (b) $\hat{K}_{Ic} = 100$.

sufficient level of accuracy, and larger numbers of nodes are not be examined here, while $N = 300$ will be taken in subsequent sections when investigating solution behaviour.

In the viscosity dominated regime it can be seen that there is a lower sensitivity of e_w and e_v to the value of n, however even in the toughness dominated mode the dependence of e_w on the fluid behaviour index becomes less pronounced as $\hat{K}_{Ic}$ grows. A general trend can be observed, in that the convergence rate is magnified as the self-similar material toughness $\hat{K}_{Ic}$ increases. This is due to the fact that, for large values of $\hat{K}_{Ic}$, the solution tends to the limiting case of a uniformly pressurized immobile crack with a parabolic

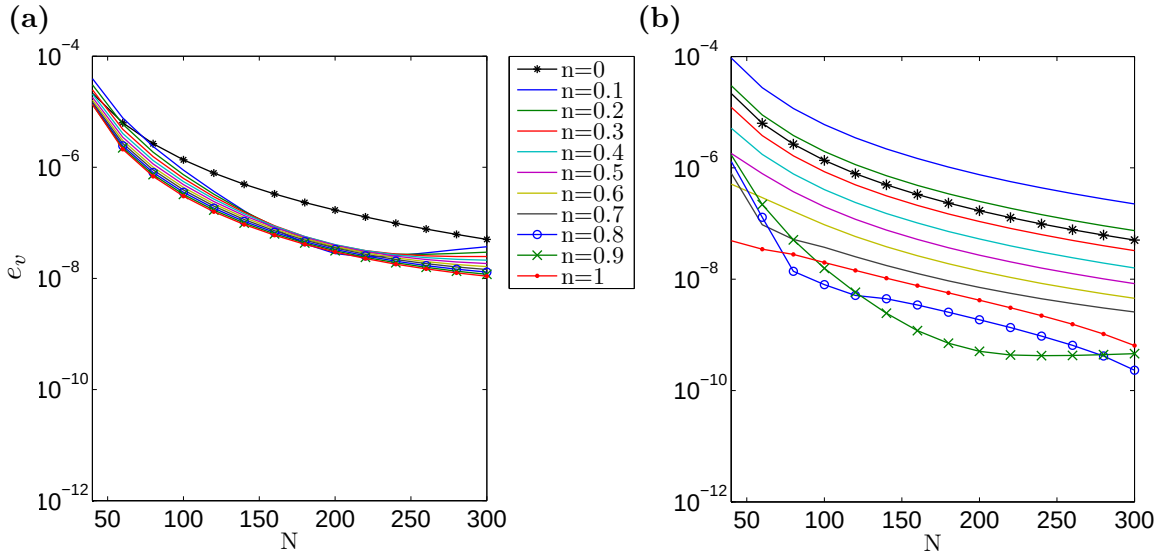

FIGURE 4.11: Rate of convergence e_v (4.112) of the numerical solution when $Q_0 = 1$ with no fluid leak-off for the: (a) viscosity dominated regime, (b) toughness dominated regime with $\hat{K}_{Ic} = 1$.

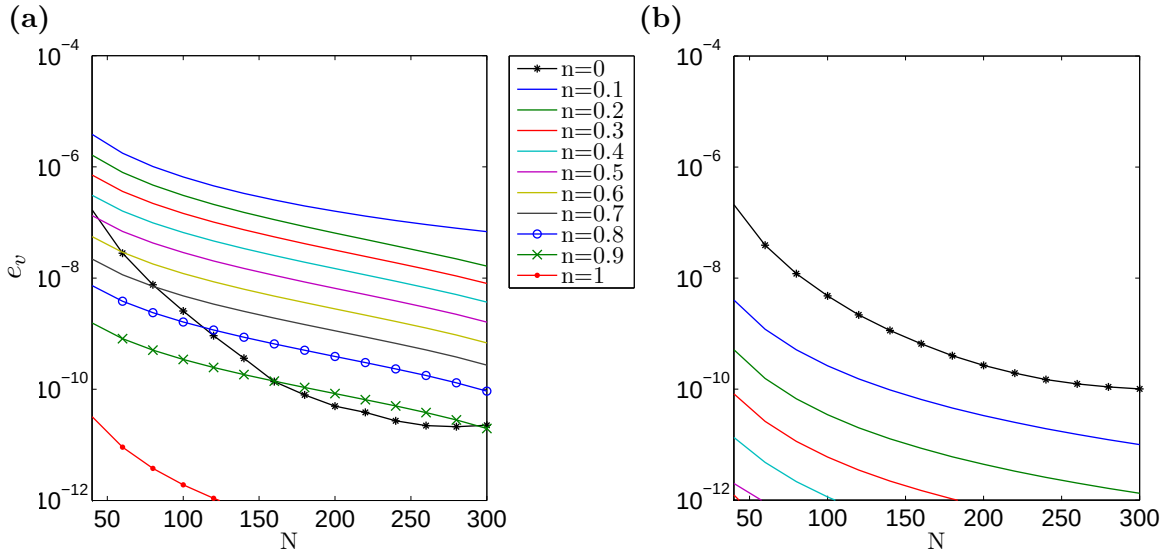

FIGURE 4.12: Rate of convergence e_v (4.112) of the numerical solution when $Q_0 = 1$ with no fluid leak-off for the toughness dominated regime with: (a) $\hat{K}_{Ic} = 10$ and (b) $\hat{K}_{Ic} = 100$.

profile. To explain this tendency we present in Figs. 4.13-4.16 some additional data for a single value of the fluid behavior index ($n = 0.5$).

It is immediately obvious that for $\hat{K}_{Ic} > 2$ the fracture aperture is almost entirely described by the leading term of its crack tip asymptotics (for $\hat{K}_{Ic} = 2$ the maximal deviation between them is approximately 1 percent). For the particle velocity it can be seen that, while the effect is not as substantial as for the aperture, the crack propagation speed $\hat{v}_0$ does become a better predictor of the parameter's behaviour for larger values of the material toughness. Meanwhile, the fluid pressure increases with growing $\hat{K}_{Ic}$,

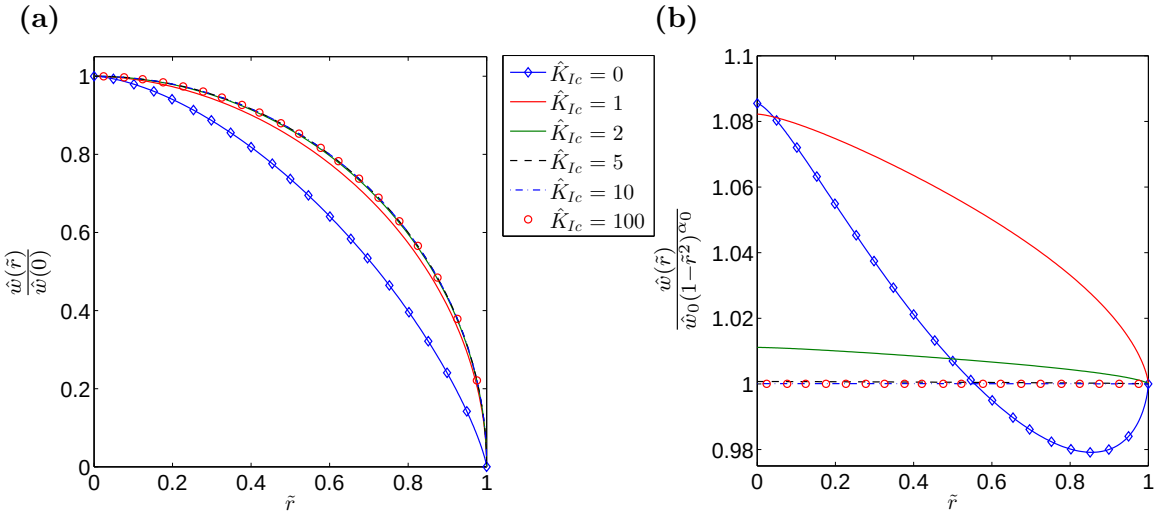

FIGURE 4.13: The aperture for $n = 0.5$ for different values of the fracture toughness: (a) the normalized self-similar aperture, (b) the self-similar aperture divided by the leading term of the crack tip asymptotics (4.73).

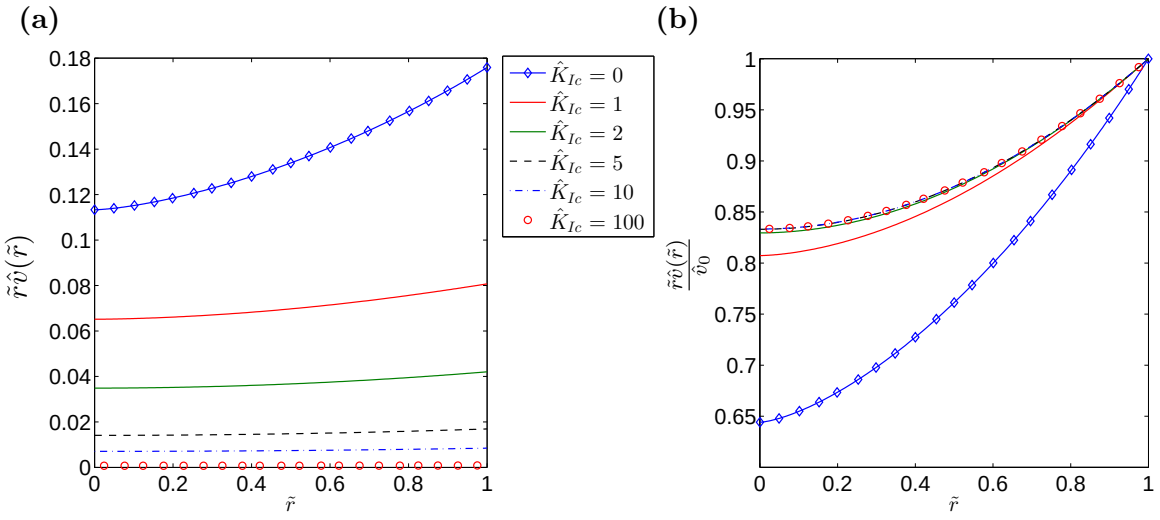

FIGURE 4.14: The particle velocity for $n = 0.5$ for different values of the fracture toughness: (a) the self-similar particle velocity, (b) the self-similar particle velocity divided by the leading term of the crack tip asymptotics (4.75).

eventually becoming uniformly distributed over $\tilde{r}$. As a result of the decreasing pressure gradient the velocity of the fluid flow is reduced. In Fig. 4.16 it can be seen that the fluid flow rate rapidly converges to the limiting case with growing $\hat{K}_{Ic}$, however the rate of convergence is greater for larger values of n. Indeed, as can be seen in Fig. 4.17, for $n = 1$ the curves for $\hat{K}_{Ic} = 1$ and $\hat{K}_{Ic} = 100$ are indistinguishable, which is not the case when $n = 0$.

In fact, the behaviour of the solution as $\hat{K}_{Ic} \to \infty$ can easily be shown to take the form:

$$\hat{w}(\tilde{r}) \sim \frac{4}{\sqrt{\pi}} \hat{K}_I \sqrt{1 - \tilde{r}^2}, \quad \hat{p}(\tilde{r}) \sim \frac{\sqrt{\pi}}{2} \hat{K}_I, \quad \hat{v}_0 \sim \frac{3}{8\sqrt{\pi} \hat{K}_I (3 - s_n)}, \tag{4.113}$$

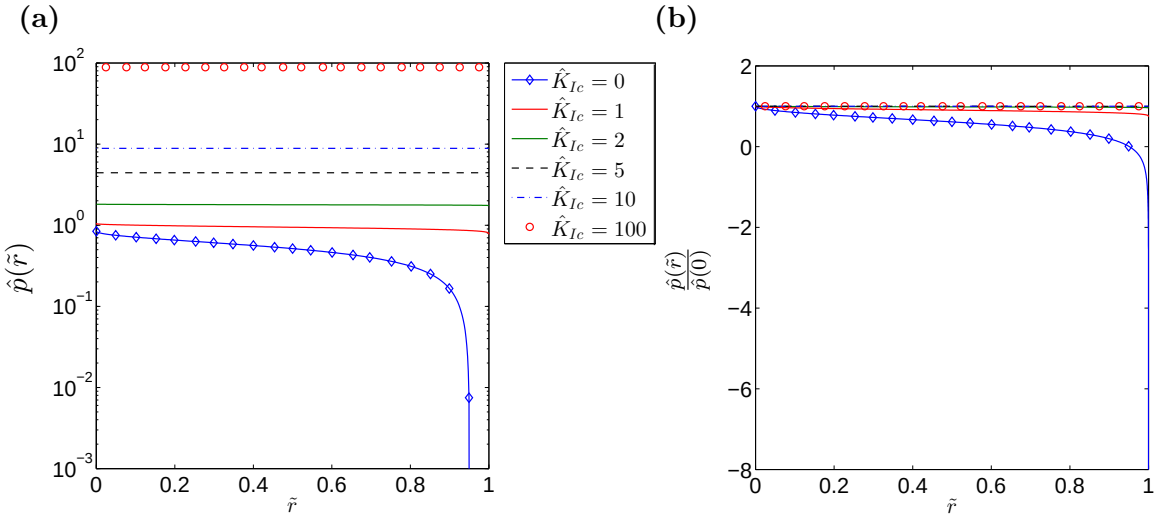

FIGURE 4.15: The pressure function for $n = 0.5$ for different values of the fracture toughness: (a) the self-similar pressure function, (b) the self-similar pressure divided by the value of the pressure at the fracture opening.

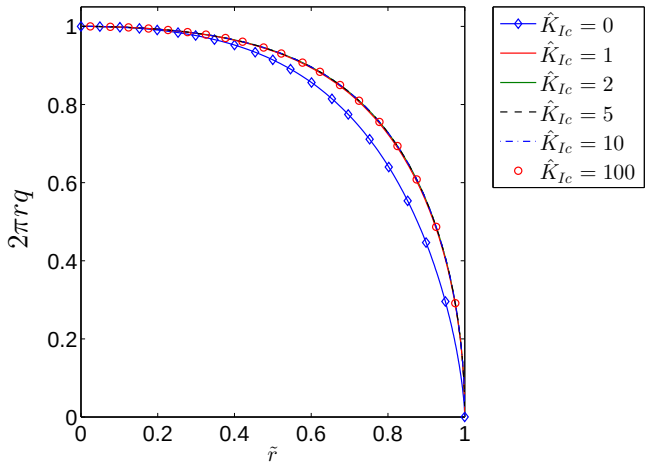

FIGURE 4.16: The self-similar fluid flow rate for $n = 0.5$ for different values of the fracture toughness.

$$\tilde{r}\hat{v}(\tilde{r}) = \hat{v}_0 \left[\tilde{r}^2 + \frac{3 - s_n}{3}\left(1 - \tilde{r}^2\right)\right] + O\left(\hat{K}_{Ic}^{-1}\right), \tag{4.114}$$

$$\tilde{r}\hat{q}(\tilde{r}) = \frac{\sqrt{1 - \tilde{r}^2}}{2\pi}\left[\frac{3\tilde{r}^2}{3 - s_n} + \left(1 - \tilde{r}^2\right)\right] + O\left(\hat{K}_{Ic}^{-1}\right), \tag{4.115}$$

where s_n is defined in Table 4.2. As a result the computations become far more efficient in this case and the resulting solution is calculated to a far higher level of accuracy.

Combining the results shown above in Figs. 4.5 - 4.12, it is clear that the computations presented here achieve a very high level of accuracy for both the aperture and particle velocity regardless of the crack propagation regime. When using $N = 300$ the accuracy of computations can almost always be assumed to be correct to a level of at least 10^{-7} for the fracture aperture, and 2.5×10^{-7} for the particle velocity. In this way the obtained

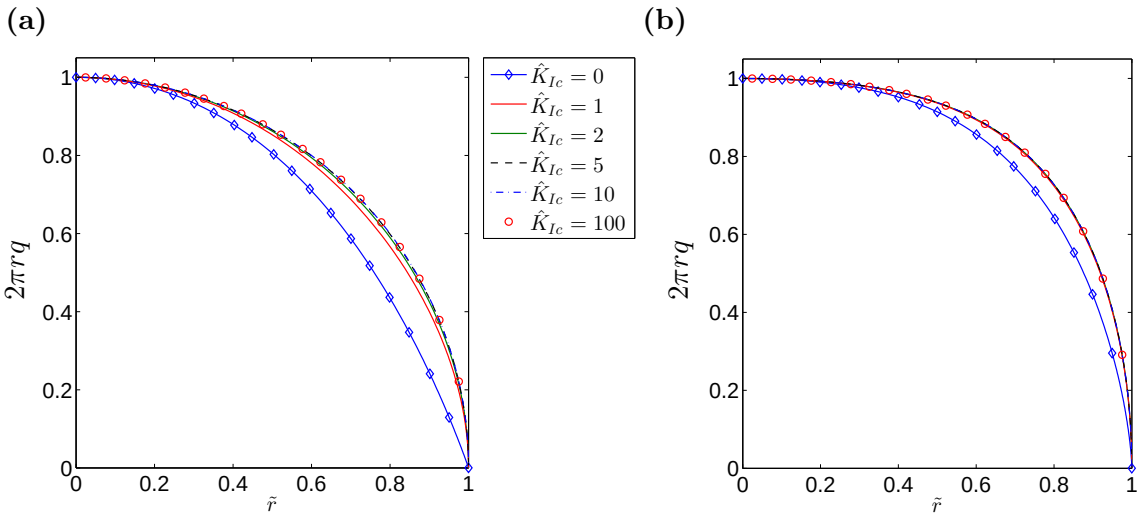

FIGURE 4.17: The self-similar fluid flow rate for different values of the fracture toughness when the fluid behaviour index is: (a) n=0 and (b) n=1.

data constitutes a very convenient and credible reference solution when testing other computational schemes.

It is worth mentioning that the efficiency of computations achieved by this algorithm means that this high level of accuracy does not come at the expense of simulation time. The final algorithm requires fewer than 20 iterations to produce a solution. Simulation times are also very short with this scheme, a more detailed analysis of which will be provided in Sect. 4.3.5.5.

4.2.5.5 Verification of other results from the literature

In the following, using our highly accurate numerical scheme, we will verify the results provided so far by other authors. Unfortunately, there are only a handful of papers where respective data is provided in a form which enables comparison. In most cases only graphs of the dependent variables are given. In order to make sure that the data is comparable the zero leak-off case will again be examined, taking fixed $\hat{Q}_0 = 1$, with transformations between the schemes outlined as necessary. Throughout this subsection we will use $N = 300$ nodal points, which in previous subsections we have shown is accurate to 7 significant digits.

We begin by analyzing the solution delivered by *Linkov* in [132] for the viscosity dominated regime ($\hat{K}_{Ic} = 0$). Note that, as slightly different normalizations are used to obtain the self-similar solution, the following transformations are required to obtain a comparison between the results:

$$\hat{w}(\tilde{r}) = \zeta^{\frac{n}{n+2}} \hat{w}^L(\tilde{r}), \quad \hat{p}(\tilde{r}) = \zeta^{\frac{n}{n+2}} \hat{p}^L(\tilde{r}),$$

$$\hat{v}(\tilde{r}) = \zeta \hat{v}^L(\tilde{r}), \quad \hat{Q}_0 = \frac{1}{\xi_{*,n}^3} \zeta^{\frac{2\left(n^2+2\right)}{n+2}} \hat{Q}_0^L, \tag{4.116}$$

$$\hat{q}_l(\tilde{r}) = \zeta^{\frac{n}{n+2}} \hat{q}_l^L(\tilde{r}), \quad \xi_{*,n} = \left(2\pi \int_0^1 \varsigma \hat{w}^L(\varsigma)\, d\varsigma\right)^{-\frac{1}{3}},$$

where:

$$\zeta = \frac{3\hat{v}_0\,(n+2)}{2n+2}. \tag{4.117}$$

Here $\xi_{*,n}$ is *Linkov's* normalized fracture length when $Q_0 = 1$. It can easily be shown using the equation for fracture length from Table 4.2 that, in order for the two formulations to coincide, the following scaling condition must be met:

$$\xi_{*,n} = \zeta^{\frac{2(n+1)}{3(n+2)}}. \tag{4.118}$$

The values of the self-similar fracture opening, crack propagation speed and fracture half-length are shown in Table 4.3. The results obtained in [132] are included for completeness, and denoted with a superscript L. The notation $\hat{w}^T(0)$ represents the transformed crack opening computed according to $(4.116)_1$ (this value is to be compared with $\hat{w}^L(0)$).

n	$\hat{v}_0$	$\hat{w}(0)$	$\hat{w}^T(0)$	$\xi_{*,n}$	$\hat{w}^L(0)$	$\xi_{*,n}^L$
0	0.1314342	1.688787	1.688787	0.7332914	1.6889	0.7330
0.1	0.1427914	1.602559	1.672277	0.7317711	1.6724	0.7318
0.2	0.1527660	1.535686	1.661661	0.7295243	1.6617	0.7296
0.3	0.1615208	1.482567	1.655773	0.7267291		
0.4	0.1691971	1.439637	1.653833	0.7235073	1.6537	0.7236
0.5	0.1759138	1.404539	1.655334	0.7199395		
0.6	0.1817680	1.375680	1.659981	0.7160755	1.6599	0.7162
0.7	0.1868366	1.351968	1.667648	0.7119399		
0.8	0.1911776	1.332662	1.678369	0.7075363	1.6784	0.7076
0.9	0.1948308	1.317280	1.692338	0.7028480		
1	0.1978175	1.305555	1.709934	0.6978375	1.7092	0.6978

TABLE 4.3: The values of fracture opening, crack propagation speed and half-length, given to an accuracy of seven significant figures (which defines the solution accuracy achievable for $N = 300$ using the authors' solver). The final two columns, denoted with superscript L, show the values provided in [132]. The symbols $\hat{w}^T$ and $\xi_{*,n}$ stand for the transformed fracture opening and fracture half-length computed according to (4.116). These values are to be compared with the last two columns.

It can easily be seen that there is a high level of correspondence between the results in this paper and those provided by *Linkov* for different values of the fluid behaviour index n. The maximum relative discrepancy is of the order 4.3×10^{-4}, which considering the accuracy of our solution demonstrated in Sect. 4.2.5.3, describes the level of accuracy

achieved by the solution from [132]. We note that, in our approach, it is sufficient to take merely $N = 40$ points to have a similar accuracy (see Figs. 4.5-4.10).

Another solution to be analyzed is that from *Savitski/Detournay* [196], which provides asymptotic approximations for both the viscosity and toughness dominated regimes in the case of a Newtonian fracturing fluid. The interrelations between the self-similar crack opening and crack propagation speed given in [196] and our results are as follows:

$$\bar{\Omega}_{m,0}(\tilde{r}) = \left[\frac{4}{9\hat{v}_0}\right]^{\frac{1}{3}} \hat{w}(\tilde{r}), \quad V(\tilde{r}) = \frac{4}{9\hat{v}_0}\hat{v}(\tilde{r}). \tag{4.119}$$

Savitski/Detournay specify the following asymptotic approximation for the self-similar aperture:

$$\bar{\Omega}_{m,0}(\tilde{r}) = 2^{\frac{1}{3}} \times 3^{\frac{1}{6}} \left(1-\tilde{r}^2\right)^{\frac{2}{3}} + O\left(\left(1-\tilde{r}^2\right)^{\frac{5}{3}}\right), \quad \tilde{r} \to 1. \tag{4.120}$$

Using the relevant transformations yields:

$$\hat{w}(\tilde{r}) = 2^{\frac{1}{3}} \times 3^{\frac{1}{6}} \left[\frac{9\hat{v}_0}{4}\right]^{\frac{1}{3}} \left(1-\tilde{r}^2\right)^{\frac{2}{3}} + O\left(\left(1-\tilde{r}^2\right)^{\frac{5}{3}}\right), \quad \tilde{r} \to 1. \tag{4.121}$$

Note that interrelation between $\hat{w}_0$ and $\hat{v}_0$ resulting from (4.121) is exactly the same as the one defined by equations (4.76)-(4.77) based on the speed equation. Thus, any solution in the viscosity dominated regime (for $n = 1$) preserving the latter will be equivalent in terms of $\hat{w}_0$ and $\hat{v}_0$ to the data provided in [196].

For the toughness dominated regime it is unfortunately not possible to perform the same comparison as above with the results from [196]. This is due to the fact that *Savitski & Detournay's* solution is only self-similar in the limiting cases $K_I = \{0, \infty\}$, and is a time dependent function of $K_I(t)$ in the interim. It is however possible to check the ratio between the fracture pressure and aperture with the following equality:

$$\frac{\hat{w}(\tilde{r})}{\hat{p}(\tilde{r})} = \frac{\Omega_k(\tilde{r})}{\gamma_0 \Pi_k(\tilde{r})}, \tag{4.122}$$

where Ω_k is *Savitski & Detournay's* normalized aperture, Π_k is the normalized pressure and $\gamma_0 = \left(3/\pi\sqrt{2}\right)^{\frac{2}{5}}$ is the first term of the normalized asymptotic expansion of the fracture length [196]. Noting that the paper gives the limiting values for $K_{Ic} \to \infty$ as being $\Omega_{k,0} = (3/8\pi)^{\frac{1}{5}} \sqrt{1-\tilde{r}^2}$ and $\Pi_{k,0} = \pi\,(\pi/12)^{\frac{1}{5}}/8$, it can easily be seen from (4.113) that ratio (4.122) is satisfied in the limit. As such, we can evaluate the validity of the asymptotic fromulae from [196] by examining the relative ratio between the two sides of (4.122), which we will label δS, and define as follows:

$$S = \frac{\Omega_k(\tilde{r})}{\gamma_0 \Pi_k(\tilde{r})}, \quad S^* = \frac{\hat{w}(\tilde{r})}{\hat{p}(\tilde{r})}, \quad \delta S = \frac{|S - S^*|}{|S^*|}. \tag{4.123}$$

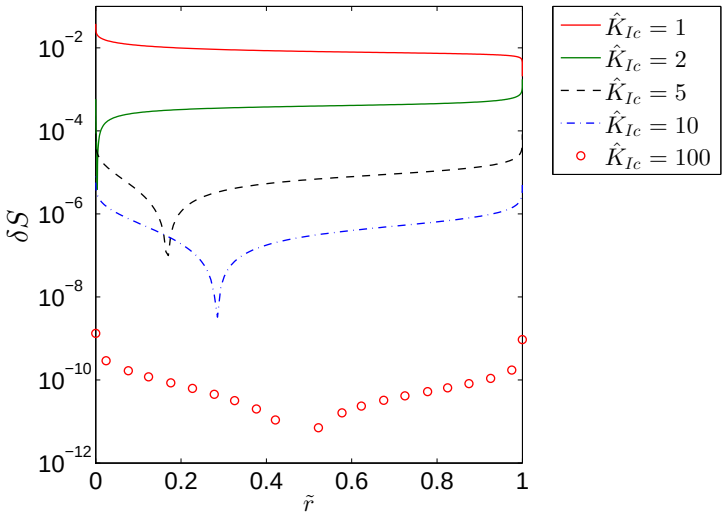

FIGURE 4.18: Comparison of the ratio between the fracture aperture and pressure for *Savitski & Detournay's* solution and that presented in this paper for a few values of the fracture toughness. Here δS shows the relative error.

In this way, the rate at which $\delta S \to 0$ as $\hat{K}_{Ic} \to \infty$ will determine the domain over which the asympotic limit given in [196] (for infinite toughness) provides an accurate approximation for the key system parameters. The results for this metric, pertaining to the values $\hat{K}_I = \{1, 2, 5, 10, 100\}$, are provided in Fig. 4.18.

It is evident from this comparison that there is a clear correspondence between the results of this paper and those obtained by *Savitski/Detournay*. The disparity between respective data in the large toughness case, $\hat{K}_{Ic} = 100$, is compatible with the error of our solution demonstrated for this model in Fig. 4.10. This is a strong verification of the validity of the asymptotic formulae from [196]. However, the accuracy of those approximations diminishes greatly for lower values of the fracture toughness, with an error of order 10^{-1} when $\hat{K}_I = 1$. This, in turn, provides us with an estimate of when the formula in [196] loses its practical applicability.

4.2.6 Summary of results for the classical model

In this section, the stated aim was to construct a high accuracy numerical solver for a penny-shaped hydraulic fracture containing a fluid described by a power-law. It is clear that this has now been achieved. The accuracy of the final algorithm was demonstrated both against specially constructed analytical benchmarks, as well as through alternative measures which utilized the solutions known rate of convergence as the number of nodes increased. This model has been used to provide benchmark solutions for the particle velocity and fracture opening, as well as to verify other results available in the literature.

It should also be stated here that high accuracy numerical approximations of the solutions obtained by this algorithm, in the case of an impermeable solid, have been created. These simple formulae, which capture the behaviour of the benchmark solutions, make it far easier for others to perform comparisons, which is particularly useful when examining more advanced algorithms. A full description of these semi-analytical solutions is provided in the published paper[1].

As a result, we can confidently state that incorporating the *speed equation* into computations involving the penny-shaped model provides clear advantages, in both the viscosity and toughness dominated regimes. By incorporating aspects of the universal algorithm, originally proposed in [165, 229], it is possible to develop a highly efficient algorithm for studying the penny-shaped model of hydraulic fracture.

4.3 Radial model with tangential stress

4.3.1 Introduction and motivation

In the previous study of the classical penny-shaped model, a scheme was developed for the case of a toughness dominated fracture. With this framework in place, it is possible to incorporate the recent results of *Wrobel, Mishuris & Piccolroaz* [230], which are briefly outlined in Sect. 2.3.3. Here it was demonstrated that the tangential stress induced by the fluid on the fracture walls was not negligible as previously assumed, and that the standard assumption used in the classical model, stated in (4.49), is not valid.

Taking the tangential stress into account, *Wrobel, Mishuris & Piccolroaz* managed to obtain a new fracture criterion from an examination of the energy release rate at the fracture tip. It was demonstrated that the fracture will always have the asymptotic representation traditionally reserved for the toughness dominated regime (even when $K_{Ic} = 0$).

In the original paper however, this new formulation was only provided in the KGD case. In order to remedy this, here we provide an initial examination of the radial model when tangential stresses are included. This will primarily consist of including the new fracture criterion, stated in (2.45), into the model. Alongside this, in order to remain consistent with the approach of the original authors, new normalization and self-similar schemes will be utilized.

[1] These approximations were constructed by coauthor *M. Perkowska*, and as such are not included here.

One caveat is that, given this is only a preliminary investigation, we will not incorporate the updated elasticity equation into the model. This is because, while the shear-stress plays a significant qualitative role on the behaviour at the fracture tip, it is almost negligible throughout the rest of the domain (in comparison with other evaluated terms). Given the non-local nature of the elasticity operator and its inverse, the addition of this term will not have a significant quantitative effect on the final system, and will likely be overshadowed by the errors introduced into the solution by its inclusion. The negligible nature of incorporating this term into the elasticity equation was demonstrated numerically in the original investigation of the KGD case by *Wrobel, Mishuris & Piccolroaz* [230]. The form of the elasticity equation in this case is however provided in Appendix. E.

The structure of this section is as follows. In Sect. 4.3.2 the system of equations describing a radial hydraulic fracture driven by a Newtonian fluid is outlined, alongside the asymptotics describing key parameters at the crack tip, and the new fracture criterion and shear stress intensity factor are introduced. With the full mathematical description of the problem thus provided, an appropriate normalization scheme is introduced in Sect. 4.3.3. The self-similar form of the problem, with the time component defined by an exponential function, is given in Sect. 4.3.4. With the problem fully described, in Sect. 4.3.5 the computational scheme for obtaining results is outlined, and its accuracy demonstrated. An examination of the behaviour of key parameters is given in the case of an impermeable solid. This is followed by a comparison of the updated scheme with that developed previously for the classical formulation, both in terms of the solution behaviour, as well as the efficiency of computations. Finally, a summary of the results is given in Sect. 4.3.6

4.3.2 Problem formulation

We consider a 3D penny-shaped crack, defined in polar coordinates by the system $\{r, \theta, z\}$, with associated crack dimensions $\{l(t), w(t)\}$ denoting the fracture radius and aperture respectively. As the flow is axisymmetric, all variables will be independent of the angle θ. Here we only consider the case when the fracture is driven by a Newtonian fluid. As a result, many of the equations will be identical to those provided in Sect. 4.2.2, setting the fluid index $n = 1$. They are repeated here for the sake of completeness.

The fluid mass balance equation is as follows:

$$\frac{\partial w}{\partial t} + \frac{1}{r}\frac{\partial}{\partial r}\left(rq\right) + q_l = 0, \quad 0 < r < l(t). \tag{4.124}$$

where $q_l(r,t)$ is the fluid leak-off function, representing the volumetric fluid loss to the rock formation in the direction perpendicular to the crack surface per unit length of the fracture. Throughout this paper we will assume it to be predefined and bounded at the fracture tip.

Meanwhile $q(r,t)$ is the fluid flow rate inside the crack, given by the Poiseuille law:

$$q = -\frac{w^3}{M}\frac{\partial p}{\partial r}, \tag{4.125}$$

where the constant $M = 12\mu$ is the fluid consistency index. The elasticity relation defining the deformation of the rock, without shear-stress terms, is given by:

$$p(r,t) = -\frac{k_2}{l(t)}\int_0^1 \frac{\partial w(\eta l(t))}{\partial \eta}\mathcal{M}\left(\frac{r}{l(t)},\eta\right)\,d\eta, \quad 0 \le r < l(t), \tag{4.126}$$

with its inverse:

$$w(r,t) = \frac{8(1-\nu^2)}{\pi E}l(t)\int_{r/l(t)}^1 \frac{\xi}{\sqrt{\xi^2-(r/l(t))^2}}\int_0^1 \frac{\eta p(\eta\xi l(t),t)}{\sqrt{1-\eta^2}}\,d\eta d\xi, \tag{4.127}$$

where:

$$k_2 = \frac{E}{2\pi(1-\nu^2)}. \tag{4.128}$$

These equations are supplemented by the boundary condition at $r = 0$, which defines the intensity of the fluid source, Q_0:

$$\lim_{r\to 0} rq(r,t) = \frac{Q_0(t)}{2\pi}, \tag{4.129}$$

alongside the tip boundary conditions:

$$w(l(t),t) = 0, \quad q(l(t),t) = 0. \tag{4.130}$$

We assume that there is a preexisting fracture, starting with appropriate non-zero initial conditions for the crack opening and length:

$$w(r,0) = w_*(r), \quad l(0) = l_0, \tag{4.131}$$

Finally the global balance equation takes the form:

$$\int_0^{l(t)} r\left[w(r,t) - w_*(r)\right]\,dr + \int_0^t\int_0^{l(t)} rq_l(r,\tau)\,dr\,d\tau = \frac{1}{2\pi}\int_0^t Q_0(\tau)\,d\tau. \tag{4.132}$$

In addition to the above, we employ a new dependent variable named the particle velocity, v, defined by:

$$v(r,t) = \frac{q(r,t)}{w(r,t)} = -\frac{w^2(r,t)}{M}\frac{\partial p}{\partial r}, \tag{4.133}$$

It has the useful property that, provided the fluid leak-off q_l is finite at the crack tip:

$$\lim_{r \to l(t)} v(r,t) = v_0(t) < \infty, \tag{4.134}$$

which, given that the fracture apex coincides with the fluid front (no lag), allows for fracture front tracing through the so-called speed equation [127]:

$$\frac{dl}{dt} = v_0(t). \tag{4.135}$$

This Stefan-type condition has previously been employed in 1D hydraulic fracture models, the advantages of which (alongside technical details) are shown in [118, 165, 228–230].

4.3.2.1 Crack tip asymptotics

In the classic radial model the basic modes of fracture propagation can be related to the material toughness, with $K_{Ic} = 0$ indicating the viscosity dominated regime, while $K_{Ic} > 0$ defines the toughness dominated regime. These two modes have been extensively studied, and have qualitatively different asymptotic behaviour, leading to a singular perturbation problem when transitioning between the cases. In the revised HF formulation however this problem is eliminated, as the introduction of shear stress induced by the fluid ensures that the tip asymptotics remain the same irrespective of the value of K_{Ic}.

The revised crack tip asymptotics are as follows [230]:

$$w(r,t) = w_0(t)\sqrt{1-R^2} + w_1(t)\left(1-R^2\right) + w_2(t)\left(1-R^2\right)^{\frac{3}{2}}\log\left(1-R^2\right) + \ldots, \quad R = \frac{r}{l(t)} \to 1, \tag{4.136}$$

$$p(r,t) = p_0(t)\log\left(1-R^2\right) + p_1(t) + p_2(t)\sqrt{1-R^2} + p_3(t)\left(1-R^2\right)\log\left(1-R^2\right) + \ldots, \quad R = \frac{r}{l(t)} \to 1, \tag{4.137}$$

additionally, we immediately have the following asymptotics for the particle velocity:

$$v(r,t) = v_0(t) + v_1(t)\sqrt{1-R^2} + \ldots, \quad R = \frac{r}{l(t)} \to 1, \tag{4.138}$$

where:

$$v_0(t) = \frac{2w_0^2(t)p_0(t)}{Ml(t)}, \quad v_1(t) = \frac{w_0^2(t)p_2(t) + 4w_0(t)w_1(t)p_0(t)}{Ml(t)}, \tag{4.139}$$

4.3.2.2 Energy release rate

It has previously been shown that the crack tip asymptotics play a crucial role in the behaviour of a hydraulic fracture [67, 196]. As such these must be examined in more detail, which is achieved through an examination of the energy release rate (ERR), accounting for the effect of tangential traction. The resulting steps are identical to those provided in the KGD case, as the investigation is conducted in the vicinity of the fracture front. Due to this fact, only the relevant results are provided here, while a detailed explanation is provided in [230].

The form of the first term of the apertures asymptotic representation (4.136) is as follows:

$$w_0(t) = \gamma \left(K_I(t) + K_f(t)\right), \quad K_f = \frac{w_0(t)p_0(t)}{Bl(t)}, \quad B = \frac{4}{\sqrt{\pi}}(1-\nu), \tag{4.140}$$

where:

$$\gamma = \frac{4}{\sqrt{\pi}}\frac{(1-\nu^2)}{E}. \tag{4.141}$$

Here the term K_f is denoted the shear stress intensity factor. The following relationships exist between the stress intensity factors and the material toughness K_{Ic}:

$$K_I = \frac{K_{Ic}}{\sqrt{1+4(1-\nu)\bar{\omega}}}, \quad K_f = \frac{K_{Ic}\bar{\omega}}{\sqrt{1+4(1-\nu)\bar{\omega}}}, \quad \bar{\omega} = \frac{p_0}{G-p_0}, \tag{4.142}$$

where G is the shear modulus and p_0 is the first term of the pressures asymptotic representation at the fracture front (4.137). As such we can represent (4.140) in the following form:

$$w_0(t) = \frac{\gamma(1+\bar{\omega})}{\sqrt{1+4(1-\nu)\bar{\omega}}}K_{Ic}. \tag{4.143}$$

4.3.3 Normalisation

We introduce the following normalization scheme:

$$\begin{gathered}\tilde{r} = \frac{r}{l(t)}, \quad \tilde{t} = \frac{t}{t_n}, \quad \tilde{w}(\tilde{r},\tilde{t}) = \frac{w(r,t)}{l_*}, \quad L(\tilde{t}) = \frac{l(t)}{l_*}, \quad \tilde{q}_l(\tilde{r},\tilde{t}) = \frac{t_n}{l_*}q_l(r,t), \\ \tilde{q}(\tilde{r},\tilde{t}) = \frac{t_n}{l_*^2}q(r,t), \quad \tilde{Q}_0(\tilde{t}) = \frac{t_n}{2\pi l_*^2 l(t)}Q_0(t), \quad \tilde{v}(\tilde{r},\tilde{t}) = \frac{t_n}{l_*}v(r,t), \\ \tilde{p}(\tilde{r},\tilde{t}) = \frac{t_n}{M}p(r,t), \quad \tilde{K}_{\{Ic,I,f\}} = \frac{\gamma}{\sqrt{l_*}}K_{\{Ic,I,f\}}, \quad t_n = \frac{M}{k_2},\end{gathered} \tag{4.144}$$

where $\tilde{r} \in [0,1]$ and l_* is chosen for convenience.

Under this scheme, the Poiseuille equation provides the following relation for the particle velocity (4.133):

$$\tilde{v} = -\frac{\tilde{w}^2}{L(\tilde{t})}\frac{\partial \tilde{p}}{\partial \tilde{r}}, \tag{4.145}$$

As such the fluid mass balance equation (4.124), alongside the global balance equation (4.132), become:

$$\frac{\partial \tilde{w}}{\partial \tilde{t}} - \frac{L'(\tilde{t})}{L(\tilde{t})}\tilde{r}\frac{\partial \tilde{w}}{\partial \tilde{r}} + \frac{1}{\tilde{r}L(\tilde{t})}\frac{\partial}{\partial \tilde{r}}\left(\tilde{r}\tilde{w}\tilde{v}\right) + \tilde{q}_l = 0, \tag{4.146}$$

$$\int_0^1 \tilde{r}\left[L^2(\tilde{t})\tilde{w}(\tilde{r},\tilde{t}) - L^2(0)\tilde{w}_*(\tilde{r})\right]\, d\tilde{r} + \int_0^{\tilde{t}}\int_0^1 \tilde{r}L^2(s)\tilde{q}_l(\tilde{r},s)\, d\tilde{r}\, ds = \int_0^{\tilde{t}} L(s)\tilde{Q}_0(s)\, ds. \tag{4.147}$$

The elasticity equation (4.126) takes the form:

$$\tilde{p}(\tilde{r},\tilde{t}) = -\frac{1}{L(\tilde{t})}\int_0^1 \frac{\partial \tilde{w}}{\partial \eta}\mathcal{M}\left[\tilde{r},\eta\right]\, d\eta, \tag{4.148}$$

alongside associated inverse (4.127):

$$\tilde{w}(\tilde{r},\tilde{t}) = \frac{4}{\pi^2}L(\tilde{t})\int_{\tilde{r}}^1 \frac{\xi}{\sqrt{\xi^2-\tilde{r}^2}}\int_0^1 \frac{\eta\tilde{p}(\eta\xi,\tilde{t})}{\sqrt{1-\eta^2}}\, d\eta d\xi. \tag{4.149}$$

We note that, following the approach from Sect. 4.2.2.1 (see Appendix. E), we can rewrite this as:

$$\tilde{w}(\tilde{r},\tilde{t}) = \frac{4}{\pi^2}L(\tilde{t})\left[\int_0^1 \frac{\partial \tilde{p}(y,\tilde{t})}{\partial y}\mathcal{K}(y,\tilde{r})\, dy + \sqrt{1-\tilde{r}^2}\int_0^1 \frac{\eta\tilde{p}(\eta,\tilde{t})}{\sqrt{1-\eta^2}}\, d\eta\right], \tag{4.150}$$

where:

$$\mathcal{K}(y,\tilde{r}) = y\left[E\left(\arcsin(y)\,\middle|\,\frac{\tilde{r}^2}{y^2}\right) - E\left(\arcsin(\chi)\,\middle|\,\frac{\tilde{r}^2}{y^2}\right)\right], \quad \chi = \min\left(\frac{y}{\tilde{r}}, 1\right). \tag{4.151}$$

By evaluating the asymptotic limit of (4.150) at the crack tip, it can be shown that:

$$\tilde{w}_0 = \frac{4}{\pi^2}L(\tilde{t})\int_0^1 \frac{\eta\tilde{p}(\eta,\tilde{t})}{\sqrt{1-\eta^2}}\, d\eta, \tag{4.152}$$

which replaces the standard integral definition of the stress intensity factor.

The boundary conditions for the problem (4.129)-(4.130) are now given by:

$$\lim_{\tilde{r}\to 0}\tilde{r}\tilde{w}\tilde{v} = \tilde{Q}_0, \tag{4.153}$$

$$\tilde{w}(1,\tilde{t}) = 0, \quad \tilde{q}(1,\tilde{t}) = 0, \tag{4.154}$$

where the system has initial conditions (4.131):

$$\tilde{w}(\tilde{r},0)=\tilde{w}_*(r),\quad L(0)=L_0, \tag{4.155}$$

The crack tip asymptotics (4.136), (4.137), (4.138) now take the form:

$$\tilde{w}(\tilde{r},\tilde{t})=\tilde{w}_0(\tilde{t})\sqrt{1-\tilde{r}^2}+\tilde{w}_1(\tilde{t})\left(1-\tilde{r}^2\right)+\tilde{w}_2(\tilde{t})\left(1-\tilde{r}^2\right)^{\frac{3}{2}}\log\left(1-\tilde{r}^2\right)+\ldots,\quad \tilde{r}\to 1, \tag{4.156}$$

$$\tilde{p}(\tilde{r},\tilde{t})=\tilde{p}_0(\tilde{t})\log\left(1-\tilde{r}^2\right)+\tilde{p}_1(\tilde{t})+\tilde{p}_2(\tilde{t})\sqrt{1-\tilde{r}^2}+\tilde{p}_3\left(1-\tilde{r}^2\right)\log\left(1-\tilde{r}^2\right)+\ldots,\quad \tilde{r}\to 1, \tag{4.157}$$

$$\tilde{v}(\tilde{r},\tilde{t})=\tilde{v}_0(\tilde{t})+\tilde{v}_1(\tilde{t})\sqrt{1-\tilde{r}^2}+\ldots,\tilde{r}\to 1, \tag{4.158}$$

We note that we can rewrite the parameter $\bar{\omega}$ $(4.142)_3$ as:

$$\tilde{\omega}=\frac{\tilde{p}_0}{\pi(1-\nu)-\tilde{p}_0}. \tag{4.159}$$

as such, the first term of the aperture asymptotics at the fracture tip are given by (4.140), (4.143):

$$\tilde{w}_0(\tilde{t})=\sqrt{L(\tilde{t})}\frac{1+\tilde{\omega}}{\sqrt{1+4(1-\nu)\tilde{\omega}}}\tilde{K}_{Ic}=\sqrt{L(\tilde{t})}\left[\tilde{K}_I+\tilde{K}_f\right], \tag{4.160}$$

while the stress intensity factors (4.142) are described by:

$$\tilde{K}_I=\frac{\tilde{K}_{Ic}}{\sqrt{1+4(1-\nu)\tilde{\omega}}},\quad \tilde{K}_f=\frac{\tilde{K}_{Ic}\tilde{\omega}}{\sqrt{1+4(1-\nu)\tilde{\omega}}}, \tag{4.161}$$

The Steffan condition (4.135), utilizing the Poiseuille equation (4.145) and terms from the asymptotic representation (4.156)-(4.157), can be expressed as:

$$\frac{dL}{d\tilde{t}}=\tilde{v}_0(\tilde{t})=-\frac{1}{L(\tilde{t})}\lim_{\tilde{r}\to 1}\tilde{w}^2\frac{\partial\tilde{p}}{\partial\tilde{r}}=\frac{2\tilde{w}_0^2\tilde{p}_0}{L(\tilde{t})}, \tag{4.162}$$

Utilizing (4.160), we can rewrite this condition as follows:

$$\frac{1}{\tilde{K}_{Ic}^2}\tilde{v}_0=\tilde{p}_0F\left(\tilde{p}_0\right), \tag{4.163}$$

where:

$$F\left(\tilde{p}_0\right)=\frac{2\pi^2\left(1-\nu\right)^2}{\left[\pi\left(1-\nu\right)+\left(3-4\nu\right)\tilde{p}_0\right]\left[\pi\left(1-\nu\right)-\tilde{p}_0\right]}. \tag{4.164}$$

Noting the above definition, we can rewrite (4.160) in the form:

$$\tilde{w}_0(\tilde{t})=\tilde{K}_{Ic}\sqrt{L(\tilde{t})F(\tilde{p}_0)}, \tag{4.165}$$

Further, by integrating (4.162), we can obtain a formula for the crack length:

$$L(\tilde{t}) = \sqrt{L^2(0) + 4\int_0^{\tilde{t}} \tilde{w}_0^2(s)\tilde{p}_0(s)\,ds}. \tag{4.166}$$

4.3.4 Self-similar formulation

4.3.4.1 General case ($K_{Ic} > 0$)

We wish to formulate a self-similar solution described by an exponential function, such that:

$$\tilde{Q}_0(\tilde{t}) = \hat{Q}_0 e^{2\alpha\tilde{t}}, \tag{4.167}$$

We search for a solution in the form:

$$\tilde{w}(\tilde{r},\tilde{t}) = \sqrt{L_0\hat{Q}_0}e^{\alpha\tilde{t}}\hat{w}(\tilde{r}), \quad L(t) = L_0^{\frac{3}{2}}\sqrt{\hat{Q}_0}e^{\alpha\tilde{t}}, \quad \tilde{p}(\tilde{r},\tilde{t}) = \hat{p}(\tilde{r}),$$

$$\tilde{q}_l(\tilde{r},\tilde{t}) = \alpha\sqrt{L_0\hat{Q}_0}e^{\alpha\tilde{t}}\hat{q}_l(\tilde{r}), \quad \tilde{v}(\tilde{r},\tilde{t}) = \sqrt{\frac{\hat{Q}_0}{L_0}}e^{\alpha\tilde{t}}\hat{v}(\tilde{r}), \quad \tilde{q}(\tilde{r},\tilde{t}) = \hat{Q}_0 e^{2\alpha\tilde{t}}\hat{q}(\tilde{r}), \tag{4.168}$$

$$\tilde{K}_{\{Ic,I,f\}} = \left(L_0\hat{Q}_0\right)^{\frac{1}{4}} e^{\frac{\alpha\tilde{t}}{2}}\hat{K}_{\{Ic,I,f\}},$$

where:

$$\hat{v}_0 = \hat{v}(1), \quad L_0 = \sqrt{\frac{\hat{v}_0}{\alpha}}. \tag{4.169}$$

As such, the self-similar particle velocity will be defined as (4.145):

$$\hat{v}(\tilde{r}) = -\hat{w}^2(\tilde{r})\frac{d\hat{p}(\tilde{r})}{d\tilde{r}}, \tag{4.170}$$

The fluid mass and global balance equations (4.146)-(4.147) become:

$$\hat{w} - \tilde{r}\frac{d\hat{w}}{d\tilde{r}} + \frac{1}{\hat{v}_0\tilde{r}}\frac{d}{d\tilde{r}}\left(\tilde{r}\hat{w}\hat{v}\right) + \hat{q}_l = 0, \tag{4.171}$$

$$3\int_0^1 \tilde{r}\hat{w}(\tilde{r})\,d\tilde{r} + \int_0^1 \tilde{r}\hat{q}_l(\tilde{r})\,d\tilde{r} = \frac{1}{\hat{v}_0}, \tag{4.172}$$

The relationships between the pressure and aperture (4.148), (4.150) are given by:

$$\hat{p}(\tilde{r}) = -\frac{1}{L_0}\int_0^1 \frac{d\hat{w}}{d\eta}\mathcal{M}\left[\tilde{r},\eta\right]\,d\eta, \tag{4.173}$$

$$\hat{w}(\tilde{r}) = \frac{4}{\pi^2} L_0 \left[\int_0^1 \frac{d\hat{p}}{dy} \mathcal{K}(y, \tilde{r})\, dy + \sqrt{1-\tilde{r}^2} \int_0^1 \frac{\eta \hat{p}(\eta)}{\sqrt{1-\eta^2}}\, d\eta \right], \tag{4.174}$$

while (4.152) becomes:

$$\hat{w}_0 = \frac{4}{\pi^2} L_0 \int_0^1 \frac{\eta \hat{p}(\eta)}{\sqrt{1-\eta^2}}\, d\eta, \tag{4.175}$$

Alongside the source intensity and boundary conditions:

$$\lim_{\tilde{r}\to 0} \tilde{r}\hat{w}\hat{v} = 1, \tag{4.176}$$

$$\hat{w}(1) = 0, \quad \hat{q}(1) = 0, \tag{4.177}$$

The crack tip asymptotics (4.156), (4.157), (4.158) now take the form:

$$\hat{w}(\tilde{r}) = \hat{w}_0 \sqrt{1-\tilde{r}^2} + \hat{w}_1 \left(1-\tilde{r}^2\right) + \hat{w}_2 \left(1-\tilde{r}^2\right)^{\frac{3}{2}} \log\left(1-\tilde{r}^2\right) + \ldots, \quad \tilde{r} \to 1, \tag{4.178}$$

$$\hat{p}(\tilde{r}) = \hat{p}_0 \log\left(1-\tilde{r}^2\right) + \hat{p}_1 + \hat{p}_2 \sqrt{1-\tilde{r}^2} + \hat{p}_3 \left(1-\tilde{r}^2\right) \log\left(1-\tilde{r}^2\right) + \ldots, \quad \tilde{r} \to 1, \tag{4.179}$$

$$\hat{v}(\tilde{r}) = \hat{v}_0 + \hat{v}_1 \sqrt{1-\tilde{r}^2} + \ldots, \quad \tilde{r} \to 1, \tag{4.180}$$

Taking (4.169), (4.170) into account, the following relations are immediately apparent:

$$\hat{v}_0 = 2\hat{w}_0^2 \hat{p}_0, \quad L_0 = \hat{w}_0 \sqrt{\frac{2\hat{p}_0}{\alpha}}, \tag{4.181}$$

We note that we can rewrite the parameter $\tilde{\omega}$ (4.159) as:

$$\hat{\omega} = \frac{\hat{p}_0}{\pi(1-\nu) - \hat{p}_0}. \tag{4.182}$$

As such, the first term of the aperture asymptotics at the fracture tip (4.160) are given by:

$$\hat{w}_0 = \sqrt{L_0} \frac{1+\hat{\omega}}{\sqrt{1+4(1-\nu)\hat{\omega}}} \hat{K}_{Ic} = \sqrt{L_0} \left[\hat{K}_I + \hat{K}_f\right] = \hat{K}_{Ic} \sqrt{L_0 F(\hat{p}_0)}, \tag{4.183}$$

where the stress intensity factors (4.161) are described by:

$$\hat{K}_I = \frac{\hat{K}_{Ic}}{\sqrt{1+4(1-\nu)\hat{\omega}}}, \quad \hat{K}_f = \frac{\hat{K}_{Ic}\hat{\omega}}{\sqrt{1+4(1-\nu)\hat{\omega}}}, \tag{4.184}$$

Noting the definition of $F(\hat{p}_0)$ from (4.164), the relationships (4.181) and (4.183) immediately yield:

$$(4\nu-3)\hat{p}_0^2 + 2\pi(1-\nu)(1-2\nu)\hat{p}_0 - \frac{\sqrt{2}\pi^2 (1-\nu)^2 \hat{K}_{Ic}^2}{\hat{w}_0 \sqrt{\alpha}} \sqrt{\hat{p}_0} + \pi^2 (1-\nu)^2 = 0, \tag{4.185}$$

4.3.4.2 Viscosity dominated case ($K_{Ic} \equiv 0$)

It can easily be shown from (4.185) that, noting we require $\hat{p}_0 > 0$ to have a physically realistic result, we have the following in the viscosity dominated regime:

$$\hat{p}_0 = \pi\,(1-\nu) + O\left(\hat{K}_{Ic}^2\right), \quad \hat{K}_{Ic} \to 0. \tag{4.186}$$

From this, alongside (4.183) and (4.184), it can be shown that:

$$\hat{\omega} = \frac{4(1-\nu)\hat{w}_0^2}{L_0\hat{K}_{Ic}^2} + O(1), \quad \hat{K}_f \sim \frac{\hat{w}_0}{\sqrt{L_0}}, \quad \hat{v}_0 \sim \pi(1-\nu)L_0\hat{K}_f^2, \quad \hat{K}_{Ic} \to 0, \tag{4.187}$$

4.3.5 Numerical results

4.3.5.1 Computational scheme

The computation scheme utilized in this case is based on the approach outlined in Sect. 4.2.5.1, and more fully described in Appendix. F. A brief outline is given below:

1. An initial approximation of the aperture $\hat{w} = \hat{w}^{j-1}$ is taken, such that it has the correct asymptotic behaviour and satisfies the boundary conditions.

2. The fluid balance equation (4.172) is used to obtain the first asymptotic term of the aperture $\hat{w}_0^j$. Equation (4.185) is used to find $\hat{p}_0^j$ and the parameters $\hat{v}_0^j$, L_0^j follow immediately from (4.181). Further asymptotic terms for the aperture, particle velocity and pressure can also be obtained using analytical relations between them, as well as numerical techniques.

3. Having the above, the (reduced) particle velocity is reconstructed from direct integration of (4.171), with the asymptotics of the functions used to increase the accuracy and computation time. Tikhonov type regularization is employed at this stage.

4. Equation (4.170) is now used to obtain an approximation of the (modified) pressure derivative, and the elasticity equation (4.174), (4.175) serves to compute the next approximation of the fracture aperture $\hat{w}^j$.

5. The system is iterated until the variables $\hat{w}$, $\hat{p}_0$, $\hat{v}$, have converged to within prescribed tolerances.

It should be noted that, in this case, we will not incorporate the new inverse elasticity operator into computations. The reason for this is that, in the radial case, computing

the elasticity operator presents the greatest challenge of any step in the algorithm. This is especially true when we have $\hat{K}_{Ic} < 1$, as the first asymptotic coefficients (i.e. $\hat{w}_0$, $\hat{v}_0$,...) decrease in value, with a larger part of the solution being determined by later terms. As such, numerical errors in this step are not as easily reduced by removing asymptotic terms in this case. Adding additional terms will undoubtedly increase such errors.

Meanwhile, the paper by *Wrobel, Mishuris & Piccolroaz* [230] demonstrated that incorporating the new elasticity operator into the algorithm had no significant effect on the final result. As such, it is likely that any effect introducing this operator would have will be hidden by the error it introduces. Given these facts, it has been decided not to introduce a revised inverse elasticity equation into the algorithm at this stage.

4.3.5.2 Accuracy against analytical benchmarks

In order to obtain the accuracy of the numerical solution, analytical benchmark functions are constructed. These are built from a series of base functions, which are known solutions to the elasticity equation (4.174). The details of their construction are outlined in Appendix. D.

The final computational algorithm utilizes a non-uniform mesh, consisting of N nodal points. The accuracy of computations, using the measures provided by (4.109), are depicted for varying N in Fig. 4.19. In these graphs, the maximum error over the spacial distribution is also provided. Plots showing the full spacial distribution of the relative errors is depicted in Fig. 4.20.

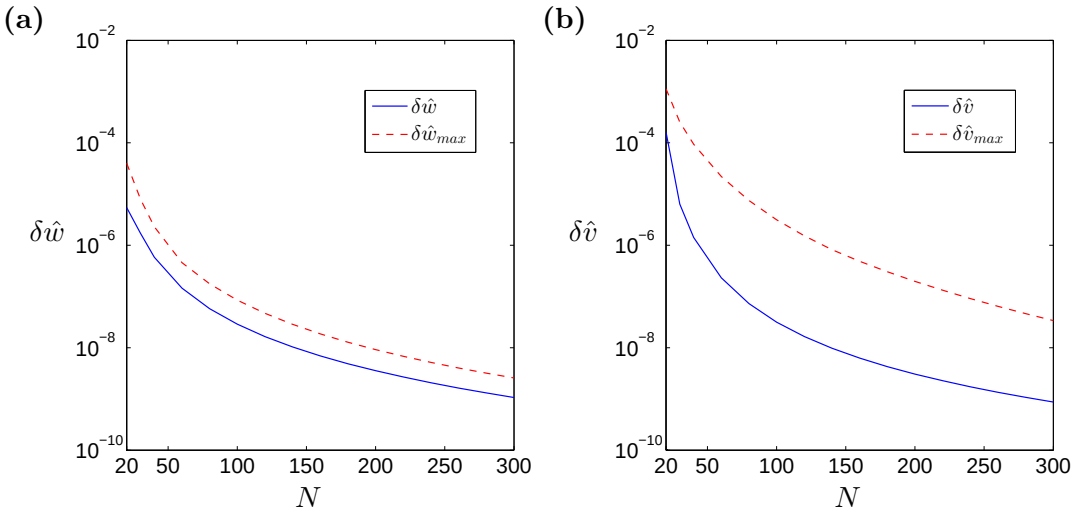

FIGURE 4.19: Relative and maximum error of the numerical solution in comparison with analytical benchmarks, for: (a) the fracture aperture, (b) the particle velocity.

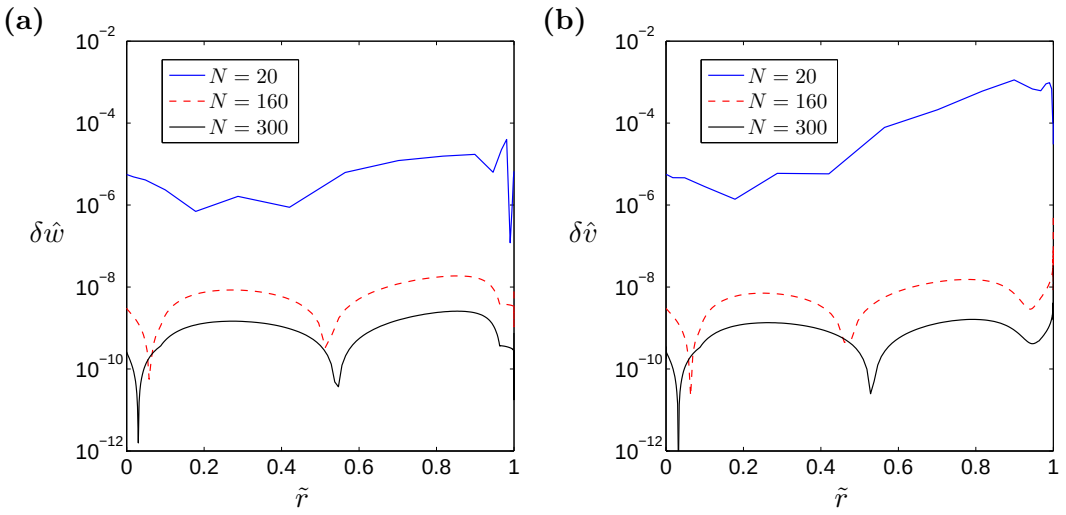

FIGURE 4.20: Spacial distribution of the relative error, obtained from the numerical solution in comparison with analytical benchmarks, for: (a) the fracture aperture, (b) the particle velocity.

It is clear from both of these figures that the numerical solution provides a high accuracy approximation, even when taking a low number of nodal points. The maximum error of solution for the aperture is below 10^{-4} when only $N = 20$ nodal points are used, while the computation time is under five seconds. Meanwhile, when $N = 300$ spacial nodes are taken, the solution accuracy is better than 10^{-7} at all points in the spacial domain, while the average relative error is below 10^{-8} in for both the aperture and particle velocity. As such, the numerical algorithm can both offer a high-speed result with a reasonable accuracy, or a very high accuracy result with only slightly longer computation times.

4.3.5.3 Results for an impermeable solid

While testing against the numerical benchmark provides a useful method of analyzing the error in the case when the exact solution is known, we once again require an approach to testing the error level of the solution when no prescribed solution is known. In order to achieve this we utilize the fact that, as in the classical case, the solution converges at a known rate with respect to the number of nodal points: $1/N^3$. As such we can again utilize (4.110)-(4.112), providing an alternative error measure for the solution.

We examine the case of an impermeable solid, such that the leak-off function is zero valued. The rates of convergence are provided in Fig. 4.21, for various fixed values of the stress intensity factor $\hat{K}_{Ic}$.

It is clear from Fig. 4.21 that, while the solution convergence provides a high level of confidence in the solution when $\hat{K}_{Ic} \geq 1$, universally achieving a level below 10^{-8} when taking $N = 300$. Unfortunately, the case when $\hat{K}_{Ic} = 0$ does not exhibit the same

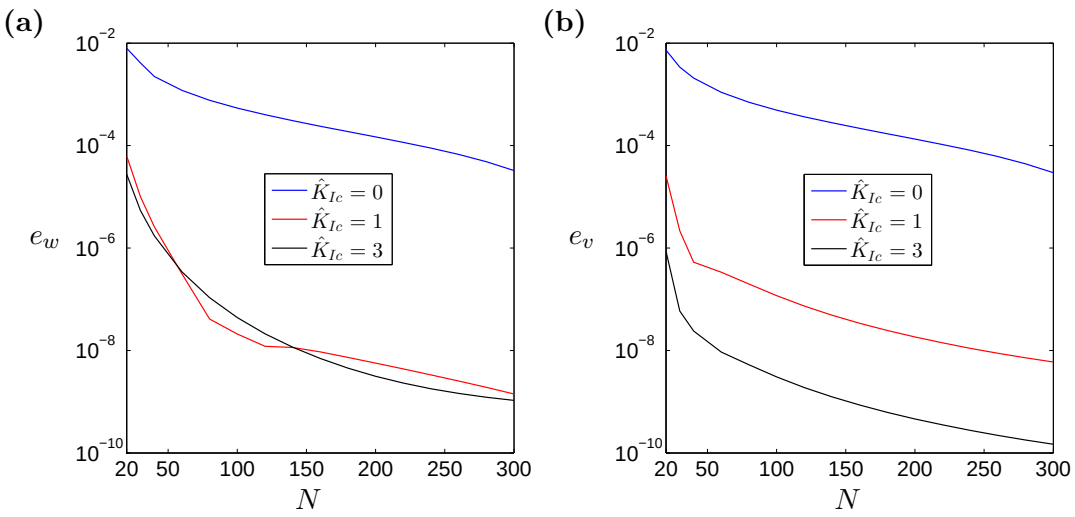

FIGURE 4.21: Rate of convergence of the solution, obtained using a least-squares method, for: (a) the fracture aperture, (b) the particle velocity.

behaviour. However, the error level obtained for $\hat{K}_{Ic} \leq 1$ still remains below 10^{-4} when $N = 300$, meaning that it still achieves a higher level of accuracy than that of comparable solvers (see Sect. 4.2.5.5). As such, it can be said that the numerical solution provides a suitable benchmark regardless of the value of $\hat{K}_{Ic}$.

With the validity of the benchmark demonstrated, an examination of the results can be conducted.

Results for the primary problem variables, namely the aperture, particle velocity and pressure, are given in Fig. 4.22. Meanwhile, a more substantial examination of the relationship between the self-similar material toughness and the important problem parameters is provided in Figs. 4.23 & 4.24.

It is clear to see that, for small $\hat{K}_{Ic}$, the shear-stress plays a significant role in the qualitative behaviour of the system. As seen in Fig. 4.23, when taking $\hat{K}_{Ic} < 1$ the shear-stress is the larger of the two stress intensity factors. As a result, the asymptotics at the fracture aperture are primarily defined by this parameter. This fact is important, as it shows that it isn't only the viscosity dominated case ($\hat{K}_{Ic} = 0$) which is affected by the new formulation.

As the material toughness increases however, the significance of incorporating shear stress into the model begins to rapidly decrease. In the limiting case $\hat{K}_{Ic} \to \infty$, the behaviour of the system will coincide with those in the classical formulation (see [196]). It should be noted however that, due to the algorithms high level of stability in the case of large fracture toughness, incorporating the effect of tangential stress into the model does not have any noticable downsides in terms of solution accuracy or computation time.

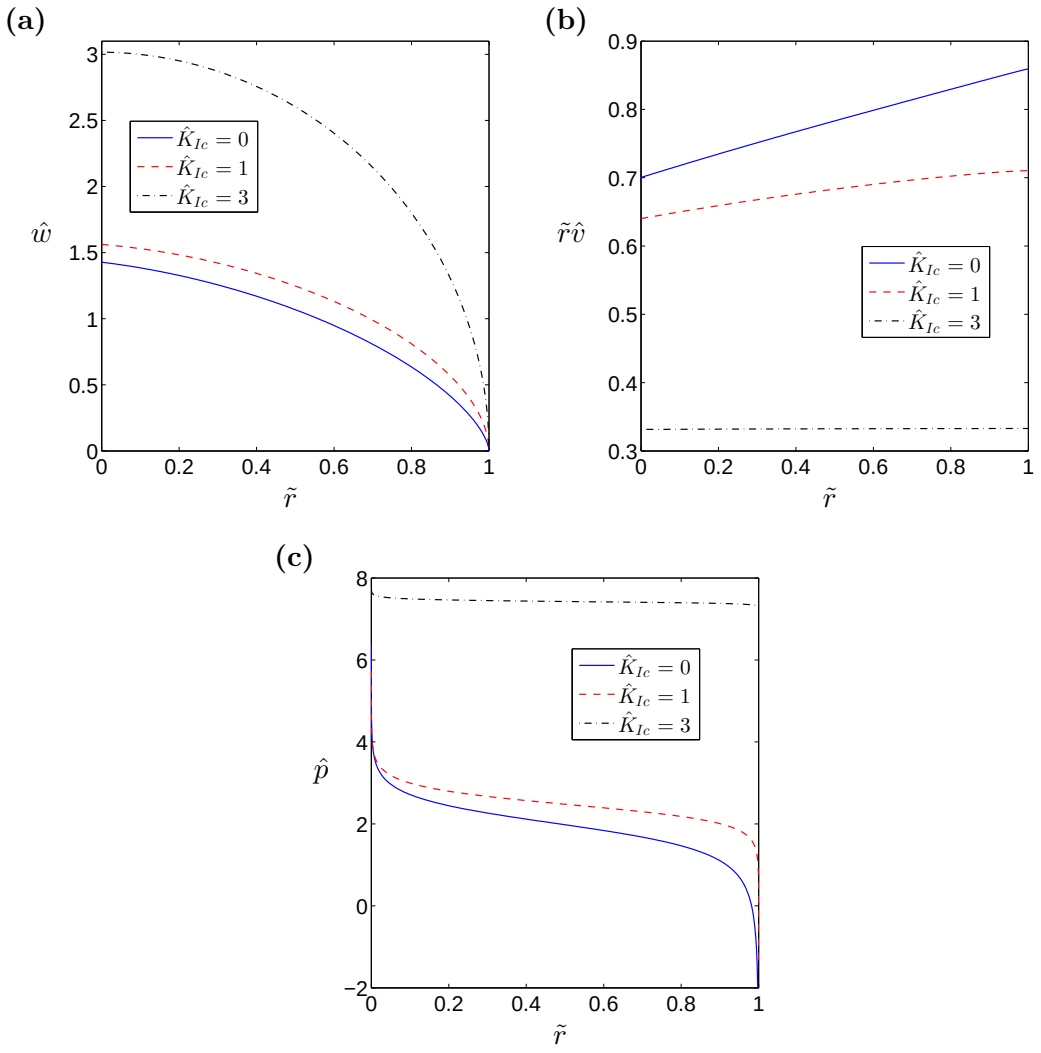

FIGURE 4.22: Behaviour of the problem parameters when $\nu = 0.3$. Here we display: (a) the crack aperture, (b) the particle velocity, (c) the pressure inside the fracture.

One final thing to note is the similarity between the results for the penny-shaped in comparison with the KGD case. The qualitative and quantitative behaviour of the stress intensity factors is almost identical to that obtained by *Wrobel, Mishuris & Piccolroaz* [230]. This is unsuprising, given the almost identical nature of the fracture front between the two cases.

4.3.5.4 Comparison with the classical formulation

With numerical solvers for both the classical and reformulated models of radial HF now developed, it is possible to examine the quantitative difference in parameter behaviour between the two. To this end, the relative difference in the solution for the aperture and particle velocity are provided in Fig. 4.25, with the relative and absolute differences for the pressure function given in Fig. 4.26.

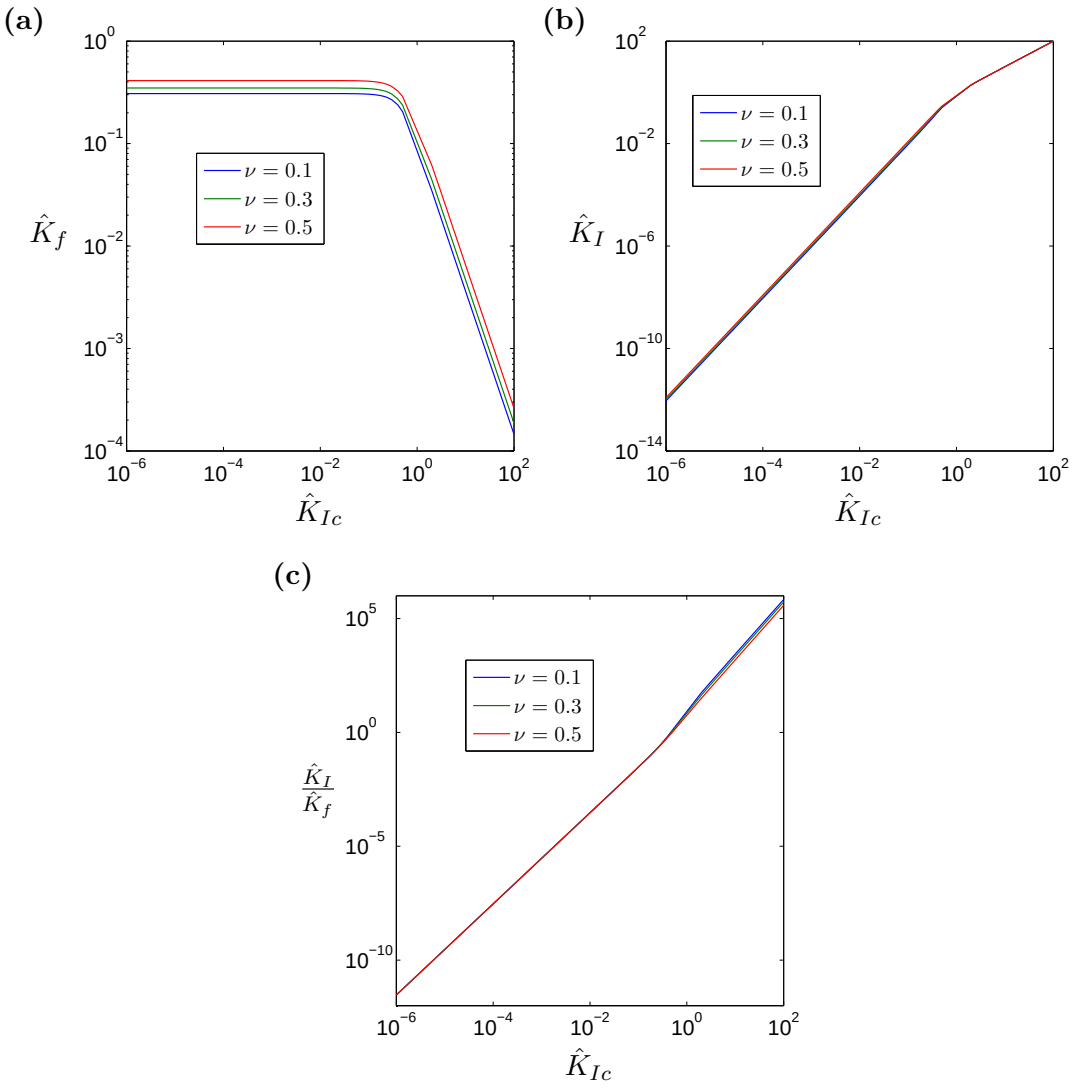

FIGURE 4.23: The relationship between the self-similar material toughness $\hat{K}_{Ic}$ and the system stress intensity factors. Here we show the self-similar forms of: (a) the shear stress indensity factor $\hat{K}_f$, (b) the stress intensity factor $\hat{K}_I$, (c) the ratio between the stress intensity factors.

It is clear from Fig. 4.25 that the maximum relative deviation between the solutions for the new and classical formulations is approximately 3%, for the fracture aperture at the crack tip. This is almost identical to the difference reported in the KGD case [230], which is not surprising given the identical behaviour of the two formulations in that region. The relative difference in the particle velocity however is notably smaller, not even surpassing 0.03% regardless of the value of $\hat{K}_{Ic}$ taken.

Interestingly, the difference in solution for the aperture explains why the experimental investigation by *Bunger & Detournay* [34] obtained incorrect values for the crack tip asymptote in the viscosity dominated regime. As can be seen in Fig. 4.25a, the aperture remains almost identical to the classical solution, with an asymptotic exponent of 2/3, until very close to the fracture front. Given that their experimental data was described as

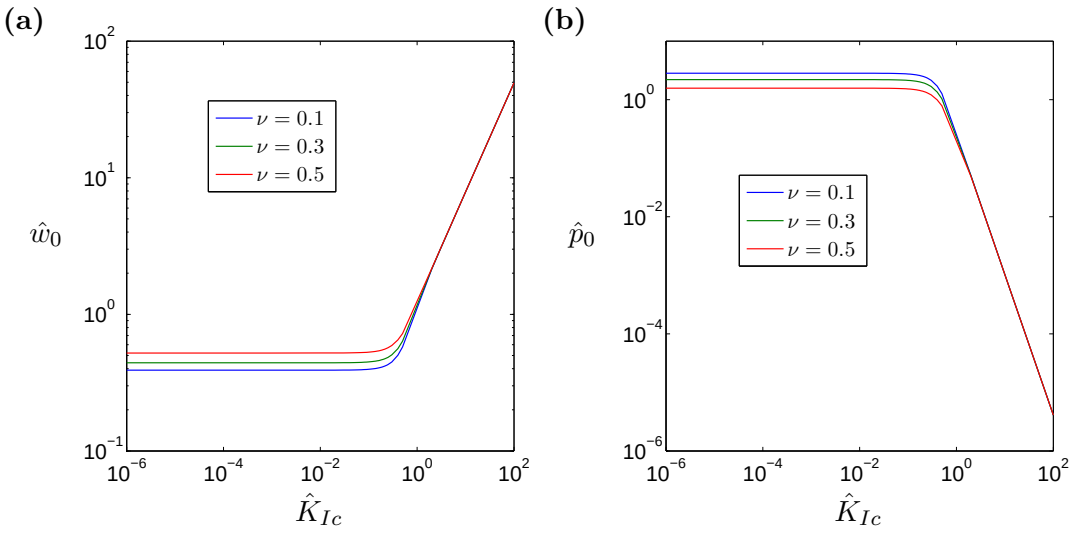

FIGURE 4.24: The relationship between the self-similar material toughness $\hat{K}_{Ic}$ and the leading terms of the system asymptotics. Here we show the coefficients for: (a) the fracture aperture $\hat{w}_0$, (b) the pressure function $\hat{p}_0$.

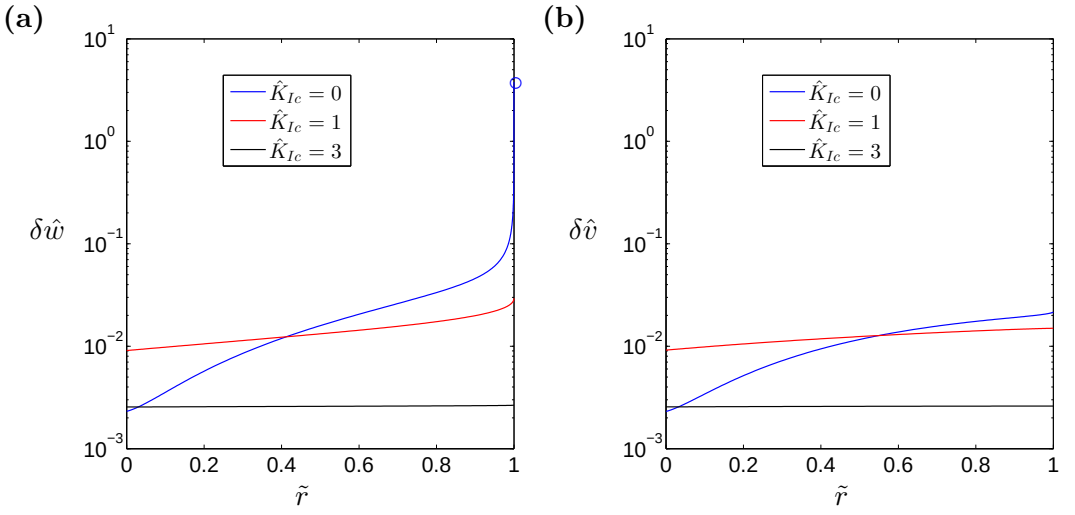

FIGURE 4.25: Relative difference in the solutions obtained for a penny-shaped fracture with or without tangential stress, for: (a) the fracture aperture (with the blue circle indicating the maximum deviation when $\hat{K}_{Ic} = 0$), (b) the particle velocity.

"measuring the full-field crack opening within 10% accuracy", their experiment was not capable of measuring the actual crack tip asymptote, and instead obtained the leading near-tip term, which has an exponent of 2/3 in both formulations. As such, the model presented here remains in line with current experimental results.

Meanwhile, for the pressure function, there is a far larger relative difference between the solutions for the two formulations, achieving a maximum just below 10^2 in the viscosity dominated regime. This is due to the pressure crossing the x-axis (i.e. $\hat{p}(\tilde{r}) = 0$ for some $\tilde{r}$ near to 1, see Fig. 4.22c), and as such isn't seen when taking the absolute value (compare Fig. 4.26a & 4.26b). The absolute difference however becomes very large at

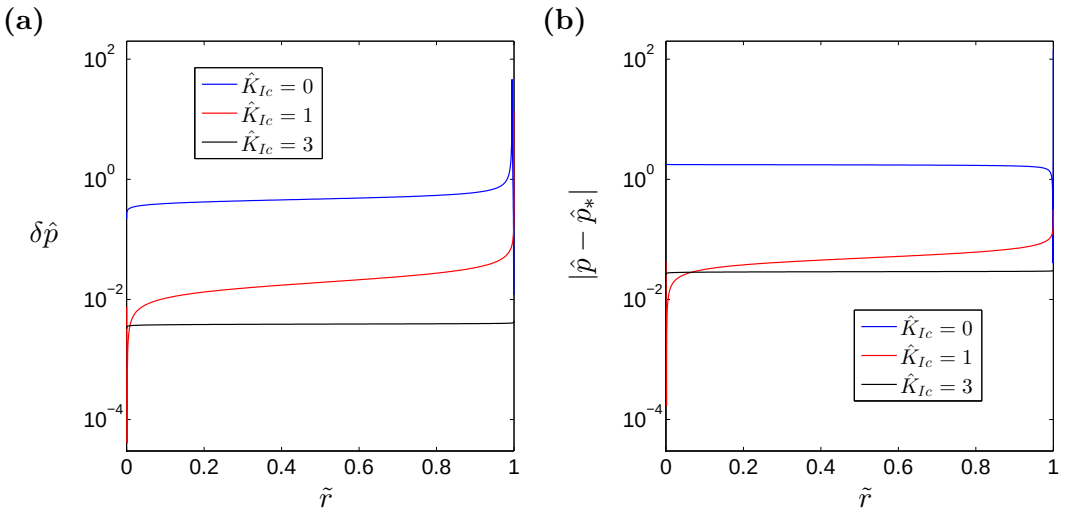

FIGURE 4.26: Relative difference in the solutions pressure function obtained for a penny-shaped fracture with or without tangential stress: (a) the relative difference, (b) the absolute difference.

the crack tip, exceeding 10^2, as the qualitative difference between the pressure solutions leads to differing singularities, greatly affecting the result.

Overall, it is clear that over most of the fracture domain the difference in parameter behaviour between the two formulations is not large. It should be noted however that, while the quantitative differences between the solutions may not be overly significant, the qualitative behaviour for small $\hat{K}_{Ic}$ clearly is. This is most notable in terms of the system asymptotics at the fracture tip, which are radically different in the classical formulation. In addition, this change also eliminates the singular perturbation problem which is typically encountered when transitioning from the viscosity to toughness dominated regimes.

4.3.5.5 Effect of introducing tangential stress on computation times

One of the key concerns expressed by those working in HF about incorporating shear-stress into the model, is that typically simulating a toughness dominated fracture takes noticeably more time than for the viscosity dominated case[2]. Given that one of the stated aims of this work on devising a new model of penny-shaped fracture was to indeed reduce computation time, we will here investigate the effect on the algorithms efficiency which has occurred due to incorporating the tangential stress.

The run-time of simulations of radial hydraulic fracture, when $\hat{K}_{Ic}=0$, are provided in Fig. 4.27. Here we show the simulation times, alongside the ratio between them, defined

[2]This view comes from discussions between colleagues and individuals working in the HF industry.

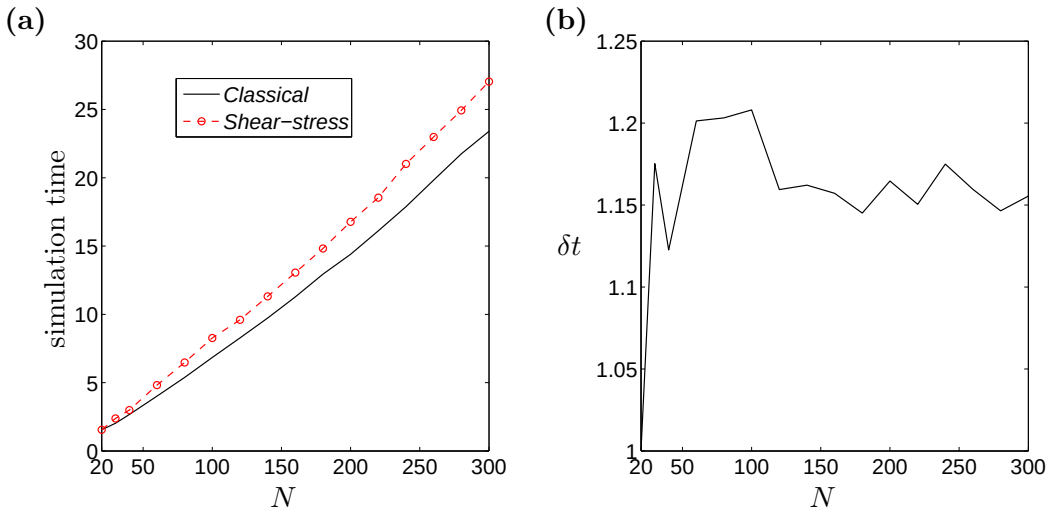

FIGURE 4.27: Simulation times when obtaining solutions for penny-shaped HF when $\hat{K}_{Ic} = 0$, in both the classical case and the model reformulated to include shear-stress, for varying number of nodal points N. Here we show: (a) the simulation times, (b) the ratio between simulation times.

as:

$$\delta t = \frac{\text{Simulation time with shear-stress}}{\text{Simulation time in the classical case}}, \tag{4.188}$$

It is clear from the results that, while the incorporation of the tangential stress into the model has had an effect on simulation times, it is not overly significant. This is especially true given that, as can be seen in Fig. 4.27a, the total duration of simulations in either case is less than 30 seconds, which is still faster than other comparable solvers. Whats more, neglecting the effect of shear-stress leads to the theory failing to describe the true qualitative behaviour of the system, whilst also causing a singular perturbation problem in the case of small fracture toughness. Given that the difference in computation times is less than 4 seconds, even when taking $N = 300$ nodal points, this seems like a high price to pay.

4.3.6 Summary for radial HF with shear-stress

In this section the recently developed fracture criterion, incorporating the effects of shear-stress, was introduced into the modeling of a penny-shaped hydraulic fracture. A numerical algorithm capable of obtaining high accuracy solutions has been created, which is sufficiently efficient to prevent a significant increase in computation times compared with the classical formulation. A comparison of results obtained when including the effect of tangential stresses, against those using the traditional fracture criterion, has been conducted.

It was demonstrated that, while there is not a large quantitative difference between the results obtained for the classical and reformulated models of radial HF, there was a clear disparity between the qualitative behaviour of the system parameters in the viscosity dominated regime (when $\hat{K}_{Ic} = 0$). Namely, the system asymptotics at the crack tip remain the same as in the toughness dominated regime ($\hat{K}_{Ic} > 0$), eliminating the singular perturbation problem which plagued previous attempts at examining fractures with small toughness, or cracks transitioning between the two regimes.

The model presented here however is not yet complete. The reformulated (inverse) elasticity operator has yet to be incorporated which, while not expected to yield a significant qualitative or quantitative difference to the final result, is needed for completeness. Additionally, while the model presented here enjoys a high level of accuracy in all regimes, there is still room for improvement in the viscosity dominated case. Finally, the numerical algorithm presented here deals exclusively with the self-similar formulation of the problem. In order to ensure that the final results enjoy as greater degree of applicability as possible, this method should be extended to the transient (time-dependent) regime, similar to that previously achieved for the PKN/KGD models [165].

4.4 Conclusions for the penny-shaped model

In this chapter, the case of an axisymmetric fluid driven fracture was examined, with the aim of providing a highly accurate description of the moving boundary. The axisymmetric formulation is of particular relevance to problems of this type, as the high level of complexity makes modeling a 'true' 3D variant of the problem incredibly difficult, meaning that the radial case both offers the simplest method of analyzing a fully 3D model, while also providing a method of testing advanced 3D (computational) approaches.

In order to objectively assess the success of this effort, analytical benchmark solutions for the problem have been developed. This allows the accuracy of the numerical solver to be examined and determined, something which was not previously possible. As a result, it can confidently be stated that the numerical algorithm presented here achieves a solution error below 10^{-8} in most cases. This was confirmed in the case of a impermeable solid using a secondary error measure, based on the known rate of convergence of the numerical solution. It is interesting to note that achieving this high level of accuracy was made possible through proper application of the associated Stefan-type condition (the *speed equation*), which helped to alleviate many of the difficulties arising from this complicated solid-fluid interaction.

Additionally, the first steps towards incorporating the effects of shear-stress into the model have also been completed. This important modification, which requires updating the fracture criterion, fundamentally changes the qualitative behaviour of the problem parameters in the case with small fracture toughness. Further work is still required to fully reformulate the problem, namely deriving the new form of the inverse elasticity equation and incorporating it into the numerical algorithm. It should be noted however that doing so is for the sake of completion, and will not significantly affect the final results obtained by the solver.

Finally, although the model and numerical algorithm provided here present a significant step forward in the modeling of axisymmetric HF, the work is far from completed. Most notably, the results presented here only cover the self-similar variant of the problem. This is not uncommon in the literature, however a more thorough understanding of this phenomena will require simulating the transient (truly time dependent) regime. Additionally, important effects such as the fluid lag, and the associated piecewise extension of the crack tip, are not incorporated into the given approach, despite playing a crucial role in understanding how the fracture boundary develops over time. As such, there is still much work to be done before we have a complete and comprehensive model of this phenomena.

Chapter 5

Simulating the Hele-Shaw flow in the presence of various obstacles and moving particles

This work was published in the paper:
Simulating the Hele-Shaw flow in the presence of various obstacles and moving particles, Meccanica, 51(5):1041-1055, 2016

5.1 Theoretical background and literature review

5.1.1 Problem description and motivation

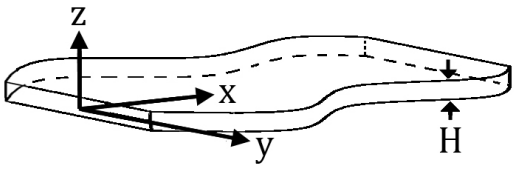

FIGURE 5.1: Diagram of the Hele-Shaw configuration (credit: Wikimedia Commons). Here $h \ll 1$ is the gap between the plates.

The Hele-Shaw flow was an experimental setup first devised in 1898 by *H.S. Hele-Shaw* [91]. The system involves using two plates, pressed tightly together, with a fluid flowing between them (see Fig. 5.1). The Hele-Shaw cell presents a similar setup, however the fluid within the cell does not extend to the edges of the plates. The result is the existence of a continuous fluid boundary, which expands or shrinks as fluid is either added to, or removed from, the system. The advantage of this setup is that, provided the plates are

close enough together, fluid flow between the plates (along the z-axis) ceases, and the in simple cases involving a single source/sink (within the fluid), and a single fluid, the system will no longer experiences turbulent effects. This type of flow is analogous to other problems in microfluidics, and presents a valuable approximation for numerous problems.

5.1.2 Governing equations

5.1.2.1 The Stefan-type equation

The Stefan-type equation for boundary development in the Hele-Shaw cell is analogous to that in hydraulic fracturing, outlined in Sect. 4.1.3.1. It begins with an examination of the unidirectional fluid flow between two parallel boundary walls, in this case the plates of the cell. The key difference is that here in this case it will reduce to the study of a two dimensional system, rather than the 1D system considered in the previous chapter.

The initial problem formulation is identical to that in equations (4.1)-(4.5). The investigation again begins with the *Navier-Stokes* equations, which describe fluid movement. This flow is assumed to be slow, and to move parallel to the plates of the cell. In addition, we assume that the (Newtonian) fluid is incompressible.

The first deviation between the two approaches is to note that, in this case, the rate of deformation tensor $\dot{\gamma}$ is defined by:

$$\dot{\gamma} = \begin{bmatrix} 0 & 0 & \frac{\partial v_x}{\partial z} \\ 0 & 0 & \frac{\partial v_y}{\partial z} \\ \frac{\partial v_x}{\partial z} & \frac{\partial v_y}{\partial z} & 0 \end{bmatrix} \tag{5.1}$$

As we are only considering the case when the Hele-Shaw cell contains a Newtonian fluid, we can utilize the definition:

$$\tau = \mu\dot{\gamma}, \tag{5.2}$$

where μ is the viscosity coefficient of the fluid in the cell.

Now, it is apparent from (5.1)-(5.2) that the shear term will be proportional to the acceleration of the fluid (for each coordinate pair). Noting this, alongside the fact that the length scales for x and y are $O(1)$, while the length scale in the z direction is $O(h)$, while the fluid flow in the x and y directions is assumed to be slow, it can be safely assumed that the shear terms acting between the plates of the cell will be significantly larger than those acting in other directions. As a result of this, shear terms which are not acting in the z-direction can be safely neglected, and the system of equations (4.5)

will be approximated by:

$$\frac{\partial p}{\partial x} = \frac{\partial \tau_{xz}}{\partial z}, \quad \frac{\partial p}{\partial y} = \frac{\partial \tau_{yz}}{\partial z}, \quad \frac{\partial p}{\partial z} = \frac{\partial \tau_{zz}}{\partial z}. \tag{5.3}$$

This, when combined with (5.1)-(5.2), and noting the symmetry conditions:

$$\left.\frac{\partial v_x}{\partial z}\right|_{z=0} = 0, \quad \left.\frac{\partial v_y}{\partial z}\right|_{z=0} = 0, \tag{5.4}$$

gives:

$$\frac{\partial v_x}{\partial z} = \frac{1}{\mu} z \frac{\partial p}{\partial x}, \quad \frac{\partial v_y}{\partial z} = \frac{1}{\mu} z \frac{\partial p}{\partial y}. \tag{5.5}$$

If we impose a no-slip condition on the plates of the cell:

$$v_x\left(z = \pm\frac{h}{2}\right) = 0, \quad v_y\left(z = \pm\frac{h}{2}\right) = 0, \tag{5.6}$$

the above immediately yields the velocity profiles:

$$v_x = \frac{1}{2\mu}\left[z^2 - \frac{h^2}{4}\right]\frac{\partial p}{\partial x}, \quad v_y = \frac{1}{2\mu}\left[z^2 - \frac{h^2}{4}\right]\frac{\partial p}{\partial y}. \tag{5.7}$$

As such we can evaluate the average velocity by taking the integral:

$$\frac{\partial \mathbf{w}}{\partial t} = \frac{2}{h}\int_0^{\frac{h}{2}} \mathbf{v}\, dz = -\frac{h^2}{12\mu}\nabla p, \tag{5.8}$$

This is often referred to as the Hele-Shaw equation. It is important to note that it is independent of the z coordinate, being considered as a purely 2D problem. Due to this fact, and for convenience, from this point on we consider the problem in terms of complex variable $z = x + iy$.

The similarity between the form of the Hele-Shaw equation and that of *Darcy's law*, which describes the flow of a viscous fluid through a porous medium, is immediately apparent [47]. As such investigations of the Hele-Shaw flow in 2D can yield valuable insight into some of the underlying mechanisms at play in 3D problems with viscous fluids. This simplified model can also produce reasonable approximations in some specific cases.

5.1.2.2 The Polubarinova-Galin equation

While studies of the Hele-Shaw flow provided interesting analogies for microfluidic effects, it was *Polubarinova-Kochina* and *Galin* who independently recognized that the

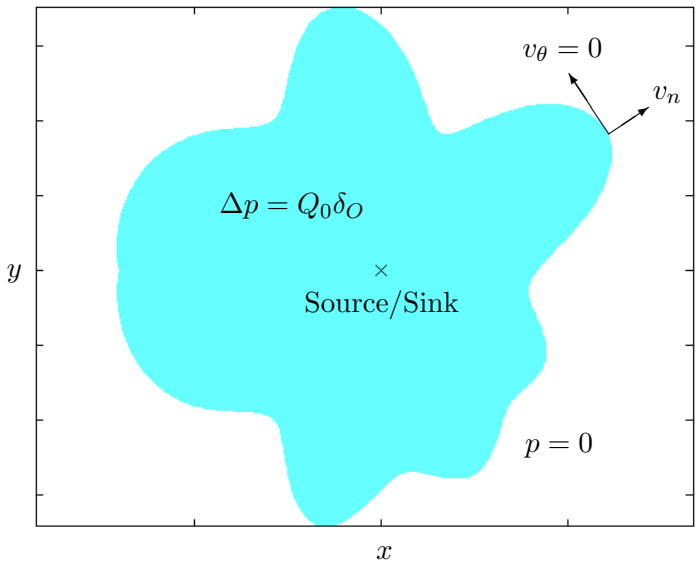

FIGURE 5.2: Problem formulation for a Hele-Shaw cell with free moving boundary. The system is governed by the fluid pressure, which is defined by a Laplace equation in the fluid, and a zero pressure boundary condition. Boundary evolution is defined by its movement in the normal direction (no rotation).

free boundary formulation of the problem, with a finite pointwise source/sink, had potential applications to the oil industry [64, 179, 223]. This setup is typically labeled as the Hele-Shaw cell.

In this case we choose to examine the dimensionless form of the pressure, such that $p = 0$ corresponds to atmospheric pressure, immediately yielding the zero surface tension dynamic boundary condition:

$$p(z,t) = 0 \quad \forall \quad z \in \Gamma(t) = \delta\Omega(t), \quad z = x + iy, \tag{5.9}$$

where $\Omega(t)$ indicates the domain of the fluid with free moving boundary $\Gamma(t) = \delta\Omega(t)$. Additionally, the Hele-Shaw equation can be reduced to the Laplace equation. Incorporating the assumption that there is no rotation on the boundary provides the kinematic boundary condition $(5.11)_1$ (i.e. the free boundary evolution is defined by its normal velocity). Combining these elements, the free boundary problem will be formulated as follows:

$$\Delta p = Q_0 \delta_O(z), \quad z \in \Omega(t), \tag{5.10}$$

$$v_n = \mathbf{v}|_{\Gamma(t)}.\mathbf{n}(t), \quad \left.\frac{\partial p}{\partial \mathbf{n}}\right|_{z\in\Gamma(t)} = -v_n, \tag{5.11}$$

here Q_0 is the strength of the fluid source/sink, δ_O is the Dirac measure centered on the fluid source/sink at point $O \in \Omega(t)$ and $\mathbf{n}$ denotes the normal vector. A diagram of this initial problem setup is provided in Fig. 5.2.

We note that the Laplace equation directly implies that this problem can be examined through the use of a Green's function, transforming (5.8) into:

$$\frac{\partial \mathbf{w}}{dt} = -\frac{Q_0 h^2}{12\mu} \nabla \mathcal{G}(\mathbf{w}; \mathbf{O}; t), \tag{5.12}$$

with $\mathcal{G}(\mathbf{w}; \mathbf{O}; t)$ being the Green's function for the problem.

In addition to being described by a Green's function, as the fluid flow is incompressible and non-rotating we can introduce a complex potential $W(z,t)$, $\Re(W) = p$ to describe this problem. The real part of will satisfy the Dirichlet problem given by (5.9) and (5.10), while being a multi-valued analytic function on $\Omega(t)$ for each fixed t. We can now utilize the Cauchy-Riemann equations:

$$\frac{\partial W}{\partial z} = \frac{\partial p}{\partial x} - i\frac{\partial p}{\partial y}. \tag{5.13}$$

Further, as we have already noted that a Green's function can be used to describe the problem, it immediately follows that the complex potential can be represented in the form:

$$W(z,t) = \frac{Q_0}{2\pi} \log(z) + w_0(z,t), \tag{5.14}$$

where $w_0(z,t)$ is an analytic regular function in $\Omega(t)$.

In order to make full use of the complex potential, we introduce a conformal mapping $f(\zeta, t) : \mathbb{U} \to \Omega(t)$, where $\mathbb{U} = \{\zeta \in \mathbb{C} : |\zeta| < 1\}$ is the unit disk. We specify that this mapping will have the properties that: $f(0,t) = 0$ and $\partial_z f(0,t) > 0$, while the fluid boundary can now be defined as: $\Gamma(t) = \left\{ f(e^{i\theta}, t) : \theta \in [0, 2\pi) \right\}$. The conformal mapping will also have an associated inverse $g(z,t) : \Omega(t) \to \mathbb{U}$ (more detail on conformal mappings can be found in Sect. 5.1.2.4).

With this notation in place, noting the definition of the outward normal to the boundary, equation $(5.11)_1$ yields the normal velocity:

$$v_n = -\Re\left(\frac{\partial W}{\partial \zeta} \zeta \frac{\partial_\zeta f(\zeta, t)}{|\partial_\zeta f(\zeta, t)|} \right). \tag{5.15}$$

We can also take advantage of the fact that the Green's function is invariant under conformal mapping, from which (5.14) gives:

$$(W \circ f)(\zeta, t) = \frac{Q_0}{2\pi} \log(\zeta), \quad \frac{\partial W}{\partial \zeta} \frac{\partial f}{\partial \zeta}(\zeta, t) = \frac{Q_0}{2\pi\zeta}. \tag{5.16}$$

With a little manipulation, combining the above yields the *Polubarinova-Galin equation*:

$$\Re\left[\frac{1}{\zeta}\frac{\partial f}{\partial t}\frac{\overline{\partial_\zeta f(\zeta,t)}}{|\partial_\zeta f(\zeta,t)|}\right] = -\frac{Q_0(t)}{2\pi}, \quad |\zeta| = 1, \tag{5.17}$$

it should be noted that, in some texts within the literature, the sign of Q_0 is reversed to eliminate the negative term on the right hand side. The significance of this equation is that it places stipulations on the form a conformal mapping can take whilst still describing the evolution of the fluid boundary over time in the Hele-Shaw cell. This allowed *Polubarinova-Kochina* [178, 179] and *Galin* [64] to independently develop the first non-trivial solutions to the problem. The exact form of these solutions, alongside several more recent efforts, are outlined in [86].

5.1.2.3 Modeling inclusions and particles

The study of the Hele-Shaw cell containing obstacles and particles is a rich field, in part due to the fact that the cell itself is typically inexpensive to create, and can easily be modified to provide a suitable allegory for various different practical applications. Here we attempt to provide a brief overview of the works and approaches which are most relevant to this particular investigation, namely those which incorporate a moving fluid boundary and have the fluid entering the cell through a source/sink within the fluid domain.

Recent investigations into the growth of the free flowing boundary in Hele-Shaw problems with inclusions, or in constricted domains, finds its origins in the work of *Richardson* [186]. This initial paper intended to extend the previous theories to model injection moulds, namely to obtain the optimal position for placing air vents at the last places to be filled by the fluid. Since then *Richardson* has published numerous papers on the topic, building up the methods utilized by many of the researchers in the field [187–189].

Alongside this, a small number of computation solutions for obstacles in the Hele-Shaw cell have begun to appear in recent years. There was the notable paper by *McDonald* [141], which obtained approximate solutions for the Hele-Shaw flow in a half-plane, or in the case of a circular inclusion. An alternative approach to modeling the Hele-Shaw cell with inclusions was provided by *Bogoyavlenskiy & Cotts*, which utilized a random walk approach to simulate the fluid/gas interactions around a solid obstacle at the edge of the fluid domain, with a variety of differently shaped obstacles being examined [24]. It should be noted however that the accuracy of this approach is not universally accepted (for example the comment and author's response to the original paper in [25, 222]).

The first exact analytical solutions for the Hele-Shaw cell containing a stationary inclusion were provided very recently by *Marshall*, both for the case of a circular obstacle [136], as well as for a wall of finite length [137]. These solutions were obtained by considering the Schwarz function of the free boundary, which alongside the construction of auxiliary functions and resolving a related Schwarz problem, allowed for the final representation of the conformal mapping to be given in integral form. To the best knowledge of the author, these remain the only exact solutions obtained for obstacles in the Hele-Shaw cell[1].

The possibility for a new asymptotics based approach was provided by *Maz'ya, Movchan & Nieves* in [138, 139]. Here they detailed method of examining the boundary growth in a domain containing several holes or inclusions. These developments were subsequently modified and applied to the Hele-Shaw cell in the recent papers by *Mishuris, Rogosin & Wrobel* [145, 146], with the notable advantage of being able to model both a stationary and moving inclusion. This was achieved using equation (5.12), with the Green's function updated to incorporate both the Neumann and Dirichlet conditions resulting from the particles inclusion. It was assumed to take the form:

$$\begin{aligned}\mathcal{G}_\epsilon(\mathbf{x};\mathbf{O}) = \mathcal{G}(\mathbf{x};\mathbf{O}) + \mathcal{N}\left(\frac{\mathbf{x}-\mathbf{z}_0}{\epsilon}, \frac{\mathbf{O}-\mathbf{z}_0}{\epsilon}\right) + \frac{1}{2\pi}\log\left|\frac{\mathbf{x}-\mathbf{O}}{\epsilon}\right| \\ + \epsilon\mathcal{D}\left(\frac{\mathbf{x}-\mathbf{z}_0}{\epsilon}\right).\nabla_{\mathbf{x}}H\left(\mathbf{z}_0,\mathbf{O}\right) + \epsilon\mathcal{D}\left(\frac{\mathbf{O}-\mathbf{z}_0}{\epsilon}\right).\nabla_{\mathbf{O}}H\left(\mathbf{x},\mathbf{z}_0\right) + \mathbf{r}_\epsilon(\mathbf{x},\mathbf{O}),\end{aligned} \tag{5.18}$$

where:

- the inclusion is defined by its radius $\epsilon \ll 1$ (relative to the size of the fluid domain) and center $\mathbf{z}_0 = (z_{0,x}(t), z_{0,y}(t))$.
- $|\mathbf{r}_\epsilon(\mathbf{x},\mathbf{O})| \leq Const{\cdot}\epsilon^2$ is the remainder term for the asymptotic expansion, ensuring a high level of approximation accuracy for small inclusions.
- $\mathcal{N}$ provides the Neumann function for the exterior of the re-scaled obstacle, which is analogous to calculating the effect of the circular particle on the streamlines for the fluid flow (see Fig. 5.3). Note that properly incorporating this effect requires incorporating a log term (following the $\mathcal{N}$ in (5.18)), which acts as a correction term.
- $\mathcal{D}$ gives the Dirichlet data on the boundary of the fluid domain. This describes how the solution to the standard Dirichlet problem for the Hele-Shaw cell with a free-moving boundary (5.9)-(5.10) (see also Fig. 5.2) has to be updated to account

[1] Other solutions for the Hele-Shaw cell containing particles exist, e.g. [180], however these focus only on the effect of the Stokes flow on the particle, and provide no information about the fluid boundary.

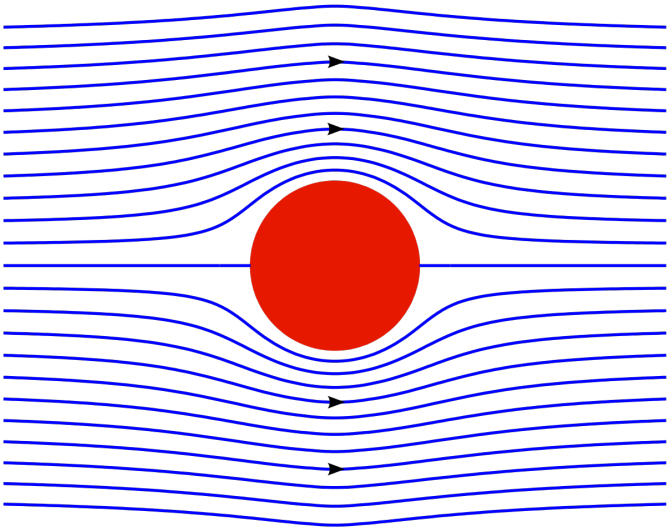

FIGURE 5.3: Streamlines around a circle cylinder without turbulent effects (e.g. in the Hele-Shaw flow). As the flow is anti-symmetric around the particle it will not induce rotation (Credit: Wikimedia commons).

for the transmission conditions resulting from the particles inclusion. This term appears twice in order to satisfy the necessary symmetry conditions (i.e. if the x and y coordinates are switched, that the solution will remain the same subject to the corresponding transformation).

- $\mathcal{G}$, H are the Green's function for the fluid domain in the absence of inclusions alongside its regular part (respectively).

A more rigorous definition of each component is provided in [146]. Furthermore, this approach can be extended to objects in three dimensions (as opposed to the quasi-2D formulation of the Hele-Shaw cell), as outlined by *Nieves* in [155].

In addition to the above, a secondary equation, dictating the movement of the particle in the cell, is obtained using Newton's equation of motion while accounting for the drag caused by the contact between the circular inclusion and the cell walls. This equation will therefore take the form:

$$m\mathbf{z}_0'' = \int_{\Gamma_\epsilon} p(s)\, ds - \kappa\pi\epsilon^2\mathbf{z}_0', \tag{5.19}$$

with κ being the friction coefficient of the particle with the plates of the Hele-Shaw cell, while the integral provides the hydrodynamic forces acting on the particle boundary. Simplifying this, and replacing the pressure term with the corresponding Green's function approximation ($p = Q_0\mathcal{G}$), the final equation for particle motion will be provided

by:

$$\mathbf{z}_0'' + \frac{\kappa\pi\epsilon^2}{m}\mathbf{z}_0' = \frac{Q_0\epsilon}{m}\int_0^{2\pi} \mathcal{G}_\epsilon\left(z_{0,x} + \epsilon\cos\theta, z_{0,y} + \epsilon\sin\theta; \mathbf{O}; t\right).\mathbf{n}^{(in)}(\theta)\, d\theta, \tag{5.20}$$

$$\mathbf{z}_0(0) = \mathbf{z}^{(0)}, \quad \mathbf{z}_0'(0) = \mathbf{z}^{(1)}, \tag{5.21}$$

and $\mathbf{n}^{(in)}$ denoting the internal normal vector on the boundary of the inclusion. It should be noted that the particle was assumed circular, and as such non-rotating due to: i) the flow being anti-symmetric on the particle boundary, causing rotational effects induced by the flow to cancel out (see Fig. 5.3), ii) the inclusion being asymptotically small, meaning that the pressure exerted by the fluid around the particle boundary can be typically assumed constant (i.e. rotation will not result from hydrodynamic forces alone).

5.1.2.4 The Schwarz-Christoffel mapping

When using the asymptotic methods outlined in the previous subsection, the end result is a system of ordinary differential equations, which must then be resolved numerically. Because of this, the evolving fluid boundary has to be replaced with a discrete approximation, which is achieved using a series of boundary nodes. Computing the final system is complicated by the fact that the differential equations involved contain conformal mappings. While multiple techniques exist to incorporate such transformations (for a review of several, see e.g. [88]), here we will focus on utilizing the *Schwarz-Christoffel* mapping. A detailed explanation of the theory behind, and implementation of, this mapping can be found in [54], while a brief outline will be provided below.

To describe the process, the conformal mapping must first be defined. For some arbitrary domain $\Omega \in \mathbb{R}^2$, this will be a function $g(x, y) : \Omega \to \mathbb{U}$, where $\mathbb{U}$ denotes the unit circle. We will label the unique inverse mapping $g^{-1}(\varsigma, \zeta)$ (see Fig. 5.4).

Then, the *Schwarz-Christoffel* mapping begins by approximating the boundary using a series of discrete nodal points, which we will label $w_1, \ldots, w_N$. It can be shown that the mapping from the unit circle, defined by nodal points $z_1, \ldots, z_N$, to this boundary can be described by the equation:

$$g^{-1}(z) = A + C\int^z \prod_{k=1}^{N}\left(1 - \frac{\xi}{z_k}\right)^{\alpha_k - 1} d\xi, \quad A, C \in \mathbb{C}, \tag{5.22}$$

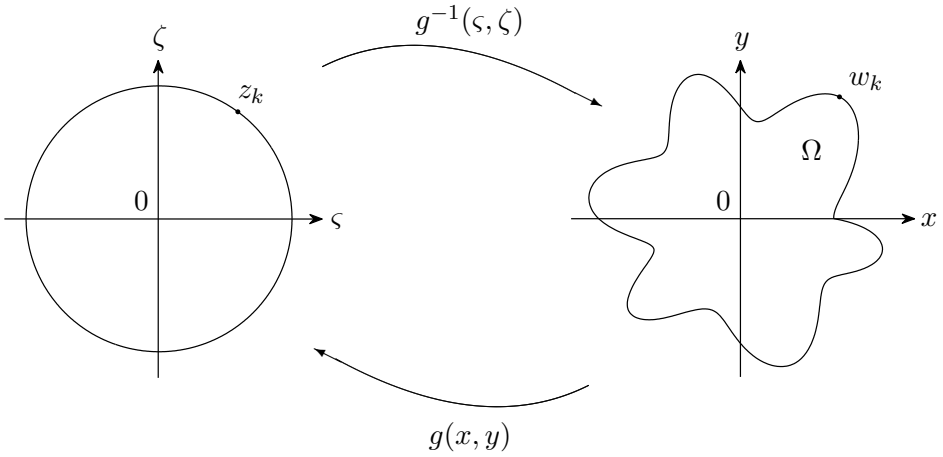

FIGURE 5.4: Diagram illustrating the conformal mapping from an arbitrarily shaped domain to the unit circle. Here the map $g(x,y)$ transforms the point w_k to an associated nodal point on the unit circle, denoted z_k. The unique inverse transform g^{-1} allows the original system to be obtained from the data about the unit circle.

where we have $w_k = g^{-1}(z_k)$. The constants α_k take values in the range $0 < \alpha_k \leq 2$ for finite valued w_k, subject to the following constraint:

$$\sum_{k=1}^{N} \alpha_k = N - 2, \tag{5.23}$$

The constant A describes the location of the center of the domain; in the case of the Hele-Shaw cell the position of the fluid source **O**. It should be noted that the most computationally intensive step when resolving this mapping is obtaining the integral in (5.22). Unfortunately, no general equation exists for calculating the inverse transformation $g(w)$. Instead, numerical techniques must be employed, the two most common of which are outlined in [217].

In this work, the mapping is implemented using the *Schwarz-Christoffel toolbox* created by *Driscoll* [52, 53] for use in a MatLab environment. Several numerical techniques are utilized to ensure that this toolbox is employed as efficiently and effectively as possible, the most important of which is briefly detailed below.

One problem encountered when computing solutions to the final system of equations (provided in Sect. 5.2.4.1) is that both the conformal mapping and its derivative need to be computed. In the case of a regularly shaped fluid domain (e.g. a unit circle) this is not an issue, however for more irregular shaped domains the approximation of the derivative obtained for the conformal mapping may be well below that needed to ensure accurate computations in certain cases (in particular, when low numbers of boundary nodes, i.e. 20 or fewer, are being utilized). By way of illustration, imagine approximating the shape

provided in the right hand side of Fig. 5.4 using only a small number of nodal points. It is clear that not all of the shapes complexity will be incorporated, and approximations of the derivative will likely be inaccurate for at least a portion of the domain.

To combat this issue, the derivatives are instead transformed to be calculated from the inverse mapping. As a result, computations take place on the unit circle, providing a far better approximation when a smaller number of boundary nodes are used, and as such yielding a more accurate result for the derivative. Interestingly, this approach also means that, when shapes such as the unit circle are approximated using this scheme, the results provided for the conformal mapping will be highly accurate even when only a small number of boundary nodes are utilized. The accuracy achieved by the scheme, and consequences of utilizing this particular transformation, will be outlined in more detail in Sect. 5.2.5.1.

5.1.3 Alternative approaches to modeling the Hele-Shaw cell

In studies of the classical Hele-Shaw cell, in the case of fluid injection without obstacles, approaches based on the *Polubarinova-Galin* equation are the most regularly utilized for studies of the Hele-Shaw cell with a free moving boundary (except perhaps for unstable configurations, such as the fingering effect), however they are not alone. One recently introduced method instead constructs the problem as an equivalent minimisation problem in the L^1 norm [216]. The final numerical algorithm is able to resolve the movement of the free boundary with great efficiency and to a high level of accuracy. Unfortunately, possibly because this approach is fairly new and underdeveloped, it is only valid in stable, well-posed cases. As such, it doesn't present a significant improvement on previous methods at the current time.

Many of the alternative avenues of investigation of the Hele-Shaw cell focus on the so-called fingering effect (sometimes referred to as *Saffman-Taylor* instability [194]). This occurs when there is an initial fluid within the Hele-Shaw cell, into which a second, less viscous, fluid is subsequently injected. Modeling the resulting growing interface between the two fluids is an ill-posed problem in the case of a fluid sink (although can be well-posed for a fluid source), and as such can only be investigated using the methods described above for a small class of initial configurations [8]. It should be noted that understanding this phenomena would be of great benefit in the study of hydraulic fracturing, where the fingering effect can cause significant difficulties during the secondary displacement processes involved in oil recovery [79].

One such approach is to examine the Hele-Shaw moving boundary problem through the use of kinetic undercooling regularization techniques [100, 183, 191]. This works by

placing an additional constraint on the pressure at the fluid boundary, which is linked to its rate of change. This small change in the problem formulation can lead to the problem becoming well-posed in the case of fluid suction, or when investigating the fingering effect, which it was not previously [71]. It should be noted that the utilization of this condition has already been used to describe small bubbles in the Hele-Shaw cell [45]. It can also be combined with the asymptotic formulation provided in Sect. 5.1.2.3 to provide a more stable and accurate approach to modeling inclusions within the fluid, although work towards this is still ongoing [190].

In spite of such approaches, theory has often struggled to explain crucial features in the results [40], which are often only identified through the numerous experiments that have been conducted into Saffman-Taylor problems (e.g. [140, 181, 211]). Because of this, a more general examination often requires highly accurate numerical algorithms, for example: [41, 99, 102].

There are however downsides to these approaches, which prevent their use attempting to model large numbers of small inclusions, as proposed here. Most notably, such an approach would clearly be too computationally intensive to produce accurate results within a reasonable time frame using current methods, and would certainly struggle to produce the large number of solutions required for an investigation of the kind outlined in Appendix. G (for investigating the relationship between the volume fraction of particles within the fluid and the apparent viscosity). For this reason, the most practical method of completing this task is through extending representation (5.18) to cover multiple inclusions.

5.1.4 Practical applications of modeling particles in the Hele-Shaw cell

5.1.4.1 Hydraulic fracturing and the Hele-Shaw cell

It has already been noted in Sect. 4.1.3.1 that the formulation of the governing equations of the fluid in HF rely on mostly identical assumptions to those used in the Hele-Shaw cell. Namely, they begin by approximating an incompressible fluid flowing between two parallel plates, with a no slip condition on the solid boundaries, and the velocity of the fluid front is assumed to have a parabolic distribution. In both cases there is a moving boundary, defined by a Stefan-type condition (outlined in Sect. 2.2). In addition, the Reynolds equation in both cases, provided by (4.33) and (5.12), are both inherently non-linear. The key difference between the cases is only in the form of the solid boundaries, which are assumed to be elastic in the case of HF, while perfectly rigid for the Hele-Shaw cell.

When noting the similarities in the formulation of these problems, it is unsuprising that the Hele-Shaw cell has been seen as a useful analogy for problems in the oil industry for some time [64, 179, 223], including hydraulic fracturing (see e.g. [194]). One crucial application is to study the behaviour of granular material in confined spaces, analogous to the proppant particles which form a key component of the fluids used during HF [42, 55, 135]. This is particularly important during the flowback stage, which occurs when draining fluids from hydraulic fractures, as clumping of the material can lead to a blockage. A good review of this topic can be found in [158].

Additionally, understanding the influence of the proppant on fluid behaviour at the fracture tip is of critical importance, especially in the cases with fluid lag or piecewise extension of the crack, where the narrow channel geometry will be well approximated by the Hele-Shaw cell. One particular parameter which is poorly understood is the apparent viscosity of the fracturing fluid. The fact that the apparent viscosity may vary throughout the medium has previously been utilized in studies of two or three-phase porous media, where the fracture is approximated using a Hele-Shaw cell [48, 75, 193]. However, little work has been carried out to determine the relation between the proppant volume fracture and the apparent viscosity at the crack tip. This problem is exacerbated by the fact that there is no clear concensus as to the most accurate form of this parameter even in the general case. A more thorough discussion of the apparent viscosity, and potential methods of using the model presented here to examine it, are presented in Appendix. G.

5.1.4.2 Injection moulding

One of the key motivations provided in the literature for modeling inclusions in the Hele-Shaw cell is its applications in the plastics industry. The most frequently noted example is that of injection moulding, where a high viscosity fluid is pumped through a strategically placed hole into a mould of prescribed shape. During the injection process air must be allowed to escape from the mould, and as such vents must be properly placed around the mould at the locations which will be the last to be filled by the fluid. In the simple case this reduces to studying the free moving boundary of a Hele-Shaw cell containing stationary obstacles (see [186] for a more extensive description).

Previously developed models, discussed in Sect. 5.1.2.3, have allowed for the growth of the fluid boundary to be known in the case of a single inclusion or wall. However none of the methods typically applied in the study of injection moulding are able to examine the case with multiple inclusions (i.e. more than one vent in the plastic mould), which greatly restricts the mould geometries which could be examined. The method presented

here will therefore provide a considerable extension to the utilization of the Hele-Shaw cell in this case.

5.1.4.3 Biology and biomedical experiments

The use of microfluidic devices, including so called 'lab on a chip' technology, has been a growing trend in the field of experimental biology over the last few decades, with multiple journals devoted to its study. One particular example is the case of biomedicine, where such devices were initially used to produce a large number of near-perfect spheres, uniformly coated in a desired pharmaceutical substance, quickly and at a very low cost. Since then, such systems have evolved to allow experimentation on numerous moving micro-scale objects (e.g. red blood cells) simultaneously, and with a greater level of control than might otherwise be possible. The recent colllection of papers edited by *Li & Zhou* [126] provides a good introduction to some of these applications.

Many of these 'lab on a chip' devices are Hele-Shaw cells in all but name, relying on the unique properties of a fluid whose movement is constrained in one dimension (see e.g. [57, 212]). Given this, it is somewhat unsuprising that interest in the Hele-Shaw cell has also been growing within these fields in recent years.

One such experimental paper is the work of *Abbyad et al* [1], which not only utilized the Hele-Shaw cell to conduct repeatable experiments on red blood cells, but also outlined new techniques for increasing the level of control the operator had over the design of the experiment. Namely, they demonstrated that through small alterations to the height of the plates in specific areas (referred to as 'anchors'), or etching a groove in the plates of the cell (referred to as 'rails'), any droplets or cells flowing through the medium could be either held in place or directed to follow a prescribed path. Further, by anchoring a specific cell in place, the fluid flowing through the Hele-Shaw cell could be used to regulate its environment. *Abbyad et al* demonstrated this by anchoring a red blood cell beneath a microscope, and cyclically increasing and decreasing the oxygen levels surrounding it, allowing them to reproduce and study the sickling of the cells.

While experiments such as these do not include a moving fluid boundary, it is clearly advantageous to be able to predict in advance the fluid flow around the inclusions within the fluid, for example to ensure the even distribution of any substance added to the medium. It should be noted however, that any successful model to fully describe the more complicated 'lab on a chip' designs would also need to incorporate the effect of walls within the fluid. As such, the approach provided here can at present only be utilized for simple cases, such as the above reference paper, with further additions required to fully describe more complicated experiments.

Finally, the method utilized here to represent inelastic collisions means that the model may be used to examine problems where particles coalesce (or clump), such as the study of biological systems where agglutination occurs.

5.2 Multiple obstacles and moving particles in the Hele-Shaw flow

5.2.1 Introduction and outline

We consider a slow viscous flow in a narrow space between two parallel plates in presence of various fixed or moving obstacles. The model is a modification of the well-known Hele-Shaw moving boundary value problem, which in turn is an analogous to a one-phase Stefan problem, and is a special case of the Navier-Stokes problem (see Sect. 2.2.2 & 5.1.2.1).

It is supposed that the driving mechanism for the flow is a one-point source/sink. The movement of particles in the flow depends not only on the source/sink intensity, but also on the friction between obstacles and plates, as well as on the particle interaction. In addition, particle collisions must also be accounted for, however this can be approximated to a reasonable level of accuracy during numerical implementation, and as such will not be directly incorporated into the analytical model.

Such an investigation is achieved by reducing the problem to a mixed boundary value problem for the Laplace equation in a multiply connected domain. Supposing the existence of moving particles in the flow, we have to add extra equations describing this movement (also accounting for the different friction properties of the particles). Its geometric solution (parametrization of the moving front and trajectories of the moving particles) is sought from equations given in terms of the Green's function for the above mixed boundary value problem.

The primary theoretical tool is an asymptotic analysis of the model based on the approximation of the Green's function. This is obtained using the methods developed by *Maz'ya, Movchan & Nieves*, who provided several uniform asymptotic formulas for Green's functions related to different boundary value problems for a number of differential operators in the case of singular perturbations of the domain [138, 139]. The relevant formulation for the case of a single particle was given by *Mishuris, Rogosin & Wrobel* [145, 146], and is provided here as (5.18)-(5.21) (see Sect. 5.1.2.3).

The intention of this work is to extended these results to the case of a Hele-Shaw cell containing numerous small inclusions. This requires extending the asymptotic formulation,

however the main body of the work is involved in developing a new numerical scheme to accurately simulate the effect of multiple particle inclusion on the moving fluid boundary. Of significant importance is ensuring that the computation times remain reasonable without reducing solution accuracy (even when hundreds of asymptotically small particles are within the fluid), enforcing the previous and newly introduced assumptions of the model, and achieving all of this in such a way as to allow for the potential incorporation of inter-particle effects (although these will not be fully introduced here). In doing so, it must be demonstrated that the developed method continues to provide comparably good results.

The motivation behind this is primarily for use as an analogy to slurry flow in hydraulic fracturing, most notably at the fracture tip. In particular, by taking an axisymmetrical initial fluid domain containing inclusions, it is possible to examine the relationship between the volume fraction of the system and the apparent viscosity. An initial outline of the key concepts, as well as the methodology which would be used to investigate such a relationship, is provided in Appendix. G.

This chapter is organised as follows. The problem is formulated in Sect. 5.2.2, with the final set of equations describing the model being collected under the title **Problem $\mathbf{HS_M}$**. Next, a modified form of the *Mazya-Movchan-Nieves* formula for the Green's function of a mixed boundary value problem for the Laplace equation is presented in Sect. 5.2.3. It accounts for all the geometrical and physical assumptions of the considered model. The components of the proposed uniform asymptotic formula are also presented in this chapter. The full nature and possible representations of the asymptotic formula is similar to that provided in [145, 146], and as such will not be fully examined in this text[2].

The final system of equations is presented in Sect. 5.2.4.1, with an explanation of the computer model developed to solve the approximate system being provided in Sect. 5.2.4.2. The accuracy of the computational model is examined in Sect. 5.2.5. This is followed by an examination of numerical simulations involving different scenarios for the particles movement, in particular noting the effect of the inclusions on the fluid flow.

5.2.2 Problem formulation

We consider a two-dimensional potential flow of viscous incompressible fluid in the Hele-Shaw cell, caused by a source/sink placed at the origin 0. There are a finite number of

[2] A full explanation of the steps taken is available in the supplementary material of the published paper.

rigid obstacles in the flow, which is supposed to be very slow. Each obstacle is moving without rotation due to the pressure in the flow. Their movement can be faster or slower depending on specific friction between an obstacle and the plates of the Hele-Shaw cell.

Let us denote the domain containing the fluid and particles by $\Omega(t) \ni 0$, which will be an open simply connected domain encircled by the free boundary $\Gamma(t) = \partial\Omega(t)$ at each time instant $t \geq 0$. We study the flow over an, in principle, unknown time interval $I = [0, T]$. Here the maximum permissible value of time T will correspond with the blow-up time of any potential solution (i.e. this may correspond with the moment when the conformal mapping begins to experience cusp formation, or the solution breaks down in some other capacity), and this time may be rather small, particularly in the case of a fluid sink (extraction of the fluid).

The fluid is assumed to contain M obstacles, represented by closed subdomains of $\Omega(t)$. Each of these are assumed to have a fixed circle-cylinder shape, and as such can be defined in terms of their radius, denoted ε_k, alongside their moving or stationary center, given by $\mathbf{z}_k(t)$. The closed subdomains can therefore be defined as: $F_k(t) := \{\mathbf{z} \in \mathbb{R}^2 : |\mathbf{z} - \mathbf{z}_k(t)| \leq \varepsilon_k\}$, $k = 1, \ldots, M$. Meanwhile, the corresponding domain occupied by the fluid is denoted $\Omega_M(t) = \Omega(t) \setminus \bigcup_{k=1}^{M} F_k$.

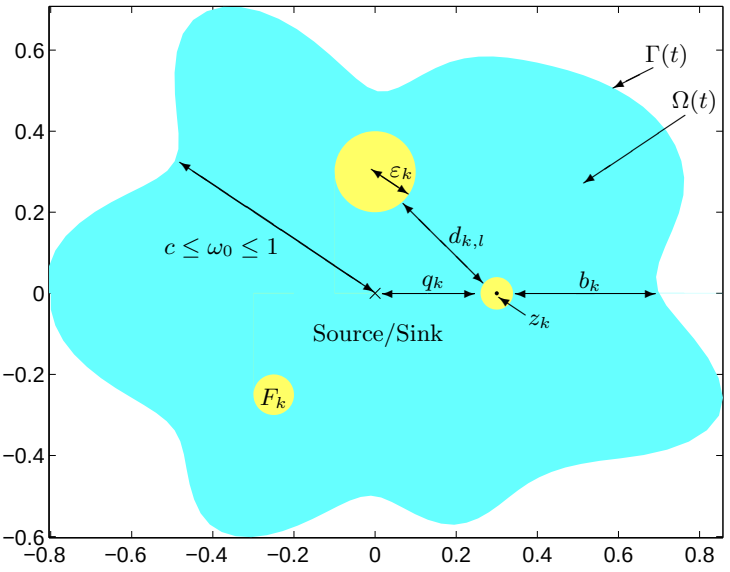

FIGURE 5.5: Diagram of the initial configuration of the Hele-Shaw cell for an arbitrary domain Ω. Here $\omega_0 = dist\{\mathbf{0}, \Gamma(0)\}$.

This formulation is demonstrated graphically in Fig. 5.5, as well as certain natural assumptions which the parameters of the initial geometry must satisfy[3]:

1. **Particle distribution:**
   - The initial distribution of the particles/obstacles must not place them too close to the boundary, with the minimum distance determined by the radius of the particle. Stated explicitly: $dist\{\delta F_k(0), \delta\Omega(0)\} = b_k > \varepsilon_k$.
   - Similarly the obstacles/particles must not come too close to the source/sink, with the radius of the particle determining the minimum: $dist\{\delta F_k(0), \mathbf{0}\} = q_k > \varepsilon_k$.
   - The inclusions must not overlap with each other, this can be stated as $\bigcap_{k=1}^{M} F_k = \emptyset$. More explicitly we have, for all $k, l = 1, \ldots, M$, $k \neq l$, $t \in I$: $: d_{k,l} = |z_k(t) - z_l(t)| > \varepsilon_k + \varepsilon_l$
2. **Domain size:** The characteristic size of the initial domain $\Omega(0)$ is of order 1, with bounds on the minimum and maximum initial distance as follows: $0 < c \leq \min dist\{0, \Omega(0)\} \leq \max dist\{0, \Omega(0)\} \leq 1$, where $c < b_k + 2\varepsilon_k$.

It is convenient to re-scale the domains F_k by introducing new variables:

$$\xi_k = \frac{1}{\varepsilon_k} (\mathbf{x} - \mathbf{z}_k), \tag{5.24}$$

as a result of this transformation, the domain of each particle being considered (previously F_k) will now be represented by a unit circle centered on the origin, which can be represented by defining the updated domain:

$$F_0(t) := B(O; 1), \tag{5.25}$$

which will allow us to obtain a generalized formulae for the effect of each inclusion on the boundary. It should be noted however that the variable ξ_k will be different for each particle, which must be accounted for when using this simplification to obtain solutions.

In order to ensure regularity of the boundary with time (that it is smooth and does not experience solution blow-up before time T), we impose the following initial condition on the boundary (this is often referred to as the maximum regularity assertion, see [9]):

$$\partial\Omega(0) \in \mathcal{C}^{2,\alpha}, \quad 0 < \alpha < 1, \tag{5.26}$$

[3]It is worth noting that the constants c, b_k, $d_{k,l}$ and q_k aren't dependent on any individual ε_k.

where $\mathcal{C}^{2,\alpha}$ represents the space of functions which are Hölder continuous (i.e. in this case the boundary is continuous twice differentiable).

Now we are at the position to formulate our problem (compare with: [87], [97]), which is a generalization of the models considered in [145], [146]. Note that we will first explicitly state each part of the problem using the standard notation, before providing a more detailed explanation below.

Problem $\mathbf{HS_M}$. Find $2M+3$ unknown real-valued functions
$\{\mathbf{w}(s,t);\ \mathcal{G}(\mathbf{z};\zeta;t);\mathbf{z}_1(t),\dots,\mathbf{z}_M(t)\}$, where $\mathbf{z}_k(t)=(z_{k,1}(t),z_{k,2}(t))$,
$k=1,\dots,M$, and $\mathbf{w}(s,t)=(w_1(s,t),w_2(s,t)):\partial\mathbb{U}\times I\to\mathbb{R}^2$ satisfying[4]

1. $\mathbf{w}(s,t)\in\Gamma(t)$ for all $(s,t)\in\partial\mathbb{U}\times I$.
   Here the function $\mathbf{w}$ defines a mapping from the boundary of a unit circle to the free-moving boundary of the fluid, over the prescribed time interval I. This term will be used to model the growth of the fluid boundary.

2. $\mathbf{w}(\cdot,t):\partial\mathbb{U}\to\Gamma(t)$ is a $\mathcal{C}^2$-diffeomorphism for each fixed $t\in I$.
   The function $\mathbf{w}$, defining the growth of the fluid boundary, must abide by the previously stated regularity condition (5.26). That is to say it will be continuous twice differentiable at all points in time over the interval I.

3. $\mathbf{w}^{(0)}(s)=\mathbf{w}(s,0)$ is a given $\mathcal{C}^2$-diffeomorphism of the unit circle $\partial\mathbb{U}$, which describes the boundary $\Gamma(0)$ of initial domain $\Omega_M(0)$.
   This will be the (known) initial condition for the function $\mathbf{w}$, which ensures that it corresponds to the boundary $\Gamma(0)$ which we wish to model.

4. $\mathcal{G}(\mathbf{z};\zeta;t)$ is Green's function of the operator $-\triangle$ subject to the mixed boundary value problem, i.e. for each fixed $t\in I$:

$$\Delta\mathcal{G}(\mathbf{z};\zeta;t)+\delta(\mathbf{z}-\zeta)=0,\ \mathbf{z},\zeta\in\Omega_M(t);$$

$$\mathcal{G}(\mathbf{z};\zeta;t)=0,\ z\in\Gamma(t),\zeta\in\Omega_M(t);$$

$$\frac{\partial\mathcal{G}(\mathbf{z};\zeta;t)}{\partial n_{\mathbf{z}}}=0,\ z\in\partial F_k(t),\zeta\in\Omega_N(t),k=1,\dots,M;$$

   This is the definition of the Green's function for this problem. These are simply a restatement of the classical definition of the Hele-Shaw problem, detailed previously by (5.9)-(5.11) in Sect. 5.1.2.2, taking the Green's function to be related to the fluid pressure by: $p=Q_0\mathcal{G}$.

[4] Unknown magnitudes $\mathbf{w}$, $\mathcal{G}$, $\mathbf{z}_0$ depend on time t from a right-sided neighborhood I of $t=0$. In fact, for our problem we need to determine the value of $\mathcal{G}(\mathbf{z};\zeta;t)$ only at the point $\zeta=O$, but we keep the extra variable ζ for computational reasons.

5. $\partial_t \mathbf{w}(s,t) = -\frac{Q_0 h^2}{12\mu} \cdot \nabla \mathcal{G}(\mathbf{w}(s,t); O; t)$ for all $(s,t) \in \partial\,\mathbb{U} \times I$.
   The Stefan-type governing equation for the evolution of the fluid boundary over time. The way in which this is derived from the Navier-Stokes equation was detailed in Sect. 5.1.2.1, while the final form shown here again follows from replacing the pressure with the Green's function.

6. $\frac{d^2\mathbf{z}_k(t)}{dt^2} + \frac{\kappa_k \pi \varepsilon_k^2}{m_k}\frac{d\mathbf{z}_k(t)}{dt} = \frac{Q_0 \varepsilon_k}{m_k}\int\limits_0^{2\pi} \mathcal{G}(z_{k,1}(t) + \varepsilon_k \cos\theta, z_{k,2}(t) + \varepsilon_k \sin\theta; \zeta; t) \cdot \mathbf{n}^{(k)}(\theta) d\theta;$
   This is the equation determining the movement of the particles within the Hele-Shaw cell over time. It is obtained identically to the case of a single inclusion (outlined in Sect. 5.1.2.3), utilizing Newton's law of motion while accounting for the drag between the particle and the walls of the cell, as well as noting the relationship between the fluid pressure and the Green's function.

7. $\mathbf{z}_k(0) = \mathbf{z}_k^{(0)}$, $\mathbf{z}_k'(0) = \mathbf{z}_k^{(1)}$.
   The (known) initial conditions governing the movement of the particles.

Here h is the width of the Hele-Shaw cell, μ is viscosity coefficient of fluid in the cell, Q_0 is the strength of the source/sink, κ_k are the friction coefficients for the contact of k-th obstacle and the plates of the cell, $m_k = \pi\varepsilon_k^2\rho_k$ is the mass of the k-th obstacle, $\mathbf{n}^{(k)}(\theta)$ is the internal normal vector on the boundary of k-th obstacle, $k = 1, \ldots, M$.

The function $\mathbf{w}(s,t) = (w_1(s,t), w_2(s,t))$ determines the parameterization of the unknown free boundary $\partial\Omega(t)$. Meanwhile the movement of each obstacle can be described in terms of the location of its variable center $\mathbf{z}_k(t)$, which is permissible as the inclusions are moving as rotation free rigid bodies. The assumption of non-rotation is valid as the small size and circular shape of each particle mean that the pressure function around its boundary can be assumed constant, while the term for friction with the fluid will be negligible compared to that between the particle and the plates of the cell. It is worth noting that the lubricative force between particles is not modeled in this chapter, as it is not required to test the accuracy and limitations of the proposed asymptotic formulation (in particular those detailing the relationships between the particles and the evolution of the fluid boundary), however this can be added at a later time without requiring modification of the underlying analytical formulation (as it would effect particle motion, not the relationship with the free boundary).

The existence of a solution to the above problem can be shown in a way similar to that for the Hele-Shaw cell with air bubbles in the flow (see, e.g. [58] and references therein), or, alternatively, as we know there will be a unique solution in the case without inclusions, by demonstrating that the contribution of the particles to the evolution of the free-boundary will be both bounded and abide by the regularity condition (5.26) prior to the time of solution blow-up.

The aim of our study is to get an approximate solution to the problem $\mathbf{HS_M}$, and to create a numerical system based upon it which describes the different behaviour of small obstacles in the Hele-Shaw flow.

5.2.3 Uniform representation of Green's function

The method of uniform asymptotic approximation of the Green's function related to different boundary value problems for a number of differential operators in singularly and regularly perturbed domains was created and developed by *Maz'ya, Movchan & Nieves*, a summary of which can be found in [139]. This method has additionally been used to successfully examine the effect of an individual obstacle or particle in the Hele-Shaw cell [145, 146] (see Sect. 5.1.2.3). In this analysis of **Problem $\mathbf{HS_M}$**, some slight modifications to the asymptotic formula for N_ε [138, (7.1)] is required, however as the method remains similar it won't be repeated here in full[5].

Let $\mathcal{G}_\varepsilon(\mathbf{x},\mathbf{y})$ be a Green's function of the Laplace operator $-\Delta$ with the zero Neumann data on $\partial F_k, k=1,\dots,M$, and the zero Dirichlet data on Γ. The function $\mathcal{G}_\varepsilon(\mathbf{x},\mathbf{y})$ has the following asymptotic representation

$$\mathcal{G}_\varepsilon(\mathbf{x},\mathbf{y}) = G^\Omega(\mathbf{x},\mathbf{y}) + \sum_{k=1}^{M}\left\{\mathcal{N}^{(k)}\left(\frac{\mathbf{x}-\mathbf{z}_k}{\varepsilon_k},\frac{\mathbf{y}-\mathbf{z}_k}{\varepsilon_k}\right) + \frac{1}{2\pi}\log\left|\frac{\mathbf{x}-\mathbf{y}}{\varepsilon_k}\right|\right\} + \tag{5.27}$$

$$+\sum_{k=1}^{M}\varepsilon_k\left\{\mathcal{D}^{(k)}\left(\frac{\mathbf{x}-\mathbf{z}_k}{\varepsilon_k}\right)\cdot\nabla_{\mathbf{x}}H(\mathbf{z}_k,\mathbf{y}) + \mathcal{D}^{(k)}\left(\frac{\mathbf{y}-\mathbf{z}_k}{\varepsilon_k}\right)\cdot\nabla_{\mathbf{y}}H(\mathbf{x},\mathbf{z}_k)\right\} + \mathbf{r}_\varepsilon(\mathbf{x},\mathbf{y}),$$

where

$$|\mathbf{r}_\varepsilon(\mathbf{x},\mathbf{y})| \le Const\cdot\varepsilon^2.$$

Here, analogous to that provided for the case of a single inclusion in Sect. 5.1.2.3, we have:

- $\mathcal{N}^{(k)}$ are solutions to the modified Neumann problems in the exterior of $cl\,\omega_\varepsilon^{(k)}$. These are the Neumann conditions describing the flow around each individual obstacle $\omega_\varepsilon^{(k)}$,
- $\mathcal{D}^{(k)}$ are dipole vectors corresponding to inclusion $\omega_\varepsilon^{(k)}$. These are the Dirichlet data describing the transmission conditions between each

[5] A large part of the omitted work was completed by co-authors Prof. G. Mishuris and Prof. S.V. Rogosin, and as such only the steps necessary to properly outline the approach philosophy will be provided.

inclusion and the free-moving fluid boundary. Combined with the Neumann conditions above they provide a complete description of the effect of each particle on the evolution of the boundary in the Hele-Shaw cell.

- H corresponds to the regular part of the Green's function.
- $\mathbf{r}_\varepsilon(\mathbf{x},\mathbf{y})$ describes the order of the asymptotic approximation.
  As we are dealing with asymptotically small inclusions, this term will be neglegible, ensuring that the Green's function approximation provided by this scheme will be highly accurate.

The uniform estimate for the remainder in the above mentioned [138, Thm 7.1] is proven in the L_∞-norm for the general case of a two-dimensional domain containing several small inclusions. This estimate therefore remains valid in our case for any multiply connected domain $\Omega_M(t)$ with sufficiently small interval I of time variable t.

In this case, we accept the following notation for each instant of time $t \in I$.[6] $G^\Omega(\mathbf{x},\mathbf{y}) = G(\mathbf{x},\mathbf{y};t)$ is Green's function of the Laplace operator $-\Delta$ for the simply connected domain $\Omega = \Omega(t)$ with zero Dirichlet data on $\partial\Omega(t)$, which is identical to that generating the representation presented in the case of one obstacle in [145], [146].

$$G^\Omega(\mathbf{x};\mathbf{y}) := G(\mathbf{x};\mathbf{y};t) = -\frac{1}{2\pi}\log|g(\mathbf{x},\mathbf{y})| \tag{5.28}$$

This is the Green's function for the interior simply connected domain $\Omega(t)$. Here $g(\mathbf{x},\mathbf{y}) = (g_1(\mathbf{y},\mathbf{y}), g_2(\mathbf{x},\mathbf{y})) : \Omega(t) \to \mathbb{U}$ is the normalized conformal mapping of $\Omega(t)$ onto the unit disc $\mathbb{U}$ ($g(\mathbf{x},\mathbf{y})\big|_{\mathbf{x}=\mathbf{y}} = 0$, and $g'(\mathbf{x},\mathbf{y})\big|_{\mathbf{x}=\mathbf{y}} > 0$). Without loss of generality, we can simplify by only considering the case $\mathbf{y} = \mathbf{O}$. If $g_0(\mathbf{x}) : \Omega(t) \to \mathbb{U}$ is any (non-normalized) mapping, then

$$g(\mathbf{x},\mathbf{y}) = e^{-\arg g_0'(\mathbf{y})}\frac{g_0(\mathbf{x}) - g_0(\mathbf{y})}{1 - \overline{g_0(\mathbf{y})}g_0(\mathbf{x})}.$$

Next, to more easily express the final Neumann and Dirichlet functions we introduce auxiliary variables, which are related to the scaling of the small obstacles:

$$\xi_k = \frac{1}{\varepsilon_k}(\mathbf{x} - \mathbf{z}_k), \quad \eta_k = \frac{1}{\varepsilon_k}(\mathbf{y} - \mathbf{z}_k), \quad k = 1,\dots,M. \tag{5.29}$$

In this notation, $\mathcal{N}^{(k)}(\xi_k,\eta_k)$, $k = 1,\dots,M$, are the Neumann functions for the exterior of the re-scaled obstacles F_k. In this case, they can be represented explicitly (see, e.g.,

[6] Note that, in the case of one obstacle, this modified formula coincides with that provided by *Maz'ya, Movchan & Nieves* [139, (2.72)], see also [146].

[160, p. 68]):

$$\mathcal{N}^{(k)}(\xi_k,\eta_k) = -\frac{1}{4\pi}\log|\xi_k-\eta_k|^2 - \\ -\frac{1}{4\pi}\log\left[\frac{(|\xi_k|^2-1)(|\eta_k|^2-1)+|\xi_k-\eta_k|^2}{|\xi_k|^2|\eta_k|^2}\right]. \tag{5.30}$$

Meanwhile the Dirichlet functions, expressed for circular obstacles, are calculated from integrals using formula [82, (4.397.6)]:

$$\mathcal{D}_1^{(k)}(\xi_k) = \frac{1}{2}\frac{\xi_{k,1}}{(\xi_{k,1})^2+(\xi_{k,2})^2},\ \mathcal{D}_2^{(k)}(\xi_k) = \frac{1}{2}\frac{\xi_{k,2}}{(\xi_{k,1})^2+(\xi_{k,2})^2},\ k=1,\dots,M. \tag{5.31}$$

In addition to the formulae for these functions, solving **Problem $\mathbf{HS_M}$** requires both the derivatives and integrals to be calculated. These calculations are not included here, however they are available in the supplementary material included with the published paper, and the results are expressed in Sect. 5.2.4.1.

5.2.4 Computational algorithm

With the asymptotic relationships required now derived, it is possible to articulate the approximate solution to **Problem $\mathbf{HS_M}$** and create a numerical model capable of performing simulations for multiple particles within the Hele-Shaw cell. Additionally, the results of these simulations can be used to more carefully examine the effect of initial particle distribution on both the evolution of the fluid boundary and the dynamic behaviour of the particles themselves.

5.2.4.1 Final system of differential equations

It follows from the potential theory (see, e.g. [73, Ch. 8], also [138, Lemma 5.1]), that for any compact subset D, $\overline{D}\subset\Omega_N(t)$

$$(r_\varepsilon(\mathbf{x},\mathbf{y}))'_{x_j} \le \varepsilon^3,\ j=1,2,\ \mathbf{x},\mathbf{y}\in\overline{D}.$$

Thus, the Problem ($\mathbf{HS_M}$) can be asymptotically approximated by the following system of equations

$$\partial_t w_j(\mathbf{w};\mathbf{0};\mathbf{z}) = -\frac{Q_0h^2}{12\mu}\left(\partial_{x_j}G(\mathbf{w};\mathbf{O}) + \Upsilon_j(\mathbf{w};\mathbf{0};\mathbf{z})\right) \tag{5.32}$$

$$\frac{d^2z_{k,j}}{dt^2} + \frac{\kappa\pi\varepsilon_k^2}{m_k}\frac{dz_{k,j}(t)}{dt} = \frac{Q_0\varepsilon_k^2}{m_k}I_j^{(k)} - c\,\mathrm{sign}\left(\frac{dz_{k,j}(t)}{dt}\right)\left|\frac{dz_{k,j}(t)}{dt}\right|^2,\quad k=1,\dots,M, \tag{5.33}$$

where:

$$\Upsilon_j = \sum_{k=1}^{M} \left(K_j^{(k)} + \partial_{w_j} J_1^{(k)}(\mathbf{w}; \mathbf{O}) + \partial_{w_j} J_2^{(k)}(\mathbf{w}; \mathbf{O}) \right), \quad j = 1, 2 \tag{5.34}$$

with initial conditions $\mathbf{z}_k(0) = \mathbf{z}_k^{(0)}$, $\mathbf{z}_k'(0) = \mathbf{z}_k^{(1)}$. Here $\mathbf{w} = (w_1(s,t), w_2(s,t))$ is an unknown parametrization of the external boundary $\partial D(t)$,
$\mathbf{z}_k = (z_{k,1}(t), z_{k,2}(t))$ are unknown position of the center of the moving obstacles. The additional term in the right side of (5.33) represents the drag force, where c is a constant computed as: $c = 0.5hc_x\varepsilon_k\rho_f/m_k$, and c_x stands for the drag coefficient, while ρ_f denotes the fluid density.

Here, in the right hand-side of equations (5.32), (5.34) we use the formulae:

$$\partial_{x_j} G^{\Omega}(w_1(s,t), w_2(s,t); 0, 0) = \tag{5.35}$$

$$= -\frac{1}{2\pi} \left(g_1(w_1(s,t), w_2(s,t); 0, 0) \partial_{w_j} g_1(w_1(s,t), w_2(s,t); 0, 0) + \right.$$

$$\left. + g_2(w_1(s,t), w_2(s,t); 0, 0) \partial_{w_j} g_2(w_1(s,t), w_2(s,t); 0, 0) \right).$$

$$K_j^{(k)} = -\frac{1}{2\pi} \left\{ \frac{(w_j - z_{k,j})(z_{k,1}^2 + z_{k,2}^2) + \varepsilon_k^2 z_{k,j}}{[(w_1 - z_{k,1})^2 + (w_2 - z_{k,2})^2 - \varepsilon_k^2][z_{k,1}^2 + z_{k,2}^2 - \varepsilon_k^2] + \varepsilon_k^2(w_1^2 + w_2^2)} - \right. \tag{5.36}$$

$$\left. - \frac{w_j - z_{k,j}}{(w_1 - z_{k,1})^2 + (w_2 - z_{k,2})^2} \right\}.$$

$$\partial_{x_1} J_1^{(k)}(\mathbf{w}, O) = \frac{\varepsilon_k^2}{2} \left(\frac{(w_2 - z_{k,2})^2 - (w_1 - z_{k,1})^2}{((w_1 - z_{k,1})^2 + (w_2 - z_{k,2})^2)^2} \cdot \partial_{x_1} H(\mathbf{z}_k; O) - \right. \tag{5.37}$$

$$\left. - \frac{2(w_1 - z_{k,1})(w_2 - z_{k,2})}{((w_1 - z_{k,1})^2 + (w_2 - z_{k,2})^2)^2} \cdot \partial_{x_2} H(\mathbf{z}_k; O) \right),$$

and

$$\partial_{x_2} J_1^{(k)}(\mathbf{w}, O) = \frac{\varepsilon_k^2}{2} \left(- \frac{2(w_1 - z_{k,1})(w_2 - z_{k,2})}{((w_1 - z_{k,1})^2 + (w_2 - z_{k,2})^2)^2} \cdot \partial_{x_1} H(\mathbf{z}_k; O) - \right. \tag{5.38}$$

$$\left. - \frac{(w_2 - z_{k,2})^2 - (w_1 - z_{k,1})^2}{((w_1 - z_{k,1})^2 + (w_2 - z_{k,2})^2)^2} \cdot \partial_{x_2} H(\mathbf{z}_k; O) \right),$$

where the derivatives $\partial_{x_j} H(\mathbf{z}_k; \mathbf{O})$ are:.

$$\partial_{x_j} H(\mathbf{z}_k; O) = \frac{1}{2\pi} \frac{g_1(\mathbf{z}_k; O) \partial_{z_{k,j}} g_1(\mathbf{z}_k; O) + g_2(\mathbf{z}_k; O) \partial_{z_{k,j}} g_2(\mathbf{z}_k; O)}{g_1^2(\mathbf{z}_k; O) + g_2^2(\mathbf{z}_k; O)} - \tag{5.39}$$

$$- \frac{1}{2\pi} \frac{z_{k,j}}{z_{k,1}^2 + z_{k,2}^2}.$$

At last

$$\partial_{x_j} J_2^{(k)}(\mathbf{w}, O) = \frac{\varepsilon_k^2}{2} \frac{z_{k,1}}{z_{k,1}^2 + z_{k,1}^2} \cdot \partial_{w_j} F_1(\mathbf{w}; \mathbf{z}_k) + \frac{\varepsilon_k^2}{2} \frac{z_{k,2}}{z_{k,1}^2 + z_{k,1}^2} \cdot \partial_{w_j} F_2(\mathbf{w}; \mathbf{z}_k). \tag{5.40}$$

where

$$F_j := \partial_{y_j} H(\mathbf{w}; \mathbf{z}_k) = \frac{1}{2\pi} \frac{g_1(\mathbf{w}; \mathbf{z}_k)\partial_{z_{k,j}} g_1(\mathbf{w}; \mathbf{z}_k) + g_2(\mathbf{w}; \mathbf{z}_k)\partial_{z_{k,j}} g_2(\mathbf{w}; \mathbf{z}_k)}{g_1^2(\mathbf{w}; \mathbf{z}_k) + g_2^2(\mathbf{w}; \mathbf{z}_k)} + \tag{5.41}$$

$$+ \frac{1}{2\pi} \frac{w_j - z_{k,j}}{(w_1 - z_{k,1})^2 + (w_2 - z_{k,2})^2}, \; j = 1, 2, \; k = 1, \ldots, M.$$

Finally, the right-hand side of remaining equations (5.33) is given by:

$$I_j^{(k)} = \frac{g_1(\mathbf{z}_k; \mathbf{O})\partial_{z_{k,j}} g_1(\mathbf{z}_k; \mathbf{O}) + g_2(\mathbf{z}_k; \mathbf{O})\partial_{z_{k,j}} g_2(\mathbf{z}_k; \mathbf{O})}{g_1^2(\mathbf{z}_k; \mathbf{O}) + g_2^2(\mathbf{z}_k; \mathbf{O})} + 3\frac{z_{k,j}}{z_{k,1}^2 + z_{k,2}^2}. \tag{5.42}$$

5.2.4.2 Description of the scheme

The computational scheme to solve the problem is analogical to that presented in [146]. It employs reduction of the system of governing equations (5.32)-(5.33) to the dynamic system of the first order. To this end an additional dependent variable, the velocity of particle, is introduced:

$$\mathbf{v}_k = \mathbf{z}_k'. \tag{5.43}$$

Thus, for the boundary curve discretized by N points and for the M inclusions inside the domain, one obtains a system composed of $2N+4M$ ordinary differential equations. The system is solved by the standard MatLab ODE tool: ode45. The conformal mappings of the domain free boundary are performed by the Schwarz-Christoffel toolbox [52, 53], with the derivatives of the mapping calculated using subroutines based on spline approximation. When the particles collisions are detected, using an "event locator" inside the MatLab ode solver, the computations are discontinued. New initial conditions are then defined assuming either; a perfectly elastic impact, or a purely inelastic impact (which is achieved by 'fusing' the original particles together into a single, perfectly circular, particle with a larger radius and preserving the objects mass). Next, the computational process is resumed with the new initial conditions.

In all simulations, as the asymptotic approximation reduces in accuracy near the source/sink, or near to the fluid boundary, three conditions are imposed to prevent the results being adversely affected. The first two conditions are that, for any particle k, there must

always be a minimum distance of ε_k to the source/sink and to the fluid boundary. Additionally it will be required that the minimum radial distance between the source/sink and the fluid boundary always remains larger than 0.1.

5.2.5 Numerical examples and discussions

5.2.5.1 Computational accuracy

In order to investigate the accuracy of computations we use two analytical benchmarks. The first one is based on the classical solution by Polubarinova-Kochina [87, p. 29]. It describes evolution of the fluid front in the domain without inclusions ($\varepsilon = 0$) for both, the fluid sink and source. In [146] it was used to define the accuracy of computations for such a limiting case. Meanwhile, to gauge the accuracy when particles are included, we shall modify the basic system of equations by supplementing relation (5.32) with an additional term:

$$\partial_t w_j(\mathbf{w};\mathbf{0};\mathbf{z}) = -\frac{Q_0 h^2}{12\mu}\left(\partial_{x_j} G(\mathbf{w};\mathbf{O}) + \Upsilon_j(\mathbf{w};\mathbf{0};\mathbf{z}) - \Upsilon_j(\tilde{\mathbf{w}};\mathbf{0};\mathbf{z})\right), \tag{5.44}$$

where $\tilde{\mathbf{w}}(s,t)$ is a solution by Polubarinova-Kochina. In this way, $\tilde{\mathbf{w}}(s,t)$ becomes a solution of the system: (5.33), (5.44). Modification (5.44) can be interpreted as the introduction of a special leak-off function (see [229]).

The second benchmark is built in exactly the same way on the assumption that the reference solution, $\tilde{\mathbf{w}}(s,t)$, describes a circular shape. Its evolution in time, defined by the radius $R(t)$, can be easily determined from the fluid balance.

Note that the aforementioned manner of benchmark construction can be applied for any known $\mathbf{w}(s,t)$ being a solution of the system:

$$\partial_t w_j(\mathbf{w};\mathbf{0};\mathbf{z}) = -\frac{Q_0 h^2}{12\mu}\partial_{x_j} G(\mathbf{w};\mathbf{O}). \tag{5.45}$$

In Fig. 5.6 we present the evolution of the fluid free boundary for both benchmark cases. For the fluid sink variant a transition from curve 1 to curve 2 is implemented (domain contraction), while for the fluid source a reverse direction of domain transformation takes place (domain expansion). The initial positions of inclusions are marked schematically by two types of circles: solid line for three inclusions, dashed line for eight inclusions. In our analysis we will consider both, the immobile (fixed at initial positions) and moving inclusions. For the fixed inclusions the governing system of equations reduces to (5.44), where in the right hand side the predefined values of $\mathbf{z}$ are introduced. The error of

computations will be described by the relative error of radius vector $r(\theta, t)$ defining the fluid boundary.

In the first test we investigate the influence of the number and size of inclusions on the solution accuracy. To this end, the Polubarinova benchmark is considered. The boundary curve is discretized by $N = 140$ points. The computational errors at the final time, $\delta r(\theta, t_{max})$, are shown in Fig. 5.7-5.8 for the fluid sink and source respectively, for the case of immobile inclusions. Three different values of ε (0.1, 0.01, 0.001) are used. For a reference we depict also the error distribution for the case of no inclusions. The preliminary conclusion from this test is that regardless of the number and sizes of inclusions slightly better accuracy is obtained for the domain expansion. This observation is in line with the trend reported in [146], where also a better stability of computations for the fluid source variant was noted. It shows that a general tendency of accuracy deterioration with growing ε is present. The results for $\varepsilon = 0.001$ are in fact of the same quality as those for $\varepsilon = 0$, but even for $\varepsilon = 0.01$ the error distribution indicates that its average value is very close to that for $\varepsilon = 0$. There is not much difference in accuracy for different number of inclusions, except for the case of $\varepsilon = 0.1$, where for the fluid sink one obtains distinctly worse results. However, even then the maximal solution error is still below one percent. Note that in such a case ε is no longer a small parameter.

For the second benchmark example, the circular domain, we obtained similar trends (for this reason we do not illustrate them), but the solution accuracy was slightly better.

In the next test we shall consider to what degree the inclusions movement affects the accuracy of computations. Let us analyze the Polubarinova benchmark in the fluid source configuration for eight inclusions. Again three values of ε are considered: 0.1, 0.01,

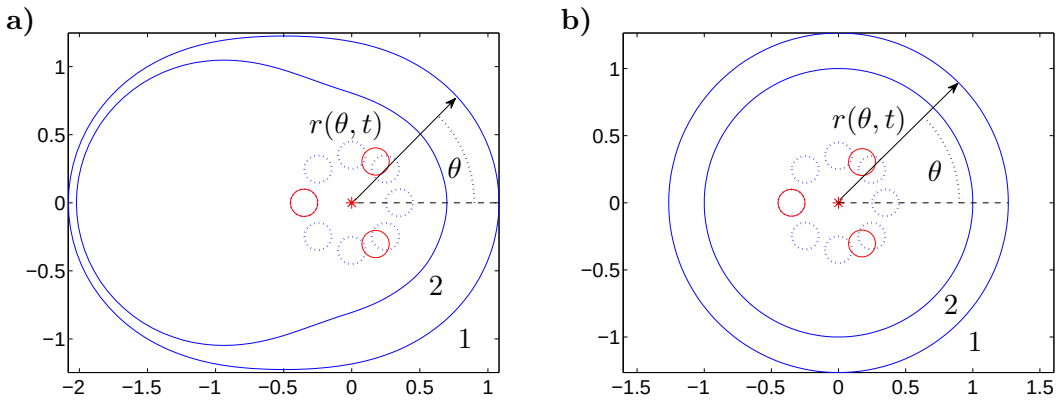

FIGURE 5.6: Domain configuration for the benchmark examples: a) Polubarinova solution, b) circular domain. Fluid source/sink is located at the origin. Depending on the chosen variant, the domain expands from curve 2 to 1 or contracts from 1 to 2. Radius vector $r(\theta, t)$ defines the boundary shape. Two configuration of inclusions are shown: solid lines - three inclusions, dashed lines - eight inclusions.

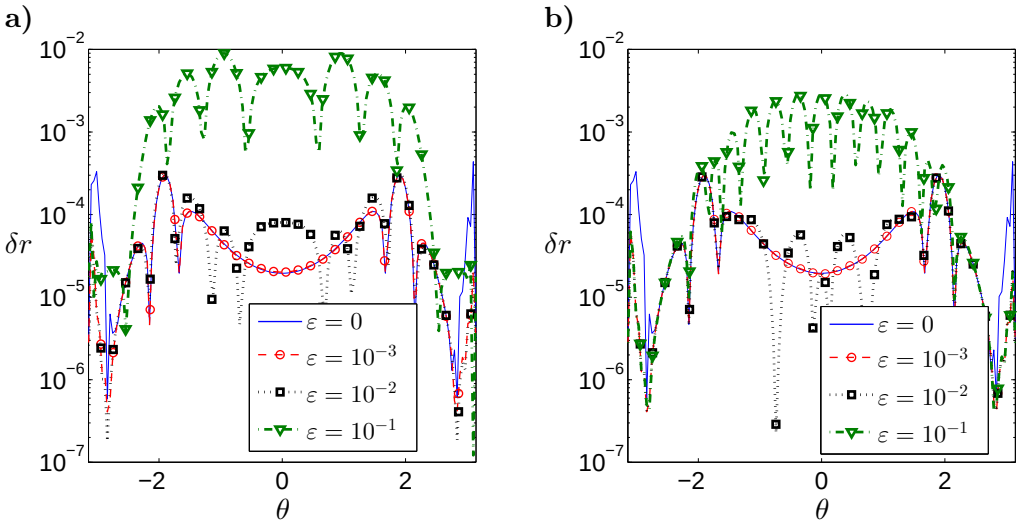

FIGURE 5.7: The relative error of the radius vector $r(\theta, t_{max})$ for the Polubarinova benchmark for: a) three immobile inclusions, b) eight immobile inclusions. The fluid sink variant was analyzed. The boundary curve was discretized by N=140 points.

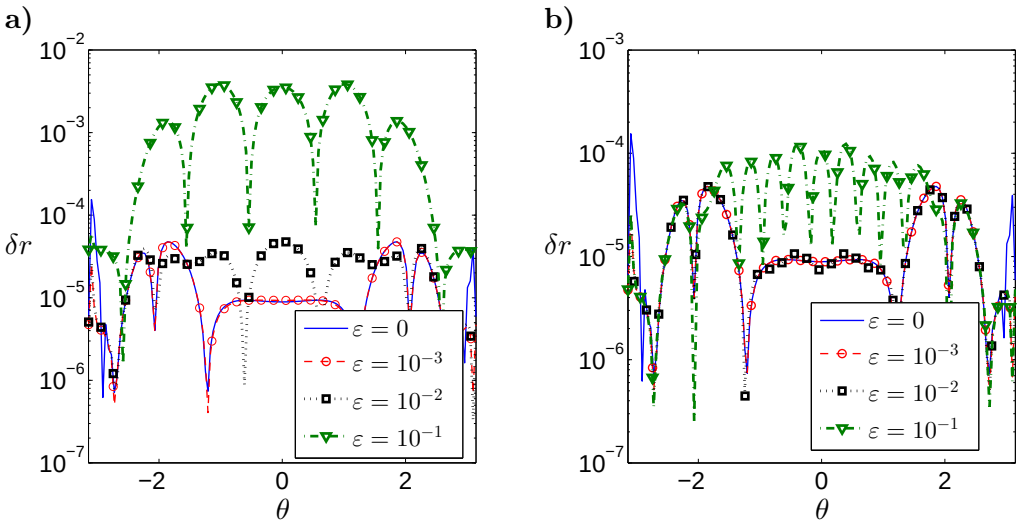

FIGURE 5.8: The relative error of the radius vector $r(\theta, t_{max})$ for the Polubarinova benchmark for: a) three immobile inclusions, b) eight immobile inclusions. The fluid source variant was analyzed. The boundary curve was discretized by N=140 points.

0.001. For each of these variants we compare the error of computations, δr, obtained for moving and immobile inclusions. The results of this comparison are depicted in Fig. 5.9. It shows that the level of accuracy is the same for both, moving and immobile inclusions. Only some slight differences in error distribution can be observed. Again, the accuracy gradation depends on the size of inclusions, giving the substantial deterioration only for the biggest inclusion $\varepsilon = 0.1$.

In the last test we investigate to what degree the density of discretization of the fluid free boundary affects the accuracy of computations. This time both benchmarks, the Polubarinova and circular domain solutions, are in use. We consider the fluid sink variant

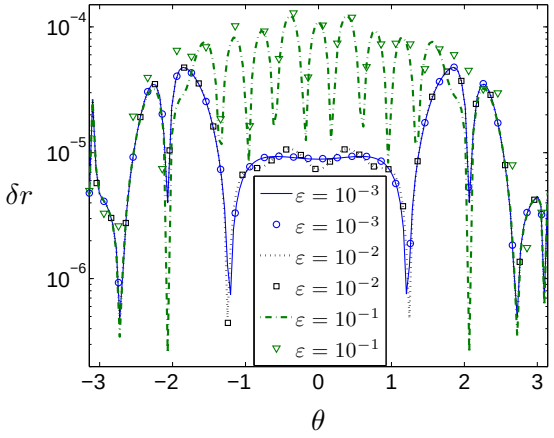

FIGURE 5.9: The relative error of the radius vector $r(\theta, t_{max})$ for 8 fixed and moving inclusions of different sizes. The Polubarinova benchmark for the fluid source configuration was used. The boundary curve was discretized by $N = 140$ nodes. The results denoted by markers only refer to the moving inclusions.

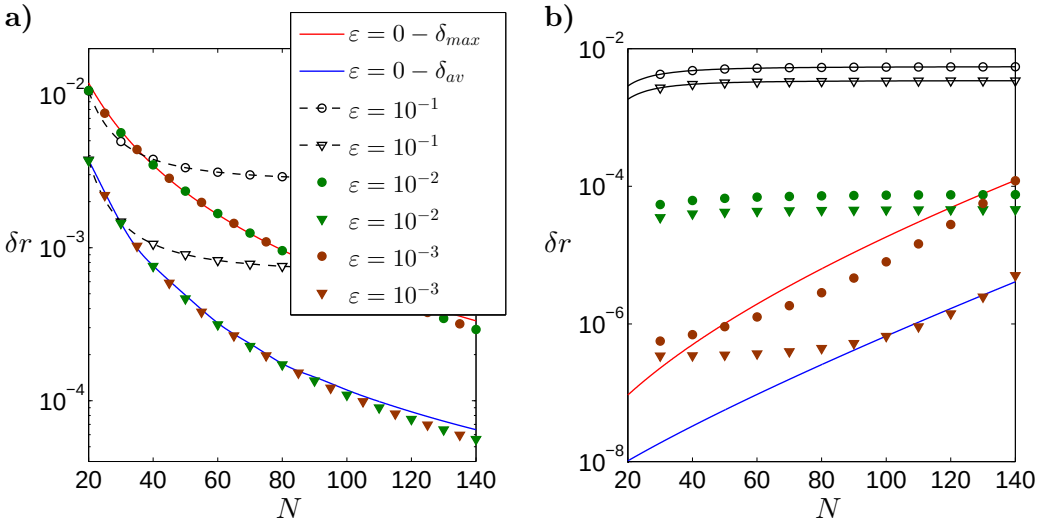

FIGURE 5.10: The relative errors of the radius vector for the sink variant of the problem related to the number of the boundary nodes N: δ_{max} - the maximal error (circular markers), δ_{av} - the average error (triangular markers). Respective graphs refer to: a) the Polubarinova benchmark, b) the circular domain benchmark.

for eight inclusions of different sizes ($\varepsilon = \{0.1, 0.01, 0.001\}$). A number of simulations was performed for N varying from 20 to 140. For every value of N, the maximal and average errors of the radius vector $r(\theta, t_{max})$ were computed. The results are depicted in Fig. 5.10, where for comparison also the curves for $\varepsilon = 0$ are shown. Respective curves for the maximal error are distinguished by the circular markers, while triangular markers are used for the average errors. The make the graphs more legible, the results for $\varepsilon = \{0.01, 0.001\}$ are denoted by markers only. For the Polubarinova benchmark there is a clear trend of accuracy increase with growing N. The results for $\varepsilon = \{0.01, 0.001\}$ are almost identical as those for no-inclusions case. Appreciable deterioration of accuracy is obtained for $\varepsilon = 0$, however even here the errors stabilize at the level 10^{-3}.

Quite a different situation is observed for the circular domain benchmark. Here, there is a counterintuitive tendency of the error, with it increasing with growing numbers of boundary nodes. This can be explained by the addition to the algorithm which was outlined at the end of Sect. 5.1.2.4, where we compute the derivatives of our conformal mapping along the boundary on the unit circle rather than on the original domain, with splines being employed to increase the approximation even further. For regular shaped domains, this approach is almost exact (observe that in the case without inclusions the average relative error is approximately 10^{-8} for $N = 20$ boundary nodes, see Fig. 5.10b). As a result of this already minuscule level of error for even small values of N, the accuracy of the approximation can't significantly increase, and the only effect of using larger numbers of boundary node is to increase the rate at which computational errors accumulate. For this reason, such a trend is much less distinct for $\varepsilon = 0$, where it is the presence of very large inclusions which introduces the greatest errors. Note that the results for $\varepsilon = \{0, 0.001, 0.01\}$ obtained when taking $N = 140$ are of the same accuracy level as for the Polubarinova benchmark (from Fig. 5.10, when $N = 140$ we have that the average error for the Polubarinova benchmark is of order 10^{-4}, which is identical to the circular domains average, although it should be noted that the maximal errors are clearly lower for the circular domain).

5.2.5.2 Collision strategies and particle interactions

In any fluid containing multiple particles and an explicit boundary there exist a multitude of forces which aren't directly accounted for within the present model. Rotational forces needn't be considered here as the model assumes that the particles are non-rotating. The effect of other forces influencing the particle movement are likely to be negligible compared to that of the friction term from the inclusions contact with the cell wall (see [232] for more information on related forces). It should be noted however that these effects can be incorporated at a later date with minimal difficulty, as the Green's function (5.27) will not need to be rederived. However, given that this is only an initial examination to determine the accuracy and viability of the suggested method for approximating the Hele-Shaw cell with multiple inclusions, this will not be done here.

The primary situation in which forces arise for which additional algorithms are required is the case of particle collision. Complicating matters is the fact that, for particle collisions within a fluid, the lubricative force prevents both perfectly elastic and inelastic collisions, and it also decelerates particles near to the boundary (see [121]). Determining the exact effect of this force on the final dynamics of the system however is beyond the

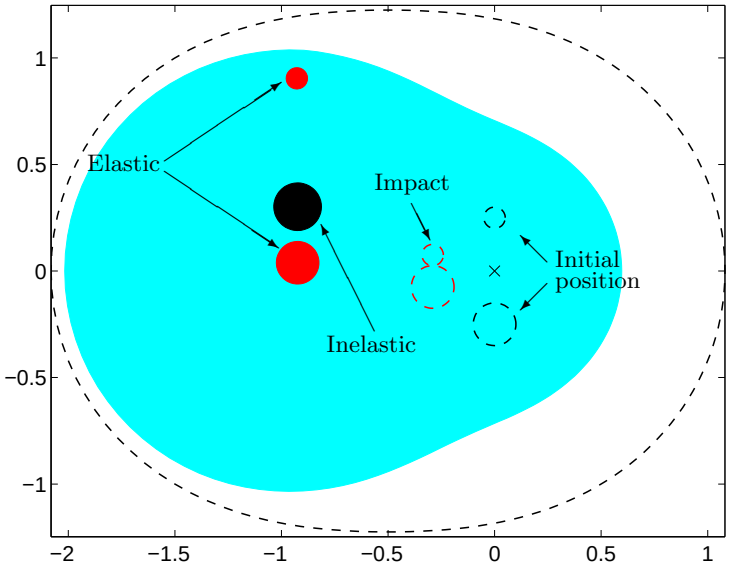

FIGURE 5.11: Diagram of the simulation for elastic and inelastic impacts. Here the black dotted lines show the initial positions, the red dotted line indicates the moment of particle collision, the red and blue coloured areas provide the final particle and fluid positions respectively, and the marker 'x' indicates the position of the fluid sink.

scope of this work.

To compensate for this two separate steps are taken. The first is to increase the friction coefficient of particles which become close to the boundary, which can be easily achieved and prevents any objects leaving the fluid domain. The second is that, in the case of particle collisions, both the perfectly elastic and inelastic cases will be modeled. While this will not produce the most accurate representation of the dynamics of particle interaction within the fluid these two cases provide the opposing ends of the spectrum, and as such if both can be modeled then the more accurate case involving the lubricative force can added later through the use of additional algorithms. Further these cases are very computationally efficient, and will ensure the model does not become overly cumbersome.

Simulations in the case of two particles with various properties, obtained for both elastic and inelastic collisions, are shown in Fig. 5.12, while the setup is displayed in Fig. 5.11. The post-collision particle movement is determined from the conservation of momentum combined with; conservation of energy in the elastic case, and the conservation of mass and volume for inelastic events. The initial fluid boundary is taken from the solution to the first order Polubarinova-Kochina system in the case of a sink, with the final time taken as $t = 0.7$ seconds. Here $Q_0 h^2/24\pi\mu = 1$, $\rho_k = 2.8$ kg/m^3 for both particles,

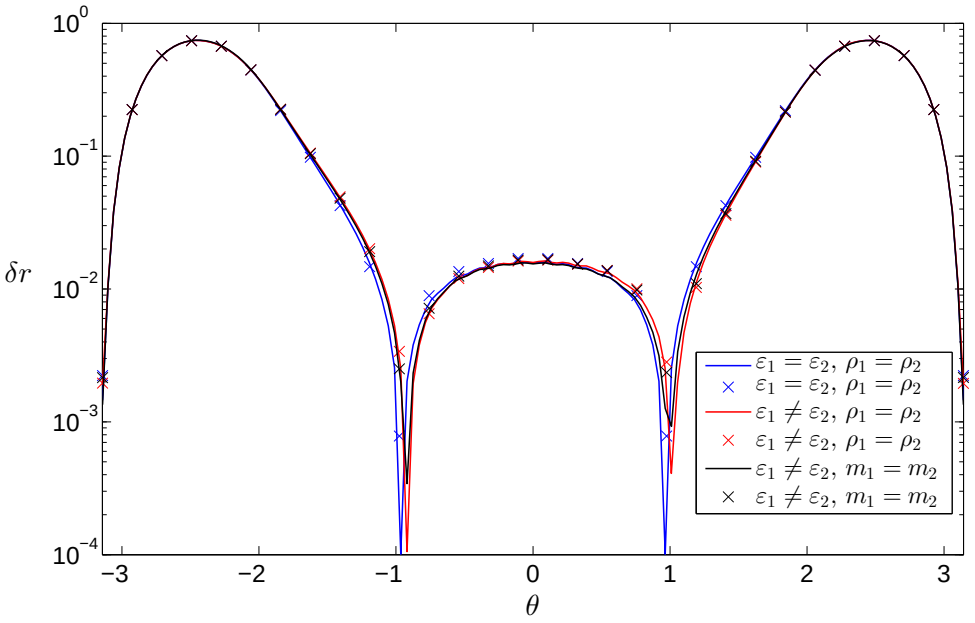

FIGURE 5.12: The deviation of the final boundary, relative to the case without inclusions, when two particles collide. Here the lines indicate elastic collisions, while markers indicate inelastic collisions. The particles properties are defined by their radius, ε, density, ρ and mass m.

$\kappa = 0.01$ (dimensionless) and initially $\varepsilon = \{0.1, 0.05\}$ meters.

In the conducted tests, the presence of a small number of particle collisions lead to only a minimal increase in the computation time (compared to similar systems without collisions), and the decrease in accuracy was negligible compared to that induced by other parameters (verified using the methods previously outlined in the previous sub-chapter). Additionally it is clear from results concerning the relative boundary deformation between cases (Fig. 5.12) that the difference between perfectly elastic and inelastic collisions is relatively small compared with the total change in boundary deformation. The fact that the collision type has only a minor influence on the deformation of the free boundary only improves the case for these efficient approximations over the more intensive option of computing the lubricative force.

5.2.5.3 Particle position and parameters

With the abilities of the model established, we can now use it to examine the effect of particle inclusion on the fluid flow within the Hele-Shaw cell. In the case of a unit circle or Polubarinova initial fluid domain (considered here), the flow can best be understood as traveling in the shortest possible straight line to the boundary (sink) from the source

(boundary). Particles placed in the path of this line will redirect the flow around it. Therefore positioning objects near to the source/sink will disrupt the largest portion of the domain, as the proportion of the flow disturbed is greatest, and the fluid on the opposite side of the source/sink will extend/drain faster to compensate. Conversely obstacles near the boundary will produce very localized effects, although these effects will be far larger in magnitude (compare variant 1&2 - close to the source, and variant 7&8 closer to the boundary, in Fig. 5.14a).

As a result of the fluid flow behaving in this manner the shape of the domain, size of the inclusions and movement of the particles over time will play a crucial role in determining the effect of particle placement on the fluid boundary evolution. Particles with a low (or zero) initial velocity, or a sufficiently high friction coefficient, will remain almost stationary relative to the movement of the fluid. In such situations the large magnitude localized effects are often only present over short time periods. Similarly a small inclusion size will only disrupt a small portion of the fluid flow, and as such the overall effects will be minimal.

These differing effects on the boundary can be displayed using simple system in which a

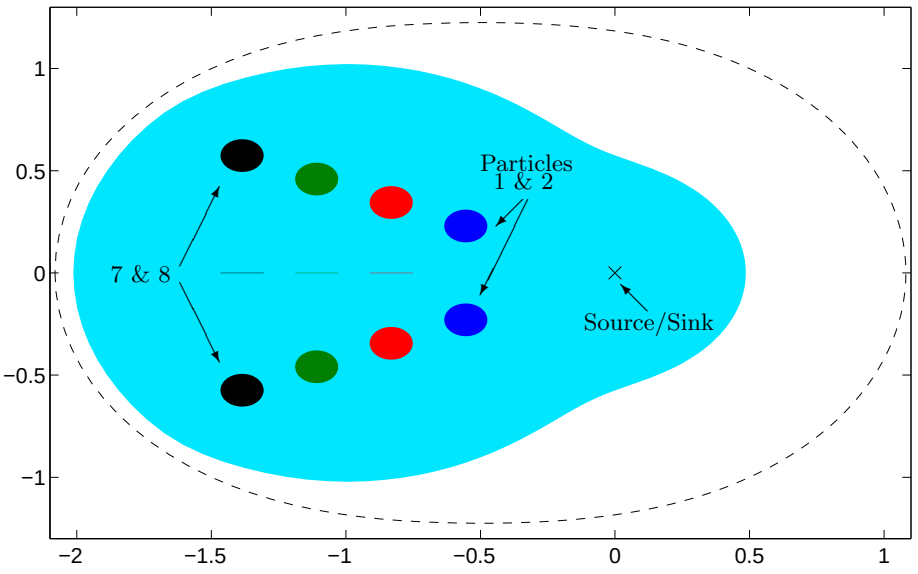

FIGURE 5.13: Diagram simulation for initially stationary particles in a 'Line' formation. Here the black dotted line shows the final boundary position, the light blue coloured area provides the initial fluid position and the marker 'x' indicates the position of the fluid source. The coloured circles indicate the initial particle positions, with particles: (1,2) heavy blue, (3,4) red, (5,6) green and (7,8) black.

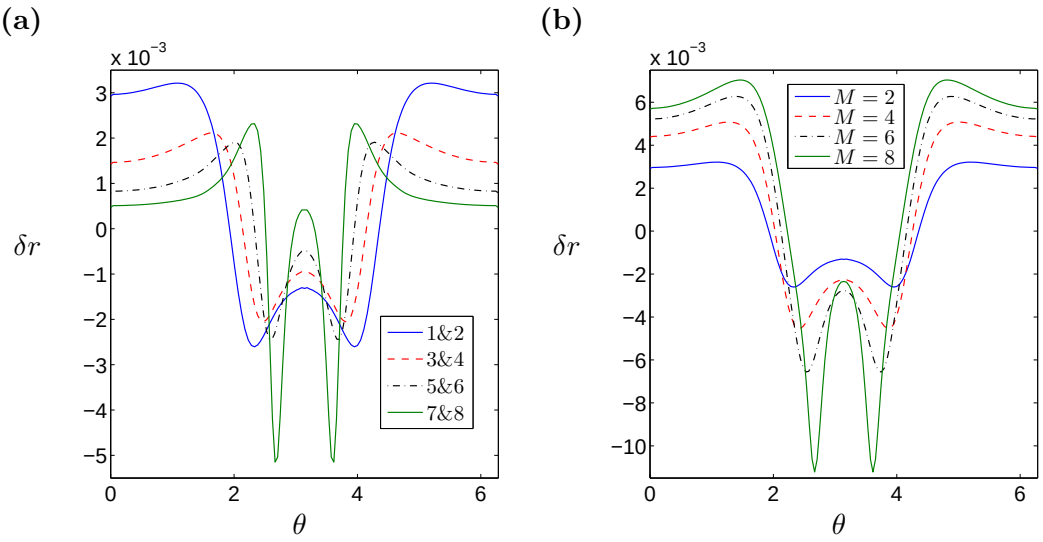

FIGURE 5.14: Comparison of the relative radial distance to the fluid boundary, δr, measured at the final time, when there are (a) two particles (b) M particles within the fluid at different radial distances to the boundary in the case of a fluid source.

variety of particles are placed within an initial domain defined by the Polubarinova solution. Note that differing configurations of particles will be utilized. A diagram showing the setup is provided in Fig. 5.13, while the relative deviation of the boundary from the case without inclusions is provided in Fig. 5.14. It is worth stating that, in the case with M particles, inclusions $k = 1, .., M$ will be taken. Additionally the particles are given an initial velocity of zero, as this will best demonstrate the effects on the boundary in absence of additional factors, with the remaining material parameters kept identical to those used in the previous subsection.

The localized effects for particles near the boundary, and wider domain effects for particles near the source, are both clearly present in Fig. 5.14a. Additionally it can be seen in Fig. 5.14b that these effects compound as the number of particles increases. These results perfectly match the previous description in terms of the fluid flowing between the source and the boundary. Further the results are well within the expected level of accuracy for this problem variant (see Fig. 5.8, $\varepsilon = 10^{-1}$).

5.2.5.4 Simulations with many particles

While there is no theoretical maximum for the number of particles which can be simulated the computation time will obviously become a limiting factor. In practice the particle numbers which can be reasonably computed is far more dependent on the distance between each particle and; adjacent particles, the source/sink and the boundary. As a result, with proper initial distribution (i.e. which does not violate initial assumptions,

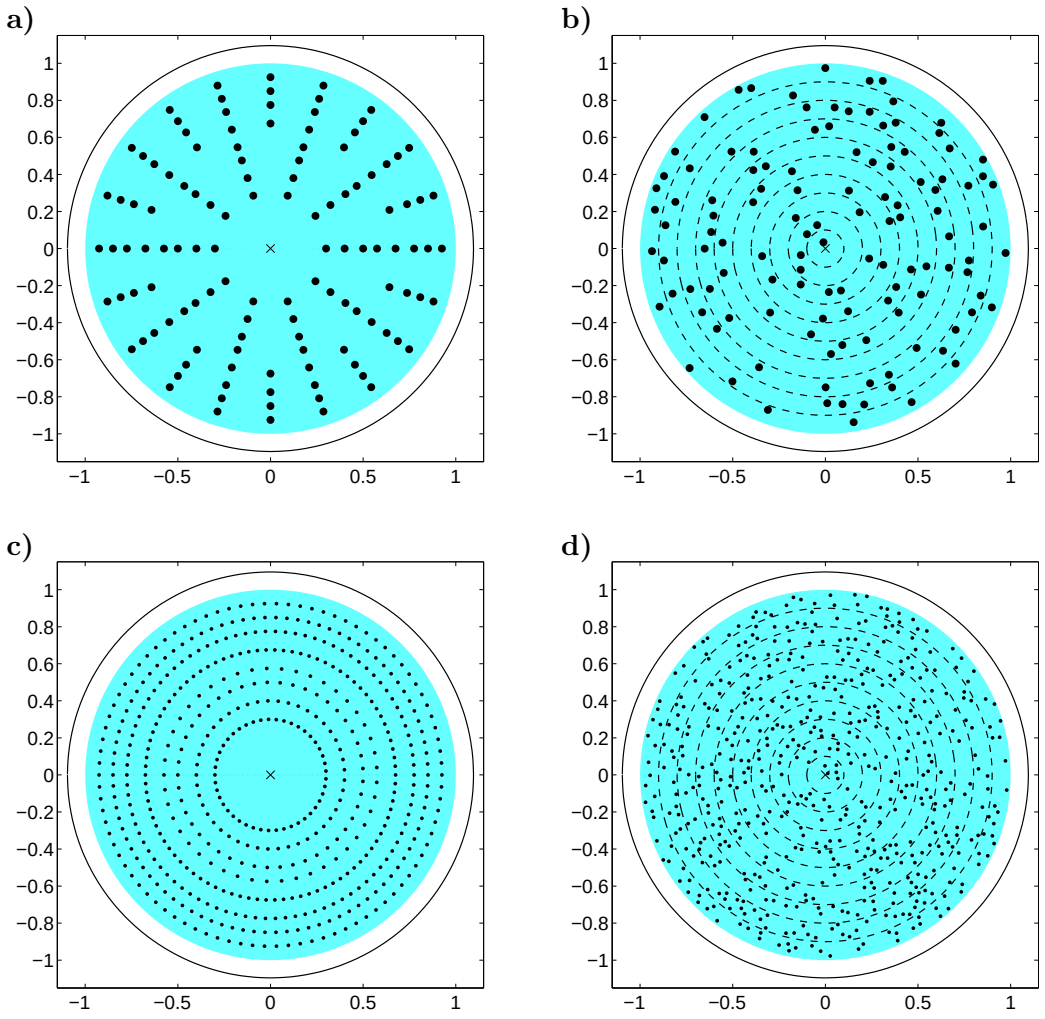

FIGURE 5.15: Diagram showing the initial position of the boundary (blue fill), the initial distribution of the (a,b) $M = 120$ (c,d) $M = 540$ particles, and the expected final boundary position is denoted by a black dashed line. Here the particle distributions are (a,c) ordered or (b,d) generated semi-randomly.

or be designed to ensure more collisions than particles present), simulations involving hundreds of particles can be easily completed within a reasonable computation time (typically $1.5 - 4.5$ hours).

Four demonstrative examples are considered, with systems containing either 120 or 540 particles in an ordered or semi-random distribution. The ordered system was defined by distributing particles into 8 rings around the source, within a fluid domain defined by a unit circle. Semi-random distributions where meanwhile created by splitting the initial domain into separate rings, and choosing particle angles and radial positions within each ring using MatLab's random number function, rejecting particle positions which lead to overlaps. The initial volume fraction of particles within the fluid was kept constant

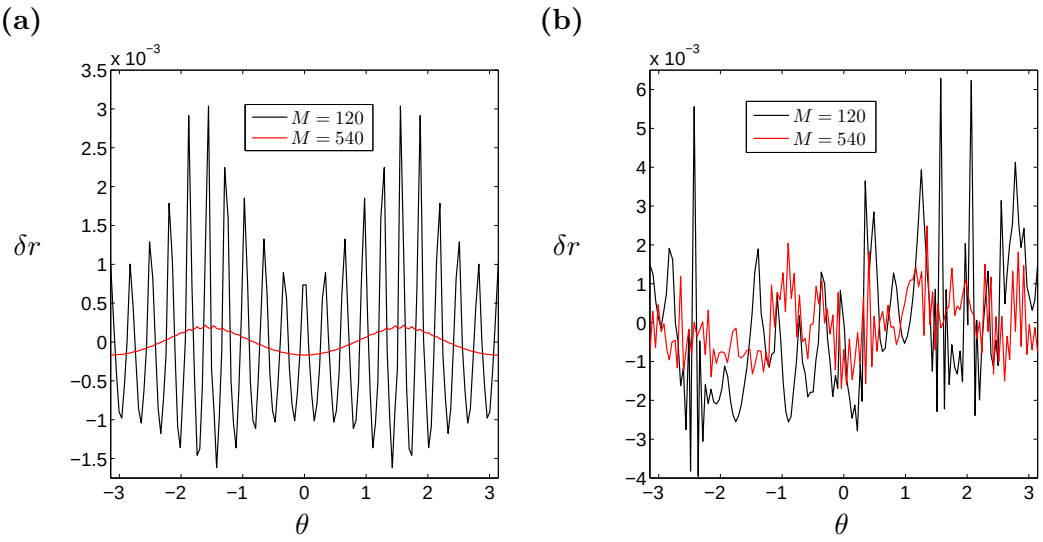

FIGURE 5.16: The relative deformation of the boundary between the cases with $M = 120, 540$ particles and the case without inclusions. Here (a) is for particles in an ordered distribution, while (b) is for a semi-random distribution.

between cases, such that $\varepsilon = 10^{-2}$ for 540 particles. A diagram showing the initial distributions is shown in Fig. 5.15, while the resulting boundary deformation over a time period of $t = 0.1$ is shown in Fig. 5.16.

It is clear from Fig. 5.16 that the deformation of the boundary in the case with many particles is far more complicated than those previously examined, with systems containing particles with a similar distribution and identical volume fractions resulting in notably different changes to the fluid boundary. That the systems with particles in an ordered distribution had a more periodic and predictable effect on the boundary deformation is not surprising, however the fact that simulations involving large numbers of particles lead to a far smoother boundary deformation in both cases, and can easily be conducted using this model, provides a method by which internal effects can be more readily studied.

5.3 Conclusions for modeling multiple inclusions in the Hele-Shaw cell

The evolution of a free moving fluid boundary, subject to the effect of moving particles in the fluid flow from a point source/sink, has been examined. The proper Stefan condition has been applied, alongside the use of conformal mappings and a Green's function based approach.

In this way, an asymptotic approximation of the fluid flow within a Hele-Shaw cell containing multiple free-moving particles has been obtained, which models both the movement of the fluid boundary and the inclusions. A model based on this system of equations has been created in a MatLab environment, which is capable of dealing with situations involving hundreds of particles and any potential collisions between them. The accuracy of the final model was assessed for various numbers and sizes of inclusions.

A brief examination into the effect of the particle inclusion on the fluid flow, primarily through the resulting boundary distortion, was conducted. The key finding of the model was the dual nature of the effect of initial particle distribution on the fluid boundary, with particles close to the boundary causing very localized effects, while those near to the source/sink affect the wider domain.

We now have a credible tool with which to simulate the fluid flow in a narrow channel subject to the presence of multiple different inclusions and obstacles. The applicability of this is clear, namely with regards to investigating the effective properties of the fluid when it contains a large number of particles. This can be achieved through the use of an axisymmetric formulation, however the exact method requires further development to ensure a high level of rigor (the full details of this are outlined in detail in Appendix. G). Once this is accomplished however, it has the potential to provide a new avenue of investigation into the behaviour of fluids used in hydraulic fracturing near to the crack tip, among other uses.

Chapter 6

Summary and final conclusions

In the course of this work, a series of axisymmetric problems with moving boundaries and related to fracture were examined. In this way, the unique aspects of such systems has been demonstrated.

The problem of solid particle erosion by a single rigid indenter was examined in Chapter 3. Through a thorough investigation into the relationship between the indenter geometry and the initial energy required to cause a fracture, it was demonstrated that inertial terms in the impacted medium play a crucial role on the qualitative behaviour of the system if there is a supersonic stage of the impact. In this way, it was shown that the temporal effects, traditionally ignored during erosion studies, have to be incorporated to properly explain dynamic impacts by small indenters. This includes incorporating the proper Stefan-type condition to model the evolution of the contact area during the initial stages, as well as choosing a fracture criterion which takes account of the ability of the impacted material to dissipate energy induced by the impact loading pulse.

Unfortunately, while the final model produced in this chapter was able to provide a qualitative description of the threshold fracture energy, much work still needs to be done in order to provide a complete model of such erosion impacts. Most notably, the transition between the supersonic and subsonic stages of the indentation are sewn together using a gluing function, which does not provide a physically realistic description of the transition. A proper model of this period of the impact would need to be derived in order to produce an accurate formulation. Additionally, the current approach examines the stress function along the impacts contact area, rather than at fixed spacial points. This would have to be changed if the model is to produce a quantitative description of the phenomena.

In Chapter 4, the case of a radial hydraulic fracture was considered. It was demonstrated that utilizing the proper Stefan-type condition, namely the speed equation, allows for the movement of the fracture front to be more accurately traced. This eliminates many of the previously noted difficulties, which arise due to the singular nature of the pressure at the crack tip. As such, combined with intelligent use of data on the system asymptotics, and a modular algorithm structure of the universal solver type, the final computer model is able to produce very high accuracy solutions, typically with a relative error below 10^{-8}. This was confirmed both against newly constructed analytical benchmarks, as well as an error measure based on the known rate of solution convergence.

Additionally, the effect of shear-stress was also incorporated into the axisymmetric model of hydraulic fracture, which primarily involved updating the fracture criterion used to determine the crack growth. In doing so it was shown that, while the quantitative difference in solution behaviour was only significant at the fracture tip, the qualitative behaviour of the solution was fundamentally altered in the case with zero fracture toughness. Similarly, in the case of low fracture toughness, the singular perturbation problem which existed previously was eliminated entirely.

Finally, the evolution of a free moving fluid boundary in the Hele-Shaw cell, subject to the effects of moving particles and stationary obstacles in the fluid, was considered in Chapter 5. This involved defining the Stefan condition in terms of a Green's function, which was then approximated using an asymptotic representation. This was resolved to provide a final system of equations, with some terms being given in the form of a conformal mapping to the unit circle. The final numerical model was demonstrated to achieve a high level of accuracy, and was able to simulate large numbers of inclusions as well as particle collisions.

One immediately apparent conclusion is the importance of properly applying the Stefan(-type) condition when studying problems involving moving boundaries. In all of the cases examined, this equation was either necessary to correctly model the qualitative physical behaviour of the system, or at the very least massively simplified, and increased the effectiveness of, any attempt to do so. Unfortunately, obtaining such a condition will not always be possible for all problems of this type, however it is clear that it should be the preferred route if it is available.

Finally, the fact that it is critical to take the appropriate fracture criterion in such investigations has also been demonstrated. In the case of dynamic erosion by small-sized indenters, failure to properly account for the ability of the material to dissipate impact energy leads to results with little real-world applicability. Similarly, the failure of the previous approaches to radial HF to use a fracture criterion which incorporated

shear-stress effects lead to incorrect predictions of the systems qualitative behaviour, most notably the parameters crack tip asymptotics.

Appendix A

Comparison with the Hertzian formulation

The *Hertzian* formulation of erosion impacts, outlined in Sect. 3.1.2, still represents a useful benchmark against which other approaches can be compared. While the two are by no means identical, with the *Hertzian* model assuming a static impact compared to the pulse loading of the presented formulation, a high level of corrolation in the initial steps is to be expected, especially for the stress function provided in (3.30).

As such, a comparison of the three special cases, for which comparable results are available, is presented below.

A.1 Rigid cone ($\lambda = 1$)

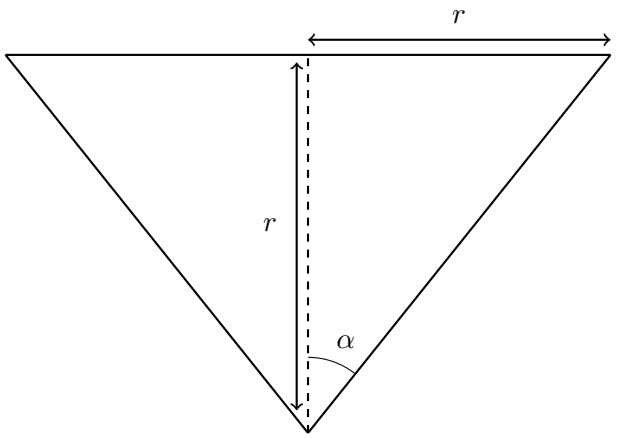

FIGURE A.1: Geometry of the rigid cone indenter when $\lambda = 1$, here $\alpha = \pi/2$ is the half-angle used to define the shape of the cone in the Hertz formulation.

In the case when of a rigid cone, the shape function for the indenter becomes $z = r$. As such, the only comparison with the *Sneddon* formulation is the specific case when $\alpha = \pi/2$ (see Fig. A.1), for which the *Hertzian* solution presented in Sect. 3.1.2.1 reduces to:

$$P = \frac{2E}{\pi\left(1-\nu^2\right)} w^2, \quad p = \frac{E}{2\left(1-\nu^2\right)}, \tag{A.1}$$

$$\sigma_r(r) = \begin{cases} \left[-\operatorname{arccosh}\left(\frac{1}{\rho}\right) + \frac{(1-2\nu)}{2\rho^2}\left\{1 - \sqrt{1-\rho^2} + \rho^2 \log\left(\frac{1+\sqrt{1-\rho^2}}{\rho}\right)\right\}\right] p, & \rho \leq 1 \\ \frac{(1-2\nu)}{2\rho^2} p, & \rho > 1 \end{cases} \tag{A.2}$$

where $\rho = r/a$ is the dimensionless coordinate.

Meanwhile, for the formulation presented in Sect. 3.2.2, we note from (3.16) that:

$$\lim_{\lambda \to 1} \Pi_1(\lambda) = 2\pi, \quad \lim_{\lambda \to 1} k_1 = \frac{2\pi E}{1-\nu^2}, \tag{A.3}$$

as such, the form of the contact force is immediately obtained from (3.15):

$$P = \frac{2\pi E}{1-\nu^2} w^2, \tag{A.4}$$

which does not correlate with the solution provided by *Sneddon*. The contact pressure distribution is given by:

$$p = \frac{P}{\pi a^2} = \frac{2E}{1-\nu^2}, \tag{A.5}$$

where the contact radius a was obtained from (3.25). Additionally, the stress function (3.30) reduces to:

$$\sigma_r(r) = \left[-\log\left(\frac{1+\sqrt{1-\rho^2}}{\rho}\right) + \frac{1-2\nu}{\rho^2} \int_0^\rho \eta \log\left(\frac{1+\sqrt{1-\eta^2}}{\eta}\right) d\eta \right] p, \quad r \leq a, \tag{A.6}$$

which yields:

$$\sigma_r(r) = \left[-\operatorname{arccosh}\left(\frac{1}{\rho}\right) + \frac{(1-2\nu)}{2\rho^2}\left\{1 - \sqrt{1-\rho^2} + \rho^2 \log\left(\frac{1+\sqrt{1-\rho^2}}{\rho}\right)\right\}\right] p, \quad r \leq a, \tag{A.7}$$

noting that:

$$\operatorname{arccosh}\left(\frac{1}{\rho}\right) = \log\left(\frac{1+\sqrt{1-\rho^2}}{\rho}\right), \quad 0 \leq \rho \leq 1. \tag{A.8}$$

Finally, for $r > a$, the stress function is yielded from (3.31) to be:

$$\sigma_r(r) = \frac{1-2\nu}{2\rho^2} p, \quad r > a. \tag{A.9}$$

Combining the above, it is clear that there is a noticeable disparity between the *Hertzian* formulation for impact by a rigid cone indenter and the presented formulation. It should be noted however, that the formulation was only designed to deal with cases where $\lambda > 1$.

A.2 Spherical indenter ($\lambda = 2$)

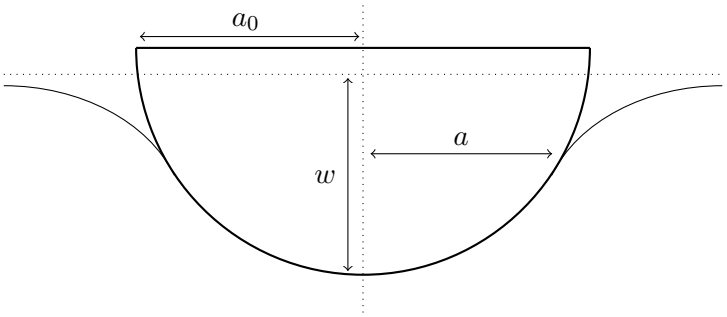

FIGURE A.2: Geometry of the half-sphere indenter, with radius a_0, obtained when taking $\lambda = 2$.

We begin by noting that, in order for the shape function defined in (3.14) to provide a spherical indenter with radius a_0, we require the shape constant $B = a_0$. It should be pointed out however that taking such a value means that the indenter in the presented formulation will define a half-sphere, rather than the full sphere approximated by *Hertz*. As such, minor disparities between the formulation are to be expected. The *Hertzian* formulation then remains identical to that presented in Sect. 3.1.2.2, and won't be repeated here.

In this case, the loading force can be shown from (3.15) to be:

$$P = \frac{2\sqrt{2}E\sqrt{a_0}}{3\left(1-\nu^2\right)} w^{\frac{3}{2}}. \tag{A.10}$$

The disparity between this result and that obtained by *Hertz* is simply a result of the different indenter geometry assumed in the two cases. In fact, it has been shown in previous investigations that loading force will coincide between the two cases if the same geometry is assumed [224].

Next, the contact pressure from (3.24) becomes:

$$p(r) = \frac{3P}{2\pi a^2}\sqrt{1-\frac{r^2}{a^2}}. \tag{A.11}$$

The stress function inside the contact area will be given by:

$$\sigma_r(r) = \frac{3P}{2\pi a^2}\left[-\sqrt{1-\rho^2} + \frac{1-2\nu}{\rho^2}\int_0^{\rho} \eta\sqrt{1-\eta^2}\,d\eta\right], \quad \rho \leq 1, \tag{A.12}$$

resolving the integral, we have:

$$\sigma_r(r) = \frac{3P}{2\pi a^2}\left[-\sqrt{1-\rho^2} + \frac{1-2\nu}{\rho^2}\left\{1-\left(1-\rho^2\right)^{\frac{3}{2}}\right\}\right], \quad \rho \leq 1, \tag{A.13}$$

while if $\rho > 1$, the stress function is given by (3.31).

In the case of a spherical indenter, it is clear that the only difference between the formulations is the value of the total loading force P. This is easily explained by the difference in geometry between the two models, with the loading force being higher for the larger *Hertzian* indenter, but the distribution of that force remaining the same between the cases.

A.3 Flat-bottomed cylinder ($\lambda \to \infty$)

The model completed by *Sneddon* for a static impact by a flat-bottomed cylinder into an elastic half-plane, the details of which are displayed in Sect. 3.1.2.3, is the case in which the closest correspondence between the two formulations is to be expected. It does however represent the most difficult to accurately obtain using the presented model, as it is the limiting case $\lambda \to \infty$ rather than an explicit value of the shape parameter. As such, numerical methods will have to be employed for certain steps rather than taking a purely analytical approach.

In this case, we have from $(3.16)_2$ that:

$$\lim_{\lambda\to\infty} \Pi_1(\lambda) = 2, \tag{A.14}$$

as such (3.15) yields the contact force for this case:

$$P = \frac{2EB}{1-\nu^2}w. \tag{A.15}$$

It is clear that, setting $B = a_0$ yields the same result as obtained by *Sneddon*. Next, the mean contact pressure is obtained from (3.24):

$$p(r) = \frac{P}{2\pi a^2}\lim_{\lambda\to\infty}(\lambda+1)\int_0^{\sqrt{1-\rho^2}} \left(\rho^2+\xi^2\right)^{\frac{\lambda-2}{2}}\,d\xi. \tag{A.16}$$

As such, for the two formulations two coincide (compare with (3.10)), we require that:

$$\lim_{\lambda\to\infty}(\lambda+1)\int_0^{\sqrt{1-\rho^2}}\left(\rho^2+\xi^2\right)^{\frac{\lambda-2}{2}}\,d\xi=\frac{1}{\sqrt{1-\rho^2}}. \tag{A.17}$$

This will have to be demonstrated numerically, which we will achieve by examining the function:

$$\mathcal{P}(\rho,\lambda)=(\lambda+1)\sqrt{1-\rho^2}\int_0^{\sqrt{1-\rho^2}}\left(\rho^2+\xi^2\right)^{\frac{\lambda-2}{2}}\,d\xi, \tag{A.18}$$

which should tend to unity as $\lambda\to\infty$ if (A.17) holds. The distribution of $\mathcal{P}$ for various large λ is provided in Fig. A.3.

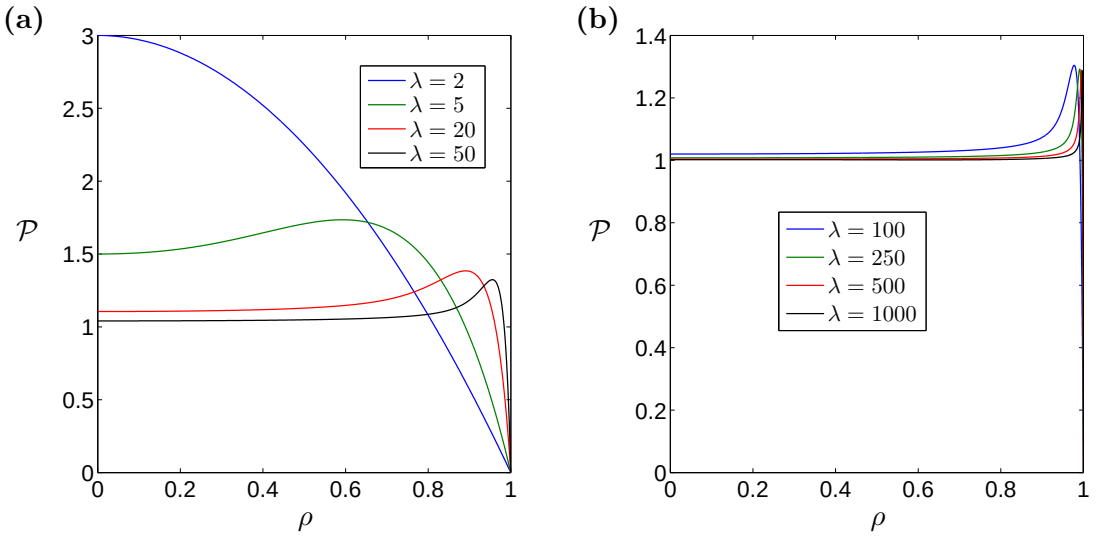

FIGURE A.3: Comparison with the *Sneddon* solution, for the pressure distribution beneath a cylindrical indenter. Here $\mathcal{P}$ provides the ratio between the solutions (A.18), with the requirement that $\mathcal{P}(\rho,\lambda)\to 1$ as $\lambda\to\infty$, for all $\rho\in[0,1]$, if the two formulations are identical.

As can be seen from the numerical examination of $\mathcal{P}$, the formulations coincide for all $\rho\in[0,1-\epsilon]$, where $\epsilon(\lambda)\ll 1$ for large λ. It can be shown analytically that the two formulations will not coincide in the limit at the point $\rho=1$, where the *Sneddon* solution is singular, while the contact pressure provided by (3.24) is undefined.

Given this high level of correspondence between the solutions, with the only significant deviation occurring arbitrarily close to a singular point in the pressure distribution, it is not unreasonable to state that the two formulations do coincide in the case of a flat-bottomed cylindrical indenter.

Finally, inserting (A.17) into the formula for the stress function (3.30), we have:

$$\sigma_r(r)=\frac{P}{2\pi a^2}\left[-\frac{1}{\sqrt{1-\rho^2}}+\frac{1-2\nu}{\rho^2}\int_0^{\rho}\frac{\eta}{\sqrt{1-\eta^2}}\,d\eta\right],\quad \rho\in[0,1). \tag{A.19}$$

Resolving the integral, it is clear that this coincides with the *Hertzian* formulation.

Appendix B

Appropriate time intervals

In Sect. 3.3.4.1 we evaluate the system over some small time interval $t_p = \{t_p^1, t_p^2\}$, using the results in order to approximate the behaviour of the threshold fracture energy as $t \to 0$. It is clear however that the choice of t_p will influence the final result, and as such we use this appendix to provide further information about how this interval is chosen.

The first problem we examine is that, in the limit, we have that $v_0 \to \infty$ as $t \to 0$. As a result taking points in time too close to zero may lead to results with little applicability to real world situations. In order to investigate further we define:

$$T_{**}(\lambda) = \left\{\max\left(t_{**}\right) : v_0(\lambda, t_{**}) \geq 3 \times 10^8\right\} \tag{B.1}$$

which, in other words, provides the smallest impact duration for which the initial velocity is less than the speed of light. This function can be easily obtained by iterative methods, the results of which are shown in Fig. B.1.

It is obvious that we must take $t_p^1 > T_{**}(\lambda)$ when conducting any serious investigation, however even taking t_p^1 close to $T_{**}(\lambda)$ will clearly still produce results which rely on infeasible physical characteristics. It is similarly apparent that, as this papers approach relies on the existence of an initial supersonic stage, the initial velocity of the indenter must be sufficiently large for this stage to exist. These constraints place bounds on the values of $t_p^{1,2}$ which can be used, but won't provide an exact interval over which the most representative results may be obtained.

A secondary, although not insignificant, problem facing such an investigation is that of ensuring accurate numerical results. This is particularly apparent for small impact durations, where the extreme values taken by the functions, with the some tending to

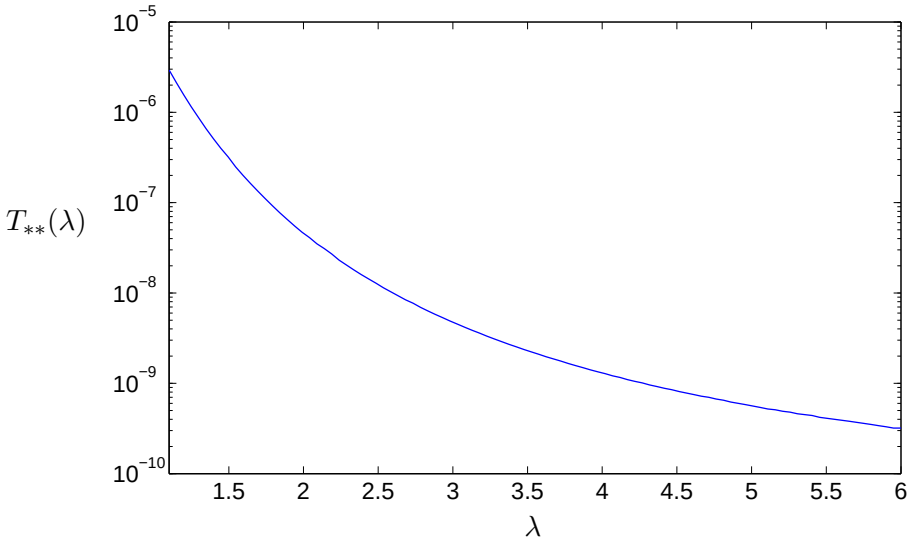

FIGURE B.1: The function (B.1) over a range of λ. This curve provides the minimum time duration over which results have any real-world applicability.

infinity while others tend to zero, inevitably resulting in a loss of accuracy, particularly during the supersonic stage. This provides not just an additional reason for accepting a lower bound on the value of t_p^1, but also an additional constraint which should be applied to t_p^2. Namely, in order to ensure that inaccuracies in the numerical results don't adversely effect our estimation of the gradient, we must have that the interval t_p is sufficiently large to ensure a significant difference in the values of the threshold fracture energy at either end of the interval. This will decrease the tightness of the lower bound obtained on the value of λ^*, but must be done to ensure reliable results.

Combining the above with the results of numerical experiments it was found that, when maintaining t_p^1 as a constant rather than as a function of λ, the best balance between accuracy and ensuring physically meaningful results was obtained when taking $t_p^1 \approx 2 \times 10^{-6}$, $t_p^2 \approx 2.5 \times 10^{-6}$ seconds.

Appendix C

Limiting cases: Newtonian and plastic fluids

C.1 Newtonian fluid: $n = 1$

In the case of a Newtonian fluid the majority of the results remains the same as in the general case (setting $n = 1$), but a few constants and functions will take alternate forms. These are detailed below.

The crack tip asymptotics in the viscosity dominated regime can be described by general relations (4.73)-(4.75). However, in the toughness dominated mode one has:

$$\begin{aligned}\tilde{w}(\tilde{r},\tilde{t}) = \tilde{w}_0(\tilde{t})\sqrt{1-\tilde{r}^2} + \tilde{w}_1(\tilde{t})\left(1-\tilde{r}^2\right) + \tilde{w}_2(\tilde{t})\left(1-\tilde{r}^2\right)^{\frac{3}{2}}\log\left(1-\tilde{r}^2\right) \\ + O\left(\left(1-\tilde{r}^2\right)^{\frac{3}{2}}\right), \quad \tilde{r}\to 1,\end{aligned} \tag{C.1}$$

$$\frac{\partial\tilde{p}}{\partial\tilde{r}} = \tilde{p}_0(\tilde{t})\left(1-\tilde{r}^2\right)^{-1} + \tilde{p}_1(\tilde{t})\left(1-\tilde{r}^2\right)^{-\frac{1}{2}} + O\left(1\right), \quad \tilde{r}\to 1. \tag{C.2}$$

The respective asymptotic expansions at the crack inlet, for both the viscosity and toughness dominated regimes, yield:

$$\tilde{w}(\tilde{r},\tilde{t}) = \tilde{w}_0^o + \tilde{w}_1^o\tilde{r} + O\left(\tilde{r}^2\log(\tilde{r})\right), \quad \tilde{r}\to 0, \tag{C.3}$$

$$\tilde{p}(\tilde{r},\tilde{t}) = \tilde{p}_0^o(\tilde{t}) + \tilde{p}_1^o(\tilde{t})\log\left(\tilde{r}\right) + O\left(\tilde{r}\right), \quad \tilde{r}\to 0. \tag{C.4}$$

It should be noted that the pressure is singular at the fracture origin, which is not the case for non-Newtonian ($n < 1$) fluids.

Meanwhile, the relationship between the new variable Ω and the pressure, in the time-dependent formulation, follows from the definition (4.82):

$$\tilde{p}(\tilde{r},\tilde{t}) = \Omega_0(\tilde{t})\log(\tilde{r}) + C_p(\tilde{t}) + \int_0^{\tilde{r}} \Omega(\xi,\tilde{t})d\xi, \tag{C.5}$$

where the time dependent constant $C_p(\tilde{t})$ is obtained by expanding (4.63) using (4.82):

$$C_p(\tilde{t}) = \frac{1}{2}\sqrt{\frac{\pi}{L(\tilde{t})}}\tilde{K}_I + [1-\log(2)]\,\Omega_0(\tilde{t}) - \int_0^1 \Omega(y,\tilde{t})\sqrt{1-y^2}\,dy. \tag{C.6}$$

Transforming into the self-similar formulation (4.92), these become:

$$\hat{p}(\tilde{r}) = \hat{\Omega}_0\log(\tilde{r}) + \hat{C}_p + \int_0^{\tilde{r}} \hat{\Omega}(\xi)\,d\xi, \tag{C.7}$$

$$\hat{C}_p = \frac{\sqrt{\pi}}{2}\hat{K}_I + [1-\log(2)]\,\hat{\Omega}_0 - \int_0^1 \hat{\Omega}(y)\sqrt{1-y^2}\,dy. \tag{C.8}$$

Finally, the auxiliary function $\mathcal{X}_n(\tilde{r})$ will now be expressed as:

$$\mathcal{X}_n(\tilde{r}) = \tilde{r}\left(\frac{\pi}{2} - \arctan\left(\frac{\tilde{r}}{\sqrt{1-\tilde{r}^2}}\right)\right) - \sqrt{1-\tilde{r}^2} \equiv \tilde{r}\arccos(\tilde{r}) - \sqrt{1-\tilde{r}^2}. \tag{C.9}$$

C.2 Perfectly plastic fluid: $n = 0$

In the case of a perfectly plastic fluid, alongside changes to the system asymptotics and reformulated equations, the degeneration of the Poiseuille equation means that it cannot be used to define the particle velocity $\tilde{v}$, or the reduced particle velocity Φ. As a result fundamental changes to the scheme are required. These are outlined below.

The crack tip asymptotics in the viscosity dominated regime remains in the same form as was outlined in (4.73)-(4.75). In the toughness dominated mode however it now yields:

$$\begin{aligned}\tilde{w}(\tilde{r},\tilde{t}) = \tilde{w}_0(\tilde{t})\sqrt{1-\tilde{r}^2} + \tilde{w}_1(\tilde{t})\left(1-\tilde{r}^2\right)^{\frac{3}{2}}\log\left(1-\tilde{r}^2\right) + \tilde{w}_2(\tilde{t})\left(1-\tilde{r}^2\right)^{\frac{3}{2}} \\ + O\left(\left(1-\tilde{r}^2\right)^{\frac{5}{2}}\right), \quad \tilde{r}\to 1,\end{aligned} \tag{C.10}$$

$$\frac{\partial\tilde{p}}{\partial\tilde{r}} = \tilde{p}_0(\tilde{t})\left(1-\tilde{r}^2\right)^{-\frac{1}{2}} + O(1), \quad \tilde{r}\to 1. \tag{C.11}$$

The fracture opening and the fluid pressure can be estimated at the crack inlet as:

$$\tilde{w}(\tilde{r},\tilde{t}) = \tilde{w}_0^o(\tilde{t}) + O\left(\tilde{r}^2\log(\tilde{r})\right), \quad \tilde{r}\to 0, \tag{C.12}$$

$$\tilde{p}(\tilde{r},\tilde{t}) = \tilde{p}_0^o(\tilde{t}) + \tilde{p}_1^o(\tilde{t})\tilde{r} + O\left(\tilde{r}^2\right), \quad \tilde{r} \to 0. \tag{C.13}$$

Meanwhile, the relationship between the modified pressure derivative and the pressure follows from the definition (4.82):

$$\tilde{p}(\tilde{r},\tilde{t}) = \tilde{r}\Omega_0(\tilde{t}) + C_p(\tilde{t}) + \int_0^{\tilde{r}} \Omega(\xi,\tilde{t})\, d\xi, \tag{C.14}$$

where the constant $\hat{C}_p$ takes the form (4.63):

$$C_p = \frac{1}{2}\sqrt{\frac{\pi}{L(\tilde{t})}}\tilde{K}_I - \frac{\pi}{4}\Omega_0(\tilde{t}) - \int_0^1 \hat{\Omega}(y,\tilde{t})\sqrt{1-y^2}\, dy. \tag{C.15}$$

Note, from the form of the above, that the pressure is not be singular at the injection point in this case. Transforming into the self-similar formulation (4.92) these become:

$$\hat{p}(\tilde{r}) = \tilde{r}\hat{\Omega}_0 + \hat{C}_p + \int_0^{\tilde{r}} \Omega(\xi)\, d\xi, \tag{C.16}$$

$$\hat{C}_p = \frac{\sqrt{\pi}}{2}\hat{K}_I - \frac{\pi}{4}\hat{\Omega}_0 - \int_0^1 \hat{\Omega}(y)\sqrt{1-y^2}\, dy. \tag{C.17}$$

It can be shown that the relationship between Ω and the fracture aperture (4.90) still holds, with the function $\mathcal{X}_n(\tilde{r})$ being given by:

$$\begin{aligned}\mathcal{X}_n(\tilde{r}) &= -\frac{\pi}{8}\left[\sqrt{1-\tilde{r}^2} + \tilde{r}^2 \log\left(\frac{\tilde{r}}{1+\sqrt{1-\tilde{r}^2}}\right)\right] \\ &\equiv -\frac{\pi}{8}\left[\sqrt{1-\tilde{r}^2} - \tilde{r}^2 \operatorname{arctanh}\left(\sqrt{1-\tilde{r}^2}\right)\right].\end{aligned} \tag{C.18}$$

In practice however, the degeneration of the Poiseuille equation means that a new scheme for solving the governing equations must be devised. The first step towards this is to note that the fracture aperture can be expressed as a non-linear integral equation:

$$\hat{w}(\tilde{r}) = -\frac{8}{\pi}\int_0^1 \frac{1}{\hat{w}(y)}\mathcal{K}(y,\tilde{r}),\, dy + \frac{4}{\sqrt{\pi}}\hat{K}_I\sqrt{1-\tilde{r}^2}, \tag{C.19}$$

while the crack-propagation speed is calculated from the fluid balance equation (4.106) as follows:

$$\hat{v}_0 = \frac{\hat{Q}_0}{2\pi\left[(3-\rho)\int_0^1 \tilde{r}\hat{w}(\tilde{r})\, d\tilde{r} + \frac{1-\rho}{\gamma}\int_0^1 \tilde{r}\hat{q}_l\, d\tilde{r}\right]}. \tag{C.20}$$

The reduced particle velocity $\hat{\Phi}$ can be determined by integrating (4.105):

$$\hat{\Phi}(\tilde{r}) = \frac{\hat{v}_0}{\hat{w}(\tilde{r})}\int_{\tilde{r}}^1 \xi\left[(3-\rho)\,\hat{w}(\xi) + (1-\rho)\,\frac{\hat{q}_l(\xi)}{\gamma}\right] d\xi. \tag{C.21}$$

Appendix D

Analytical benchmarks for a penny-shaped fracture

D.1 The classical formulation of radial HF

In the following we will present a way to construct a set of analytical benchmark solutions that satisfy the system of governing equations (4.99)-(4.108) for the self-similar problem. Those solutions can be easily extended through the relations (4.57)-(4.59), (4.63), (4.67), (4.89) and (4.90) to the time dependent forms. In this way one can formulate a set of analytical benchmark examples for both, the self-similar and the time dependent versions of the problem.

The basic concept employed to derive the self-similar solutions is the same as that in [229] for the KGD model. We assume that the crack aperture can be expressed as a weighted sum of properly chosen base functions:

$$\hat{w}(\tilde{r}) = \sum_{i=0}^{M} \lambda_i h_i(\tilde{r}). \tag{D.1}$$

The functions h_i are selected in a way that enables one to: i) comply with the asymptotic representation (4.73), ii) satisfy the respective boundary conditions (4.108), iii) compute analytically the elasticity operator (4.101). The multipliers λ_i are to be chosen properly to ensure the physically justified behaviour and desired properties of the solution.

Provided that iii) is satisfied, the fluid pressure function can be computed in a closed form from (4.101) to give:

$$\hat{p}(\tilde{r}) = \sum_{i=0}^{M} \lambda_i \pi_i(\tilde{r}), \tag{D.2}$$

where each function π_i corresponds to respective function h_i.

The self-similar stress intensity factor follows immediately from the asymptotic bahviour of functions h_i and complies with (4.107). Next, the self-similar crack propagation speed, $\hat{v}_0$ can be determined according to (4.99), while the particle velocity is computed from (62) to produce:

$$\hat{v}(\tilde{r}) = \left\{ -\left[\sum_{i=0}^{M} \lambda_i h_i(\tilde{r})\right]^{n+1} \cdot \sum_{i=0}^{M} \lambda_i \pi_i'(\tilde{r}) \right\}^{1/n}. \tag{D.3}$$

Consequently, the reduced particle velocity is defined by employing (D.2) in $(4.95)_1$. The influx magnitude, $\hat{Q}_0$, is computed from (4.108), while the modified pressure derivative can be obtained from the definition $(4.95)_2$, (4.97). Finally, the benchmark leak-off function is determined by a transformation of (4.105) as:

$$\hat{q}_l(\tilde{r}) = \frac{\gamma}{1-\rho}\left[(\rho-3)\hat{w}(\tilde{r}) - \frac{1}{r\hat{v}_0}\left(\hat{w}(\tilde{r})\hat{\phi}(\tilde{r})\right)'\right], \tag{D.4}$$

where the quantities on the right hand side are taken according to (D.1)-(D.3).

In this way, by using different values of the coefficients λ_i and different functions $h_i(\tilde{r})$, $\pi_i(\tilde{r})$ one can construct a number of self-similar problems for various fluid behaviour indices and crack propagation regimes, for which there exist known purely analytical solutions in the form (D.1)-(D.3). The values of pumping rate, $\hat{Q}_0$, and the self-similar material toughness, $\hat{K}_{Ic}$, can be tuned by the choice of magnitudes of respective coefficients λ_i.

The examples of base functions $h_i(\tilde{r})$, $\pi_i(\tilde{r})$ are collected in Table D.1.

To provide a very simple example of a numerical benchmarks which can be created using the aforementioned methodology, we consider the following composite functions:

$$h_A(\tilde{r},\alpha) = h_5(\tilde{r},\alpha) + \frac{\pi}{1+2\alpha}h_0(\tilde{r}) - \frac{2}{1+2\alpha}h_1(\tilde{r}), \tag{D.5}$$

$$h_B(\tilde{r},n) = -h_2(\tilde{r},n) + \frac{n\sqrt{\pi}\,\Gamma\left(\frac{3-n}{2}\right)}{2\Gamma\left(2-\frac{n}{2}\right)}h_0(\tilde{r}) + \frac{2\,(1-n)\,\Gamma\left(\frac{3-n}{2}\right)}{\sqrt{\pi}\,\Gamma\left(2-\frac{n}{2}\right)}h_1(\tilde{r}), \tag{D.6}$$

with the corresponding pressure terms:

$$\pi_A(\tilde{r},\alpha) = \pi_5(\tilde{r},\alpha) + \frac{\pi}{1+2\alpha}\pi_0 - \frac{2}{1+2\alpha}\pi_1(\tilde{r}), \tag{D.7}$$

i	$\pi_i(\tilde{r})$	$h_i(\tilde{r})$
0	1	$\frac{8}{\pi}\sqrt{1-\tilde{r}^2}$
1	$\tilde{r}$	$\sqrt{1-\tilde{r}^2}+\tilde{r}^2\log\left(\frac{1+\sqrt{1-\tilde{r}^2}}{\tilde{r}}\right)$
2	$\tilde{r}^{1-n}$	$\frac{2\Gamma\left(\frac{3}{2}-\frac{n}{2}\right)\Gamma\left(\frac{n}{2}-1\right)}{\Gamma\left(2-\frac{n}{2}\right)\Gamma\left(\frac{n}{2}-\frac{1}{2}\right)}\left[\tilde{r}^{2-n}-\frac{\Gamma\left(\frac{n}{2}-\frac{1}{2}\right)}{\sqrt{\pi}\Gamma\left(\frac{n}{2}\right)}{}_2F_1\left(\frac{1}{2},\frac{n}{2}-1;\frac{n}{2};\tilde{r}^2\right)\right]$
3	$\tilde{r}^{2-n}$	$\frac{2\Gamma\left(2-\frac{n}{2}\right)\Gamma\left(\frac{n-3}{2}\right)}{\Gamma\left(\frac{5-n}{2}\right)\Gamma\left(\frac{n}{2}-1\right)}\left[\tilde{r}^{3-n}-\frac{\Gamma\left(\frac{n}{2}-1\right)}{\sqrt{\pi}\Gamma\left(\frac{n-1}{2}\right)}{}_2F_1\left(\frac{1}{2},\frac{n-3}{2};\frac{n-1}{2};\tilde{r}^2\right)\right]$
4	$\log(\tilde{r})$	$\frac{8}{\pi}\left[\tilde{r}\arccos\left(\tilde{r}\right)+\left(\log(2)-2\right)\sqrt{1-\tilde{r}^2}\right]$
5	$\sum_k \tilde{r}\,{}_2F_1\left(\frac{1}{2}-\alpha_k,1;\frac{1}{2};\tilde{r}^2\right)$	$\sum_k \frac{2\sqrt{\pi}\left(1-\tilde{r}^2\right)^{\alpha_k}}{1+2\alpha_k}\left[\frac{\Gamma\left(\alpha_k+\frac{1}{2}\right)}{\Gamma(1+\alpha_k)}{}_2F_1\left(\frac{1}{2},\frac{1}{2}+\alpha_k;1+\alpha_k;1-\tilde{r}^2\right)\right.$ $\left.+\frac{4\Gamma\left(\frac{3}{2}+\alpha_k\right)}{(1+2\alpha_k)\Gamma(\alpha_k)}{}_2F_1\left(-\frac{1}{2},\frac{1}{2}+\alpha_k;1+\alpha_k;1-\tilde{r}^2\right)\right]$ $-\frac{4}{1+2\alpha_k}\log\left(\frac{1+\sqrt{1-\tilde{r}^2}}{\tilde{r}}\right)$
6	$\operatorname{arctanh}(\tilde{r})$	$4\left[E\left(1-\tilde{r}^2\right)-K\left(1-\tilde{r}^2\right)+\log\left(\frac{1+\sqrt{1-\tilde{r}^2}}{\tilde{r}}\right)\right]$

TABLE D.1: Table showing the components of the benchmark solutions. Here ${}_2F_1$ is the Gaussian hypergeometric function, while functions K, E represent the complete elliptic integral of the first and second kinds respectively. Note that we adopt the notation $\pi_5(x,\alpha_0,\ldots,\alpha_M)$, $h_5(x,\alpha_0,\ldots,\alpha_M)$ to indicate a summation over $k=1,2,\ldots,M$ for this section of the text.

$$\pi_B(\tilde{r},n)=-\pi_2(\tilde{r},n)+\frac{n\sqrt{\pi}\Gamma\left(\frac{3-n}{2}\right)}{2\Gamma\left(2-\frac{n}{2}\right)}\pi_0+\frac{2\left(1-n\right)\Gamma\left(\frac{3-n}{2}\right)}{\sqrt{\pi}\Gamma\left(2-\frac{n}{2}\right)}\pi_1(\tilde{r}). \tag{D.8}$$

Then the asymptotic behaviour of the respective functions at the fracture tip is: Then the asymptotic behaviour of the respective functions at the fracture tip is:

$$h_A(\tilde{r},\alpha)=\frac{2\sqrt{\pi}\Gamma\left(\alpha+\frac{1}{2}\right)}{\Gamma\left(\alpha+1\right)}\left(1-\tilde{r}^2\right)^{\alpha}+O\left(\left(1-\tilde{r}^2\right)^{\min\left(\frac{5}{2},\alpha+1\right)}\right),\quad \tilde{r}\to 1, \tag{D.9}$$

$$\begin{aligned}\pi_A(\tilde{r},\alpha)=&\frac{\sqrt{\pi}\left(1-2\alpha\right)\Gamma\left(2-\alpha\right)}{2(1-\alpha)\Gamma\left(\frac{3}{2}-\alpha\right)}\left(1-\tilde{r}^2\right)^{\alpha-1}+\\&\left[\frac{\pi}{1+2\alpha}-\frac{2}{1+2\alpha}-\frac{\Gamma\left(\alpha-1\right)}{2\Gamma\left(\alpha\right)}\right]+O\left(\left(1-\tilde{r}^2\right)^{\min(1,\alpha)}\right),\quad \tilde{r}\to 1,\end{aligned} \tag{D.10}$$

$$h_B(x,n)=O\left(\left(1-\tilde{r}^2\right)^{\frac{5}{2}}\right),\quad \tilde{r}\to 1, \tag{D.11}$$

$$\pi_B(x,n) = \frac{\Gamma\left(\frac{3-n}{2}\right)}{\Gamma\left(2-\frac{n}{2}\right)}\left[\frac{n\sqrt{\pi}}{2} + \frac{2(1-n)}{\sqrt{\pi}}\right] - 1 + O\left(1-\tilde{r}^2\right), \quad \tilde{r} \to 1. \tag{D.12}$$

It can easily be seen from the above equations that the functions h_A and π_A will provide the proper first term of the crack tip asymptotics for the aperture (4.73) and pressure derivative (4.74), (4.79), provided that α is taken in accordance with Table 4.1. Further terms may also be constructed, although subsequent (known) asymptotic terms of h_A and π_A must be accounted for. Additionally the behaviour of h_B, π_B at the crack tip ensures that it will not interfere with the final asymptotics of the benchmark at the fracture front in a notable way.

Meanwhile, at the crack inlet, we have:

$$h_A(\tilde{r},\alpha) = \frac{2}{1+2\alpha}\left[3 + \frac{4\alpha}{1+2\alpha} - H\left(\alpha - \frac{1}{2}\right)\right] + O(\tilde{r}^2\log(\tilde{r})), \quad \tilde{r} \to 0, \tag{D.13}$$

$$\pi_A(\tilde{r},\alpha) = \frac{\pi}{1+2\alpha} + O(\tilde{r}), \quad \tilde{r} \to 0, \tag{D.14}$$

$$h_B(\tilde{r},n) = -\frac{2n\sqrt{\pi}\,(1-n)\sec\left(\frac{n\pi}{2}\right)}{(2-n)\,\Gamma\left(2-\frac{n}{2}\right)\Gamma\left(\frac{n-1}{2}\right)} + O(\tilde{r}^{2-n}), \quad \tilde{r} \to 0, \tag{D.15}$$

$$\pi_B(x,n) = \frac{n\sqrt{\pi}\Gamma\left(\frac{3-n}{2}\right)}{2\Gamma\left(2-\frac{n}{2}\right)} + O\left(\tilde{r}^{1-n}\right), \quad \tilde{r} \to 0, \tag{D.16}$$

where H is the harmonic number function and α can be taken in accordance with Table 4.1. From this it can be easily seen that the required asymptotic representations of the aperture (4.72) and pressure derivative (4.70) will be satisfied by h_B and π_B, while the fracture opening asymptotics of h_A and π_A will not prevent the benchmark from displaying the correct behaviour. As with the crack tip, here further asymptotic terms can be accounted for using additional functions.

In this way, by linear combination of functions (D.5)-(D.8) and other functions from Table D.1 one can build a benchmark example for the viscosity dominated regime of crack propagation for a number of shear-thinning fluids, provided that $\alpha = \alpha_0$. Moreover, by incorporation of function h_0 from Table D.1 we obtain a solution which mimics the toughness dominated mode.

The above strategy have been successfully employed to create a set of analytical benchmark examples for the the varying crack propagation regimes and fluid behaviour indices. The benchmarks used in Sect. 4.2.5 are outlined below.

D.1.1 Viscosity dominated case ($\hat{K}_{Ic} = 0$)

D.1.1.1 Newtonian fluid ($n = 1$)

In this case, the constants λ_i take the following values:

$$\lambda_0 = \frac{\pi\left[34 + 7\log(2)\right]}{112}, \quad \lambda_1 = -\frac{17}{28}, \quad \lambda_2 = 0, \quad \lambda_3 = 0, \quad \lambda_4 = -\frac{\pi}{16}, \quad \lambda_5 = 1, \quad \lambda_6 = 0, \tag{D.17}$$

where we have $h_5\left(\tilde{r}, \alpha_0\right)$, $\pi_5\left(\tilde{r}, \alpha_0\right)$. As such, the asymptotic behaviour at the fracture tip is given by:

$$\hat{w}(\tilde{r}) = \frac{2\sqrt{\pi}\Gamma\left(\frac{7}{6}\right)}{\Gamma\left(\frac{5}{3}\right)}\left(1-\tilde{r}^2\right)^{\frac{2}{3}} + O\left(\left(1-\tilde{r}^2\right)^{\frac{5}{3}}\right), \quad \tilde{r} \to 1, \tag{D.18}$$

$$\frac{d\hat{p}(\tilde{r})}{d\tilde{r}} = -\frac{\sqrt{\pi}\Gamma\left(\frac{4}{3}\right)}{3\Gamma\left(\frac{5}{6}\right)}\left(1-\tilde{r}^2\right)^{-\frac{4}{3}} + O\left(\left(1-\tilde{r}^2\right)^{-\frac{1}{3}}\right), \quad \tilde{r} \to 1, \tag{D.19}$$

It can easily be shown that the aperture and pressure have the following properties at the fracture opening:

$$\hat{w}(0) = \frac{745}{196} - \frac{6}{7}H\left(\frac{1}{6}\right) = \frac{6}{7}\left[\frac{\pi\sqrt{3}}{2} + \frac{3\log(3)}{2} + \log(4) - \frac{263}{168}\right], \tag{D.20}$$

$$\lim_{\tilde{r}\to 0}\tilde{r}\frac{d\hat{p}}{d\tilde{r}} = -\frac{\pi}{16}, \tag{D.21}$$

where $H(x)$ represents the harmonic number function. From this, we obtain the value of the source intensity:

$$\hat{Q}_0 = -2\pi w^3(0)\lim_{\tilde{r}\to 0}\tilde{r}\frac{d\hat{p}}{d\tilde{r}} = \frac{27\pi^2}{343}\left[\frac{\pi\sqrt{3}}{2} + \frac{3\log(3)}{2} + \log(4) - \frac{263}{168}\right]^3, \tag{D.22}$$

Additionally, we obtain:

$$\hat{v}_0 = -\lim_{\tilde{r}\to 1}\hat{w}^2\frac{d\hat{p}}{d\tilde{r}} = \frac{4\pi^{\frac{3}{2}}\Gamma\left(\frac{4}{3}\right)}{3\Gamma\left(\frac{5}{6}\right)}\left[\frac{\Gamma\left(\frac{7}{6}\right)}{\Gamma\left(\frac{5}{3}\right)}\right]^2 = \frac{\sqrt{3}}{64\pi^3}\left[\Gamma\left(\frac{1}{3}\right)\right]^9. \tag{D.23}$$

The exact form of the particle velocity is obtained from (D.3), while the fluid leak-off are calculated numerically from (D.4), noting that $\hat{\phi} = \tilde{r}\hat{v} - \tilde{r}^2\hat{v}_0$.

D.1.1.2 Shear thinning fluid ($0 < n < 1$)

To ensure proper behaviour of the benchmark, we define the constants λ_i in formulation (D.1), (D.2) in terms of three arbitrary functions of n, denoted $\sigma_j(n)$, $j = 0, 1, 2$, as

follows:

$$\begin{aligned}
\lambda_0 &= \frac{\pi(n+2)}{n+6}\sigma_0(n) + \frac{n\sqrt{\pi}\Gamma\left(\frac{3-n}{2}\right)}{2\Gamma\left(2-\frac{n}{2}\right)}\sigma_1(n) + \frac{(n-1)\sqrt{\pi}\Gamma\left(2-\frac{n}{2}\right)}{2\Gamma\left(\frac{5-n}{2}\right)}\sigma_2(n),\\
\lambda_1 &= -\frac{2(n+2)}{n+6}\sigma_0(n) + \frac{2(1-n)\Gamma\left(\frac{3-n}{2}\right)}{\sqrt{\pi}\Gamma\left(2-\frac{n}{2}\right)}\sigma_1(n) + \frac{2(2-n)\Gamma\left(2-\frac{n}{2}\right)}{\sqrt{\pi}\Gamma\left(\frac{5-n}{2}\right)}\sigma_2(n),\\
\lambda_2 &= -\sigma_1(n), \quad \lambda_3 = -\sigma_2(n), \quad \lambda_4 = 0, \quad \lambda_5 = \sigma_0(n), \quad \lambda_6 = 0,
\end{aligned} \tag{D.24}$$

where we have $h_5(\tilde{r}, \alpha_0)$, $\pi_5(\tilde{r}, \alpha_0)$. The values of $\sigma_j(n)$ used for various values of n are given in Table. D.2. These functions are chosen to ensure that the benchmark solution is physically realistic. For intermediate values of n a spline based approximation of functions $\sigma_j(n)$ is used to choose appropriate values.

n	σ_0	σ_1	σ_2
0.1	0.525	0.500	0.575
0.2	0.680	0.300	0.650
0.3	0.600	0.270	0.850
0.4	0.550	0.250	0.900
0.5	0.550	0.270	0.210
0.6	0.540	0.250	0.220
0.7	0.540	0.250	0.225
0.8	0.550	0.250	0.250
0.9	0.580	0.300	0.290
1.0	0.550	0.033	0.000

TABLE D.2: The values of $\sigma_j(n)$, $j = 1, 2, 3$, used for the analytical benchmark in numerical simulations. The value $n = 1$ is used to approximate values when $0.9 < n < 1$.

The benchmark solution will now have the following asymptotics at the crack tip:

$$\hat{w}(\tilde{r}) = \frac{2\sqrt{\pi}\Gamma\left(\frac{n+6}{2(n+2)}\right)}{\Gamma\left(\frac{n+4}{n+2}\right)}\sigma_0(n)\left(1-\tilde{r}^2\right)^{\alpha_0} + O\left(\left(1-\tilde{r}^2\right)^{\alpha_0+1}\right), \quad \tilde{r} \to 1, \tag{D.25}$$

$$\frac{d\hat{p}(\tilde{r})}{d\tilde{r}} = -\frac{(2-n)\sqrt{\pi}\Gamma\left(\frac{2n+2}{n+2}\right)}{(n+2)\Gamma\left(\frac{3n+2}{2(n+2)}\right)}\sigma_0(n)\left(1-\tilde{r}^2\right)^{\alpha_0-2} + O\left(\left(1-\tilde{r}^2\right)^{\alpha_0-1}\right), \quad \tilde{r} \to 1. \tag{D.26}$$

Meanwhile, it can easily be shown that:

$$\begin{aligned}
\hat{w}(0) = \frac{2(n+2)}{n+6}\left[\frac{3n+26}{n+6} - H\left(\frac{2-n}{2(n+2)}\right)\right]\sigma_0(n) + \frac{2n\Gamma\left(\frac{3-n}{2}\right)}{\sqrt{\pi}\Gamma\left(2-\frac{n}{2}\right)}\left[1-\frac{1}{2-n}\right]\sigma_1(n)\\
+ \frac{2\Gamma\left(2-\frac{n}{2}\right)}{\sqrt{\pi}\Gamma\left(\frac{5-n}{2}\right)}\left[\frac{2}{3-n} - n\right]\sigma_2(n),
\end{aligned} \tag{D.27}$$

$$\lim_{\tilde{r}\to 0}\tilde{r}^n\frac{d\hat{p}(\tilde{r})}{d\tilde{r}} = -(1-n)\sigma_1(n), \tag{D.28}$$

As such, the source intensity will be given by:

$$\hat{Q}_0 = 2\pi \left[(1-n)\sigma_1(n)\hat{w}^{2n+1}(0)\right]^{\frac{1}{n}}, \tag{D.29}$$

While we also obtain:

$$\hat{v}_0 = \left\{ \frac{(2-n)\sqrt{\pi}\Gamma\left(\frac{2n+2}{n+2}\right)}{(n+2)\Gamma\left(\frac{3n+2}{2(n+2)}\right)} \left[\frac{2\sqrt{\pi}\Gamma\left(\frac{n+6}{2(n+2)}\right)}{\Gamma\left(\frac{n+4}{n+2}\right)} \right]^{n+1} \right\}^{\frac{1}{n}} \sigma_0^{\frac{n+2}{n}}(n), \tag{D.30}$$

The exact form of the particle velocity is obtained from (D.3), while the fluid leak-off are calculated numerically from (D.4), noting that $\hat{\phi} = \tilde{r}\hat{v} - \tilde{r}^2\hat{v}_0$.

D.1.2 Toughness dominated ($\hat{K}_{Ic} > 0$)

D.1.2.1 Newtonian fluid ($n = 1$)

We take the following values for constants λ_i:

$$\lambda_0 = 1, \quad \lambda_1 = 0.5, \quad \lambda_2 = 0, \quad \lambda_3 = 0, \quad \lambda_4 = -0.25, \quad \lambda_5 = 0, \quad \lambda_6 = -0.35, \tag{D.31}$$

where we have $h_5(\tilde{r}, \alpha_1)$, $\pi_5(\tilde{r}, \alpha_1)$. As such the asymptotic representations at the fracture tip will be given by:

$$\hat{w}(\tilde{r}) = \left\{ \frac{2}{\pi}\left[5 - \log(2)\right] - \frac{2}{5} \right\} \sqrt{1-\tilde{r}^2} + \frac{7\pi}{20}\left(1-\tilde{r}^2\right) + O\left(\left(1-\tilde{r}^2\right)^{\frac{3}{2}}\right), \quad \tilde{r} \to 1, \tag{D.32}$$

$$\frac{d\hat{p}(\tilde{r})}{d\tilde{r}} = -\frac{7}{20}(1-\tilde{r}^2)^{-1} + O\left(1\right), \quad \tilde{r} \to 1, \tag{D.33}$$

Meanwhile, it can easily be shown that:

$$\hat{w}(0) = \frac{14\log(2) - 9}{10} + \frac{2\left(6 - \log(2)\right)}{\pi}, \quad \lim_{\tilde{r}\to 0} \tilde{r}\frac{d\hat{p}(\tilde{r})}{d\tilde{r}} = -\frac{1}{4}, \tag{D.34}$$

As such the source intensity is given by:

$$\hat{Q}_0 = \frac{\pi}{2}\left[\frac{14\log(2) - 9}{10} + \frac{2\left(6 - \log(2)\right)}{\pi}\right]^3, \tag{D.35}$$

Additionally, the stress intensity factor takes the form:

$$\hat{K}_{Ic} = \hat{K}_I = \frac{5 - \log(2)}{2\sqrt{\pi}} - \frac{\sqrt{\pi}}{10}, \tag{D.36}$$

While we also obtain:

$$\hat{v}_0 = \frac{7}{20}\left\{\frac{2}{\pi}\left[5 - \log(2)\right] - \frac{2}{5}\right\}^2, \tag{D.37}$$

D.1.2.2 Shear thinning fluid ($0 < n < 1$)

To ensure proper behaviour of the benchmark, we define the constants λ_i in formulation (D.1), (D.2) in terms of four arbitrary functions of n, denoted $\sigma_j(n)$, $j = 0, 1, 2, 3$, as follows:

$$\begin{gathered}
\lambda_0 = \frac{\pi}{8}\sigma_0(n) + \frac{\pi\left(10 - 3n\right)}{2(3-n)(4-n)}\sigma_1(n) + \frac{n\sqrt{\pi}\Gamma\left(\frac{3-n}{2}\right)}{2\Gamma\left(2 - \frac{n}{2}\right)}\sigma_2(n) + \frac{(n-1)\sqrt{\pi}\Gamma\left(2 - \frac{n}{2}\right)}{2\Gamma\left(\frac{5-n}{2}\right)}\sigma_3(n), \\
\lambda_1 = \frac{3n - 10}{(3-n)(4-n)}\sigma_1(n) + \frac{2(1-n)\Gamma\left(\frac{3-n}{2}\right)}{\sqrt{\pi}\Gamma\left(2 - \frac{n}{2}\right)}\sigma_2(n) + \frac{2(2-n)\Gamma\left(2 - \frac{n}{2}\right)}{\sqrt{\pi}\Gamma\left(\frac{5-n}{2}\right)}\sigma_3(n), \\
\lambda_2 = -\sigma_2(n), \quad \lambda_3 = -\sigma_3(n), \quad \lambda_4 = 0, \quad \lambda_5 = \sigma_1(n), \quad \lambda_6 = 0,
\end{gathered} \tag{D.38}$$

where we have $h_5(\tilde{r}, \alpha_1, \alpha_2)$, $\pi_5(\tilde{r}, \alpha_1, \alpha_2)$. The values of $\sigma_j(n)$ used for various values of n are given in Table. D.3. These functions are chosen to ensure that the benchmark solution is physically realistic. For intermediate values of n a spline based approximation of functions $\sigma_j(n)$ is used to choose appropriate values.

n	σ_0	σ_1	σ_2	σ_3
0.050	5.00	1.200	0.100	-1.00
0.100	2.75	1.000	0.125	-1.00
0.200	2.50	0.400	1.750	-0.05
0.300	2.25	0.500	1.450	-0.05
0.400	2.20	0.350	1.100	-0.05
0.500	1.75	0.500	1.000	-0.05
0.600	1.20	0.650	1.100	-0.05
0.700	1.20	0.650	1.500	-0.05
0.800	1.00	0.650	2.000	-0.05
0.900	1.00	0.750	2.200	-0.05
0.990	1.50	0.050	2.200	-0.50
0.999	2.00	0.005	2.500	-1.00

TABLE D.3: The values of σ_j, $j = 0, 1, 2, 3$, used for the analytical benchmark in numerical simulations.

The benchmarks asymptotic representation at the fracture front are given by:

$$\hat{w}(\tilde{r}) = \sigma_0(n)\sqrt{1-\tilde{r}^2} + \frac{2\sqrt{\pi}\Gamma\left(2 - \frac{n}{2}\right)}{\Gamma\left(\frac{5-n}{2}\right)}\sigma_1(n)\left(1-\tilde{r}^2\right)^{\alpha_1} + O\left(\left(1-\tilde{r}^2\right)^{\alpha_1+1}\right), \quad \tilde{r} \to 1, \tag{D.39}$$

$$\frac{d\hat{p}(\tilde{r})}{d\tilde{r}} = -\frac{\sqrt{\pi}(2-n)\Gamma\left(\frac{n+1}{2}\right)}{\Gamma\left(\frac{n}{2}\right)}\sigma_1(n)\left(1-\tilde{r}^2\right)^{\alpha_1-2} + O\left(\left(1-\tilde{r}^2\right)^{\alpha_1-1}\right), \quad \tilde{r} \to 1, \tag{D.40}$$

$$\hat{p}(x) = \frac{\pi}{8}\sigma_0(n) + \left[\frac{\pi}{1+2\alpha_1} - \frac{2}{1+2\alpha_1} - \frac{\Gamma(\alpha_1-1)}{2\Gamma(\alpha_1)} + \frac{\pi}{1+2\alpha_2} - \frac{2}{1+2\alpha_2} - \frac{\Gamma(\alpha_2-1)}{2\Gamma(\alpha_2)}\right]\sigma_1(n) + \left[\frac{\Gamma\left(\frac{3-n}{2}\right)}{\Gamma\left(2-\frac{n}{2}\right)}\left(\frac{n\sqrt{\pi}}{2} + \frac{2(1-n)}{\sqrt{\pi}}\right) - 1\right]\sigma_2(n) + \left[\frac{\Gamma\left(2-\frac{n}{2}\right)}{\Gamma\left(\frac{5-n}{2}\right)}\left(\frac{(n-1)\sqrt{\pi}}{2} + \frac{2(2-n)}{\sqrt{\pi}}\right) - 1\right]\sigma_3(n) + \frac{\sqrt{\pi}(1-2\alpha_1)\Gamma(2-\alpha_1)}{2(1-\alpha_1)\Gamma\left(\frac{3}{2}-\alpha_1\right)}\sigma_1(n)\left(1-x^2\right)^{\alpha_1-1} + O\left(1-x^2\right), \quad x \to 1. \tag{D.41}$$

Meanwhile, the values at the fracture opening are given by:

$$\hat{w}(0) = \sigma_0(n) + \left\{\frac{2}{4-n}\left[\frac{18-5n}{4-n} - H\left(1-\frac{n}{2}\right)\right] + \frac{1}{3-n}\left[\frac{14-5n}{3-n} - H(2-n)\right]\right\}\sigma_1(n) - \frac{2n\sqrt{\pi}(1-n)\sec\left(\frac{n\pi}{2}\right)}{(2-n)\Gamma\left(2-\frac{n}{2}\right)\Gamma\left(\frac{n-1}{2}\right)}\sigma_2(n) - \frac{2\sqrt{\pi}(n-1)(2-n)\sec\left(\frac{(n-1)\pi}{2}\right)}{(3-n)\Gamma\left(\frac{5-n}{2}\right)\Gamma\left(\frac{n}{2}-1\right)}\sigma_3(n), \tag{D.42}$$

$$\lim_{\tilde{r}\to 0}\tilde{r}^n\frac{d\hat{p}(\tilde{r})}{d\tilde{r}} = -(1-n)\sigma_2(n), \tag{D.43}$$

As such the source strength intensity is:

$$\hat{Q}_0 = 2\pi\left[(1-n)\sigma_2(n)\hat{w}^{2n+1}(0)\right]^{\frac{1}{n}}, \tag{D.44}$$

Additionally, it can be shown that:

$$\hat{K}_{Ic} = \hat{K}_I = \frac{\sqrt{\pi}}{4}\sigma_0(n), \tag{D.45}$$

while we have:

$$\hat{v}_0 = \left[\frac{\sqrt{\pi}(2-n)\Gamma\left(\frac{n+1}{2}\right)}{\Gamma\left(\frac{n}{2}\right)}\sigma_1(n)\right]^{\frac{1}{n}}\sigma_0^{\frac{n+1}{n}}(n), \tag{D.46}$$

D.2 Radial fracture with shear-stress

While the methodology in this case will be largely identical to the previous section, the different normalization scheme and self-similar formulation will require that we slightly modify the approach.

We now take a solution in the form:

$$\hat{w}(\tilde{r}) = L_0\sum_{i=0}^{N}\lambda_i\hat{h}_i(\tilde{r}), \quad \hat{p}(\tilde{r}) = \sum_{i=0}^{N}\lambda_i\pi_i(\tilde{r}), \tag{D.47}$$

Examples of the base functions $\hat{h}_i(\tilde{r})$, $\pi_i(\tilde{r})$ are collected in Table. D.4. The subscript indices are chosen to ensure consistency with the previous section.

i	$\pi_i(\tilde{r})$	$h_i(\tilde{r})$
0	1	$\frac{4}{\pi^2}\sqrt{1-\tilde{r}^2}$
1	$\tilde{r}$	$\frac{1}{2\pi}\left[\sqrt{1-\tilde{r}^2}+\tilde{r}^2\log\left(\frac{1+\sqrt{1-\tilde{r}^2}}{\tilde{r}}\right)\right]$
4	$\log(\tilde{r})$	$\frac{4}{\pi^2}\left[\tilde{r}\arccos(\tilde{r})+(\log(2)-2)\sqrt{1-\tilde{r}^2}\right]$
6	$\operatorname{arctanh}(\tilde{r})$	$\frac{2}{\pi}\left[E\left(1-\tilde{r}^2\right)-K\left(1-\tilde{r}^2\right)+\log\left(\frac{1+\sqrt{1-\tilde{r}^2}}{\tilde{r}}\right)\right]$

TABLE D.4: Table showing the components of the benchmark solutions. Here functions K, E represent the complete elliptic integral of the first and second kinds respectively.

As a result, the system asymptotics will be as follows:

$$\begin{aligned}\hat{w}(\tilde{r}) = \frac{L_0}{\pi}\left[\frac{4\lambda_0}{\pi}+\lambda_1+\frac{4\lambda_4\left[\log(2)-1\right]}{\pi}+2\lambda_6\right]\sqrt{1-\tilde{r}^2} \\ -\frac{\lambda_6}{2}L_0(1-\tilde{r}^2)+O\left(\left(1-\tilde{r}^2\right)^{\frac{3}{2}}\right), \quad \tilde{r}\to 1,\end{aligned} \tag{D.48}$$

$$\begin{aligned}\hat{p}(\tilde{r}) = -\frac{\lambda_6}{2}\log\left(1-\tilde{r}^2\right)+\left[\lambda_0+\lambda_1+\log(2)\lambda_6\right]-\frac{1}{2}\left[\lambda_1+\lambda_4+\frac{\lambda_6}{2}\right]\left(1-\tilde{r}^2\right) \\ +O\left((1-\tilde{r})^2\right), \quad \tilde{r}\to 1\end{aligned} \tag{D.49}$$

It is immediately apparent that we require $\lambda_6 < 0$ for a physically realistic solution. Meanwhile, the definition of L_0 provides the condition:

$$\frac{1}{\pi}\left[\frac{4\lambda_0}{\pi}+\lambda_1+\frac{4\lambda_4\left[\log(2)-1\right]}{\pi}+2\lambda_6\right]\sqrt{-\frac{\lambda_6}{\alpha}}=1, \tag{D.50}$$

which we satisfy by taking:

$$\lambda_0 = \frac{\pi}{4}\left[\pi\sqrt{-\frac{\alpha}{\lambda_6}}-\lambda_1-\frac{4\lambda_4\left[\log(2)-1\right]}{\pi}-2\lambda_6\right]. \tag{D.51}$$

We must also satisfy the boundary condition:

$$\lim_{\tilde{r}\to 0}-\hat{w}^3\tilde{r}\frac{d\hat{p}}{d\tilde{r}}=1, \tag{D.52}$$

noting that:

$$\hat{w}(0) = \frac{L_0}{\pi}\left[\frac{4\lambda_0}{\pi} + \frac{\lambda_1}{2} + \frac{4\lambda_4\left[\log(2)-2\right]}{\pi} + \lambda_6\left[2-\log(4)\right]\right], \tag{D.53}$$

$$\lim_{\tilde{r}\to 0}\tilde{r}\frac{d\hat{p}}{d\tilde{r}} = \lambda_4, \tag{D.54}$$

As such this condition becomes:

$$-\lambda_4\frac{L_0^3}{\pi^3}\left\{\frac{4\lambda_0}{\pi} + \frac{\lambda_1}{2} + \frac{4\lambda_4\left[\log(2)-2\right]}{\pi} + \lambda_6\left[2-\log(4)\right]\right\}^3 = 1, \tag{D.55}$$

which we satisfy by taking:

$$L_0 = \pi\left(-\frac{1}{\lambda_4}\right)^{\frac{1}{3}}\left[\frac{4\lambda_0}{\pi} + \frac{\lambda_1}{2} + \frac{4\lambda_4\left[\log(2)-2\right]}{\pi} + \lambda_6\left[2-\log(4)\right]\right]^{-1}. \tag{D.56}$$

With the system constraints satisfied, the remaining constants and variables follow immediately from the following relations:

$$\hat{v}_0 = 2\hat{w}_0^2\hat{p}_0, \tag{D.57}$$

while (4.182) and (4.183) yield that:

$$\hat{K}_{Ic} = \frac{\hat{w}_0\sqrt{1+4(1-\nu)\hat{\omega}}}{\sqrt{L_0}\,(1+\hat{\omega})}, \quad \hat{\omega} = \frac{\hat{p}_0}{\pi(1-\nu)-\hat{p}_0}, \tag{D.58}$$

with $\hat{K}_I$ and $\hat{K}_f$ following by (4.184):

$$\hat{K}_I = \frac{\hat{K}_{Ic}}{\sqrt{1+4(1-\nu)\hat{\omega}}}, \quad \hat{K}_f = \frac{\hat{K}_{Ic}\hat{\omega}}{\sqrt{1+4(1-\nu)\hat{\omega}}}, \tag{D.59}$$

The particle velocity is given by the Poiseuille equation:

$$\Lambda = \tilde{r}\hat{v} = -\tilde{r}\hat{w}^2\frac{d\hat{p}}{d\tilde{r}}, \tag{D.60}$$

while the fluid leak-off is obtained numerically from the fluid mass equation:

$$\hat{q}_l = \tilde{r}\frac{d\hat{w}}{d\tilde{r}} - \hat{w} - \frac{1}{\hat{v}_0\tilde{r}}\frac{d}{d\tilde{r}}\left(\hat{w}\Lambda\right), \tag{D.61}$$

Appendix E

Modifications to the elasticity equation

E.1 Inverse elasticity equation with fracture propagation criterion

We begin with the following form of the normalized inverse elasticity equation (4.60)$_2$, (4.62):

$$\tilde{w}(\tilde{r},\tilde{t}) = \frac{8}{\pi} L(\tilde{t}) \int_{\tilde{r}}^{1} \frac{\xi}{\sqrt{\xi^2-\tilde{r}^2}} \int_0^1 \frac{\eta \tilde{p}(\eta\xi,\tilde{t})}{\sqrt{1-\eta^2}}\, d\eta\, d\xi, \tag{E.1}$$

alongside the fracture propagation criterion (4.63):

$$\tilde{K}_I = \tilde{K}_{Ic} = \frac{2}{\sqrt{\pi}} \sqrt{L(\tilde{t})} \int_0^1 \frac{\eta \tilde{p}(\eta,\tilde{t})}{\sqrt{1-\eta^2}}\, d\eta. \tag{E.2}$$

Now, relation (E.1) can be expanded as follows:

$$\tilde{w}(\tilde{r},\tilde{t}) = \frac{8}{\pi} L(\tilde{t}) \int_{\tilde{r}}^{1} \frac{\xi}{\sqrt{\xi^2-\tilde{r}^2}} \int_0^1 \frac{\eta}{\sqrt{1-\eta^2}} \left[\tilde{p}(\eta\xi,\tilde{t}) - \tilde{p}(\eta,\tilde{t}) + \tilde{p}(\eta,\tilde{t})\right]\, d\eta\, d\xi. \tag{E.3}$$

Removing the final pressure term from the brackets, and noting definition (E.2), this becomes:

$$\begin{aligned} \tilde{w}(\tilde{r},\tilde{t}) = \frac{8}{\pi} L(\tilde{t}) \int_{\tilde{r}}^{1} \frac{\xi}{\sqrt{\xi^2-\tilde{r}^2}} \int_0^1 \frac{\eta}{\sqrt{1-\eta^2}} \left[\tilde{p}(\eta\xi,\tilde{t}) - \tilde{p}(\eta,\tilde{t})\right]\, d\eta\, d\xi \\ + \frac{4}{\sqrt{\pi}} \sqrt{L(\tilde{t})} \tilde{K}_I \sqrt{1-\tilde{r}^2}. \end{aligned} \tag{E.4}$$

Next, utilizing the fundamental theorem of calculus, we transform the difference between the pressure functions into its integral equivalent:

$$\begin{aligned}\tilde{w}(\tilde{r},\tilde{t}) = \frac{8}{\pi}L(\tilde{t})\int_{\tilde{r}}^{1}\frac{\xi}{\sqrt{\xi^2-\tilde{r}^2}}\int_{0}^{1}\frac{\eta}{\sqrt{1-\eta^2}}\int_{\eta}^{\eta\xi}\frac{\partial\tilde{p}(y,\tilde{t})}{\partial y}\,dy\,d\eta\,d\xi \\ + \frac{4}{\sqrt{\pi}}\sqrt{L(\tilde{t})}\tilde{K}_I\sqrt{1-\tilde{r}^2}.\end{aligned} \tag{E.5}$$

Changing the order of integration, we can place this in the form:

$$\begin{aligned}\tilde{w}(\tilde{r},\tilde{t}) = -\frac{8}{\pi}L(\tilde{t})\int_{0}^{1}\frac{\eta}{\sqrt{1-\eta^2}}\int_{\eta\tilde{r}}^{\eta}\frac{\partial\tilde{p}(y,\tilde{t})}{\partial y}\int_{\tilde{r}}^{y/\eta}\frac{\xi}{\sqrt{\xi^2-\tilde{r}^2}}\,d\xi\,dy\,d\eta \\ + \frac{4}{\sqrt{\pi}}\sqrt{L(\tilde{t})}\tilde{K}_I\sqrt{1-\tilde{r}^2}.\end{aligned} \tag{E.6}$$

The integral on the right can be resolved, to yield:

$$\begin{aligned}\tilde{w}(\tilde{r},\tilde{t}) = -\frac{8}{\pi}L(\tilde{t})\int_{0}^{1}\frac{\eta}{\sqrt{1-\eta^2}}\int_{\eta\tilde{r}}^{\eta}\frac{\partial\tilde{p}(y,\tilde{t})}{\partial y}\sqrt{\left(\frac{y}{\eta}\right)^2-\tilde{r}^2}\,dy\,d\eta \\ + \frac{4}{\sqrt{\pi}}\sqrt{L(\tilde{t})}\tilde{K}_I\sqrt{1-\tilde{r}^2}.\end{aligned} \tag{E.7}$$

We once again change the order of integration, which this time requires splitting the integral into two separate domains:

$$\begin{aligned}\tilde{w}(\tilde{r},\tilde{t}) = -\frac{8}{\pi}L(\tilde{t})\int_{0}^{\tilde{r}}\frac{\partial\tilde{p}(y,\tilde{t})}{\partial y}\int_{y}^{y/\tilde{r}}\frac{\sqrt{y^2-\tilde{r}^2\eta^2}}{\sqrt{1-\eta^2}}\,d\eta\,dy \\ - \frac{8}{\pi}L(\tilde{t})\int_{\tilde{r}}^{1}\frac{\partial\tilde{p}(y,\tilde{t})}{\partial y}\int_{y}^{1}\frac{\sqrt{y^2-\tilde{r}^2\eta^2}}{\sqrt{1-\eta^2}}\,d\eta\,dy \\ + \frac{4}{\sqrt{\pi}}\sqrt{L(\tilde{t})}\tilde{K}_I\sqrt{1-\tilde{r}^2}.\end{aligned} \tag{E.8}$$

Now, noting the definition of the incomplete elliptical integral of the second kind [5], it can be shown that:

$$\int\frac{\sqrt{y^2-\tilde{r}^2\eta^2}}{\sqrt{1-\eta^2}}\,d\eta = yE\left(\arcsin(\eta)\,\middle|\,\frac{\tilde{r}^2}{y^2}\right), \tag{E.9}$$

and as such (E.8) becomes:

$$\begin{aligned}\tilde{w}(\tilde{r},\tilde{t}) = \frac{8}{\pi}L(\tilde{t})\int_{0}^{\tilde{r}}\frac{\partial\tilde{p}(y,\tilde{t})}{\partial y}y\left[E\left(\arcsin(y)\,\middle|\,\frac{\tilde{r}^2}{y^2}\right)-E\left(\arcsin\left(\frac{y}{\tilde{r}}\right)\,\middle|\,\frac{\tilde{r}^2}{y^2}\right)\right]dy \\ + \frac{8}{\pi}L(\tilde{t})\int_{\tilde{r}}^{1}\frac{\partial\tilde{p}(y,\tilde{t})}{\partial y}y\left[E\left(\arcsin(y)\,\middle|\,\frac{\tilde{r}^2}{y^2}\right)-E\left(\arcsin(1)\,\middle|\,\frac{\tilde{r}^2}{y^2}\right)\right]dy \\ + \frac{4}{\sqrt{\pi}}\sqrt{L(\tilde{t})}\tilde{K}_I\sqrt{1-\tilde{r}^2}.\end{aligned} \tag{E.10}$$

Recombining the integrals through the use of a special function, (4.66), we obtain representation (4.65).

E.2 Elasticity equation with tangential stress

We consider a 3D penny-shaped crack, defined in polar coordinates by the system $\{r, \theta, z\}$, with associated crack dimensions $\{l(t), w(t)\}$ as the fracture radius and aperture respectively. As the flow is axisymmetric, all variables will be independent of the angle θ.

The normal and tangential stress on the fracture walls (σ_0 and τ respectively), created by the fluid pressure, follows directly from lubrication theory (see for example [218]). The equation for the net fluid pressure on the fracture walls (i.e. $p = p_f - \sigma_0$, σ_0 is the confining stress), including the tangential stress term, is given in Cartesian coordinates (x_1, x_2, x_3) by [176] (see Sect. 4.1.3.2, equations (4.20)-(4.25)):

$$\begin{aligned} p(r,t) = &\frac{E}{8\pi(1-\nu^2)} \int_\Omega \frac{1}{\sqrt{(x_1-\xi_1)^2+(x_3-\xi_3)^2}} \left[\frac{\partial^2 w}{\partial \xi_1^2} + \frac{\partial^2 w}{\partial \xi_3^2}\right] d\xi_1 d\xi_3 \\ &- \frac{1-2\nu}{8\pi(1-\nu)} \int_\Omega \frac{1}{\sqrt{(x_1-\xi_1)^2+(x_3-\xi_3)^2}} \left[\frac{\partial [[p_{\xi_1}]]}{\partial \xi_1} + \frac{\partial [[p_{\xi_3}]]}{\partial \xi_3}\right] d\xi_1 d\xi_3. \end{aligned} \tag{E.11}$$

Here $[[x]]$ indicates the jump in x (i.e. $[[p]] = p_+ - p_-$), $\Omega = \left\{(x_1, x_3) : \sqrt{x_1^2 + x_3^2} \leq l(t)\right\}$ is the fracture domain, while E and ν are the Young's modulus and Poisson ratio respectively.

As the problem is invariant of the angle θ, the pressure term can be obtained by transforming this into radial coordinates (r, θ), integrated with respect to the corresponding variables (η_1, η_2). We obtain the relationship:

$$\begin{aligned} p(r,t) = &\frac{E}{8\pi(1-\nu^2)} \int_0^{l(t)} \frac{\partial}{\partial \eta_1} \left(\eta_1 \frac{\partial w(\eta_1, t)}{\partial \eta_1}\right) \int_0^{2\pi} \frac{1}{\sqrt{r^2 + \eta_1^2 - 2r\eta_1 \cos(\theta - \eta_2)}} d\eta_2 d\eta_1 \\ &- \frac{1-2\nu}{4\pi(1-\nu)} \int_0^{l(t)} \frac{\partial}{\partial \eta_1} \left(\eta_1 \tau(\eta_1, t)\right) \int_0^{2\pi} \frac{1}{\sqrt{r^2 + \eta_1^2 - 2r\eta_1 \cos(\theta - \eta_2)}} d\eta_2 \, d\eta_1. \end{aligned} \tag{E.12}$$

It can be shown that:

$$\int_0^{2\pi} \frac{1}{\sqrt{r^2 + \eta_1^2 - 2r\eta_1 \cos(\theta - \eta_2)}} d\eta_2 = \frac{4K\left(\frac{4r\eta_1}{(\eta_1 + r)^2}\right)}{|\eta_1 + r|}, \tag{E.13}$$

where $K(x)$ is the complete elliptic integral of the first kind [5].

Inserting this and using integration by parts, we have:

$$p(r,t) = -\int_0^{l(t)} \left[k_2 \frac{\partial w}{\partial \eta_1} - k_1 \tau(\eta_1) \right] \mathcal{M}(r,\eta_1)\, d\eta_1, \tag{E.14}$$

while substituting the dimensionless variable $\rho = \eta_1 / l(t)$ gives the same representation used in $(4.41)_1$-(4.42):

$$p(r,t) = -\frac{1}{l(t)} \int_0^1 \left[k_2 \frac{\partial w(\rho l(t))}{\partial \rho} - k_1 l(t) \tau(\rho l(t)) \right] \mathcal{M}\left(\frac{r}{l(t)}, \rho \right) d\rho, \tag{E.15}$$

where:

$$\begin{aligned} \mathcal{M}(\tilde{r},\rho) &= \frac{1}{2(\tilde{r}+\rho)} K\left(\frac{4\tilde{r}\rho}{(\rho+\tilde{r})^2} \right) - \frac{1}{2(\tilde{r}-\rho)} E\left(\frac{4\tilde{r}\rho}{(\rho+\tilde{r})^2} \right) \\ &= \frac{1}{2(\tilde{r}+\rho)} K\left(1 - \left(\frac{\rho-\tilde{r}}{\rho+\tilde{r}} \right)^2 \right) - \frac{1}{2(\tilde{r}-\rho)} E\left(1 - \left(\frac{\rho-\tilde{r}}{\rho+\tilde{r}} \right)^2 \right), \end{aligned} \tag{E.16}$$

$$k_1 = \frac{1-2\nu}{\pi(1-\nu)}, \quad k_2 = \frac{E}{2\pi(1-\nu^2)}. \tag{E.17}$$

Here $E(x)$ is the complete elliptic integral of the second kind [5]. It can be shown numerically that, within the corresponding domains ($0 \le \tilde{r} \le 1$, $0 \le \rho \le 1$), this kernel function $\mathcal{M}$ is merely an alternative representation of the standard kernel for this problem [113]:

$$\mathcal{M}\left[\tilde{r},\rho\right] = \frac{1}{2\pi} \begin{cases} \frac{1}{\tilde{r}} K\left(\frac{\rho^2}{\tilde{r}^2} \right) + \frac{\tilde{r}}{\rho^2 - \tilde{r}^2} E\left(\frac{\rho^2}{\tilde{r}^2} \right), & \tilde{r} > \rho \\ \frac{\rho}{\rho^2 - \tilde{r}^2} E\left(\frac{\tilde{r}^2}{\rho^2} \right), & \rho > \tilde{r} \end{cases} \tag{E.18}$$

Additionally, it is worth noting that the constants k_1, k_2, are identical to those obtained in the KGD case [230].

With the elasticity equation with tangential stresses obtained, it is clear that the next step is to invert the operator and obtain the inverse relation. This is achieved by noting that we can place (E.14) in the form:

$$p(r,t) = -\int_0^{l(t)} g'(x) \mathcal{M}\left(r,x\right) dx, \quad 0 < r < 1, \tag{E.19}$$

where:

$$g(r) = \int_r^{l(t)} \left(k_1 \tau(s,t) - k_2 \frac{\partial w}{\partial s} \right) ds = k_2 w(r,t) + k_1 \int_r^{l(t)} \tau(s,t)\, ds. \tag{E.20}$$

From this, it immediately follows that the inverse relation must be (compare with the classical result, see Sect. 4.2.2):

$$k_2 w(r,t) + k_1 \int_r^{l(t)} \tau(s,t)\, ds = \frac{4}{\pi^2} l(t) \int_{r/l(t)}^1 \frac{\xi}{\sqrt{\xi^2 - (r/l(t))^2}} \int_0^1 \frac{\eta p(\eta\xi l(t), t)}{\sqrt{1-\eta^2}}\, d\eta d\xi, \tag{E.21}$$

In practice this form of the elasticity operator will not be employed during the examination in Sect. 4.3. This is because it has already been demonstrated that incorporating the modified elasticity equation does not have a significant effect on the obtained solution (see [230]), with the primary effects instead resulting from the updated energy release rate based fracture criterion and the change in crack tip asymptotics in the viscosity dominated regime. As such, the modified elasticity equation is best neglected in this preliminary investigation.

Appendix F

Universal algorithm for a penny-shaped crack

F.1 Introduction

A truly comprehensive description of the universal algorithm scheme for the KGD formulation is provided in the thesis by *Perkowska* [164], and the underlying principles will remain the same in the case of a penny-shaped crack. Those interested in a more detailed examination of the construction philosophy are directed to the aforementioned text. However, given the central role of the algorithm, which was only briefly outlined in Sect. 4.2.5.1, the important details will be restated here for completeness.

F.1.1 Philosophy of the algorithms construction

The basis of construction of the universal algorithm is to utilize the asymptotic representation of the problem parameters at the fracture front, which are known to provide a reasonably accurate approximation of the solution (typically within 1%, see [196]), whilst also accounting for the disparity between this and the exact solution. In this way, use of the asymptotic coefficients ensures the computational method is both efficient and stable, while continuing to account for the remainder minimizes the computational error.

To accomplish this, the parameters will need to be reformulated in a more computationally friendly way. This is achieved by basing them on the first few terms of the crack tip asymptotes, (4.73) and (4.75) for the aperture and particle velocity respectively, while

also incorporating an additional term:

$$\hat{w}(\tilde{r}) = \hat{w}_0 \left(1 - \tilde{r}^2\right)^{\alpha_0} + \hat{w}_1 \left(1 - \tilde{r}^2\right)^{\alpha_1} + \delta_w(\tilde{r}), \tag{F.1}$$

$$\Lambda = \tilde{r}\hat{v}(\tilde{r}) = \hat{v}_0 + \delta_\Lambda(\tilde{r}), \tag{F.2}$$

where the term Λ is introduced to eliminate the singularity at the fluid well ($\tilde{r} = 0$), while providing a clearer demonstration of the algorithms construction than the reduced particle velocity Φ. It should be noted that, in the toughness dominated case, an additional asymptotic term $\hat{w}_2$ can also be used to increase the accuracy, however this is omitted here for the sake of simplicity.

With this representation in place, the algorithm will run using the scheme outlined in Fig. F.1. Namely, it will consist of three main blocks, each of which is designed to obtain an improved approximation for a given set of parameters, which are iterated until a desired level of solution convergence is reached.

To maximize the effect of introducing the crack tip asymptotics, these will be used to remove terms from any integrals and to resolve them analytically. Additionally, when reconstructing the particle velocity, the Tikhonov type regularization is used to strictly enforce the known asymptotic behaviour of the solution. These steps are have the effect of both improving the efficiency, as well as reducing the computational errors, of the final algorithm.

With the philosophy and general outline of the scheme in place, more specific details of the algorithms workings can now be given.

F.2 Constructing the algorithm for a shear thinning fluid

In this section the mathematical and computational underpinnings of the algorithm, for the classical penny-shaped formulation, will be outlined for the case of the a shear thinning fluid ($0 < n < 1$). The underlying principles will remain the same when a Newtonian fluid ($n = 1$) is modeled, however, for a perfectly plastic fluid ($n = 0$) degeneration of the Pouseuille equation means that some modification is required (this will be detailed later).

F.2.1 Block 1: Determining asymptotic terms

The first term of the aperture asymptotics is obtained from the fluid balance equation (4.106), which, inserting the parameter representations given above, can be rearranged

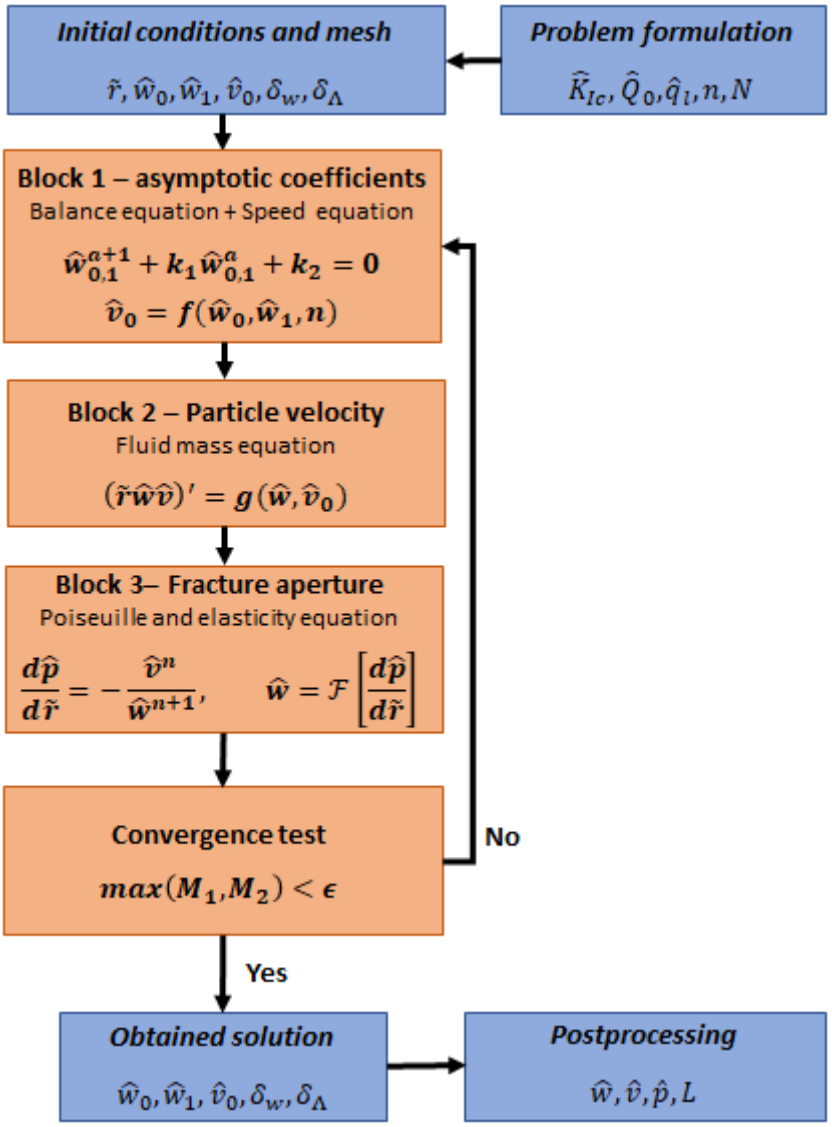

FIGURE F.1: A general overview of the universal algorithm used to obtain numerical solutions for the self-similar radial formulation. The parameters asymptotic coefficients and remainder terms are treated separately until post-processing. Blocks coloured in orange are iterated until a desired level of solution convergence is reached. The full details of each step are given in this appendix.

into the following form:

$$\begin{aligned}(3-s_n)\,\hat{w}_0\hat{v}_0 \int_0^1 \tilde{r}\left(1-\tilde{r}^2\right)^{\alpha_0}\,d\tilde{r} - \frac{\hat{Q}_0}{2\pi} \\ + \hat{v}_0\left\{(3-s_n)\int_0^1 \tilde{r}\left[\hat{w}_1\left(1-\tilde{r}^2\right)^{\alpha_1} + \delta_w(\tilde{r})\right]\,d\tilde{r} + \frac{1-s_n}{\gamma}\int_0^1 \tilde{r}\hat{q}_l(\tilde{r})\,d\tilde{r}\right\} = 0.\end{aligned} \tag{F.3}$$

The next step will depend on whether it is the viscosity or toughness dominated mode being considered. Both are outlined below.

F.2.1.1 Viscosity dominated regime ($\hat{K}_{Ic} = 0$)

In the viscosity dominated regime, the relationship between asymptotic parameters is given by (4.77) and the *speed equation* (4.99), namely:

$$\hat{v}_0 = \left[\mathcal{C}\hat{w}_0^{n+2}\right]^{\frac{1}{n}} = \mathcal{C}^{\frac{1}{n}}\hat{w}_0^{1+\frac{2}{n}}, \quad \mathcal{C} = \frac{2n}{(n+2)^2}\cot\left(\frac{n\pi}{n+2}\right). \tag{F.4}$$

Inserting the above into (F.3), and resolving integrals where possible, yields:

$$\frac{\hat{w}_0^{2+\frac{2}{n}}}{\alpha_0+1} + \left[\frac{\hat{w}_1}{\alpha_1+1} + 2\int_0^1 \tilde{r}\delta_w(\tilde{r})\,d\tilde{r} + \frac{2\,(1-s_n)}{\gamma\,(3-s_n)}\int_0^1 \tilde{r}\hat{q}_l(\tilde{r})\,d\tilde{r}\right]\hat{w}_0^{1+\frac{2}{n}} - \frac{\hat{Q}_0}{\pi\,(3-s_n)\,\mathcal{C}^{\frac{1}{n}}} = 0, \tag{F.5}$$

from which a solution for $\hat{w}_0$ can be obtained numerically using either the *Newton-Raphson* or *Halley* iterative methods, both of which are too well known to need explaining here. Once $\hat{w}_0$ is known, the constant $\hat{v}_0$ follows immediately from (F.4).

The only improved estimate for an asymptotic multiplier which has not yet been described is for the constant $\hat{w}_1$. While it is possible to determine it analytically from the improved estimates for $\hat{w}_0$ and $\hat{v}_0$, using relations between the various asymptotic multipliers, this may require determining additional asymptotic coefficients for the pressure and the particle velocity (some of which would need to be determined numerically), leading to an increase in the error and computation times. Alternatively, $\hat{w}_1$ can be computed first, doing so either numerically, or using the aforementioned relationships between asymptotic multipliers, from the result for the fracture aperture provided by the previous iteration. If this can not be achieved, or does not create a stable or efficient algorithm, then $\hat{w}_1$ can be set to zero (meaning that the associated asymptotic term is instead incorporated into $\delta_w(\tilde{r})$).

The option which is best suited may depend on the number of nodal points or the fluid behaviour index, and the choice made for the final algorithm was determined through experimentation. As such, it will not be provided in further detail here.

F.2.1.2 Toughness dominated regime ($\hat{K}_{Ic} > 0$)

In the toughness dominated regime, the first term of the aperture asymptotics $\hat{w}_0$ is given by (4.103), while its updated relation to the *speed equation* (4.99) is given by (4.80):

$$\hat{v}_0 = \left[\mathcal{C}\hat{w}_0^{n+1}\hat{w}_1\right]^{\frac{1}{n}} = \mathcal{C}^{\frac{1}{n}}\hat{w}_0^{1+\frac{1}{n}}\hat{w}_1^{\frac{1}{n}}, \quad \mathcal{C} = \frac{(3-n)(1-n)}{4}\tan\left(\frac{n\pi}{2}\right). \tag{F.6}$$

Following the same steps as previously, inserting the above into (F.3) yields:

$$\frac{\hat{w}_1^{1+\frac{1}{n}}}{\alpha_1+1}+\left[\frac{\hat{w}_0}{\alpha_0+1}+2\int_0^1\tilde{r}\delta_w(\tilde{r})\,d\tilde{r}+\frac{2\,(1-s_n)}{\gamma\,(3-s_n)}\int_0^1\tilde{r}\hat{q}_l(\tilde{r})\,d\tilde{r}\right]\hat{w}_1^{\frac{1}{n}}-\frac{\hat{Q}_0\hat{w}_0^{-\left(1+\frac{1}{n}\right)}}{\pi\,(3-s_n)\,\mathcal{C}^{\frac{1}{n}}}=0. \tag{F.7}$$

Utilizing the same method as in the viscosity dominated case (either the *Newton-Raphson* or *Halley* iterative methods) the asymptotic multiplier $\hat{w}_1$ can now be obtained, with $\hat{v}_0$ following immediately after from (F.6).

F.2.2 Block 2: Reconstructing the particle velocity

With the main asymptotic terms obtained, it is now time to move onto reconstructing their associated parameters. The first to undergo this process is the particle velocity parameter Λ, which is achieved utilizing Tikhonov type regularization, the important principles of which will be outlined below.

F.2.2.1 Initial results

The particle velocity will be reconstructed using the fluid mass balance equation (4.105). Placing it in terms of parameter Λ, using (4.95) and (F.2), it takes the form:

$$\frac{d}{d\tilde{r}}\left(\hat{w}\Lambda\right)=\hat{v}_0\left[\frac{d}{d\tilde{r}}\left(\tilde{r}^2\hat{w}\right)-(3-s_n)\,\tilde{r}\hat{w}-\frac{1-s_n}{\gamma}\tilde{r}\hat{q}_l\right]. \tag{F.8}$$

Next, expanding this using definition (F.2), gives:

$$\frac{d}{d\tilde{r}}\left(\hat{w}\delta_\Lambda\right)=-\hat{v}_0\left[\left(1-\tilde{r}^2\right)\frac{d\hat{w}}{d\tilde{r}}+(1-s_n)\,\tilde{r}\hat{w}+\frac{1-s_n}{\gamma}\tilde{r}\hat{q}_l\right]=\mathcal{R}(\tilde{r}), \tag{F.9}$$

which, noting that a discrete approximation of each variable is used, yields:

$$\hat{w}_{i+1}\delta_{\Lambda,i+1}-\hat{w}_i\delta_{\Lambda,i}=\int_{\tilde{r}_i}^{\tilde{r}_{i+1}}\mathcal{R}(\tilde{r})\,d\tilde{r}=\hat{\mathcal{R}}_{i+1}, \tag{F.10}$$

where $i=1,2,\ldots,N$ represents the nodal points (with $r_1=0$ and r_N the closest to the fracture tip, while $r_i<r_{i+1}$ for all i), while the notation $\mathcal{R}$, $\hat{\mathcal{R}}_i$ has been introduced for the sake of convenience.

To increase the accuracy to which $\hat{\mathcal{R}}_i$ is computed, terms that can be computed analytically will be removed. This is achieved by introducing the asymptotic terms from (F.1)

into (F.9), giving:

$$\mathcal{R}(\tilde{r}) = -\hat{v}_0 \Big[\hat{w}_0 \tilde{r} \left(1 - s_n - 2\alpha_0\right) \left(1 - \tilde{r}^2\right)^{\alpha_0} + \hat{w}_1 \tilde{r} \left(1 - s_n - 2\alpha_1\right) \left(1 - \tilde{r}^2\right)^{\alpha_1} + \left(1 - \tilde{r}^2\right) \frac{d}{d\tilde{r}} \left(\delta_w\right) + \left(1 - s_n\right) \tilde{r} \delta_w + \frac{1 - s_n}{\gamma} \tilde{r} \hat{q}_l \Big] . \tag{F.11}$$

Integrating this, an alternate representation of $\hat{\mathcal{R}}_i$ is obtained:

$$\hat{\mathcal{R}}_{i+1} = -\hat{v}_0 \Bigg\{ \Bigg[-\frac{\left(1 - s_n - 2\alpha_0\right) \hat{w}_0}{2\left(\alpha_0 + 1\right)} \left(1 - \tilde{r}^2\right)^{\alpha_0 + 1} - \frac{\left(1 - s_n - 2\alpha_1\right) \hat{w}_1}{2\left(\alpha_1 + 1\right)} \left(1 - \tilde{r}^2\right)^{\alpha_1 + 1} + \left(1 - \tilde{r}^2\right) \delta_w \Bigg]_{\tilde{r} = \tilde{r}_i}^{\tilde{r}_{i+1}} + \left(3 - s_n\right) \int_{r_i}^{r_{i+1}} \tilde{r} \delta_w \, d\tilde{r} + \frac{1 - s_n}{\gamma} \int_{r_i}^{r_{i+1}} \tilde{r} \hat{q}_l \, d\tilde{r} \Bigg\}. \tag{F.12}$$

With this in place, the value of $\hat{\mathcal{R}}_i$ will be known to a high level of accuracy. Now all that remains is to reconstruct the discrete approximation of function δ_Λ from this known result. The Tikhonov type regularization scheme used to do this is outlined below.

F.2.2.2 Tikhonov type regularization

We begin by noting that, from (F.10), we have that:

$$\delta_{\Lambda,i} = \frac{w_{i+1} \delta_{\Lambda,i+1} - \hat{\mathcal{R}}_{i+1}}{w_i}. \tag{F.13}$$

As such, given that all other terms are considered known, the particle velocity can automatically be reconstructed once the value of $\delta_{\Lambda,N}$ has been determined.

The regularization scheme employed to reconstruct this point relies on the fact that the parameters asymptotic representation at the crack tip is already known (see (4.75)). Because of this, and noting that the point being sought, $\delta_{\Lambda,N}$, is the closest to the fracture front, it is clear that the following will provide a highly accurate approximation of the remainder term:

$$\delta_\Lambda(\tilde{r}) = \Lambda_0 \left(1 - \tilde{r}\right)^{\beta_1} + \Lambda_1 \left(1 - \tilde{r}\right)^{\beta_2}, \tag{F.14}$$

where constants β_1, β_2 are given in Table. 4.1 for the various regimes, while Λ_0 and Λ_1 still need to be computed.

Next, applying this to the discrete mesh used to approximate the fracture, it is clear that the following will be true:

$$\begin{cases} \delta_{\Lambda,N-1} = \Lambda_0 y_{N-1}^{\beta_1} + \Lambda_1 y_{N-1}^{\beta_2}, \\ \delta_{\Lambda,N-2} = \Lambda_0 y_{N-2}^{\beta_1} + \Lambda_1 y_{N-2}^{\beta_2}, \end{cases} \tag{F.15}$$

where $y_i = 1 - r_i$. With a small amount of manipulation, equations for Λ_0 and Λ_1 can be obtained:

$$\Lambda_0 = \frac{\delta_{\Lambda,N-1} y_{N-2}^{\beta_2} - \delta_{\Lambda,N-2} y_{N-1}^{\beta_2}}{y_{N-1}^{\beta_1} y_{N-2}^{\beta_2} - y_{N-1}^{\beta_2} y_{N-2}^{\beta_1}}, \quad \Lambda_1 = \frac{\delta_{\Lambda,N-1} y_{N-2}^{\beta_1} - \delta_{\Lambda,N-2} y_{N-1}^{\beta_1}}{y_{N-1}^{\beta_2} y_{N-2}^{\beta_1} - y_{N-1}^{\beta_1} y_{N-2}^{\beta_2}}, \tag{F.16}$$

from which it can easily be deduced that:

$$\delta_{\Lambda,N} = \Lambda_0 y_N^{\beta_1} + \Lambda_1 y_N^{\beta_2} = K_1 \delta_{\Lambda,N-1} + K_2 \delta_{\Lambda,N-2}, \tag{F.17}$$

with:

$$K_1 = \frac{y_{N-2}^{\beta_2} y_N^{\beta_1} - y_{N-2}^{\beta_1} y_N^{\beta_2}}{y_{N-1}^{\beta_1} y_{N-2}^{\beta_2} - y_{N-1}^{\beta_2} y_{N-2}^{\beta_1}}, \quad K_2 = \frac{y_{N-1}^{\beta_1} y_N^{\beta_2} - y_{N-1}^{\beta_2} y_N^{\beta_1}}{y_{N-1}^{\beta_1} y_{N-2}^{\beta_2} - y_{N-1}^{\beta_2} y_{N-2}^{\beta_1}}. \tag{F.18}$$

Finally, combining the above with the definition of $\hat{\mathcal{R}}_i$ (F.10), we have that the following will hold:

$$\begin{cases} \hat{w}_N \delta_{\Lambda,N} - \hat{w}_{N-1} \delta_{\Lambda,N-1} = \hat{\mathcal{R}}_N, \\ \hat{w}_{N-1} \delta_{\Lambda,N-1} - \hat{w}_{N-2} \delta_{\Lambda,N-2} = \hat{\mathcal{R}}_{N-1}, \\ \delta_{\Lambda,N} = K_1 \delta_{\Lambda,N-1} + K_2 \delta_{\Lambda,N-2}, \end{cases} \tag{F.19}$$

which, combining to eliminate $\delta_{\Lambda,N-1}$ and $\delta_{\Lambda,N-2}$, provides the value of the remainder term at the crack tip:

$$\delta_{\Lambda,N} = \frac{-K_2 \left(\hat{\mathcal{R}}_N + \hat{\mathcal{R}}_{N-1} \right) \hat{w}_{N-1} - K_1 \hat{\mathcal{R}}_N \hat{w}_{N-2}}{\hat{w}_{N-1} \hat{w}_{N-2} - K_2 \hat{w}_N \hat{w}_{N-1} - K_1 \hat{w}_N \hat{w}_{N-2}}. \tag{F.20}$$

As such, the scheme for reconstructing the particle velocity is clear. First, a high accuracy evaluation of the integral $\hat{\mathcal{R}}_i$, $i = 1, \ldots, N$, is obtained from (F.12). Next, the final term of the remainder is given by (F.20), with the rest of the remainder function δ_Λ following immediately by (F.13). With this reconstructed, the full discrete approximation of the particle velocity is provided by inserting the improved approximations for $\hat{v}_0$ and δ_Λ into (F.2).

F.2.3 Block 3: Reconstructing the fracture aperture

F.2.3.1 Initial results and approach outline

With the first two blocks complete, improved estimates of the asymptotic multipliers ($\hat{w}_0$, $\hat{w}_1$, $\hat{v}_0$) and the particle velocity (Λ) have been obtained. Now all that remains is to determine the remainder term for the fracture aperture δ_w. This will be determined using the elasticity equation (4.102), however small modifications are made to increase the algorithms accuracy and stability. First, the pressure derivative must be calculated, which follows directly from the Poiseuille equation (4.104):

$$\tilde{r}^n \frac{d\hat{p}}{d\tilde{r}} = -\frac{\Lambda^n}{\hat{w}^{n+1}}, \tag{F.21}$$

where the additional $\tilde{r}$ term is included to avoid introducing unnecessary singularities. The modified pressure derivative then follows directly from the definitions $(4.95)_2$, (4.97):

$$\hat{\Omega}(\tilde{r}) = \frac{1}{\tilde{r}^n}\left[\tilde{r}^n \frac{d\hat{p}}{d\tilde{r}} + \left(\frac{\hat{Q}_0}{2\pi}\right)^n \frac{1}{\hat{w}^{2n+1}(0)}\right], \tag{F.22}$$

which will take a constant value at the fracture well ($\tilde{r} = 0$), but still be singular at the crack tip (see (4.74), (4.79)).

The elasticity equation in this case (4.102) takes the form:

$$\hat{w}(\tilde{r}) = \frac{8}{\pi}\int_0^1 \hat{\Omega}(y)\mathcal{K}(y,\tilde{r})\,dy + \frac{4}{\sqrt{\pi}}\hat{K}_I\sqrt{1-\tilde{r}^2} + \frac{8}{\pi}\hat{\Omega}_0\mathcal{X}_n(\tilde{r}). \tag{F.23}$$

In order to calculate this accurately and efficiently, the approach taken is to remove the singular terms of the modified pressure derivative analytically. This is possible because the asymptotic representation at the crack tip is known (see (4.74), (4.79)), allowing us to describe $\hat{\Omega}$ in the form:

$$\hat{\Omega}(\tilde{r}) = \hat{\Omega}_1\left(1-\tilde{r}^2\right)^{\alpha_j - 2} + \hat{\Omega}_2\left(1-\tilde{r}^2\right)^{\alpha_{j+1}-2} + \delta_\Omega(\tilde{r}), \tag{F.24}$$

where $j = 0$ in the viscosity dominated case, while $j = 1$ for the toughness dominated regime. Now, using the Poiseuille equation (4.104), it can easily be shown that:

$$\hat{\Omega}_1 = -\frac{\hat{v}_0^{n+1}}{\hat{w}_0^{n+1}}. \tag{F.25}$$

Given this, removing the $\hat{\Omega}_{\{1,2\}}$ terms simply requires that we find known function pairs $\{h_j, \Pi_j\}$ which satisfy the condition:

$$h_j(\tilde{r}) = \frac{8}{\pi}\int_0^1 \frac{d\Pi_j}{dy}\mathcal{K}(y,\tilde{r})\,dy, \quad \frac{d\Pi_j}{d\tilde{r}} \sim c_1\left(1-\tilde{r}^2\right)^{\alpha_j-2}, \quad c_1 \in \mathbb{R}, \tag{F.26}$$

Fortunately, such pairs have already been obtained when constructing the analytical benchmarks (see Appendix. D), and are given in Table. D.1.

As a result, from the properties of $\hat{\Omega}$ and $\{h_j, \Pi_j\}$ (F.24), (F.26), it immediately follows that the integral in (F.23) can be represented as:

$$\frac{8}{\pi}\int_0^1 \hat{\Omega}(y)\mathcal{K}(y,\tilde{r})\,dy = \frac{\hat{\Omega}_1}{c_1}h_j(\tilde{r}) + \frac{8}{\pi}\int_0^1 \left[\hat{\Omega}(y) - \frac{\hat{\Omega}_1}{c_1}\frac{d\Pi_j}{d\tilde{r}}\right]\mathcal{K}(y,\tilde{r})\,dy, \tag{F.27}$$

with the leading singularity of the integrand now being eliminated and evaluated analytically. This process can be repeated as necessary, although calculating the multiplier needed to cancel out the leading term will clearly become more complicated as more are added.

The technique presented above to remove subsequent asymptotic terms and evaluate them analytically, preferably until the integrand is bounded over the whole domain, is the basis of ensuring rapid and highly accurate evaluation of the elasticity equation. However, given that the asymptotic expansion of the modified pressure derivative is regime dependent (i.e. viscosity or toughness dominated), the final scheme will need to be tailored to each specific case.

F.2.3.2 Viscosity dominated regime ($\hat{K}_{Ic} = 0$)

In the viscosity dominated regime with a shear-thinning fluid, the first combination used to remove terms analytically are $h_A(\tilde{r}, \alpha_0)$ defined in (D.5), alongside associated pairing $\Pi_A(\tilde{r}, \alpha_0)$ given by (D.7). These have the property that:

$$h_A(\tilde{r}, \alpha_0) = \frac{8}{\pi}\int_0^1 \frac{d\Pi_A(y,\alpha_0)}{dy}\mathcal{K}(y,\tilde{r})\,dy, \tag{F.28}$$

while, at the fracture front:

$$h_A(\tilde{r}, \alpha_0) \sim \frac{2\sqrt{\pi}\Gamma\left(\alpha_0+\frac{1}{2}\right)}{\Gamma\left(\alpha_0+1\right)}\left(1-\tilde{r}^2\right)^{\alpha_0}, \quad \tilde{r}\to 1, \tag{F.29}$$

$$\frac{d\Pi_A(\tilde{r},\alpha_0)}{d\tilde{r}} \sim \frac{\sqrt{\pi}(1-2\alpha_0)\Gamma\left(2-\alpha_0\right)}{\Gamma\left(\frac{3}{2}-\alpha_0\right)}\left(1-\tilde{r}^2\right)^{\alpha_0-2}, \quad \tilde{r}\to 1. \tag{F.30}$$

As a result, we immediately have that:

$$\frac{8}{\pi}\int_0^1 \hat{\Omega}(y)\mathcal{K}(y,\tilde{r})\,dy = \frac{\hat{w}_0\Gamma\left(\alpha_0+1\right)}{2\sqrt{\pi}\Gamma\left(\alpha_0+\frac{1}{2}\right)}h_A(\tilde{r},\alpha_0)+\frac{8}{\pi}\int_0^1\left[\hat{\Omega}(y)+m_1\frac{d\Pi_A(y,\alpha_0)}{dy}\right]\mathcal{K}(y,\tilde{r})\,dy, \tag{F.31}$$

where:

$$m_1 = \frac{\hat{v}_0^{n+1}\Gamma\left(\frac{3}{2}-\alpha_0\right)}{\hat{w}_0^{n+1}\sqrt{\pi}\left(1-2\alpha_0\right)\Gamma\left(2-\alpha_0\right)}, \tag{F.32}$$

eliminates the leading singularity in the integrand at the crack tip (associated with the $\hat{\Omega}_1$ multiplier in (F.24)).

The same trick can easily be used again to eliminate the remaining singular term, this time by utilizing the pair $h_A(\tilde{r},\alpha_1)$, $\Pi_A(\tilde{r},\alpha_1)$, to give:

$$\begin{aligned}&\frac{8}{\pi}\int_0^1\left[\hat{\Omega}(y)+m_1\frac{d\Pi_A(y,\alpha_0)}{dy}\right]\mathcal{K}(y,\tilde{r})\,dy = \\ &\quad m_2 h_A(\tilde{r},\alpha_1)+\frac{8}{\pi}\int_0^1\left[\hat{\Omega}(y)+m_1\frac{d\Pi_A(y,\alpha_0)}{dy}-m_2\frac{d\Pi_A(y,\alpha_1)}{dy}\right]\mathcal{K}(y,\tilde{r})\,dy,\end{aligned} \tag{F.33}$$

where the constant m_2 can be calculated analytically, accounting for both the singularities associated with $\hat{\Omega}_2$ and the derivative of $\Pi_A(\tilde{r},\alpha_0)$, however in practice calculating it numerically often produces a more stable algorithm.

Combining the above, and noting that $\hat{K}_{Ic}=0$, the elasticity equation to be computed (4.102) now takes the form:

$$\begin{aligned}\hat{w}(\tilde{r}) = &\frac{\hat{w}_0\Gamma\left(\alpha_0+1\right)}{2\sqrt{\pi}\Gamma\left(\alpha_0+\frac{1}{2}\right)}h_A(\tilde{r},\alpha_0)+m_2h_A(\tilde{r},\alpha_1)+\frac{8}{\pi}\hat{\Omega}_0\mathcal{X}_n(\tilde{r}) \\ &+\frac{8}{\pi}\int_0^1\left[\hat{\Omega}(y)+m_1\frac{d\Pi_A(y,\alpha_0)}{dy}-m_2\frac{d\Pi_A(y,\alpha_1)}{dy}\right]\mathcal{K}(y,\tilde{r})\,dy,\end{aligned} \tag{F.34}$$

where the integrand on the right side of this equation no longer has any singularities, greatly increasing the accuracy and efficiency of computations.

It should be noted that this combination of base functions is only valid in the shear-thinning case, with different function pairs $\{h_i,\Pi_i\}$ being required when modeling Newtonian or perfectly plastic fluids. The methodology however remains the same, and all relevant pairs are provided in Appendix. D.

F.2.3.3 Toughness dominated regime ($\hat{K}_{Ic}>0$)

Here, the first asymptotic term of the aperture $\hat{w}_0$ is already outside of the integral, as such only the first term for the modified pressure derivative $\hat{\Omega}_1$ needs to be extracted. This is achieved using the same approach as in the viscosity dominated case, with the

same function pair $\{h_A(\tilde{r},\alpha_1),\Pi_A(\tilde{r},\alpha_1)\}$, having the following properties:

$$h_A(\tilde{r},\alpha_1) \sim \frac{2\sqrt{\pi}\Gamma\left(\alpha_1+\frac{1}{2}\right)}{\Gamma\left(\alpha_1+1\right)}\left(1-\tilde{r}^2\right)^{\alpha_1}, \quad \tilde{r}\to 1, \tag{F.35}$$

$$\frac{d\Pi_A(\tilde{r},\alpha_1)}{d\tilde{r}} \sim \frac{\sqrt{\pi}(1-2\alpha_1)\Gamma\left(2-\alpha_1\right)}{\Gamma\left(\frac{3}{2}-\alpha_1\right)}\left(1-\tilde{r}^2\right)^{\alpha_1-2}, \quad \tilde{r}\to 1. \tag{F.36}$$

As a result, using the same method of removing asymptotic terms demonstrated in (F.27), the elasticity equation in this case takes the form:

$$\begin{aligned}\hat{w}(\tilde{r}) = \hat{w}_0\sqrt{1-\tilde{r}^2} + \frac{\hat{w}_1\Gamma\left(\alpha_1+1\right)}{2\sqrt{\pi}\Gamma\left(\alpha_1+\frac{1}{2}\right)}h_A(\tilde{r},\alpha_1) + \frac{8}{\pi}\hat{\Omega}_0\mathcal{X}_n(\tilde{r}) \\ + \frac{8}{\pi}\int_0^1\left[\hat{\Omega}(y) + \frac{\hat{v}_0^{n+1}\Gamma\left(\frac{3}{2}-\alpha_1\right)}{\hat{w}_0^{n+1}\sqrt{\pi}\left(1-2\alpha_1\right)\Gamma\left(2-\alpha_1\right)}\frac{d\Pi_A(y,\alpha_1)}{dy}\right]\mathcal{K}(y,\tilde{r})\,dy.\end{aligned} \tag{F.37}$$

While only the leading singularity at the crack tip has been eliminated, the integrand itself will now be bounded over the whole fracture domain. In practice, the efficiency of the algorithm can still be improved through the removal of the second term, however this will not be demonstrated here.

F.2.4 The completed universal algorithm

With the main blocks now in place, it is a simple matter to combine them and construct the final numerical code. A specific overview of the algorithms steps is now given below:

1. **Initial conditions**: The fluid leak-off, material toughness and fluid index are specified. The mesh defining the fracture, consisting of N nodal points, is specified over the range $[0, 1-\epsilon]$ for some small $\epsilon > 0$ (for results presented in this work, $\epsilon = 10^{-7}$ was used). The mesh is non-uniform, with the distribution of nodal points being chosen to best minimize error over the whole domain (i.e. more points are needed at the fracture front and opening).

   Appropriate initial estimates of the parameters $\hat{w}_0$, $\hat{w}_1$, $\hat{v}_0$, $\delta_w(\tilde{r})$, $\delta_\Lambda(\tilde{r})$ are chosen, ensuring that all interrelations and boundary conditions are satisfied.

2. **Block 1**: An improved estimate for the asymptotic coefficients $\hat{w}_0$, $\hat{w}_1$ and $\hat{v}_0$ is obtained. This is achieved using (F.4)-(F.5) in the viscosity dominated regime, or (4.103), (F.6)-(F.7) when $\hat{K}_{Ic} > 0$, as outlined in Sect. F.2.1.

3. **Block 2**: The particle velocity is reconstructed using Tikhonov type regularization, described in detail in Sect. F.2.2, yielding an improved estimate of $\delta_\Lambda(\tilde{r})$.

4. **Block 3**: The elasticity equation is used to determine an improved estimate of $\delta_w(\tilde{r})$, with unbounded terms within the integral being evaluated analytically to improve computational efficiency and accuracy, as explained in Sect. F.2.3. The integral is typically evaluated using spline-based techniques, as the fact that the integrand is both smooth and bounded facilitate this approach, however alternative methods (e.g. trapezoidal rule) would also suffice. The boundary condition on the fracture opening $(4.108)_1$ is enforced at this point.

5. **Picard iteration**: In order to ensure the maximum possible stability of the algorithm, the initial conditions for the next iteration are created using both the original and improved estimates, using the formulae:

$$\hat{w}_{0,i+1} = a\hat{w}_{0,i} + (1-a)\hat{w}_{0,i-1}, \quad \delta_{w,i+1}(\tilde{r}) = a\delta_{w,i}(\tilde{r}) + (1-a)\delta_{w,i-1}(\tilde{r}), \tag{F.38}$$

$$\delta_{\Lambda,i+1}(\tilde{r}) = b\delta_{\Lambda,i}(\tilde{r}) + (1-b)\delta_{\Lambda,i-1}(\tilde{r}), \tag{F.39}$$

where the subscript i denotes the iteration, and $0 < a, b < 1$. Note that we may take $a(N)$, $b(N)$, and that values are chosen optimize the codes stability whilst preserving the maximum level of efficiency. Once this is completed, the new initial conditions are ready for the next iteration.

6. **Convergence to a solution**: Steps 2-5 are repeated until a predetermined level of convergence is reached. This will typically be achieved by taking measures in the form:

$$\mathcal{M}_1 = \frac{\int_0^1 \tilde{r}|\hat{w}_{i+1}(\tilde{r}) - \hat{w}_i(\tilde{r})|\, d\tilde{r}}{\int_0^1 \tilde{r}\hat{w}_{i+1}(\tilde{r})\, d\tilde{r}}, \quad \mathcal{M}_2 = \frac{\int_0^1 |\Lambda_{i+1}(\tilde{r}) - \Lambda_i(\tilde{r})|\, d\tilde{r}}{\int_0^1 \Lambda_{i+1}(\tilde{r})\, d\tilde{r}}, \tag{F.40}$$

with the condition for ceasing further iterations being: $\max(\mathcal{M}_1, \mathcal{M}_2) < \epsilon$, for some small $\epsilon > 0$.

7. **Post-processing**: The final outputs of the algorithm are the variables $\hat{w}_0$, $\hat{w}_1$, δ_w, $\hat{v}_0$, δ_Λ. Further steps are needed to obtain the full form of the pressure function. First, the modified pressure derivative $\hat{\Omega}$ is derived using (F.22). With this, the final function can be obtained using equations (4.96)-(4.98), however, in order to reduce any computational errors the same techniques are applied to the integral as were used previously for the elasticity equation (see Sect. F.2.3). We have:

$$\hat{p}(\tilde{r}) = \frac{\hat{\Omega}_0}{1-n}\tilde{r}^{1-n} + \hat{C}_p + \int_0^{\tilde{r}} \hat{\Omega}(\xi)\, d\xi, \tag{F.41}$$

where:

$$\hat{C}_p = \frac{\sqrt{\pi}}{2}\hat{K}_I - \frac{\sqrt{\pi}\Gamma\left(\frac{3-n}{2}\right)}{2(1-n)\Gamma\left(2-\frac{n}{2}\right)}\hat{\Omega}_0 - \int_0^1 \hat{\Omega}(y)\sqrt{1-y^2}\,dy, \tag{F.42}$$

and all terms except $\hat{p}$, $\hat{C}_p$ are already explicitly known. Inserting the representation of $\hat{\Omega}$ defined in (F.24), these become:

$$\begin{aligned}\hat{p}(\tilde{r}) = \frac{\hat{\Omega}_0}{1-n}\tilde{r}^{1-n} + \hat{C}_p + \hat{\Omega}_1\tilde{r}_2F_1\left(\frac{1}{2}, 2-\alpha_j; \frac{3}{2}; \tilde{r}^2\right) \\ + \hat{\Omega}_2\tilde{r}_2F_1\left(\frac{1}{2}, 2-\alpha_{j+1}; \frac{3}{2}; \tilde{r}^2\right) + \int_0^{\tilde{r}} \delta_\Omega(\xi)\,d\xi,\end{aligned} \tag{F.43}$$

with:

$$\begin{aligned}\hat{C}_p = \frac{\sqrt{\pi}}{2}\hat{K}_I - \frac{\sqrt{\pi}\Gamma\left(\frac{3-n}{2}\right)}{2(1-n)\Gamma\left(2-\frac{n}{2}\right)}\hat{\Omega}_0 + \frac{\sqrt{\pi}\Gamma\left(\alpha_j-\frac{1}{2}\right)}{2\Gamma\left(\alpha_j\right)}\hat{\Omega}_1 \\ + \frac{\sqrt{\pi}\Gamma\left(\alpha_{j+1}-\frac{1}{2}\right)}{2\Gamma\left(\alpha_{j+1}\right)}\hat{\Omega}_2 + \int_0^1 \delta_\Omega(y)\sqrt{1-y^2}\,dy,\end{aligned} \tag{F.44}$$

where $\hat{\Omega}_0$ is given in (4.97) and $\hat{\Omega}_1$ is provided by (F.25), while $\hat{\Omega}_2$ can be obtained numerically. With this complete, we now have a high accuracy approximation of the pressure function, and the complete numerical solution.

The above represents a full description of the workings of the universal algorithm for a shear-thinning fluid. Unfortunately, modifications do have to be made in the case when the fracture is driven by either a Newtonian or perfectly plastic fluid.

In the former case (Newtonian), these changes are only slight, namely: i) in the toughness dominated regime, equation (F.7) is simply a polynomial function and does not require iterative methods to solve, ii) the function pair used to remove asymptotic terms of the elasticity equation are no longer valid (see Sect. F.2.3), and must be replaced with another $\{h_j, \Pi_j\}$ from Table. D.1. iii) the pressure function will now be obtained from $\hat{\Omega}$ using equations (C.7)-(C.8), however, the same method of removing asymptotic terms will still yield a high accuracy result.

The perfectly plastic case however requires far further modification, due to the degeneration of the Poiseuille equation. Because of this, the elasticity equation now takes the form (C.19):

$$\hat{w}(\tilde{r}) = -\frac{8}{\pi}\int_0^1 \frac{1}{\hat{w}(y)}\mathcal{K}(y,\tilde{r}),dy + \frac{4}{\sqrt{\pi}}\hat{K}_I\sqrt{1-\tilde{r}^2}, \tag{F.45}$$

where $\hat{w}$ is the only unknown parameter. As such, this step is carried out first, independently of other aspects of the algorithm, and is the only stage requiring any iterative process. Once this is completed, the final solution for the aperture is known, and the particle velocity immediately follows from (C.20)-(C.21), while the pressure is determined

using (4.97), $(4.95)_2$, (4.104) and (C.16)-(C.17), which yield:

$$\hat{p}(\tilde{r}) = -\frac{\tilde{r}}{\hat{w}(0)} + \hat{C}_p + \int_0^{\tilde{r}} \left(\frac{1}{\hat{w}(0)} - \frac{1}{\hat{w}(\xi)} \right) d\xi, \tag{F.46}$$

where:

$$\hat{C}_p = \frac{\sqrt{\pi}}{2} \hat{K}_I + \frac{\pi}{4\hat{w}(0)} - \int_0^1 \left(\frac{1}{\hat{w}(0)} - \frac{1}{\hat{w}(y)} \right) \sqrt{1-y^2}\, dy. \tag{F.47}$$

The same method of removing asymptotic terms can be applied to reduce the level of computational error, however it will not be outlined here.

F.3 Concluding remarks

In the above, the scheme used to obtain high accuracy numerical solutions for a penny-shaped fracture in the self-similar case was given. It should be noted that, while each regime and case (i.e. viscosity or toughness dominated, plastic, shear thinning or Newtonian fluid) may require different versions of each block to be used, the final code is designed to determine the applicable combination and solve it automatically, meaning that it is truly a 'universal' algorithm.

This approach can also be extended to incorporate the transient (time-dependent) case, with the necessary modifications and additions being explained in detail in [164]. This however is not performed here.

Finally, the algorithm developed for the case of a radial fracture incorporating shear stress induced by the fluid is based on the same philosophy and scheme. The key difference is that the asymptotic representation of the pressure function at the crack tip is also used extensively within the main algorithm. This means that additional work must be done to approximate a larger number of parameters (i.e. $\hat{w}_0$, $\hat{w}_1$, $\hat{v}_0$, $\hat{p}_0$, $\hat{p}_2$), however this also means that further interrelations between these asymptotic multipliers can be utilized, and the removal of additional terms from the elasticity equation becomes simpler to perform.

Appendix G

Apparent Viscosity in the Hele-Shaw Cell

G.1 An introduction to apparent viscosity

G.1.1 The concept of apparent viscosity

The concept of apparent viscosity, sometimes referred to as effective viscosity, is one of the fundamental simplifying assumptions made when modeling hydraulic fracturing (HF). Originally proposed by *Einstein* [56], it states that the presence of a large number of small particles within a fluid (the proppant) can be approximated through an increase in the viscosity. This simplifying assumption is absolutely necessary when modeling HF, as no analytical or numerical method could possibly hope to incorporate the complexity of each individual particle within the fluid. Unfortunately however, despite its integral role, there remains numerous formulations to describe the phenomena, and no clear consensus as to which provides the most accurate approximation within a hydraulic fracture.

G.1.2 Formulations for the apparent viscosity

A review of several of the most widely utilized formulations for the apparent viscosity is provided in [22], while a general outline is included below:

- *Einstein*:
  In his original paper introducing the concept of apparent viscosity, *Einstein* derived

the following relation between the volume fraction of the fluid,

$$\Phi = \frac{\text{volume of particles in the fluid}}{\text{total volume of the fluid and particles}},$$

and the apparent viscosity:

$$\frac{\mu}{\mu_0} = 1 + A\Phi. \tag{G.1}$$

Here μ is the apparent viscosity, μ_0 is the actual viscosity of the fluid, while the constant $A = 5/2$ for 3D problems, and $A = 2$ for 2D systems [32]. It should be noted however that this formulation does not take account of the interaction between individual proppant particles, in particular the effect of Brownian motion, and as such is only valid for low values of the volume fraction (typically $\Phi < 0.01$) [22, 119].

This form of the apparent viscosity, for a fluid modeled in 3D, was later expanded by *Batchelor & Green* [18] to:

$$\frac{\mu}{\mu_0} = 1 + \frac{5}{2}\Phi + \beta\Phi^2, \tag{G.2}$$

where $5.2 < \beta < 7.6$ is a constant depending on the way that the particles behave within the fluid (e.g. if they have a uniform distribution).

- *Vand*:
  An alternative model of apparent viscosity, designed to work when the volume fraction of the fluid was relatively high (typically $\Phi > 0.1$), was proposed by *Vand* [220]. He assumed the relationship to take the form:

$$\frac{\mu}{\mu_0} = \exp\left(\frac{k_1\Phi + k_2\Phi^2}{1 - k_3\Phi}\right), \tag{G.3}$$

  where $k_1 = 2.5$, $k_2 = 2.7$ and $k_3 = 0.609$. These coeffecients were derived based on a theoretical approach. It should be noted that, if this formulation is expressed in terms of a power series, then (G.2) is recovered with $\beta = 7.349$.

- *Thomas*:
  A formulation which attempted to combine the effects of those above was presented by *Thomas* [213] in the form:

$$\frac{\mu}{\mu_0} = 1 + 2.5\Phi + 10.05\Phi^2 + 0.0027\exp(16.6\Phi), \tag{G.4}$$

  where the coeffecients were extrapolated from empirical data, taken from six sources with $0.02 < \Phi < 0.6$. The primary aim of the above formulation was to

minimize the contributions from a wide range of secondary effects in the system. Unfortunately, this formulation has not been widely adopted within the literature.

- *Mooney*:
  The final relationship which we will examine here was provided by *Mooney* [148], and takes the form:
  $$\frac{\mu}{\mu_0} = \exp\left(\frac{A\Phi}{1 - k\Phi}\right), \tag{G.5}$$
  where the constant A is identical to that used in the *Einstein* formulation, while k it commonly used as a fitting parameter.

It should be noted again that the formulations provided above do not represent an exhaustive list, but merely an introduction to the most prevalent forms which these relations take. One key reason for this abundance is the significance of internal effects within the fluid, which are numerous, on the final contribution of the particles. As such, providing a general formula is beyond the reach of current methods, and so instead numerous, specialised formulations are required to provide a reasonable approximation of this important effect.

G.1.3 Apparent viscosity in the Hele-Shaw cell and hydraulic fracture

In the previous subsection, it was noted that current investigations into the apparent viscosity caused by the inclusion of particles in a fluid tend to be highly specialised, rather than taking a general form. It is therefore somewhat strange to note that, despite the significance of this assumption to all models of hydraulic fracturing, there has been a significant lack of investigations into the formulation of apparent viscosity which is best suited to this case. Other than the notable investigation by *Kuzkin et al* [119], where a computer simulation of a fluid-proppant mixture was used to etrapolate the relationship between the volume fraction and effective viscosity, the author can find no other works investigating this relationship in the case of HF.

Given the numerous links between the formulation of the Hele-Shaw cell and that used in models of hydraulic fractuing, outlined in detail in Sect. 5.1.4.1, conducting an initial investigation into the apparent viscosity in the Hele-Shaw cell seems a sensible first step towards a study of this phenomena. The simpler nature of the Hele-Shaw cell would allow such an investigation to be completed far more easily, and the use of such an approximation to study proppant in HF has already been well established in the literature [42, 55, 135].

There is, however, little analysis of apparent viscosity in the Hele-Shaw cell available in the literature. The only notable example which the author could locate was the paper

by *Luo & Pozrikidis* [133], where they examined the effect of a single large particle, inside an infinite Hele-Shaw flow, as it travelled close to one of the plane walls. The primary aim of their investigation was to examine the effect of surface slip on the system behaviour. Under these conditions, they provided the expression:

$$\frac{\mu}{\mu_0} = 1 + \frac{5\,(\beta_p + 2)}{2\,(\beta_p + 5)}\Phi, \tag{G.6}$$

where β_p is the dimensionless Basset particle-slip coefficient, with $\beta_p \to 0$ in the case of vanishing shear stresses and perfect slip (which recovers the *Einstein* formulation), while $\beta_p \to \infty$ for finite shear stresses and no-slip. The fact that this solution only models a single particle, and does not incorporate a moving fluid boundary, unfortunately mitigates the value of the solution in the study of HF. It does however offer a useful benchmark against which to test any numerical simulations into the apparent viscosity in the Hele-Shaw cell.

As such, if investigations into the apparent viscosity in the Hele-Shaw cell are to be conducted, a new approach will need to be created. The remainder of this appendix will be dedicated to outline one possible method of approach, as well as the difficulties which will be faced when ensuring that the study is rigorous, and the results reliable.

G.2 Obtaining the apparent viscosity from radial boundary growth

As the intention of this study is to use simulations of free moving particles in the Hele-Shaw cell to estimate the effect of volume fraction on apparent viscosity, it is imperative that a method is derived by which to obtain the apparent viscosity directly from the final radius of the free flowing boundary. In order to simplify the final relationship between viscosity and movement of the free flowing boundary we consider the case of a Hele-Shaw cell whose fluid is initially a unit circle.

We begin with a fluid defined by the domain $\Omega(t)$, which contains a source/sink located at point $\mathbf{y} \in \Omega(t)$, $t \geq 0$. The standard equation, in terms of a Green's function, for the growth of the boundary, $\partial\Omega(t)$, in the Hele-Shaw cell is given by (5.12):

$$\partial_t \mathbf{w}(s,t) = -\frac{Q_0 h^2}{12\mu} \cdot \nabla \mathcal{G}(\mathbf{w}(s,t),t) \tag{G.7}$$

Here $\mathbf{w}(s,t)$ is the 2D representation of the fluid boundary, which has Green's function $\mathcal{G}$, Q_0 is the strength of the source/sink, h is the height of the cell and μ is the (apparent)

fluid viscosity.

In the case without particle inclusions, the Green's function can be approximated with the following asymptotic expansion:

$$\mathcal{G}(\mathbf{x},\mathbf{y};t)=\frac{1}{2\pi}\log\left|\frac{1}{\mathbf{x}-\mathbf{y}}\right| \tag{G.8}$$

Noting that this approximation will not be valid on the boundary, i.e. for $\mathbf{x}\in\partial\Omega(t)$, $\mathbf{y}\in\Omega(t)$.

It is possible to take $\mathbf{y}=0$ without a loss of generality, and transform the system into radial coordinates. In this case if follows from (G.8) that:

$$\mathcal{G}(R,\theta;t)=\frac{1}{2\pi}\log\left|\frac{1}{R\left(\cos(\theta)+i\sin(\theta)\right)}\right|,\quad R\geq 0,\ \theta\in[0,2\pi) \tag{G.9}$$

$$\partial_R\mathcal{G}(R,\theta;t)=-\frac{1}{2\pi R} \tag{G.10}$$

As only the case of a unit circle is considered, the radius will be independent of θ. Combining this with (G.7), (G.10) yields:

$$\frac{\partial R}{\partial t}=\frac{Q_0h^2}{24\pi\mu R} \tag{G.11}$$

Solving the above, noting that $t_0=0$, and rearranging shows:

$$R(t)=\sqrt{R_0^2+\frac{Q_0h^2}{12\pi\mu}t} \tag{G.12}$$

As $R_0=1$, we have that the apparent viscosity is given by:

$$\mu\left(R,t\right)=\frac{Q_0h^2t}{12\pi\left(R(t)^2-1\right)} \tag{G.13}$$

Therefore, one possible method of determining the effect of particle inclusion on the effective viscosity in the Hele-Shaw cell is immediately apparent. Namely, we simulate the boundary growth for a domain containing a large number of particles, and use the radius of the final boundary position to determine the apparent viscosity from (G.13).

G.3 Notable complications and effects

While the method of determining the apparent viscosity outlined in the previous section works in principle, there are numerous complications which need to be taken into

account. A detailed discription of some of these difficulties, alongside potential modifications to the method to ensure it is sufficiently rigorous, and the results reliable, are given below.

G.3.1 Determining the radius of the fluid boundary

It is clear that in the limiting case, when there is an infinite number of particles evenly distributed throughout the fluid, the final radius of the fluid boundary, $R(t)$, will be independent of the angle θ. However, any simulations conducted using the algorithm developed in Sect. 5 will instead be approximating this using a finite number of particles, and as such some dependence on the angle will be present in the final result (see e.g. Figs. 5.15, 5.16). As such, an effective radius, R^*, which is independent of θ, will have to be obtained from the final boundary deformation.

One clear, physically representative, approach is to obtain the effective radius from the area of the fluid. This can be formulated as follows:

$$R^*(t) = \sqrt{\frac{1}{2\pi}\int_0^{2\pi} R^2(\theta, t)\, d\theta}, \tag{G.14}$$

where the integral can be approximated either using the trapezium rule, or through spline-based integration techniques. This effective radius can then be inserted into (G.13) to provide the approximated apparent viscosity, while the maximum and minimum of $R(\theta, t)$ can be used to provide error estimates for the final solution.

G.3.2 Maintaining a constant volume fraction

In the case of proppant particles within HF fluids, the volume fraction will remain essentially constant over time, and the particles will be evenly distributed throughout the fluid. However, in numerical simulations of the Hele-Shaw cell, the particles may be unevenly distributed, causing the volume fraction to vary throughout the domain. Similarly, as only the base liquid is being injected from the fluid source, the volume fraction of the fluid will naturally decrease over time. Depending on the movement of the particles, the regions near the fluid source or boundary may also become void of particles entirely. It is therefore imperative, that any examination into the relationship between the volume fraction and the radial boundary growth develops strategies to minimise these potentially error inducing effects.

G.3.2.1 Initial particle distribution

When attempting to model a substance uniformly distributed in a fluid using a large number of particles, their initial position will clearly play an important role in determining the accuracy of the approximation. For example, placing all of the inclusions in only one side of the cell would lead to a variation of the volume fraction throughout the fluid domain, and therefore the results may be unrepresentative. To take ordered distributions however may incur a similar effect. Additionally, in order to maintain the constraints imposed on the original system of equations (see Sect. 5.2.2), the particles must not overlap. For this reason the methodology by which initial particle distributions are chosen must be carefully considered.

While there may be numerous ways to achieve a representative distribution, the method which the author has found most effective at eliminating variations in the volume fraction throughout the fluid is to split the domain into 'rings'. Each ring is defined by its radial distance from the fluid source, with the number of rings and their width being determined based on the radius of the inclusions. The number of particles within each ring can then be selected to ensure that any variation in volume fraction between them is minimized (or ideally eliminated). Particle positions within the ring are randomly generated[1], with particle overlap prevented through the use of an additional algorithm. Examples of distributions generated by this approach are shown in Fig. G.1.

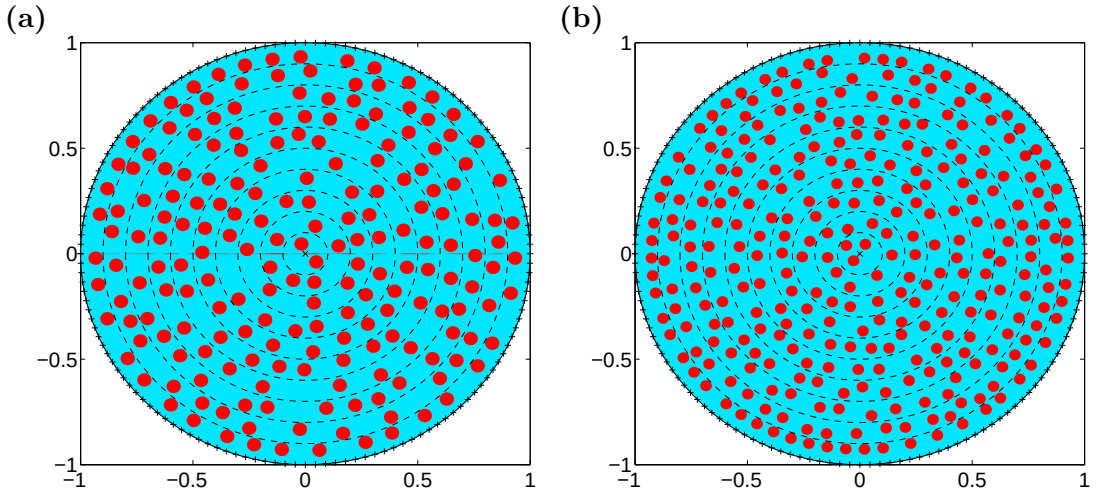

FIGURE G.1: Quasi-random distributions for (a) 200 (b) 300 particles in a circular domain defined by 140 boundary nodes. The 'rings' splitting the domain are marked by dashed lines.

[1]In the authors case; using the MatLab 'rand' function, which generates a random number in the interval (0,1) based on the uniform distribution.

One additional advantage of this ring based approach, is that the intial velocity of each particle can be defined by the ring that it is in. In this way, taking the initial velocity normal to the particle source, it is possible to ensure that, to a certain degree, the particles remain representatively distributed throughout the fluid over short time periods. As such, the volume fraction during the early stages will remain relatively constant throughout the domain.

While this method of defining the initial particle distribution accurately balances the immediate concerns, it will clearly not be entirely representative of a system with hundreds of thousands of particles. In order to counter this, multiple simulations must be undertaken for each value of the volume fraction, with each using a different, independently generated, distribution. By comparing the results of each simulation, an estimate of the apparent viscosity, alongside its associated error, may be obtained.

G.3.2.2 The volume fraction over time

As the fluid domain expands, if the number and size of the inclusions is kept constant, the volume fraction will clearly vary over the course of the simulation. Meanwhile, in hydraulic fracturing the volume fraction is maintained through the continued addition of particles as the fluid domain expands. While this effect can be partially replicated through the use of additional algorithms, it would still lead to a variation in the volume fraction, as particles could only be added in discrete steps rather than as a continuous process. An alternate method of maintaining the volume fraction involves increasing the radius of the existing particles throughout the simulation, in such a way as to ensure a constant volume fraction. This approach would be less representative of the physical process we are attempting to represent, but would reduce the level of variation over time.

Unfortunately, in practice both methods only lead to convergent results over short time periods ($t < 0.15$ seconds), after which the level of boundary deformation they predict begins to diverge significantly. Further, for such short durations, there is only a minimal difference between the results of these methods and the case when no additional action is taken[2]. As such, it seems sensible to instead avoid both methods and only simulate time periods below this threshold (without any particle addition or expansion), in order to reduce rather than eliminate this potential problem.

[2]Other than linking the inital particle velocity to that of the boundary. See previous subsection.

G.3.3 Maintaining asymptotic validity

In hydraulic fracturing, understanding the behaviour at the fracture tip is crucial when attempting to create a suitable model. Similarly, any attempt to investigate the apparent viscosity must be able to incorporate the contribution of particles near the fluid boundary. This presents by far the largest difficulty in attempting to construct a suitable method for examining this effect through the use of numerical simulations, as the initial assumptions used when creating the model require that the particles do not get too close to the boundary or the point of fluid injection (see Sect. 5.2.2). As such, there is an awkward conundrum when it comes to deciding the position of particles near to either the boundary or the source; placing them too far away will cause the simulations to miss crucial effects, while placing them too close could potentially mean simulating systems for which the asymptotic approximation is not valid. Either of these situations would severly damage the credibility of the final result. Unfortunately, there is no quick fix for this dilemma.

One possible method of avoiding the loss of asymptotic validity is to instead approximate a multi-layer radial medium, as described in [74]. In this case, the inner and outer layers would simply contain fluid with a prescribed viscosity, essentially providing a buffer between the particles and the source/boundary. The particles would then be confined to a central layer, in between the other two. This approach is not without difficulties however, most notably in providing a rigid definition of the boundary between the seperate layers. Obtaining the value for the apparent viscosity from the final radial boundary growth would also be far more complicated than in the previous example, as the interface between the layers is an ill-posed problem, leading to *Saffman-Taylor* instability (described in Sect. 5.1.3). As this instability would not be mimicked by the model outlined in Sect. 5, it would be difficult to obtain results that were comparable. In any case, this is one possible avenue for future research.

G.4 Summary

It is clear that further research into the apparent viscosity of fluids used in hydraulic fracturing is necessary. Here, the basic outline of an investigative approach, using the Hele-Shaw cell, has been given. However there are still numerous difficulties to overcome before such an examination can be conducted.

While potential solutions have been given to the problem of maintaining a constant volume fraction throughout the domain, they require a large number of simulations to be conducted in order to obtain a single result. Additionally, the final result they provide

will predominantly take the form of upper and lower bounds on the apparent viscosity in the fluid. This, combined with the bounds obtained when determining the effective radius, may lead to a range of possible values so large as to be meaningless. The only way to avoid this is to run each simulation with a very large number of particles and boundary nodes, which in itself may lead to an infeasible total computation time.

Noting this, alongside the fact that no concrete solution to the problem of asymptotic validity has been provided, means that the method outlined requires serious refinement before it can be utilized to obtain the apparent viscosity in the Hele-Shaw cell. It does however demonstrate the beginnings of a new approach which, if successfully realized, will yield valuable insights into one of the fundamental assumptions used in models of hydraulic fracture.

Bibliography

[1] P. Abbyad, R. Dangla, A. Alexandrou, and C.N. Baroud. Rails and anchors: guiding and trapping droplet microreactors in two dimensions. *Lab on a Chip*, 11:813, 2011.

[2] S.A. Abdel-Meguid. *The mechanics of the shot-peening process.* PhD thesis, University of Manchester, http://ethos.bl.uk, 1975.

[3] H. Abé, T. Mura, and L.M. Keer. Growth rate of a penny-shaped crack in hydraulic fracturing of rocks. *Journal of Geophysical Research*, 81(29):5335–5340, 1976.

[4] A.S. Abou-Sayed, D.E. Andrews, and I.M. Buhidma. Evaluation of oily waste injection below the permafrost in prudhoe bay field. In *Proceedings of the California Regional Meetings, Bakersfield, CA*, pages 129–142, Richardson, TX, 1989. Society of Petroleum Engineers.

[5] M. Abramowitz and I. Stegun. *Handbook of Mathematical Functions with Formulas, Graphs and Mathematical Tables.* Dover Publications Inc., New York, NY, 1972.

[6] J. Adachi, E. Siebrits, A. Peirce, and J. Desroches. Computer simulation of hydraulic fractures. *International Journal of Rock Mechanics and Mining Sciences*, 44:739–757, 2007.

[7] S.H. Advani, J.S. Torok, J.K. Lee, and S. Choudhry. Explicit time-dependent solutions and numerical evaluations for penny-shaped hydraulic fracture models. *Journal of Geophysical Research*, 92(B8):8049–8055, 1987.

[8] D. Andreucci, G. Caruso, and E. DiBenedetto. *Ill-Posed Hele-Shaw Flows*, pages 27–51. Birkhäuser Basel, Basel, 2004.

[9] S.N. Antontsev, C.R. Gonçalves, and A.M. Meirmanov. Exact estimate for the classical solutions to the free-boundary problem in the hele-shaw cell. *Advances in Difference Equations*, 8(10):1259, 2003.

[10] I. Argatov, G. Mishuris, and Yu. Petrov. Threshold fracture energy in solid particle erosion. *Philosophical Magazine*, 93:2485–2496, 2013.

[11] I.I. Argatov. Asymptotic modelling of the impact of a spherical indenter on an elastic half-space. *International Journal of Solids and Structures*, 45:5035–5048, 2008.

[12] I.I. Argatov. Frictionless and adhesive nanoindentation: Asymptotic modeling of size effects. *Mechanics of Materials*, 42:807–815, 2010.

[13] I.I. Argatov, N.N. Dmitriev, Yu.V. Petrov, and V.I. Smirnov. Threshold erosion fracture in the case of oblique incidence. *International Journal of Solids and Structures*, 30(3):176–181, 2009.

[14] K. Arin and F. Erdogan. Penny-shaped crack in an elastic layer bonded to dissimilar half spaces. *International Journal of Engineering Science*, 9:213–232, 1971.

[15] F. Auerbach. Absolute härtemessung. *Annalen der Physik*, 279(5):61–100, 1891.

[16] G.I. Barenblatt. *Flow, Deformation and Fracture: Lectures on Fluid Mechanics and the Mechanics of Deformable Solids for Mathematicians and Physicists*. Cambridge Texts in Applied Mathematics. Cambridge University Press, 2014.

[17] G.K. Batchelor. *An Introduction to Fluid Dynamics*. Cambridge Mathematical Library. Cambridge University Press, 2000.

[18] G.K. Batchelor and J.T. Green. The determination of the bulk stress in a suspension of spherical particles to order c2. *Journal of Fluid Mechanics*, 56(3):401–427, 1972.

[19] Z.P. Bažant and M.T. Kazemi. Determination of fracture energy, process zone longth and brittleness number from size effect, with application to rock and conerete. *International Journal of Fracture*, 44(2):111–131, 1990.

[20] A.N. Berezkin, S.I. Krivosheev, Y.V. Petrov, and A.A. Utkin. Effect of delayed crack nucleation under threshold pulse loading. *Doklady Physics*, 45(11):617–619, 2000.

[21] M.A. Biot, W.L. Medlin, and L. Masse. *Laboratory experiments in fracture propagation*, volume SPE 10377. Jan 1981.

[22] R. Blazejewski. Apparent viscosity and settling velocity of suspensions of rigid monosized spheres in stokes flow. *International Journal of Multiphase Flow*, 39:179–185, 2012.

[23] C. Bo, D. Yunhong, L. Yongjun, S. Hua, and Y. Zhenzhou. Field method research for leak-off coefficient analysis using instantaneous shut-in pressure. *Journal of Energy and Power Engineering*, 8:103–106, 2014.

[24] V.A. Bogoyavlenskiy and E.J. Cotts. Free surface hele-shaw flows around an obstacle: A random walk simulation. *Physical Review E*, 69:016310, 2004.

[25] V.A. Bogoyavlenskiy and E.J. Cotts. Reply to comment on free surface hele-shaw flows around an obstacle: A random walk simulation. *Physical Review E*, 76:038302, 2007.

[26] F.M. Borodich. Hertz contact problems for an anisotropic physically nonlinear elastic medium. *Strength of Materials*, 21:1668, 1989.

[27] F.M. Borodich. Some contact problems of anisotropic elastodynamics: integral characteristics and exact solution. *International Journal of Solids and Structures*, 37:3345–3373, 2000.

[28] F.M. Borodich and B.A. Galanov. Non-direct estimations of adhesive and elastic properties of materials by depth-sensing indentation. *Proceedings of the Royal Society of London A: Mathematical, Physical and Engineering Sciences*, 464(2098):2759–2776, 2008.

[29] F.M. Borodich, B.A. Galanov, Yu.I. Prostov, and M.M. Suarez-Alvarez. Influence of complete sticking on the indentation of a rigid cone into an elastic half-space in the presence of molecular adhesion. *Journal of Applied Mathematics and Mechanics*, 76(5):590–596, 2012.

[30] F.M. Borodich, B.A. Galanov, and M.M. Suarez-Alvarez. The jkr-type adhesive contact problems for power-law shaped axisymmetric punches. *Journal of the Mechanics and Physics of Solids*, 68:14–32, 2014.

[31] F.M. Borodich and L.M. Keer. Contact problems and depth-sensing nanoindentation for frictionless and frictional boundary conditions. *International Journal of Solids and Structures*, 41(9):2479–2499, 2004.

[32] J.F. Brady. The einstein viscosity correction in n dimensions. *International Journal of Multiphase Flow*, 10(1):113–114, 1983.

[33] J.R. Brockenbrough, S. Suresh, and J. Duffy. An analysis of dynamic fracture in microcracking brittle solids. *Philosophical Magazine A*, 58(4):619–634, 1988.

[34] A.P. Bunger and E. Detournay. Experimental validation of the tip asymptotics for a fluid-driven crack. *Journal of Mechanics and Physics of Solids*, 56:3101–3115, 2008.

[35] A.P. Bunger, E. Detournay, and D.I. Garagash. Toughness-dominated hydraulic fracture with leak-off. *International Journal of Fracture*, 134:175–190, 2005.

[36] J.R. Cameron and R.K. Prudhomme. Fracturing-fluid flow behavior. In J.L. Gidley, S.A. Holditch, D.E. Nierode, and R.W. Veatch, editors, *Recent Advances in Hydraulic Fracturing*, pages 177–209. Society of Petroleum Engineers, Richardson, 1989.

[37] T.D. Cao, E. Milanese, E.W. Remij, P. Rizzato, J.J.C. Remmers, L. Simoni, J.M. Huyghe, F. Hussain, and B.A. Schrefler. Interaction between crack tip advancement and fluid flow in fracturing saturated porous media. *Mechanics Research Communications*, 80:24–37, 2017.

[38] P.J. Carreau. Rheological equations from molecular network theories. *Transactions of the Society of Rheology (1957-1977)*, 16:99–127, 1972.

[39] E.D. Carter. Optimum fluid characteristics for fracture extension. In G.C. Howard and C.R. Fast, editors, *Drilling and Production Practices*, pages 261–270. American Petroleum Institute, OK, 1957.

[40] J. Casademunt and F.X. Magdaleno. Dynamics and selection of fingering patterns. recent developments in the saffman-taylor problem. *Physics Reports*, 337(1-2):1–35, 2000.

[41] C-Y. Chen, C-W. Huang, H. Gadêlha, and J.A. Miranda. Radial viscous fingering in miscible hele-shaw flows: A numerical study. *Physical Review E*, 78:016306, 2008.

[42] C. Chevalier, A. Lindner, and E. Clément. Destabilization of a saffman-taylor fingerlike pattern in a granular suspension. *Phys. Rev. Lett.*, 99:174501, Oct 2007.

[43] C. Clark, A. Burnham, C. Harto, and R. Horner. Hydraulic fracturing and shale gas production: Technology, impacts and regulations. Report www.afdc.energy.gov/uploads/publication/anl_hydraulic_fracturing.pdf, Argonne National Laboratory, 2013.

[44] J. Crepeau. Josef stefan: His life and legacy in the thermal sciences. *Experimental Thermal and Fluid Science*, 31(7):795–803, 2007.

[45] M.C. Dallaston and S.W McCue. Bubble extinction in hele-shaw flow with surface tension and kinetic undercooling regularization. *Nonlinearity*, 26(6):1639–1665, 2013.

[46] B. Damjanac, C. Detournay, P.A. Cundall, and Varun. Three-dimensional numerical model of hydraulic fracturing in fractured rock mass. In A.P. Bunger, J. McLennan, and R. Jeffrey, editors, *Effective and Sustainable Hydraulic Fracturing*, pages 819–830. InTech, Croatia, www.intechopen.com, 2013.

[47] H. Darcy. *Les fontaines publiques de la ville de Dijon. Exposition et application des principes à suivre et des formules à employer dans les questions de distribution d'eau: ouvrage terminé par un appendice relatif aux fournitures d'eau de plusieurs villes au filtrage des eaux et à la fabrication des tuyaux de fonte, de plomb, de tole et de bitume (in French).* Dalmont, 1856.

[48] P. Daripa, O. Orellana, and R. Meneses. On a three-layer hele-shaw model of enhanced oil recovery with a linear viscous profile. arXiv:1502.00380, 2015.

[49] C.J. de Pater, J. Groenenboom, D.B. van Dam, and R. Romijn. Active seismic monitoring of hydraulic fractures in laboratory experiments. *International Journal of Rock Mechanics and Mining Sciences*, 38(6):777–785, 2001. Application of Geophysics to Rock Engineering.

[50] E.V. Dontsov. An approximate solution for a penny-shaped hydraulic fracture that accounts for fracture toughness, fluid viscosity and leak-off. *Royal Society Open Science*, 3(12), 2016.

[51] E.V. Dontsov and A.P. Peirce. A multiscale implicit level set algorithm (ilsa) to model hydraulic fracture propagation incorporating combined viscous, toughness, and leak-off asymptotics. *Computer Methods in Applied Mechanics and Engineering*, 313:53–84, 2017.

[52] T.A. Driscoll. Algorithm 756: A matlab toolbox for schwarz-christoffel mapping. *ACM Trans. Math. Soft.*, 22:168, 1996.

[53] T.A. Driscoll. Algorithm 843: Improvements to the schwarz–christoffel toolbox for matlab. *ACM Trans. Math. Soft.*, 31:239, 2005.

[54] T.A. Driscoll and L.N. Trefethen. *Schwarz-Christoffel Mapping*. Cambridge Monographs on Applied and Computational Mathematics. Cambridge University Press, 2002.

[55] G. Dumazer, B. Sandnes, M. Ayaz, K.J. Måløy, and E.G. Flekkøy. Frictional fluid dynamics and plug formation in multiphase millifluidic flow. *Physical Review Letters*, 117:028002, 2016.

[56] A. Einstein. Eine neue bestimmung der molekuldimensionen. *Annalen der Physik*, 19:289–306, 1906.

[57] J. El-Ali, P.K. Sorger, and K.F. Jensen. Cells on chips. *Nature*, 442:403–411, 2006.

[58] V. Entov and P. Etingof. On the break of air bubbles in a hele-shaw cell. *European Journal of Applied Mathematics*, 22(2):125, 2011.

[59] A.G. Evans. On impact damage in the elastic response regime. *Journal of Applied Physics*, 49(6):3304–3310, 1978.

[60] I. Finnie, D. Dolev, and M. Khatibloo. On the physical basis of auerbach's law. *Journal of Engineering Materials and Technology*, 103(2):183–184, 1981.

[61] A.C. Fischer-Cripps. *Introduction to Contact Mechanics*. Springer, US, 2007.

[62] A.C. Fischer-Cripps and R.E. Collins. The probability of hertzian fracture. *Journal of Materials Science*, 29(8):2216–2230, 1994.

[63] G. Fu and A. Chandra. Normal indentation of elastic half-space with a rigid frictionless axisymmetric punch. *Journal of Applied Mechanics*, 69(2):142–147, 2001.

[64] L.A. Galin. Unsteady filtration with a free surface (in russian). *Doklady Akademii Nauk USSR*, 47:246–249, 1945.

[65] L.A. Galin. Spatial contact problems of the theory of elasticity for punches of circular shape in planar projection (in russian). *J. Appl. Math. Mech. (PMM)*, 10:425, 1946.

[66] L.A. Galin. *Contact Problems - The Legacy of L.A. Galin*. Number 155 in Solid Mechanics and its Applications. Springer, Netherlands, 2008.

[67] D. Garagash and E. Detournay. The tip region of a fluid-driven fracture in an elastic medium. *Journal of Applied Mechanics*, 67:183–192, 2000.

[68] D. Garagash, E. Detournay, and J. Adachi. Multiscale tip asymptotics in hydraulic fracture with leak-off. *Journal of Fluid Mechanics*, 669:260–297, 2011.

[69] D.I. Garagash. Propagation of a plane-strain hydraulic fracture with a fluid lag: Early-time solution. *International Journal of Solids and Structures*, 43:5811–5835, 2006.

[70] D.I. Garagash. *Scaling of Physical Processes in Fluid-Driven Fracture: Perspective from the Tip*, pages 91–100. Springer Netherlands, Dordrecht, 2009.

[71] B.P.J. Gardiner, S.W. McCue, M.C. Dallaston, and T.J. Moroney. Saffman-taylor fingers with kinetic undercooling. *Physical Review E*, 91:023016, 2015.

[72] J. Geertsma and F. de Klerk. A rapid method of predicting width and extent of hydraulically induced fractures. *Journal of Petroleum Technology*, 21(12):1571–1581, SPE–2458–PA, 1969.

[73] D. Gilbarg and N.S. Trudinger. *Partial Differential Equations of Second Order*. Springer, Berlin, 1983.

[74] C. Gin and P. Daripa. Stability results for multi-layer radial hele-shaw and porous media flows. *Physics of Fluids*, 27(1):012101, 2015.

[75] C. Gin and P. Daripa. A study of a non-standard eigenvalue problem and its application to three-layer immiscible porous media and hele-shaw flows with exponential viscous profile. *Journal of Mathematical Fluid Mechanics*, 17(1):155–181, 2015.

[76] N. Gorbushin and G. Mishuris. Dynamic fracture of a discrete media under moving load. arXiv:1701.02725, 2017.

[77] N.A. Gorbushin, G.A. Volkov, and Yu.V. Petrov. On the effect of the geometrical shape of a particle on threshold energy in erosion damage. *Technical Physics*, 58:388–392, 2013.

[78] E. Gordeliy and A. Peirce. Implicit level set schemes for modeling hydraulic fractures using the xfem. *Computer Methods in Applied Mechanics and Engineering*, 266:125–143, 2013.

[79] S.B. Gorell and G.M. Homsy. A theory of the optimal policy of oil recovery by secondary displacement processes. *SIAM Journal on Applied Mathematics*, 43(1):79–98, 1983.

[80] I.G. Goryacheva. *Contact Mechanics in Tribology*. Number 61 in Solid Mechanics and Its Applications. Springer Netherlands, 1998.

[81] I.G. Goryacheva and R.M. Martynyak. Contact problems for textured surfaces involving frictional effects. *Proceedings of the Institution of Mechanical Engineers, Part J: Journal of Engineering Tribology*, 228(7):707–716, 2014.

[82] I.S. Gradshteyn and I.M. Ryzhik. *Table of Integrals, Series, and Products (7th Edition)*. Academic Press, Amsterdam-Boston, 2007.

[83] J.E. Grady. Contact force history and dynamic response due to the impact of a soft projectile. Technical Report NASA-TM-100961, E-4035, NAS 1.15:100961, NASA Lewis Research Center, Cleveland, OH, United States, 1988.

[84] A.A. Griffith. The phenomena of rupture and flow in solids. *Philosophical Transactions of the Royal Society A*, 221:163–198, 1921.

[85] S.C. Gupta. *The Classical Stefan Problem: Basic Concepts, Modelling and Analysis*, volume 45 of *North-Holland Series in Applied Mathematics and Mechanics*. North-Holland, 2003.

[86] B. Gustafsson, R. Teodorescu, and A. Vasil'ev. *Classical and Stochastic Laplacian Growth*. Advances in Mathematical Fluid Mechanics. Springer, Birkhäuser, 2014.

[87] B. Gustafsson and A. Vasil'ev. *Conformal and Potential Analysis in Hele-Shaw cells*. Birkhäuser Verlag, Basel-Boston-Berlin, 2006.

[88] M.H. Gutknecht. Numerical conformal mapping methods based on function conjugation. *Journal of Computational and Applied Mathematics*, 14(1):31–77, 1986.

[89] J.W. Harding and I.N. Sneddon. The elastic stresses produced by the indentation of the plane surface of a semi-infinite elastic solid by a rigid punch. *Mathematical Proceedings of the Cambridge Philosophical Society*, 41(1):16–26, 1945.

[90] E. Harrison, W. Kieschnick, and W. McGuire. The mechanics of fracture induction and extension. *Petroleum Transactions, AIME*, 201:252–263, 1954.

[91] H.S. Hele-Shaw. The flow of water. *Nature*, 58(1489):33–36, 1898.

[92] W.H. Herschel and R. Bulkley. Konsistenzmessungen von gummi-benzollösungen (in german). *Colloid Journal*, 39:291–300, 1926.

[93] H. Hertz. Über die berührung fester elastischer körper (in german). *Journal für die reine und angewandte Matematik*, 92:156–171, 1881.

[94] H. Hertz. On hardness (in german). *Verhandlungen des Vereins zur Beförderung des Geweriefleisses*, 61:410–431, 1882.

[95] H. Hertz, D.E. Jones, and G.A. Schott. *Hertzs Miscellaneous Papers*. Macmillan & Co., London, 1896.

[96] R Hill and EH Lee. The theory of wedge penetration at oblique incidence and its application to the calculation of forces on a yawed shot impacting on armour plate at any angle. Technical report, Royal Armament Research and Development Establishment Fort Halstead (United Kingdom), 1946.

[97] Yu.E. Hohlov and M. Reissig. On classical solvability for the hele-shaw moving boundary problem with kinetic undercooling regularization. *European Journal of Applied Mathematics*, 6:421, 1995.

[98] H. Homma, D.A. Shockey, and Y. Murayama. Response of cracks in structural materials to short pulse loads. *Journal of the Mechanics and Physics of Solids*, 31(3):261–279, 1983.

[99] T.Y. Hou, Z. Li, S. Osher, and H. Zhao. A hybrid method for moving interface problems with application to the hele-shaw flow. *Journal of Computational Physics*, 134(2):236–252, 1997.

[100] S.D. Howison. Complex variable methods in hele-shaw moving boundary problems. *European Journal of Applied Mathematics*, 3(3):209–224, 1992.

[101] C.K. Hsieh. Exact solutions of stefan problems for a heat front moving at constant velocity in a quasi-steady state. *International Journal of Heat and Mass Transfer*, 38(1):71–79, 1995.

[102] Y.S. Huang and C.Y. Chen. A numerical study on radial hele-shaw flow: influence of fluid miscibility and injection scheme. *Computational Mechanics*, 55(2):407–420, 2015.

[103] M. Hubbert and D. Willis. Mechanics of hydraulic fracturing. *Journal of Petroleum Technology*, 9(6):153–168, 1957.

[104] G.R. Irwin. Analysis of stresses and strains near the end of a crack traversing a plate. *Journal of Applied Mechanics*, 24:361–364, 1957.

[105] K.A. Iyer. Relationships between multiaxial stress states and internal fracture patterns in sphere-impacted silicon carbide. *International Journal of Fracture*, 146:1–18, 2007.

[106] J. Jaeger. Analytical solutions of contact impact problems. *Applied Mechanics Reviews*, 47(2):35–54, 1994.

[107] W. Jianming, L. Feihong, Y. Feng, and Z. Gang. Shot peening simulation based on sph method. *International Journal of Advanced Manufacturing Technology*, 56:571–578, 2011.

[108] K.L. Johnson. *Contact Mechanics*. Cambridge Univ. Press, Cambridge, UK, 1985.

[109] J. Lankford Jr. The role of dynamic material properties in the performance of ceramic armor. *International Journal of Applied Ceramic Technology*, 1(3):205–210, 2004.

[110] J.F. Kalthoff and D.A. Shockey. Instability of cracks under impulse loads. *Journal of Applied Physics*, 48:986–993, 1977.

[111] S. Kanaun. Discrete model of hydraulic fracture crack propagation in homogeneous isotropic elastic media. *International Journal of Engineering Science*, 110:1–14, 2017.

[112] N.A. Kazarinov, A.D. Evstifeev, Y.V. Petrov, and V.A. Lashkov. Investigation of surface properties of ultrafine-grained aluminum alloy subjected to high speed erosion. *Doklady Physics*, 61(5):232–234, 2016.

[113] L.M. Keer, V.K. Luk, and J.M. Freedman. Circumferential edge crack in a cylindrical cavity. *Journal of Applied Mechanics*, 44(2):250–254, 1977.

[114] L.F. Kemp. Study of nordgren's equation of hydraulic fracturing. *SPE Production Engineering*, 5:311–314, 1990.

[115] K. Kendall. *Molecular Adhesion and Its Applications*. Springer US / Kluwer Academic Publishers, 2001.

[116] S. Khristianovic and Y. Zheltov. Formation of vertical fractures by means of highly viscous liquid. In *Proceedings of the fourth world petroleum congress*, pages 579–586, Rome, 1955.

[117] N.A. Kilchevsky. *The theory of solid bodies collision (in Russian)*. Naukova Dumka, Kiev, 1969.

[118] P. Kusmierczyk, G. Mishuris, and M. Wrobel. Remarks on numerical simulation of the pkn model of hydrofracturing in proper variables. various leak-off regimes. *International Journal of Fracture*, 184:185–213, 2013.

[119] V.A. Kuzkin, A.M. Krivtsov, and A.M. Linkov. Computer simulation of effective viscosity of fluid-proppant mixture used in hydraulic fracturing. *Journal of Mining Science*, 50(1):1–9, 2014.

[120] A. Lavrov. Flow of truncated power-law fluid between parallel walls for hydraulic fracturing applications. *Journal of Non-Newtonian Fluid Mechanics*, 223:141–146, 2015.

[121] A. Lavrov and H. Laux. Dem modeling of particle restitution coefficient vs stokes number: The role of lubrication force (paper s2_thu_c_54). *6th International Conference on Multiphase Flow (ICMF 2007)*, 2007.

[122] B. Lecampion and J. Desroches. Simultaneous initiation and growth of multiple radial hydraulic fractures from a horizontal wellbore. *Journal of the Mechanics and Physics of Solids*, 82:235–258, 2015.

[123] B. Lecampion, J. Desroches, R.G. Jeffrey, and A.P. Bunger. Experiments versus theory for the initiation and propagation of radial hydraulic fractures in low-permeability materials. *Journal of Geophysical Research: Solid Earth*, 122(2):1239–1263, 2017.

[124] B. Lecampion and E. Detournay. An implicit algorithm for the propagation of a hydraulic fracture with a fluid lag. *Computer Methods in Applied Mechanics and Engineering*, 196(49-52):4863–4880, 2007.

[125] B. Lecampion, A. Peirce, and E. Detournay et al. The impact of near tip logic on the accuracy and convergence of hydraulic fracture simulators compared to reference solutions. In A.P. Bunger, J. McLennan, and R. Jeffrey, editors, *Effective and Sustainable Hydraulic Fracturing*, pages 856–873. InTech, Croatia, www.intechopen.com, 2013.

[126] X-J.J. Li and Y. Zhou. *Microfluidic Devices for Biomedical Applications*. Woodhead Publishing Series in Biomaterials. Woodhead Publishing, 2013.

[127] A.M. Linkov. Speed equation and its application for solving ill-posed problems of hydraulic fracturing. *Doklady Physics*, 56(8):436–438, 2011.

[128] A.M. Linkov. On efficient simulation of hydraulic fracturing in terms of particle velocity. *International Journal of Engineering Science*, 52:77–88, 2012.

[129] A.M. Linkov. Analytical solution of hydraulic fracture problem for a non-newtonian fluid. *Journal of Mining Science*, 49(1):8–18, 2013.

[130] A.M. Linkov. Solution of hydraulic fracture problem accounting for lag. arXiv:1404.5246, 2014.

[131] A.M. Linkov. Bench-mark solution for a penny-shaped hydraulic fracture driven by a thinning fluid. arXiv:1508.07968, 2015.

[132] A.M. Linkov. Solution of axisymmetric hydraulic fracture problem for thinning fluids. *Journal of Applied Mathematics and Mechanics*, 80(2):207–217, 2016.

[133] H. Luo and C. Pozrikidis. Effect of surface slip on stokes flow past a spherical particle in infinite fluid and near a plane wall. *Journal of Engineering Mathematics*, 62(1):1–21, 2008.

[134] M. Mack and N. Warpinski. Mechanics of hydraulic fracturing. In M. Economides and K. Nolte, editors, *Reservoir Simulation*, pages Chap. 6.1–6.49. John Willey& Sons, Chichester, 2000.

[135] B. Marks, B. Sandnes, G. Dumazer, J.A. Eriksen, and J.K. Måløy. Compaction of granular material inside confined geometries. *Frontiers in Physics*, 3:41, 2015.

[136] J.S. Marshall. Analytical solutions for hele-shaw moving boundary flows in the presence of a circular cylinder. *The Quarterly Journal of Mechanics & Applied Mathematics*, 69(1):1–33, 2016.

[137] J.S. Marshall. Exact solutions for hele-shaw free boundary flows around a flat plate of finite length. *The Quarterly Journal of Mechanics & Applied Mathematics*, 69(1):35–66, 2016.

[138] V. Maz'ya, A. Movchan, and M. Nieves. *Operator Theory and Its Applications. In Memory of V.B. Lidskii (1924–2008): Green's kernels for transmission problems in bodies with small inclusions (p.127-160)*. AMS, Providence, Rhode Island, 2010.

[139] V. Maz'ya, A. Movchan, and M. Nieves. *Green's Kernel and Meso-Scale Approximations in Perforated Domains*. Number 2077 in Lecture Notes in Mathematics. Springer, Heidelberg, 2013.

[140] K.V. McCloud and J.V. Maher. Experimental perturbations to saffman-taylor flow. *Physics Reports*, 260(3):139–185, 1995.

[141] N.Robb McDonald. Computation of hele-shaw free boundary problems near obstacles. *Theoretical and Computational Fluid Dynamics*, 24:537–550, 2010.

[142] H.J. Melosh. *Impact cratering: a geologic process*. Oxford monographs on geology and geophysics. Oxford University Press, 1989.

[143] B.R. Meyer. Three-dimensional hydraulic fracturing simulation on personal computers: Theory and comparison studies. In *SPE-19329-MS*, pages 213–230, SPE Eastern Regional Meeting, 24-27 October, Morgantown, West Virginia, 1989. Society of Petroleum Engineers.

[144] A. Mikelić, M.F. Wheeler, and T. Wick. Phase-field modeling of a fluid-driven fracture in a poroelastic medium. *Computational Geosciences*, 19:1171–1195, 2015.

[145] G. Mishuris, S. Rogosin, and M. Wrobel. Hele-shaw flow with a small obstacle. *Meccanica*, 49:2037, 2014.

[146] G. Mishuris, S. Rogosin, and M. Wrobel. Moving stone in the hele-shaw flow. *LMS J. Mathematika*, 61(2):457, 2015.

[147] G. Mishuris, M. Wrobel, and A.M. Linkov. On modeling hydraulic fracture in proper variables: stiffness, accuracy, sensitivity. *International Journal of Engineering Science*, 61:10–23, 2012.

[148] M. Mooney. The viscosity of a concentrated suspension of spherical particles. *Journal of Colloid Science*, 6(2):162–170, 1951.

[149] N. Morozov and Y. Petrov. *Dynamics of Fracture*. Springer-Verlag, Berlin Heidelberg, 2000.

[150] N.F. Morozov, Yu.V. Petrov, B. Ivanov, M.Ya. Marov, and V.I. Smirnov. Prediction of the threshold fracture energy in impact cratering mechanics. *Doklady Physics*, 52(1):41–43, 2007.

[151] S. Nadimi, I. Miscovic, and J. McLennan. A 3d peridynamic simulation of hydraulic fracture process in a heterogeneous medium. *Journal of Petroleum Science and Engineering*, 145:444–452, 2016.

[152] C.E. Neal-Sturgess. A direct derivation of the griffith-irwin relationship using a crack tip unloading stress wave model. arXiv:0810.2218, 2008.

[153] S. Nemat-Nasser, H. Abé, and S. Hirakawa. *Mechanics of elastic and inelastic solids 5: Hydraulic fracturing and geothermal energy*. Springer, Netherlands, 1983.

[154] N.T. Nguyen, T.Q. Bui, and T.T. Truong. Transient dynamic fracture analysis by an extended meshfree method with different crack-tip enrichments. *Meccanica*, 52(10):2363–2390, 2017.

[155] M. Nieves. Asymptotic analysis of solutions to transmission problems in solids with many inclusions. arXiv:1607.06347, 2016.

[156] R. Nordgren. Propagation of a vertical hydraulic fracture. *Journal of Petroleum Technology*, 253:306–314, 1972.

[157] J. R. Ockendon. The role of the crank-gupta model in the theory of free and moving boundary problems. *Advances in Computational Mathematics*, 6:281–293, 1996.

[158] A.A. Osiptsov. Fluid mechanics of hydraulic fracturing: a review. *Journal of Petroleum Science and Engineering*, 156:513–535, 2017.

[159] Zh-Ch. Ou, C. Yan, Zh-Pi Duan, Ai-Gu. Pi, and Fe-Le. Huang. Dynamic behaviors of load-carrying capacity of brittle materials. *International Journal of Impact Engineering*, 42:59–65, 2012.

[160] N. Papamichael. *Lectures on Numerical Conformal Mapping*. University of Cyprus, 2008.

[161] A. Peirce and E. Detournay. An implicit level set method for modeling hydraulically driven fractures. *Computational Methods in Applied Mathematics and Engineering*, 197:2858–2885, 2008.

[162] G.S. Penny, H.E. Ripley, M.W. Conway, and W.S. Lee. The control and modelling of fluid leak-off during hydraulic fracturing. Report PETSOC-84-35-28, Petroleum Society of Canada, 1984.

[163] T. Perkins and L. Kern. Widths of hydraulic fractures. *Journal of Petroleum Technology*, 13 (9):937–949. SPE–89–PA, 1961.

[164] M. Perkowska. *Mathematical and numerical modeling of hydraulic fractures for non-Newtonian fluids.* PhD thesis, Aberystwyth University, http://cadair.aber.ac.uk/dspace/handle/2160/42786, 2016.

[165] M. Perkowska, M. Wrobel, and G. Mishuris. Universal hydrofracturing algorithm for shear-thinning fluids: particle velocity based simulation. *Computers and Geotechnics*, 71:310–377, 2016.

[166] Y. Petrov. Incubation time based fracture mechanics. *19th European Conference on Fracture, Fracture Mechanics for Durability*, 2012.

[167] Y. Petrov. Fracture, electric breakdown and phase transformations under impact loading. *Procedia Materials Science*, 3:467–472, 2014.

[168] Y. Petrov, V. Bratov, G. Volkov, and E. Dolmatov. Incubation time based fracture mechanics and optimization of energy input in the fracture process of rocks. In Y. Zhou and J. Zhao, editors, *Advances in Rock Dynamics and Applications*, pages 163–183. CRC Press, Boca Raton, 2011.

[169] Yu. V. Petrov and V. I. Smirnov. Interrelation between the threshold characteristics of erosion and spall fracture. *Technical Physics*, 55:23, 2010.

[170] Yu.V. Petrov. On the incubation stage of fracture and structural transformations in continuous media under pulse energy injection. *Mechanics of Solids*, 42:692–699, 2007.

[171] Yu.V. Petrov and Y.V. Sitnikova. Temperature dependence of spall strength and the effect of anomalous melting temperatures in shock-wave loading. *Technical Physics*, 50(8):1034–1037, 2005.

[172] Y.V. Petrov. Incubation time criterion and the pulsed strength of continua: fracture, cavitation, and electrical breakdown. *Doklady Phys*, 49:246, 2004.

[173] Y.V. Petrov, N.F. Morozov, and V.I. Smirnov. Structural macromechanics approach in dynamics of fracture. *Fatigue and Fracture of Engineering Materials and Structures*, 26:363–372, 2003.

[174] Y.V. Petrov and A.A. Utkin. Dependence of the dynamic strength on loading rate. *Soviet Materials Science*, 25(2):153–156, 1989.

[175] W.J. Phillips. Hydraulic fracturing and mineralization. *Journal of the Geological Society*, 128(4):337–359, 1972.

[176] A. Piccolroaz and G. Mishuris. Integral identities for a semi-infinite interfacial crack in 2d and 3d elasticity. *Journal of Elasticity*, 110:117–140, 2013.

[177] F. Pizzocolo, J.M. Huyghe, and K. Ito. Mode i crack propagation in hydrogels is step wise. *Engineering Fracture Mechanics*, 97:72–79, 2013.

[178] P.Ya. Polubarinova-Kochina. Concerning unsteady motions in the theory of filtration (in russian). *Prikl. Matem. Mech.*, 9:79–90, 1945.

[179] P.Ya. Polubarinova-Kochina. On a problem of the motion of the contour of a petroleum shell (in russian). *Doklady Akademii Nauk USSR*, 47:254–257, 1945.

[180] C. Pozrikidis. The motion of particles in the hele-shaw cell. *Journal of Fluid Mechanics*, 261:199–222, 1994.

[181] O. Praud and H.L. Swinney. Fractal dimension and unscreened angles measured for radial viscous fingering. *Physical Review E*, 72:011406, 2005.

[182] C.M. Preece. *Treatise on Materials Science and Technology 16: Erosion*. Academic Press, New York, 1979.

[183] M. Reissig, S.V. Rogosin, and F. Hübner. Analytical and numerical treatment of a complex model for hele-shaw moving boundary value problems with kinetic undercooling regularization. *European Journal of Applied Mathematics*, 10(6):561–579, 1999.

[184] J. Rice. Mathematical analysis in the mechanics of fracture. In H. Liebowitz, editor, *Fracture: an Advanced Treatise vol.2*, pages 191–311. Academic Press, New York, 1968.

[185] J.R. Rice. A path independent integral and the approximate analysis of strain concentration by notches and cracks. *Journal of Applied Mechanics*, 35:379–386, 1968.

[186] S. Richardson. Hele shaw flows with a free boundary produced by the injection of fluid into a narrow channel. *Journal of Fluid Mechanics*, 56(4):609, 1972.

[187] S. Richardson. Some hele-shaw flows with time-dependent free boundaries. *Journal of Fluid Mechanics*, 102:263–278, 1981.

[188] S. Richardson. Hele-shaw flows with free boundaries in a corner or around a wedge part i: Liquid at the vertex. *European Journal of Applied Mathematics*, 12:665–676, 2001.

[189] S. Richardson. Hele-shaw flows with free boundaries in a corner or around a wedge part ii: Air at the vertex. *European Journal of Applied Mathematics*, 12:677–688, 2001.

[190] S. Rogosin. Real variable hele-shaw problem with kinetic undercooling. *Lobachevskii Journal of Mathematics*, 38(3):510–519, 2017.

[191] L.A. Romero. *I. Similarity solutions of the equations of three phase flow through porous media. II. The fingering problem in a Hele-Shaw cell.* PhD thesis, California Institute of Technology, http://resolver.caltech.edu/CaltechETD:etd-09082006-131345, 1982.

[192] O.G. Ruehr. *Analytical-Numerical Treatment of the One-Phase Stefan Problem with Constant Applied Heat Flux*, pages 215–220. Birkhäuser Boston, Boston, MA, 2002.

[193] P.G. Saffman. Viscous fingering in hele-shaw cells. *Journal of Fluid Mechanics*, 173:73–94, 1986.

[194] P.G. Saffman and G. Taylor. The penetration of a fluid into a porous medium or hele-shaw cell containing a more viscous liquid. *Proceedings of the Royal Society of London A: Mathematical, Physical and Engineering Sciences*, 245(1242):312–329, 1958.

[195] S. Satapathy. Dynamic spherical cavity expansion in brittle ceramics. *International Journal of Solids and Structures*, 38:5833–5845, 2001.

[196] A.A. Savitski and E. Detournay. Propagation of a penny-shaped fluid-driven fracture in an impermeable rock: asymptotic solutions. *International Journal of Solids and Structures*, 39:6311–6337, 2002.

[197] C.B. Shah and Y.C. Yortsos. Aspects of flow of power-law fluids in porous media. *AIChE Journal*, 41:1099–1112, 1995.

[198] I.Ya. Shtaerman. On the hertz theory of local deformations resulting from the pressure of elastic solids (in russian). *Doklady Akad Nauk SSSR*, 25:360–362, 1939.

[199] I.Ya. Shtaerman. *Contact problem of the theory of elasticity (English translation).* Foreign Technology Division, Wright-Patterson Air Force Base, Ohio, 1970.

[200] M. Śledź, Ł. Bąk, F. Stachowicz, and W. Zielecki. Analysis of the effect of shot peening on mechanical properties of steel sheets used as screener sieve materials. *Journal of Physics: Conference Series*, 451(1):012029, 2013.

[201] L.I. Slepyan. *Models and Phenomena in Fracture Mechanics*. Springer-Verlag, Berlin Heidelberg, 2002.

[202] L.I. Slepyan, A.B. Movchan, and G.S. Mishuris. Crack in a lattice waveguide. *International Journal of Fracture*, 162:91–106, 2010.

[203] I.N. Sneddon. Boussinesq's problem for a flat-ended cylinder. *Mathematical Proceedings of the Cambridge Philosophical Society*, 42(1):29–39, 1946.

[204] I.N. Sneddon. The distribution of stress in the neighbourhood of a crack in an elastic solid. *Proceedings of the Royal Society A*, 187:229–260, 1946.

[205] I.N. Sneddon. Boussinesq's problem for a rigid cone. *Mathematical Proceedings of the Cambridge Philosophical Society*, 44(4):492–507, 1948.

[206] I.A. Soldatenkov. Indentation with adhesion of a symmetrical punch into an elastic half-plane. *Journal of Applied Mathematics and Mechanics*, 60(2):261–267, 1996.

[207] D. Spence and P. Sharp. Self-similar solutions for elastohydrodynamic cavity flow. *Proceedings of the Royal Society A*, 400:289–313, 1985.

[208] J. Stefan. Über einige probleme der theorie der wärmeleitung (in german). *Sitzungsber. Akad. Wiss. Berlin Math. Kl.*, 98:473–484, 1889.

[209] J. Stefan. Über die theorie der eisbildung, insbesondere über die eisbildung in polarmeere (in german). *Ann. Physik Chemie*, 42:269–286, 1891.

[210] C. Storey. Investigation into one of the assumptions of the hertz theory of contact. *British Journal of Applied Physics*, 11(2):67–68, 1960.

[211] P. Tabeling, G. Zocchi, and A. Libchaber. *An Experimental Study of the Saffman Taylor Instability*, pages 515–525. Springer US, Boston, MA, 1988.

[212] M. Tehranirokh, A.Z. Kouzani, P.S. Francis, and J.R. Kanwar. Microfluidic devices for cell cultivation and proliferation. *Biomicrofluidics*, 7(5):051502, 2013.

[213] D.G. Thomas. Transport characteristics of suspension: Viii. a note on the viscosity of newtonian suspensions of uniform spherical particles. *Journal of Colloid Science*, 20(3):267–277, 1965.

[214] J.C. Thompson and A.R. Robinson. An exact solution for the superseismic stage of dynamic contact between a punch and an elastic body. *Journal of Applied Mechanics*, 44:583–586, 1977.

[215] G.P. Tilly. A two stage mechanism of ductile erosion. *Wear*, 23:87–96, 1973.

[216] G. Tran, H. Schaeffer, W.M. Feldman, and S.J. Osher. An l^1 penalty method for general obstacle problems. *SIAM Journal on Applied Mathematics*, 75(4):1424–1444, 2015.

[217] L.N. Trefethen. Numerical computation of the schwarz-christoffel transformation. *Journal on Scientific and Statistical Computing*, 1(1):82–102, 1980.

[218] V. Tsai and J. Rice. A model for turbulent hydraulic fracture and application to crack propagation at glacier beds. *Journal of Geophysical Research*, 115:1–18, 2010.

[219] P. Valk and M.J. Economides. *Hydraulic Fracture Mechanics*. John Wiley & Sons, Chichester, 1995.

[220] V. Vand. Viscosity of solutions and suspensions; experimental determination of the viscosity-concentration function of spherical suspensions. *The Journal of Physical and Colloid Chemistry*, 52(2):300–314, 1948.

[221] L. Vandamme and J. Curran. A three-dimensional hydraulic fracturing simulator. *International Journal for Numerical Methods in Engineering*, 28:909–927, 1989.

[222] G.L. Vasconcelos. Comment on free surface hele-shaw flows around an obstacle: A random walk simulation. *Physical Review E*, 76:038301, 2007.

[223] A. Vasil'ev. From the hele-shaw experiment to integrable systems: A historical overview. *Complex Analysis and Operator Theory*, 3:551–585, 2009.

[224] G.A. Volkov, N.A. Gorbushin, and Yu.V. Petrov. On the dependence of the threshold energy of small erodent particles on their geometry in erosion fracture. *Mechanics of Solids*, 47(5):491–497, 2012.

[225] C. Vuik. Some historical notes about the stefan problem, 1993.

[226] M. Wang, N.A. Fleck, and A.G. Evans. Elastodynamic erosion of thermal barrier coatings. *Journal of the American Ceramic Society*, 94:s160–s167, 2011.

[227] Y-F. Wang and Z-G. Yang. Finite element model of erosive wear on ductile and brittle materials. *Wear*, 265:871–878, 2008.

[228] M. Wrobel and G. Mishuris. Efficient pseudo-spectral solvers for the pkn model of hydrofracturing. *International Journal of Fracture*, 184:151–170, 2013.

[229] M. Wrobel and G. Mishuris. Hydraulic fracture revisited: Particle velocity based simulation. *International Journal of Engineering Science*, 94:23–58, 2015.

[230] M. Wrobel, G. Mishuris, and A. Piccolroaz. Energy release rate in hydraulic fracture: Can we neglect an impact of the hydraulically induced shear stress? *International Journal of Engineering Science*, 111:28–51, 2017.

[231] Q. Zhou, N. Li, X. Chen, T. Xu, S. Hui, and D. Zhang. Analysis of water drop erosion on turbine blades based on a nonlinear liquidsolid impact model. *International Journal of Impact Engineering*, 36(9):1156–1171, 2009.

[232] H.P. Zhu, Z.Y. Zhou, R.Y. Yang, and A.B. Yu. Discrete particle simulation of particulate systems: Theoretical developments. *Chemical Engineering Science*, 62:3378, 2007.